Plant Organic Matter Mobilization and Export in Fluvial Systems

A case study from the eastern Nepalese Arun Valley

Kumulative

D I S S E R T A T I O N

zur Erlangung des akademischen Titels

Doctor rerum naturalium
im Fach Geologie

eingereicht an der
Mathematisch-Naturwissenschaftlichen Fakultät
Universität Potsdam

von
Dipl.-Geol. Bernd Hoffmann

Gutachter: Dr. Dirk Sachse
Ass. Prof. Sarah Feakins, PhD
Dr. Robert G. Hilton

Eingereicht am: 13.04.2016

Published online at the
Institutional Repository of the University of Potsdam:
URN urn:nbn:de:kobv:517-opus4-99336
http://nbn-resolving.de/urn:nbn:de:kobv:517-opus4-99336

Gewidmet meiner Schwester.

Abstract

The global carbon cycle is closely linked to Earth's climate. In the context of continuously unchecked anthropogenic CO_2 emissions, the importance of natural CO_2 bond and carbon storage is increasing. An important biogenic mechanism of natural atmospheric CO_2 drawdown is the photosynthetic carbon fixation in plants and the subsequent long-term deposition of plant detritus in sediments.

The main objective of this thesis is to identify factors that control mobilization and transport of plant organic matter (pOM) through rivers towards sedimentation basins. I investigated this aspect in the eastern Nepalese Arun Valley. The trans-Himalayan Arun River is characterized by a strong elevation gradient ($205 - 8848\ m\ asl$) that is accompanied by strong changes in ecology and climate ranging from wet tropical conditions in the Himalayan forelad to high alpine tundra on the Tibetan Plateau. Therefore, the Arun is an excellent natural laboratory, allowing the investigation of the effect of vegetation cover, climate, and topography on plant organic matter mobilization and export in tributaries along the gradient.

Based on hydrogen isotope measurements of plant waxes sampled along the Arun River and its tributaries, I first developed a model that allows for an indirect quantification of pOM contributed to the mainsetm by the Arun's tributaries. In order to determine the role of climatic and topographic parameters of sampled tributary catchments, I looked for significant statistical relations between the amount of tributary pOM export and tributary characteristics (e.g. catchment size, plant cover, annual precipitation or runoff, topographic measures). On one hand, I demonstrated that pOMsourced from the Arun is not uniformly derived from its entire catchment area. On the other, I showed that dense vegetation is a necessary, but not sufficient, criterion for high tributary pOM export. Instead, I identified erosion and rainfall and runoff as key factors controlling pOM sourcing in the Arun Valley. This finding is supported by terrestrial cosmogenic nuclide concentrations measured on river sands along the Arun and its tributaries in order to quantify catchment wide denudation rates. Highest denudation rates corresponded well with maximum pOM mobilization and export also suggesting the link between erosion and pOM sourcing.

The second part of this thesis focusses on the applicability of stable isotope records such as plant wax *n*-alkanes in sediment archives as qualitative and quantitative proxy

for the variability of past Indian Summer Monsoon (ISM) strength. First, I determined how ISM strength affects the hydrogen and oxygen stable isotopic composition (reported as δD and δ^{18}O values vs. Vienna Standard Mean Ocean Water) of precipitation in the Arun Valley and if this *amount effect* (Dansgaard, 1964) is strong enough to be recorded in potential paleo-ISM isotope proxies. Second, I investigated if potential isotope records across the Arun catchment reflect ISM strength dependent precipitation δD values only, or if the ISM isotope signal is superimposed by winter precipitation or glacial melt. Furthermore, I tested if δD values of plant waxes in fluvial deposits reflect δD values of environmental waters in the respective catchments.

I showed that surface water δD values in the Arun Valley and precipitation δD from south of the Himalaya both changed similarly during two consecutive years (2011 & 2012) with distinct ISM rainfall amounts (~20% less in 2012). In order to evaluate the effect of other water sources (Winter-Westerly precipitation, glacial melt) and evapotranspiration in the Arun Valley, I analysed satellite remote sensing data of rainfall distribution (TRMM 3B42V7), snow cover (MODIS MOD10C1), glacial coverage (GLIMS-database, Global Land Ice Measurements from Space), and evapotranspiration (MODIS MOD16A2). In addition to the predominant ISM in the entire catchment I found through stable isotope analysis of surface waters indications for a considerable amount of glacial melt derived from high altitude tributaries and the Tibetan Plateau. Remotely sensed snow cover data revealed that the upper portion of the Arun also receives considerable winter precipitation, but the effect of snow melt on the Arun Valley hydrology could not be evaluated as it takes place in early summer, several months prior to our sampling campaigns. However, I infer that plant wax records and other potential stable isotope proxy archives below the snowline are well-suited for qualitative, and potentially quantitative, reconstructions of past changes of ISM strength.

Zusammenfassung

Da der globale Kohlenstoffkreislauf stark mit dem Klima der Erde verknüpft ist, sind im Zusammenhang mit dem weiterhin ungebremsten anthropogenen CO_2-Ausstoß die natürliche Bindung von CO_2 und die langfristige Speicherung von Kohlenstoff um so wichtiger. Einer der wesentlichen Mechanismen des natürlichen CO_2-Abbaus ist die photosynthetische Kohlenstoffbindung in Pflanzen verknüpft mit der anschließenden langfristigen Ablagerung von Pflanzenmaterial in Sedimenten.

Hauptziel der vorliegenden Dissertation ist daher, jene Faktoren zu identifizieren, die für den Abtransport toten Pflanzenmaterials in Flüssen hin zu Sedimentationsräumen verantwortlich sind. Das entsprechende Untersuchungsgebiet ist das ost-nepalesische Arun Tal. Der Arun durchschneidet den Himalaya von Nord nach Süd und sein Einzugsgebiet ist geprägt vom stärksten Höhengradienten der Erde (8848-205 *m ü.N.N.*). Entsprechend durchfließt er mehrere Klimazonen von alpiner Tundra auf dem Tibetischen Plateau hin zu subtropischen Bedingungen im Süden Nepals. Wegen dieses starken Gefälles bietet der Arun die Möglichkeit, die Mobilisierung und den Abtransport von Pflanzenmaterial unter sehr unterschiedlichen klimatischen, ökologischen und topographischen Gegenbenheiten zu untersuchen.

Zunächst entwickelte ich ein auf Wasserstoff-Isotopen-Messungen an Pflanzenwachsen in Flusssedimenten basierendes Modell, das es ermöglicht, indirekt den Pflanzendetritus-Beitrag der Nebenflüsse in Relation zur Gesamtmasse des vom Arun abtransportierten Pflanzenmaterials zu quantifizieren. Um jene klimatischen und topografischen Eigenschaften der Seitenflüsse zu ermitteln, welche die jeweils exportierte Menge an Pflanzenmaterial kontrollieren, suchte ich im nächsten Schritt nach einem statistischen Zusammenhang zwischen exportierten Pflanzenrestmengen der Nebenflüsse sowie der Größe ihrer Einzugsgebiete, Pflanzenbedeckung, Niederschlagsmenge (bzw. Abfluss), und ihrer Topografie als Maß für Erosionsvermögen. Mit diesen Methoden kann ich einerseits klar belegen, dass das vom Arun transportierte Pflanzenmaterial nicht flächendeckend gleichmäßig aus seinem Einzugsgebiet stammt. Andererseits zeigt sich, dass dichter Pflanzenbewuchs zwar ein notwendiges, jedoch kein hinreichendes Kriterium für hohe Exportraten ist. Meine Untersuchung im Arun Tal führte letztlich zu dem Ergebnis, dass die für die Mobilisierung und den Export von Pflanzenmaterial wesentlichen Faktoren Niederschlagsmenge und Erosion sind, wobei Pflanzenbedeckung zwar vorausgesetzt ist, oft jedoch als Resultat hohen Niederschlags auftritt. Dass Erosion hierbei eine Schlüsselrolle

zukommt, legt auch die Analyse von kosmogenen Nuklid-Konzentrationen in Flusssanden zur Bestimmung von Erosionsraten nahe. Ich fand eine sehr gute räumliche Übereinstimmung von hohen Erosionsraten und maximalem Pflanzendetritus-Abtransport, die den Zusammenhang beider Parameter zusätzlich belegt.

Der zweite, im Rahmen der beschriebenen Untersuchung näher beleuchtete Aspekt, ist die potentielle Nutzung der Isotopenzusammensetzung von in Sedimenten enthaltenen Pflanzenwachsen als quantitativer Marker für Monsun-Variabilität in der Vergangenheit. Voraussetzung für eine entsprechende Nutzung ist einerseits, dass sich Schwankungen der Monsun-Intensität in der Isotopie des Regenwassers niederschlagen (der sogenannte *amount effect*, Dansgaard, 1964) und andererseits, dass die Blattwachsproduzierenden Pflanzen Monsun-Wasser aufnehmen und ausschließlich dessen Isotopie in ihre Blattwachse übernehmen.

Die erste Voraussetzung konnte ich als gegeben bestätigen, da sich die Isotopenzusammensetzung der Oberflächenwasser im Arun-Tal während zwei aufeinanderfolgender, sehr unterschiedlich starker Monsun-Regenzeiten (2011 & 2012) gleichermaßen änderte, wie es an einer Wetterstation südlich des Himalaya in Bangladesh beobachtet wurde. Zur Überprüfung der zweiten Bedingung wurde zunächst mit Fernerkundungsmethoden die Regenverteilung (TRMM 3B42V7) und Schneebedeckung (MODIS MOD10C1) im Arun-Tal vor und während der Probenkampagnen 2011 und 2012 ausgewertet. Unter Hinzuziehung der stabilen Wasserstoff und Sauerstoff Isotopen-Messungen an Oberflächenwassern konnte der Einfluss verschiedener Wasserquellen (Indischer Sommer-Monsun, Schnee der Winter-Westwinde, Gletscherschmelze) sehr gut beurteilt werden: Ich konnte zeigen, dass der Arun-Fluss stark von Monsun und Eisschmelze beeinflusst wird und dass darum davon auszugehen ist, dass Blattwachse seines Einzugsgebietes nicht nur die Isotopenzusammensetzung des Monsun-Regens repräsentieren. Die Nebenflüsse jedoch, welche südlich des Himalaya-Hauptkammes unterhalb der Schneegrenze liegen, sind klar dominiert von Monsun-Regen. Das bedeutet, dass potentielle stabile Isotopen-Archive in den entsprechenden Einzugsgebieten quantitativ interpretiert werden können und die Variabilität des Sommer-Monsuns in der Vergangenheit dort absolut rekonstruiert werden könnte.

Author Contributions

The present cumulative thesis comprises of three independent studies. At the time of thesis submission articles are published, accepted for publishing, or at least submitted.

Chapter 2
The Indian Summer Monsoon amount effect on surface water δD variability in the Arun Valley, Eastern Nepal

Bernd Hoffmann, Bodo Bookhagen, Frauke Barthold, Stephanie M. Olen, Dirk Sachse
Earth and Planetary Science Letters, 2016
EPSL–S–16–00571, submitted on April 13^{th}*, 2016*

Bernd Hoffmann, Bodo Bookhagen, and Dirk Sachse setup the design and strategy of the project. D.P. Adhikari contributed to the organization of field work. Bernd Hoffmann, Stephanie M. Olen, Bodo Bookhagen, and Dirk Sachse conducted field work and took samples. Bernd Hoffmann prepared samples for IRMS measurements, Frauke Barthold measured water stabel isotopic composition. Bernd Hoffmann and Bodo Bookhagen contributed to the remote sensing data analysis. Bernd Hoffmann wrote the manuscript with contributions from all co-authors.

Chapter 3
Climatic and geomorphic drivers of plant organic matter transport in the Arun River, E Nepal

Bernd Hoffmann, Sarah J. Feakins, Bodo Bookhagen, Stephanie M. Olen, Danda P. Adhikari, Janardan Mainali, Dirk Sachse
Earth and Planetary Science Letters, 2016
EPSL–D–15–01040R1, submitted on September 22^{nd}*, 2015*, accepted with revisions, revised manuscript from February 27^{th}, 2016

Bernd Hoffmann, Bodo Bookhagen, and Dirk Sachse setup the design and strategy of the project. D.P. Adhikari contributed to the organization of field work. Bernd

Hoffmann, Stephanie M. Olen, Bodo Bookhagen, Dirk Sachse, and Janardan Mainali conducted field work and took samples. Bernd Hoffmann did all laboratory work and measurements with guidance of Sara J. Feakins and Dirk Sachse. Bernd Hoffmann and Bodo Bookhagen contributed to the plant organic matter weighting scheme. Bernd Hoffmann wrote the manuscript with contributions from all co-authors.

Chapter 4

Understanding erosion rates in the Himalayan orogen: A case study from the Arun Valley

Stephanie M. Olen, Bodo Bookhagen, Bernd Hoffmann, Dirk Sachse, Danda P. Adhikari, and Manfred R. Strecker
Journal of Geophysical Research: Earth Surface, 2015
Issue 120
Pages 2080-2102
doi:10.1002/2014JF003410

Stephanie M. Olen, Bodo Bookhagen, and Manfred R. Strecker contributed to the design of the study. Stephanie M. Olen, Bodo Bookhagen, Bernd Hoffmann, Dirk Sachse, and D.P. Adhikari contributed to organizing and conducting field work, strategy and sample collection. Stephanie M. Olen and Bodo Bookhagen contributed to the analysis of ^{10}Be terrestrial cosmogenic nuclide samples in the laboratory and calculation of denudation rates. Stephanie M. Olen wrote the manuscript with contributions from all co-authors, including Bernd Hoffmann.

Table of Content

1 | Introduction

1.1 Motivation

The earth's climate and the global carbon cycle are coupled in multiple ways. The most obvious is the concentration of greenhouse gases (e.g. CO_2 and CH_4) in the atmosphere; the enrichment of greenhouse gases in the atmosphere leads to an increase of the global mean temperature. This has been well known for many years an has been discussed in the first scientific assessment report of the UNITED NATIONS' *Intergovernmental Panel on Climate Change (IPCC)* in 1990 (Houghton et al., 1990). In Earth's history, the variability of greenhouse gas concentrations in the atmosphere is assumed to be the key driver for climate warming and cooling on time scales from billions of years (e.g. Kasting and Ackerman, 1986; Hoffman et al., 1998) to centennial and decadal shifts (Stocker et al., 2013). In the context of the world's growing energy demand and the apparent approval of increasing CO_2 release though fossil carbon burning (coal, oil, gas), the process of natural atmospheric carbon burial as part of the global carbon cycle (fig. 1.1) is becoming increasingly important. This process is dominated by two major mechanisms: first, by silicate weathering and carbon fixation in secondary minerals, which can be schematically illustrated by

$$\begin{aligned} CaSiO_3 + 2CO_2 + 2H_2O &\rightarrow Ca^{2+} + 2HCO^{3-} + H_4SiO_4 \\ &\rightarrow CaCO_3 + SiO_2 + CO_2 + 2H_2O \end{aligned} \tag{1.1}$$

The second mechanism is mainly driven by plant photosynthesis and the fixation of atmospheric carbon in plant organic matter (OM). This can be illustrated best by the example of sugar, which is biosynthesized from atmospheric CO_2 and plant water. The endothermic photosynthesis requires sunlight and is accompanied by the release of O_2:

$$6CO_2 + 6H_2O \rightarrow C_6H_{12}O_6 + 6O_2 \tag{1.2}$$

Subsequent deposition of plant OM in sedimentary basins potentially leads to long term carbon burial (Berner, 1990; Burdige, 2005). For a long time it was assumed that silicate weathering is the major process of atmospheric carbon fixation on continents (equation 1.1, Raymo and Ruddiman, 1992; Molnar et al., 1993), but current scientific knowledge indicates an under–estimation of plant OM fixation rates (equation 1.2,

France-Lanord and Derry, 1997). This implies, that the latter process of long term carbon burial in the form of plant OM in sedimentary basins is mandatory for the balance of atmospheric CO_2 concentrations. In this dissertation, I address one vital segment of this atmospheric carbon burial process chain: I determine plant OM mobilization and export processes in fluvial systems using the eastern Nepalese Arun River as a case study. This trans-Himalayan river was chosen as research area because it represents the world's greatest altitude gradient ranging from 205 up to 8848 m asl. It provides excellent conditions across a transect of less than 150 km to study climatic and hydrological effects on erosion and plant OM mobilization and export in several distinct climate zones. Different methods and scientific techniques are applied in order to approach three main aspects of plant OM export from fluvial catchments with subsequent transport to sedimentary basins:

1. What is the source of plant-derived OM in the Arun Valley?

2. What are the main drivers controlling plant OM mobilization and export?

3. And how do independently determined erosion rates compare to plant OM source areas?

Hence, the main focus of the present thesis is deciphering plant OM sources in the Arun Valley and to determine drivers of plant OM export. As plant OM erosion processes are assumed to strongly depend on water availability, I first investigated water sources in the Arun Valley based on distinct hydrogen and oxygen stable isotope signatures of environmental water, combined with remote sensing data about rainfall and snow cover. The results of this study are presented in the submitted paper in chapter 2. Subsequently, I applied an organic-geochemistry approach combined with remote sensing data analysis in order to quantify and trace back plant wax sources in the Arun catchment. Findings of plant wax sourcing were used together with satellite remote sensing data, to test how different environmental parameters affect plant wax mobilization and export (described in chapter 3, 2^{nd} paper). In that context, I discuss the re-mobilization of petrogenic carbon (fig. 1.1) as a consequence of erosion and if it affects the applied methods in the Arun Valley. In chapter 4 (3^{rd} paper), I present a new dataset of erosion rates derived through terrestrial cosmogenic nuclide concentrations in tributary and main stem river deposits. If denudation and erosion are controlling plant organic matter mobilization, highest erosion rates should be in accordance with maximum plant OM sourcing. A synthesis of the three chapter's findings and implications for the global carbon cycle and other fields of earth and environmental sciences are summarized in the final résumé (chapter 5).

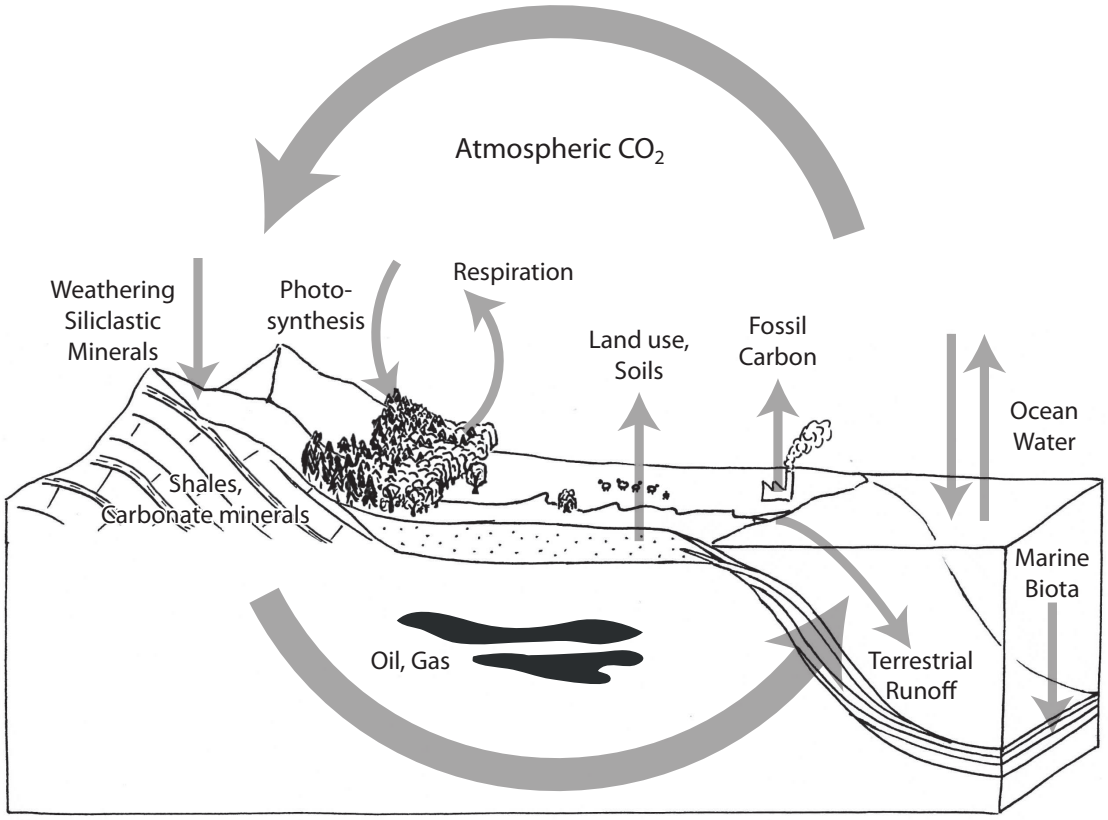

Figure 1.1: *Schematic of some of the most important processes of the global carbon cycle. Note the transport of terrestrial organic matter (Terrestrial Runoff, including plant detritus) to oceans, with part of it being stored in long term sinks in marine basins.*

1.2 Research Area

1.2.1 Geographic setting and Geology

The trans–Himalayan Arun River drains an area of 33.578 km^2, of which 84% are located on the southern Tibetan Plateau and the remaining 16% in eastern Nepal. Across a horizontal distance of ~120 km it covers the world's steepest altitudinal gradient from 205 $m\ asl$ at its confluence with the Tamor and Sapta Koshi Rivers, which drain adjacent catchments east and west of the Arun, to 8848 $m\ asl$ at Sagarmatha/Mt. Everest. South of the confluence, the river is called Sun Kosi, and joins the Ganges which subsequently empties into the Bay of Bengal in Bangladesh together with the Brahmaputra as Padma river.

The Arun catchment covers four major geological units: the northernmost part of the catchment on the Tibetan Plateau is dominated by the Tethyan Tibetan Zone (well preserved Cambrian to Eocene carbonate and siliclastic sedimentary rocks) bounded

southward by the South Tibetan Detachment (Bordet, 1961; Jessup et al., 2008; Quade et al., 2003; Stocklin, 1980) (fig. 4.1D and 4.2). South of the South Tibetan Detachment, the adjacent Greater or Higher Himalayan Crystallines are characterized by late Proterozoic to early Paleozoic paragneisses, calc–silicates and schist and form the prominent main Himalayan crest. The Main Central Thrust separates the Greater Himalayan Sequence from the oldest rocks in eastern Nepal, the Lesser Himalayan Sequence. The Lesser Himalayan Sequence is composed of early to middle Proterozoic orthogneisses, phyllite, augen-gneiss and quartzite. Focused fluvial incision along the Arun Valley forms a geologic window through the Main Central Thrust (DeCelles et al., 2000; Jessup et al., 2008; Quade et al., 2003; Stocklin, 1980). The Subhimalayan Zone is located between the Lesser Himalayan unit and the Indian plate and consists of Neogene foreland basin deposits (DeCelles et al., 2000). The Subhimalayan Zone is bounded by the Main Boundary Thrust in the north and the Main Frontal Thrust in the south (fig. 4.1D and 4.2).

As a consequence of sedimentary rock erosion, petrogenic carbon is potentially released (Galy et al., 2011) and mixed with recent plant OM in the Arun River. But of present geological units only Tethyan sedimentary rocks are a potential source of ancient organic matter contributing to the Arun's sediment load. For now I refer to Galy et al. (2007), who demonstrated that organic carbon draining the Sun Kosi River catchment is 0.05 kyr old ($cal.\ ^{14}C\ age$), implying a mostly negligible organic matter fraction of Neogene or older organic matter in the Arun River. A further, more detailed discussion about potential petrogenic carbon contributions in the Arun Valley is given in the discussion of chapter 3.

1.2.2 Climate and Hydrology of the Arun Valley

As both photosynthesis and pOM mobilization depend on the availability of water, the regional climate plays a key role in the processes I investigated. Therefore, understanding of regional climate characteristics is crucial. The eastern central Himalaya are characterized by a strong seasonal climate with heavy rainfall during the Indian Summer Monsoon (ISM) season. Due to strong summer insulation, heated air on the Tibetan Plateau rises. As a consequence, the Intertropical Convergence Zone migrates northward and moist air masses from the Arabian Sea and the nearby Bay of Bengal advance towards the Indian subcontinent (Charney, 1967; Gadgil, 2003). The southern Himalayan front acts as orographic barrier forcing the moist air to rise and rainout along the southern flanks of the orogen. The upper Arun Valley along the main Himalayan crest and the Tibetan Plateau possibly receive significant amounts of additional Winter Westerly disturbance snowfall with a Mediterranean moisture source (Bookhagen and Burbank, 2010; Hren et al., 2009; Wulf et al., 2016). The two moisture source domains are visualized by seasonal 72 h *HYSPLIT4* backward trajectory calculations based on NCEP/NCAR reanalysis data[1] shown in figure 1.3. Although winter precipitation is dominated by the

[1] National Centre for Environmental Prediction (NCEP) and National Centre for Atmospheric Research (NCAR), US

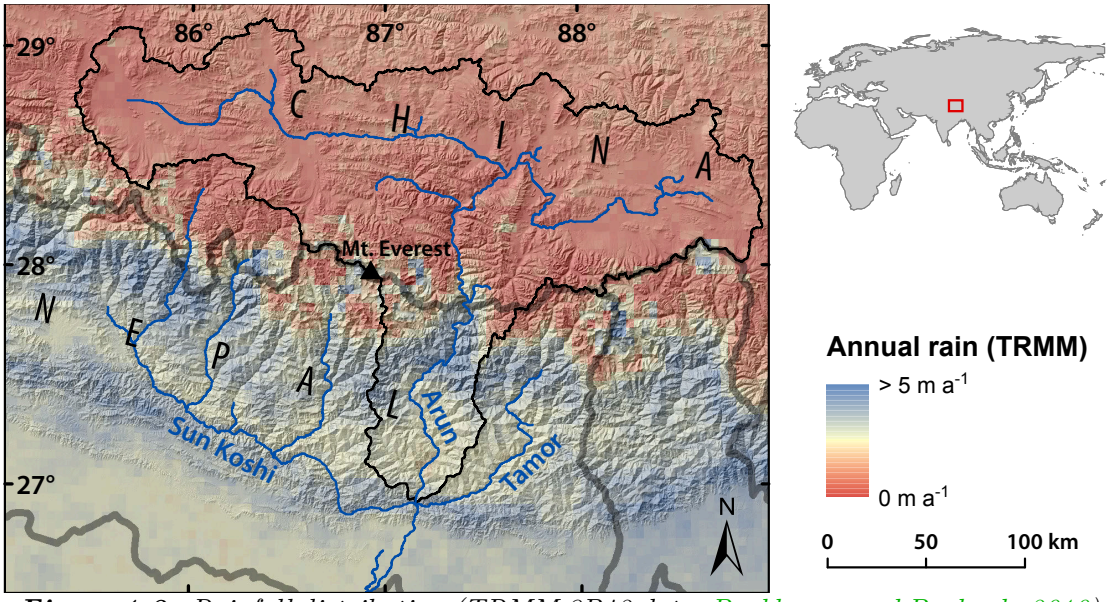

Figure 1.2: *Rainfall distribution (TRMM 3B42 data, Bookhagen and Burbank, 2010) in the research area with Arun watershed (thin black line), major rivers (blue lines), and national borders (thick grey line). The Tibetan Plateau north of the Nepalese-Chinese border receives considerably less rain compared to the Himalayan front.*

Winter Westerlies, ~90% of the total annual precipitation occurs during the period from May to October (Bookhagen and Burbank, 2010), emphasizing the importance of the ISM in driving the strong seasonality of the Arun Valley climate. In addition to the Indian Summer Monsoon and Westerly Winter Disturbances, the Arun and its high altitude tributaries are fed by glacial melt water in the upper portion of the catchment and on the Tibetan plateau. The majority of glaciers within the Arun Valley are clustered around the high peaks of the Himalayan crest (Fig. 1.3). The significance of the ISM, glacial melt and Winter Westerly snow melt for the Arun River and tributary discharge is discussed in larger detail in chapter 2.

1.2.3 Flora of the Arun Valley

The diverse biosphere in eastern Nepal is strongly related to the climatic gradient across the Himalaya. The Tibetan Plateau is characterized by sparse vegetation cover, the Arun's lower reaches are dominated by subtropical, evergreen forests. Since the uppermost region of the Arun catchment, including Sagarmatha/Mt. Everest and Mt. Makalu, is characterized by permafrost conditions, vegetation is mostly absent. Below the permafrost zone down to approximately 4900 *m asl*, including the majority of the Arun's Tibetan Plateau portion, the flora is dominated by meadows and sparse grasslands of *Cyperaceae* and *Graminae* (Dobremez and Shakya, 1975). Between 4900 *m asl* down to 3500 *m asl* squat *Juniperus* species and *Rhododendron* spp. of less than 1.5 *m* height are most common (Singh and Singh, 1987). In the lowermost subalpine level un-

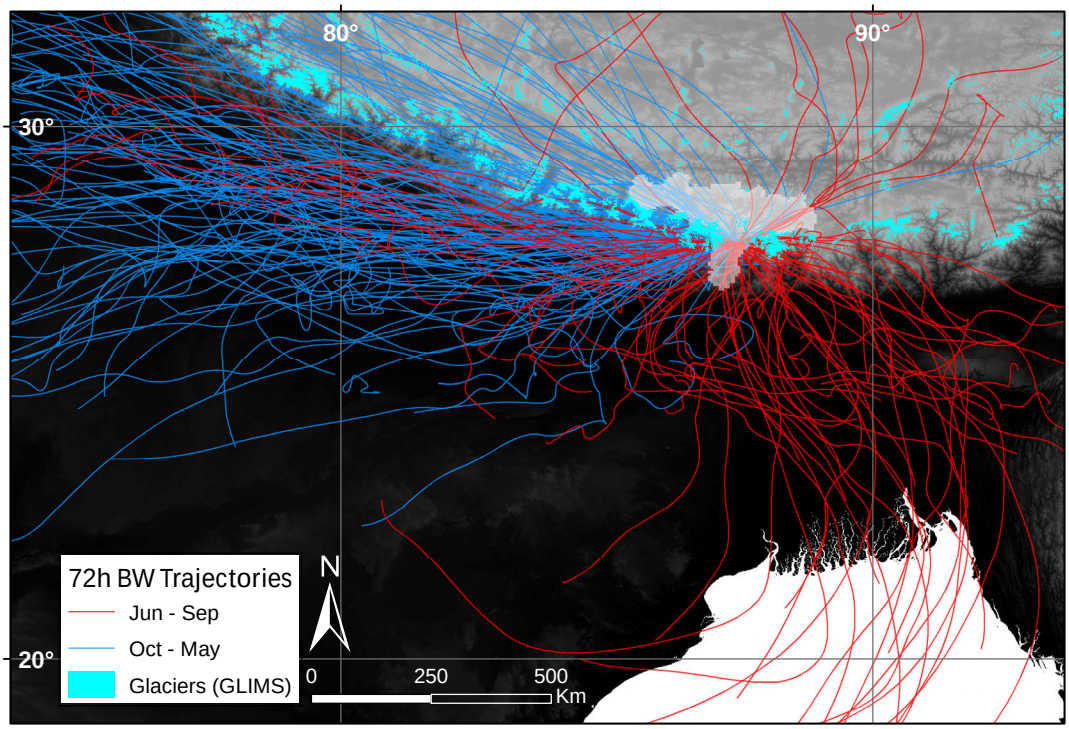

Figure 1.3: *Indian subcontinent with 72 h backward trajectories for the town of Num in the Arun catchment (white shading) at an elevation of 1.5km above ground (HYSPLIT4, NCEP/NCAR reanalysis data). The trajectories indicate daily airmass and therefore moisture sources during the Indian Summer Monsoon (ISM) seasons 2011 and 2012 (June to September, $n = 244$, red lines) and non-ISM seasons 2010/2011 and 2011/2012 (October to May, $n = 487$, blue lines). Glaciers are shown in cyan.*

til 3000 *m asl*, deciduous birch (*Betula utidis*), larch (*Larix griffithiana*), evergreen oak (*Quercus spp.*), and fir (*Abies spectabilis*) are quiet common, but more exposed sites are still dominated by *Juniperus spp.* and *Rhododendron spp* (Dobremez and Shakya, 1975; Singh and Singh, 1987). The cool temperate forests down to approximately 2500 *m asl* are characterized by *Rhododendron spp.*, pine (*Tsuga dumosa*, *Pinus wallichiana*), oak and the uppermost maple (*Acer campbellii*) appearance (Ohsawa et al., 1986). The next temperate zone between 2500 *m asl* and 2000 *m asl* is dominated by oak stands with the first appearance of *Castanopsis spp.* (Ohsawa et al., 1986; Dobremez and Shakya, 1975). The elevation range from 2000 *m asl* to 1500 *m asl* marks the transition from temperate to subtropical forests; it is dominated by *Castanopsis spp.*, alder(*Alnus nepalensis*) and the uppermost *Schima wallichii* stands. In the remaining subtropical zone until 1000 *m asl*, castanopsis and Schima dominate, whereas alder becomes seldom. The lowermost tropical zone below 1000 *m asl* is mostly Sal forest (*Shorea spp.*) (Dobremez and Shakya, 1975; Singh and Singh, 1987; Ohsawa et al., 1986).

1.3 Methods

In order to address the different aspects of the research questions that arose in section 1.1, I applied three different approaches whose results are presented in chapters 2–4. Here I briefly introduce the scientific basis of the general methods applied, and give reason why they were chosen.

1.3.1 Stable Isotopes in Precipitation

The hydrological conditions in the Arun Valley are first to investigate, because rainfall and surface runoff are known to play a key role for erosion processes as well as for pOM mobilization and export (Smith et al., 2013; Hilton et al., 2012; Clark et al., 2013). Considering the few available rain gauge stations and rare river gauge data, I applied an indirect method in order to better understand the effect of different water sources (c.f. 1.2.2) on Arun Valley hydrology: I utilized the distinct stable isotopic composition characteristic for the different water sources and analysed mixing patterns along the Arun main stem. The stable isotopic composition of water, meaning the ratio of heavy stable isotopes of hydrogen (^{2}H or D for deuterium) and oxygen (^{18}O) over ^{1}H and ^{16}O, respectively, are most commonly expressed by the δ–notation in relation to the Vienna Standard Mean Ocean Water – Standard Light Antartic Precipitation (VSMOW-SLAP) isotope standards[2]. The isotopic composition of hydrogen is expressed as per mil, such that

$$\delta\mathrm{D} = \frac{R_{sample} - R_{standard}}{R_{standard}} \times 10^3 \text{ ‰}, \tag{1.3}$$

where R_{sample} and $R_{standard}$ are mass ratios of heavy over light hydrogen isotopes of the sample and the isotope standard, respectively.

δD and δ^{18}O values of water vapour beyond the oceans at low latitudes are more or less consistent, as vapour is in isotopic equilibrium with subjacent ocean water. The basic process controlling global δD and δ^{18}O values in precipitation derived through poleward moving clouds/moisture is based on Rayleigh-type fractionation (Craig, 1961) expressed as

$$R = R_o \times f^{(\alpha-1)}, \tag{1.4}$$

where R and R_o are the moisture source stable isotope ratios before and after a precipitation event, f is the fraction of precipitation amount relative to the total moisture initially available and α is the condensation temperature dependent fractionation factor (Dansgaard, 1964). Hence, the most important controls on precipitation δD and δ^{18}O values are precipitation condensation temperature and rainfall amount. The underlying global Rayleigh-type fractionation process reflected in world wide precipitation (Craig, 1961; Dansgaard, 1964) can be disturbed on different spatial scales; e.g. locally by rain

[2] IAEA – International Atomic Energy Agency, Vienna, AT

droplet evaporation and droplet–vapour isotope exchange (Friedman et al., 1962) and regionally by mesoscale convection (Rohrmann et al., 2014; Blisniuk and Stern, 2005).

The amplified isotopic fractionation in precipitation across mountain ranges is usually referred to as *altitude effect* (Ambach et al., 1968; Gonfiantini et al., 2001; Rowley, 2007). First, mountain ranges force orographic rainout leading to an increased factor f in equation 1.4, and more importantly, the fractionation factor α increases with decreasing temperature (Merlivat and Nief, 1967; Johansson and Holmberg., 1969; Ellehoj et al., 2013) at higher altitudes. Therefore, the Himalayan front acts as an orographic barrier, showing the characteristics of the *altitude effect* at different locations (e.g. Wen et al., 2012; Rowley et al., 2001; Lechler and Niemi, 2011; Araguás Araguás and Froehlich, 1998; Poage and Chamberlain, 2001). Hence, we expect strong D-depletion in precipitation with increasing altitude along the eastern Nepalese Arun Valley, especially because the southern Arun is among the wettest places in the Himalaya with precipitation dropping from several meters of rain per year in the south to locally less than 100 mma^{-1} in the north. As surface water in the Arun Valley is directly and indirectly fed by precipitation, this strong isotopic lapse rate is likely reflected by small scale tributary surface waters. I attempt to quantify contribution amounts of the ISM and other water sources such as snow and glacial melt by analysing stable isotope mixing patterns of tributary and main stem surface water in the context of other available hydrological data (chapter 2).

1.3.2 Biomarkers as Plant OM Source Tracer

Biomarkers in Earth Sciences

The suspended and dissolved organic matter load of a river is hard to quantify and representative sampling is challenging. In order to identify organic matter sources in a fluvial catchment, a continuous quantification of organic matter content along the river would be required. Since this was not logistically possible, I again used an indirect approach based on biomarkers, a small fraction of organic matter. Biomarkers are organic molecules commonly used in geologic applications and consist mostly of carbon and hydrogen, sometimes with one or more functional groups containing also oxygen and nitrogen (Eglinton and Eglinton, 2008). Moreover, some biomarkers are persistent on geologic time scales and can therefore also be found in different concentrations in sediments and soils. Most biomarkers are not specific for one species as original producer, but some are indicative for a group of producing organisms: short chain *n*-alkanes, for example, are synthesized by the diverse group of algae (Eglinton and Eglinton, 2008). Long chain *n*-alkanes (24–36 carbon atoms), that I focus on, are synthesized by most *Embryophytes* (higher land plants) as protective leaf coating and in order to prevent evaporative water loss.

Plant Wax *n*-alkane δD

In addition to qualitative information about past living organisms inferred from the presence of certain biomarkers in sediments (e.g. Schwark et al., 2002), the isotopic

composition of biomarkers can be used in order to reconstruct past hydrological conditions. As described in section 1.3.1, the climatic and hydrological conditions at a specific site control the isotopic composition of precipitation and soil water. Soil water taken up by higher land plants may be affected by soil water evaporation to a certain extent (1.4, Smith and Freeman, 2006; Kahmen et al., 2013a), but the uptake itself is not accompanied by any isotope fractionation. Hence, the initial plant water δD value is indirectly linked to precipitation δD values and therefore to the general climatic conditions at that site. Two subsequent processes are suggested to have a much stronger effect on the δD value of final plant waxes: on one hand, leaf water is subject to evapotranspirative D-enrichment (e.g. Smith and Freeman, 2006; Kahmen et al., 2013a,b), and on the other, plant wax biosynthesis in the endoplasmatic reticulium is accompanied by strong D-depletion (biosynthetic fractionation, Sessions et al., 1999; Zhou et al., 2010; Hayes, 2001) (1.4). Whereas evapotranspirative leaf water enrichment depends on leaf temperature, ambient air temperature, relative humidity, vapour pressure deficit and vapour δD value (Kahmen et al., 2013b,a), the amount of biosynthetic fractionation is controlled by compound and genus/family specific synthesis processes; for example, the usage of isotopically distinct pools for hydrogenation (Sessions et al., 1999; Hayes, 2001).

Teh fact that plant wax δD value variability among different individuals and different species at a single site can be quite large (Hou et al., 2007), plant δD values of lacustrine surface sediments are correlated with annual mean precipitation δD at the respective site (Sachse et al., 2004; Huang et al., 2004). This implies, that lake sediments integrate the leaf wax variability between individual plants and different plant species in the respective catchment. The same integrative capacities have also been shown on a regional scale for plant wax fatty acids in tributaries of the Madre de Dios catchment in the Peruvian Andes (Ponton et al., 2014). Since the relationship between plant wax *n*-alkane δD values and annual mean precipitation δD became apparent, it is increasingly exploited for the reconstruction of past climate changes based on marine and lacustrine sedimentary plant wax archives (Schefuß et al., 2011; Tierney et al., 2008; Pagani et al., 2006; Rach et al., 2014).

Biomarker as Plant Organic Matter Source Tracer

In the Arun Valley we use plant wax long chain *n*-alkanes as source tracer for plant derived organic matter. Plant wax *n*-alkanes stand out for two important features: first, sedimentary plant detritus and waxes are likely to represent the entire vegetation within the respective catchment, at least on regional scales (Galy et al., 2011). Second, the expected strong isotopic lapse rate of environmental water (section 1.3.1) is necessarily reflected in plant wax *n*-alkane δD values. As a first step, I analysed plant wax δD values in tributary flood deposits. Second, I determined the gradual change of flood deposit *n*-alkane δD values along the Arun mainstem, reflecting a mixture with the tributary derived plant wax input. The comparison of known tributary input plant wax δD values to actual δD changes along the mainstem allows for a relative quantification of tributary derived plant waxes along the sampled transect (c.f. chapter 3).

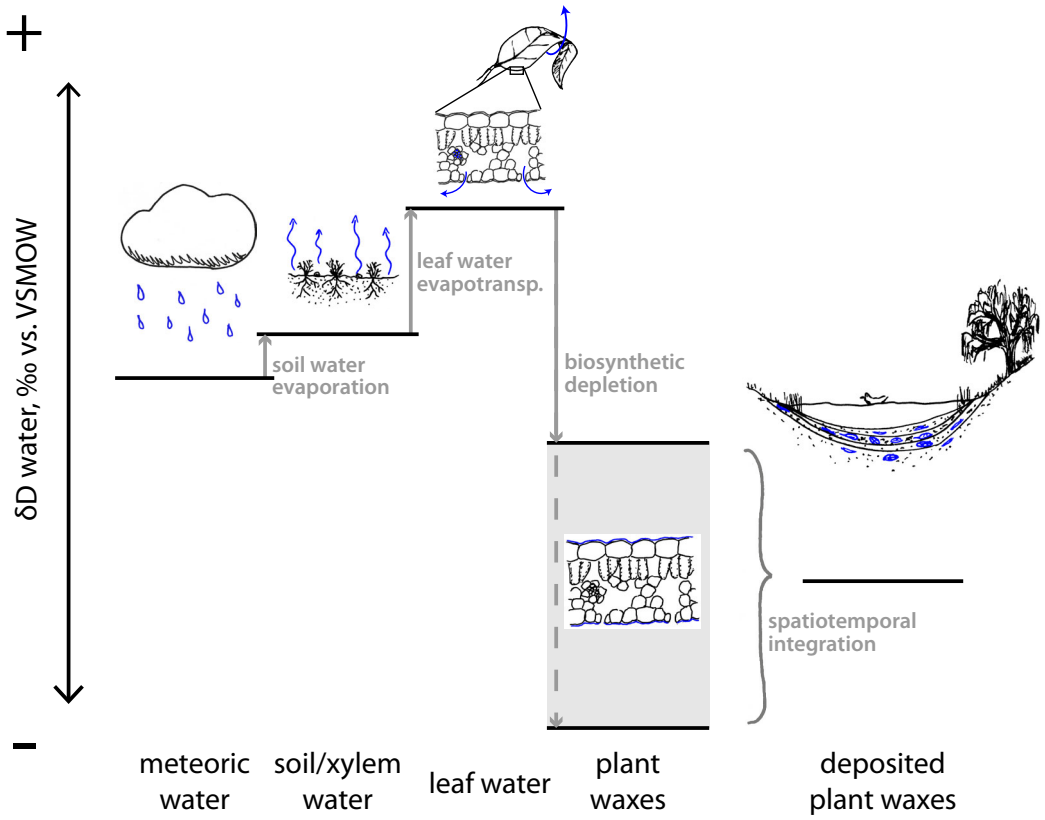

Figure 1.4: *Schematic stable isotope fractionation pathway from initial precipitation δD values to final plant wax biomarker δD values in lacustrine, fluvial or marine deposits. Key processes affecting the stable isotopic composition of water and plant waxes are labelled in grey and illustrated by blue colors.*

1.3.3 Terrestrial Cosmogenic Nuclides

Organic matter mobilization and export on a continental scale is suggested to be primarily driven by erosion (Galy et al., 2015). Hence, the comparison of the spatial distribution of erosion rates with pOM sourcing determined in chapter 3 could confirm this on a regional scale. Unfortunately, long term mass wasting and erosion in river catchments cannot be directly quantified. One well established geochronological technique to indirectly quantify landscape denudation rates is the measurement of terrestrial cosmogenic nuclide concentrations in river sands. Cosmic rays interact with the atmosphere and produce highly energetic charged neutrons (n) that potentially hit oxygen atoms of exposed quartz grains located in the uppermost depths of the earth's surface, resulting in ^{10}Be: $^{16}\mathrm{O} + \mathrm{n} \rightarrow {}^{10}\mathrm{Be} + 4\mathrm{p} + 3\mathrm{n}$, where n and p are neutrons and protons, respectively. Therefore, the concentration of ^{10}Be in quartz increases with surface exposure, whereas the mineral's natural ^{9}Be concentration remains the same. As the ^{10}Be/^{9}Be ratio in exposed quartz grains increases over time, it can be used to determine the approximate

amount of time a rock has been exposed at or near the surface. However, in fluvial sands, $^{10}Be/^{9}Be$ ratios can be interpreted as a proxy for denudation rates (Brown et al., 1995; Bierman and Steig, 1996; Granger et al., 1996), the combined rate of physical and chemical weathering and erosion processes. The higher denudation rates are, the faster surface rocks are eroded and exported. Therefore, low ^{10}Be concentrations indicate fast export of quartz grains and correlate with high denudation rates and vice versa.

2 | The effect of Indian Summer Monsoon intensity on surface water δD values in the Arun Valley, E Nepal

Bernd Hoffmann[1], Bodo Bookhagen[1], Frauke Barthold[1], Stephanie M. Olen[1], Dirk Sachse[2]

[1] Institute of Earth and Environmental Science, University of Potsdam, Potsdam, Germany
[2] Helmholtz Centre Potsdam GFZ, German Research Centre for Geosciences, Potsdam, Germany

Earth and Planetary Science Letters 2016
EPSL–S–16–00571, submitted on April 13^{th}, 2016

Abstract

Stable isotope proxy records, such as speleothems, plant-wax biomarker records, and ice cores, are suitable archives for the reconstruction of regional paleo-hydrologic conditions, including the tropics and in particular the Indian subcontinent. But the interpretation of these records, in particular with regard to Indian Summer Monsoon (ISM) strength, is difficult due to different moisture and water sources (in particular ISM, Winter Westerly precipitation, snow- and glacial melt). Here we use present-day inter-annual differences in ISM strength to understand the stable isotopic composition of surface waters in the Arun River catchment in eastern Nepal. We sampled main stem and tributary waters ($n = 204$) for stable hydrogen and oxygen isotope analysis (expressed as δ^{18}O and δD values in ‰ vs. VSMOW) in the post-monsoon phase of two subsequent years with significantly distinct ISM intensities. Additionally, we evaluated satellite remote sensing data of rainfall, snow cover, glacial coverage, and evapotranspiration. The comparison of datasets from both years revealed that surface waters of the main stem Arun and its tributaries were D-enriched by ~17‰ when ISM rainfall decreased by 20%. This indicates a strong response of surface water δD values to the amount effect of ISM rain-

fall and emphasizes the importance of the ISM for surface water runoff in the Central Himalaya. However, the spatiotemporal analysis of remote-sensing data in combination with d-excess revealed that most high altitude tributaries and the Tibetan part of the Arun catchment receive a high proportion of glacial melt and Winter Westerly precipitation. This leads to a mixing of three water sources, which potentially can be recorded in paleo-hydrologic archives along the main Himalayan ranges and on the southern Tibetan Plateau. Consequently, respective proxy records from high-altitude catchments record past changes in the relative contribution of any of the three water sources. On the other hand, surface water stable isotope values of local sources (i.e., Arun tributaries) below the snowline along the southern Himalayan front strongly reflect the ISM related amount effect implying a suitable location for potential records of paleo-monsoon intensity.

2.1 Introduction

The stable isotopic composition of water (expressed as δ^{18}O and δD values) recorded in geological archives is a widely used proxy for paleoclimate reconstructions (e.g. Freeman and Colarusso, 2001; Johnsen et al., 1995; Schefuß et al., 2003; Sinha et al., 2007; Tierney et al., 2008). As precipitation δD and δ^{18}O values are influenced by factors such as the isotopic composition of moisture sources, moisture-transportation pathway, condensation temperature and precipitation amount (Rozanski et al., 1993; Dansgaard, 1964; Gonfiantini et al., 2001), changes in any of these are imprinted in meteoric water δD and δ^{18}O values. Therefore, geological archives, such as speleothems (e.g. Hendy and Wilson, 1968; Hendy, 1971; Sinha et al., 2007), ice cores (e.g. Dansgaard et al., 1982; Johnsen et al., 1995), or organic matter such as plant wax biomarkers in sediments (Huang et al., 2004; Sachse et al., 2004; Schefuß et al., 2003; Tierney et al., 2008), provide isotope proxy records indicative of past hydrologic changes. When precipitation is derived from only one moisture source they can also be used for quantitative reconstructions of temperature and precipitation amounts (e.g. Petit et al., 1999). But in case of two or more moisture sources with distinct isotopic compositions, the interpretation of stable isotope proxies as paleo-climatic recorders is rather complex. In addition to condensation temperature and precipitation amount, potential archives are affected by temporally variable interfering moisture sources with often distinct isotope signals (Araguás Araguás and Froehlich, 1998). The observed changes in respective isotope records can either be interpreted as a change of the dominating moisture source or as past precipitation amount and temperature changes (Lister et al., 1991; Liu and Yang, 2008). Additionally, mesoscale weather anomalies along mountain ranges and plateau margins possibly affect precipitation δD and δ^{18}O values (δD_{precip} and $\delta^{18}O_{precip}$) and therefore potential stable isotope records in their vicinity (Blisniuk and Stern, 2005; Rohrmann et al., 2014).

For the reconstruction of Indian Summer Monsoon (ISM) intensity both variable moisture sources and potential weather anomalies are relevant. Regions within the central and eastern Himalaya receive maximum rainfall and are sensitive to ISM intensity. In

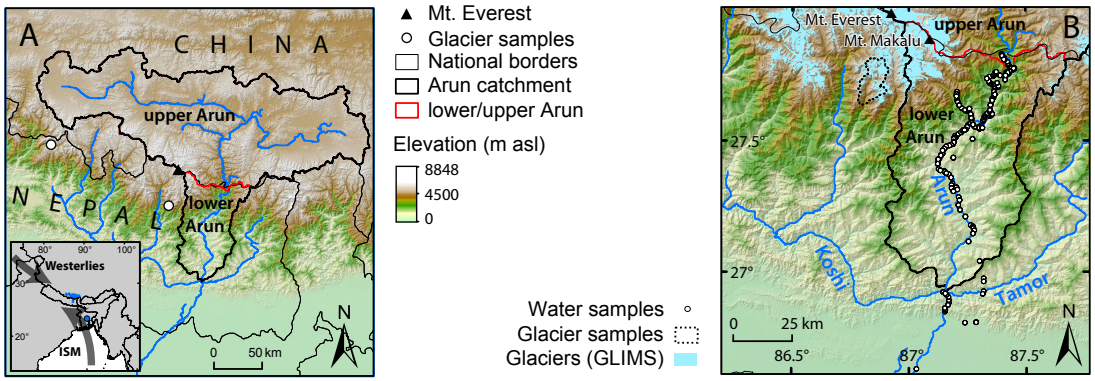

Figure 2.1: *(A) Topography of the eastern Nepalese Himalaya and adjacent regions with the Arun catchment. Upper and lower Arun are separated by red line roughly following the Nepalese-Chinese border (thin black line). The location of glaciers sampled by Racoviteanu et al. (2013) are shown as white circles. Inset indicates major moisture sources (ISM - Indian Summer Monsoon, Westerlies - Winter Westerly precipitation) and the location of the Dhaka weather station in Bangladesh (blue dot). (B) Topography of the Nepalese Arun Valley, signatures as in A. Surface water sample sites (white circles, $n = 191$). Glacial coverage derived from the GLIMS-database (GLIMS 2005, Global Land Ice Measurements from Space, www.glims.org) is indicated in cyan, origin of cited glacial melt water samples (Racoviteanu et al., 2013) is indicated by dotted outline.*

particular, the southern front of the Shillong Plateau and the southern Himalayan front are both impacted by orographic rainfall processes (Bookhagen and Burbank, 2006). For the Shillong Plateau in north-eastern India, Breitenbach et al. (2010) showed that δD_{precip} and $\delta^{18}O_{precip}$ reflect the Bay of Bengal moisture source domain. In addition to local climatic conditions, potential δD and $\delta^{18}O$ proxies along the Himalaya are possibly influenced by varying quantities of East Asian Monsoon rainfall, Winter Westerly snowfall, glacial melt (Bookhagen and Burbank, 2010; Hren et al., 2009; Wulf et al., 2016) and by mesoscale weather anomalies.

Previous studies from the Himalayan region and the Indian Subcontinent have used isotope records to reconstruct past hydrologic conditions (Berkelhammer et al., 2010; Kotlia et al., 2015, 2012; Liang et al., 2015; Ponton et al., 2012; Rowley et al., 2001; Sanwal et al., 2013; Sarkar et al., 2015; Sinha et al., 2011, 2005; Thompson et al., 2000). Except for Thompson et al. (2000), who analyzed ice core $\delta^{18}O$ values, and Ponton et al. (2012) and Sarkar et al. (2015), who analysed terrestrial biomarkers in marine and lacustrine archives, respectively, all mentioned studies used speleothem $\delta^{18}O$ value records from caves located in or close to the ISM core zone and isotopic changes were interpreted as a signal of paleo-ISM strength variability. Generally, speleothem $\delta^{18}O$ records from within the ISM region show consistent trends from the Bølling-llerød to the Holocene, reflecting insulation changes on time scales of 103 years (Li et al., 2014). Still, the

variability of δ^{18}O paleo-records on shorter time scales is difficult to interpret as they are potentially affected by Winter Westerly derived precipitation (e.g. Sanwal et al., 2013), glacial melt water contributions (Racoviteanu et al., 2013), or mesoscale weather anomalies. Even though the Himalayan front is expected to be particularly sensitive to ISM intensity changes, these additional effects are poorly understood due to sparse spatiotemporal coverage of δD_{precip} and $\delta^{18}O_{precip}$ data from the northern ISM core zone.

In our study, we aim to decipher the influence of different modern moisture sources and rainfall amount in the eastern-central Himalaya on surface water δD and δ^{18}O values using a combined stable isotope and remote sensing approach. We rely on satellite remote sensing data of rainfall distribution (TRMM data product 3B42V7, Huffman et al., 2007), snow cover (MODIS data product MOD10C1, Hall et al., 2002), and evapotranspiration (MODIS data product MOD16A2, Mu et al., 2011), together with present-day water δD and δ^{18}O values. We evaluate the consequences of our results for the interpretation of paleo-climatic data from this region. Since multi-season measurements of δD_{precip} and $\delta^{18}O_{precip}$ values from this region are rare, we analyzed surface waters of the eastern Nepalese Arun River and its tributaries (Fig. 2.1A and 2.1B) in two consecutive years (2011-2012) with different monsoonal rainfall amount (~20%). Even though the isotopic composition of stream waters can be characterized by significant excursions for hours up to a few days following heavy rainfall events (Buttle, 1994; DeWalle et al., 1997; Soulsby et al., 2000), stream base flow is the best estimate for a catchment-wide integrated signal of weighted δD_{precip} and $\delta^{18}O_{precip}$ values (Ramesh and Sarin, 1992). In the Arun Valley, a strong orographic and altitude effect (Dansgaard, 1964; Gonfiantini et al., 2001; Olen et al., 2015) is reflected by distinct water δD and δ^{18}O values (Hoffmann et al., 2016), similar to the Kali Gandaki River 350 km further west (Garzione et al., 2000). As such, our new data from the Arun Valley provide the opportunity to evaluate the ISM strength related amount effect and the potential effects of different hydrological variables on the isotopic composition of environmental waters.

2.2 Geographic and climatic setting

The Arun catchment covers the worldâs steepest altitudinal gradient ranging from 205 m asl at the confluence of the Arun, Tamur und Sun Koshi Rivers in southern Nepal to 8848 m asl at the summit of Mount Everest. The Arun River originates on the southern Tibetan Plateau in China and flows through eastern Nepal, transecting the Himalayan ranges from north to south. At its outlet in the southern Himalayan front, the Arun drains an area of 33.58 10^3 km^2, of which approximately 15% is located in Nepal and about 85% in China, mostly on the southern Tibetan Plateau at an elevation above 3000 m (Fig. 2.1A). South of the confluence of the Arun, Tamur, and Sun Kosi Rivers, the river is called Sapta Koshi and joins the Ganges, which subsequently drains to the Bay of Bengal. In this study we distinguish between the lower Arun, mostly located in the Nepalese Himalaya (catchment between $206 and 1793$ m asl river elevation, 28.32 10^3 km^2), and the upper Arun, mostly located on the southern Tibetan Plateau

(catchment above 1763 $m\ asl$, ~5.26 $10^3\ km^2$) (Fig. 2.1A). These two areas are roughly separated by the Nepalese-Chines border (Fig. 2.1A and 2.1B).

Precipitation in the Arun Valley is dominated by the Indian Summer Monsoon (ISM), originating from the Bay of Bengal (Fig. 2.1A). The ISM affects the valleyâs entire watershed and contributes ~70% of the annual rain volume during the peak ISM season between June and September (Bookhagen and Burbank, 2010). In addition to the ISM, the upper Arun receives westerly-derived winter precipitation originating from the Caspian, Black and Mediterranean Seas (Bookhagen and Burbank, 2010; Lang and Barros, 2004), although in considerably lower amounts than from the ISM. The Arun also receives glacial melt water from glaciers covering 4.91% of its total catchment area and 4.93% and 4.84% of the upper and lower Arun, respectively (GLIMS 2005, Global Land Ice Measurements from Space, www.glims.org). Hence, main stem waters and several high-altitude tributaries potentially receive glacial melt in addition to summer and winter precipitation (Fig. 2.1A and 2.1B).

The substantial inter-annual variability of ISM intensity is evidenced by flooding events and droughts on the Indian subcontinent during the past 150 years and beyond (Malik et al., 2016; Mooley and Parthasarathy, 1984). Monsoonal intensity can be described by different indices (Parthasarathy et al., 1992), most commonly based on wind-system gradients. The Indian Sumer Monsoon Index (IMI) (Wang and Fan, 1999) compares Westerly shear wind strength over the Indian Ocean at 850 hPa to those over the Himalaya and the Tibetan Plateau based on June to September NCEP/NCAR reanalysis data. It is an indirect measure of the mobilization of air masses from the Indian Ocean towards the Himalayan mountain range. The IMI is a dimensionless index normalized to the long-term (1948-2013) mean shear wind strength differential between both regions, where a value of 1 (-1) implies an increased (decreased) shear wind strength of one standard deviation above (below) the long-term mean, indicating an intensified (attenuated) ISM. In 2011, the first year of our sampling campaign, the IMI had a value of -0.563 (International Pacific Research Center, University of Hawaii, http://apdrc.soest.hawaii.edu/projects/monsoon/seasonal-monidx.html), indicating that ISM intensity was slightly below the long-term mean, but within one standard deviation. In 2012, an IMI of -1.953 indicated a very weak ISM season prior to our sampling campaign in November 2012. Data from the Bangladesh GNIP (Global Network of Isotopes in Precipitation, International Atomic Energy Agency) climate station in Dhaka (Fig. 2.1A, inset) confirm that 2012 was a less intense ISM than 2011; the recorded cumulative annual precipitation at Dhaka was 1522 $mm\ y^{-1}$ in 2011 and 902 $mm\ y^{-1}$ in 2012 (Dhaka mean 2009-2012: 1344 $mm\ y^{-1}$, $\sigma = 390\ mm\ y^{-1}$). This difference is also reflected in annual mean δD_{precip} ($\delta^{18}O_{precip}$) values. The weighted annual mean δD_{precip} ($\delta^{18}O_{precip}$) value was -41.8‰ (-6.3‰) in 2011 it was -26.0‰ (-4.2‰) in 2012, implicating a more D-enriched precipitation of 16.5‰ (2.1‰) in 2012 compared to the previous year.

2.3 Methods

2.3.1 Surface water sampling

In order to determine the spatial and temporal variability of surface water δD and δ^{18}O values, streams were sampled in September 2011 and October/November 2012. The southern section of the lower Arun Valley was sampled in 2011. In 2012 sampling was focused on the northern section of the lower Arun (Fig. 2.1A). We resampled the main stem at 2 sites (4 samples in total) and 4 tributaries that were already sampled in 2011 (Table 3.1). On average, the Arun main stem was sampled in 10-km intervals, and the outlets of tributaries every 0.5 to 3 km, depending on accessibility. Five of the sampled tributaries have a glacial coverage varying from 0.5% to 36% of respective total catchment area (Table 6.2). For sampling, 2 ml glass vials were flushed with stream water and then filled.

Measurement of surface water δD and δ^{18}O Prior to δD and δ^{18}O value measurements, all water samples were filtered through 45 μm polyethylene filters. The surface water isotopic composition was determined by laser spectroscopy on a Liquid Water Isotope Analyzer (Los Gatos Research, Mountain View, California, USA), at the Institute of Earth and Environmental Sciences, University of Potsdam. Every sample was run in six replicates; only the last three measurements were used to calculate sample means. For every fifth sample, we measured 3 isotope standards (δD = -154.3‰, -96.4‰, -9.5‰, respectively, Los Gatos Research water isotope standard). In order to convert D/H ratios to the Vienna Standard Mean Ocean Water (VSMOW)-Standard Light Antarctic Precipitation (SLAP) scale, a least square linear regression function of measured and known standard δ^{18}O and δD was determined based on isotope standard measurements. The accuracy of δ^{18}O and δD measurements is reported as one standard deviation between measured and known values of water standards (i.e. the Root-Mean-Square Error, RMSE) and was 0.06‰and 1.02‰, respectively. The precision of δ^{18}O and δD measurements is reported as one standard deviation of triplicate measurements (Table 6.2). The deuterium excess d of sampled stream waters was calculated by:

$$d = \delta D - 8 * \delta^{18}O \tag{2.1}$$

2.3.2 Raster data

For terrain analyses we used the void-filled Shuttle Radar Topography Mission (SRTM V4) digital elevation model (DEM) with a ground resolution of 90 m (Jarvis et al., 2008). We determined the Arun River catchment using standard geographic information system tools. For the evaluation of spatial temporal rainfall variability for the Himalaya we used daily Tropical Rainfall Measurement Mission (TRMM) data derived through the data product TRMM 3B42-V7 with 3-hour temporal resolution and a spatial resolution of 0.25° (~30 km) (Bookhagen and Burbank, 2010, 2006; Huffman et al., 2007). The authors are well aware of the limitations of the TRMM 3B42 dataset and the

over-prediction of rainfall at high elevation and in arid areas (Bookhagen and Burbank, 2010; Wulf et al., 2016), but most of the tributary sample sites are in the humid part of the Arun. We acknowledge the difficulties of determining discharge from these data, but we argue that relative and inter-annual variabilities are well captured (Wulf et al., 2016). The TRMM data were bilinearly resampled to a spatial resolution of 5 km. Advanced Microwave Scanning Radiometer (AMSR-E) snow water equivalent estimations were only available until October 2011 and it could not be used for snow-melt evaluation (Tedesco et al., 2004). Instead, the spatiotemporal snow analysis is based on the daily MODIS MOD10C1 snow cover data product from January 2004 until the end of 2012, with a spatial resolution of 0.05° (~5 km) (Hall et al., 2002). For a detailed rationale why MODIS snow cover data is a reasonable approach for snow melt trends during both sampling campaigns, we refer to a comparison of MODIS snow cover and AMSR snow water equivalent data in the appendix 6. In order to evaluate the amount of evapotranspiration in the Arun Valley we analyzed MODIS MOD16A2 evapotranspiration data (Mu et al., 2011) of the years 2011 and 2012 with a spatial resolution of ~5 km. For more details we refer to the appendix 6.

Lon	**Lat**	**site 2012**	**site 2011**	**δD 2011**	**δD 2012**	**ΔD**	**δ^{18}O 2011**	**δ^{18}O 2012**	**Δ^{18}O**
87.28	27.57	**12009**	**11049**	-105.7	-88.7	19.0	-14.8	-12.2	2.6
87.28	27.57	**12113**	**11049**	-105.7	-91.2	16.2	-14.8	-13.0	1.9
87.28	27.57	**12139**	**11049**	-105.7	-91.0	16.4	-14.8	-12.9	2.0
87.24	27.22	12145	11080	-59.7	-46.2	14.4	-8.8	-7.2	1.6
87.28	27.15	12146	11085	-57.6	-40.1	18.6	-8.7	-6.4	2.4
87.25	27.12	12147	11086	-58.5	-45.0	14.4	-8.8	-6.6	2.3
87.15	26.93	12149	11100	-91.9	-76.2	17.2	-13.2	-10.9	2.3
87.15	26.93	**12150**	**11102**	-92.5	-77.5	16.5	-13.2	-11.1	2.1

Table 2.1: *Surface water δD and $\delta^{18}O$ values with offset ΔD and $\Delta^{18}O$ between both years. Main stem samples are indicated by bold sample number.*

2.4 Results

2.4.1 Stream water δD values

Water δD values (δD_{sw}) of all samples ranged from -109.6‰ to -36.4‰. Tributary δD_{sw} values ($\delta D_{sw,trib}$) in 2011 ranged from -92.5‰ to -42.9‰ with an average of -56.2‰ ($\sigma = 8.5$‰, $median = -55.3$‰, $n = 74$); whereas in 2012, they were between -84.3‰ and -36.4‰ with an average of -52.1‰ ($\sigma = 7.6$‰, $median = -51.5$‰, $n = 117$) in 2012 (Fig. 2.2A, Table 6.2). The six water samples taken from five different glaciated tributary catchments were characterized by most negative $\delta D_{sw,trib}$ values (Fig. 2.2A). $\delta D_{sw,trib}$ values, including those of glaciated tributaries, were negatively correlated to the median catchment elevation with a Pearson correlation coefficients (R) of -0.73 and -0.76 and $p < 0.01$ for years 2011 and 2012, respectively. The observed isotope lapse rates were -9.56‰ km^{-1} ± 1.08‰ km^{-1} (1-sigma standard deviation) and -8.24 ± 0.65‰ km^{-1} in September 2011 and November 2012, respectively; the appropriate intercepts were

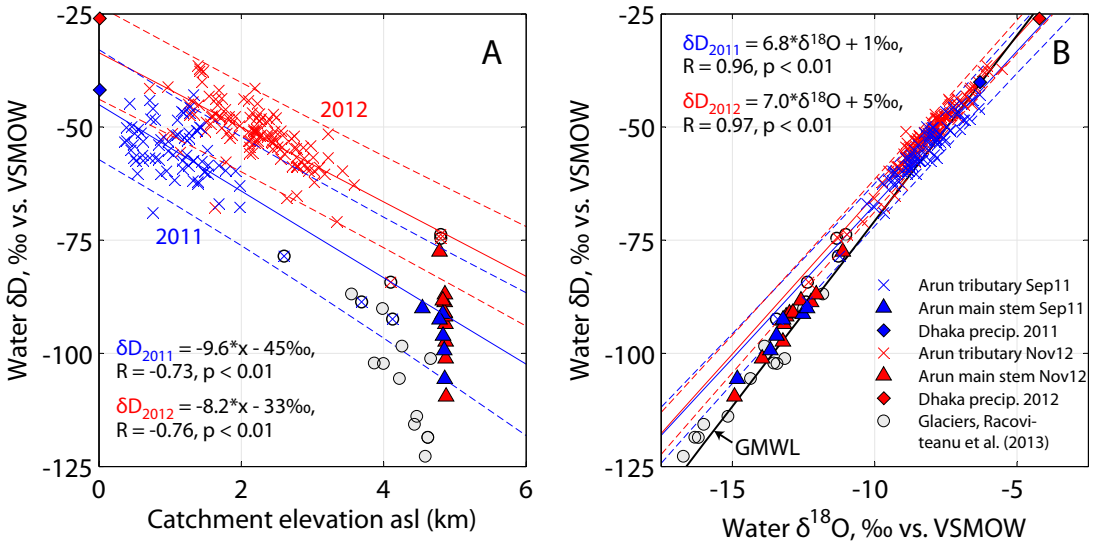

Figure 2.2: *Surface water δD and $\delta^{18}O$ values separated by sample year (2011: blue, 2012: red) of the Arun main stem (triangles) and its tributaries (crosses) (see Table 6.2 for analytical errors). Glaciated tributaries are indicated by black circles. Precipitation annual mean δD values from Dhaka, Bangladesh, are shown as filled diamond, glacial melt from Dudh Kosi and Trishuli subbasins as grey circles (c.f. Fig. 2.1A and 2.1B, Racoviteanu et al., 2013). Linear regressions of tributary δD values (solid line) are shown together with 95% confidence intervals (dashed lines). (B) Surface water δD vs. $\delta^{18}O$ values and Global Meteoric Water Line (GMWL, black, $\delta D = 8.2 * \delta^{18}O + 11.27$, Rozanski et al., 1993), glacial melt and precipitation data from Dhaka, Bangladesh. Solid and dashed lines show linear regressions with 95% confidence intervals of 2011 and 2012 tributary data (see Table 2.2 for more details).*

-45.0 ± 1.43‰ and -33.6 ± 1.54‰ (Fig. 2.2A, Table 2.2). We performed an analysis of covariance (ANCOVA) to test for significant differences between both $\delta D_{sw,trib}$–altitude relationships (lapse rates) and this revealed that slopes were not significantly different ($p = 0.27$) whereas y intercepts were ($p < 0.01$). $\delta^{18}O_{sw,trib}$ and $\delta D_{sw,trib}$ were correlated in both years ($R = 0.96$ and $R = 0.97$, $p < 0.01$ in 2011 and 2012, respectively) with regression functions less steep than the global meteoric water line (GMWL, $\delta D = 8.2 * \delta^{18}O + 11.27$,

Replicate surface water samples from 2 Arun main stem sites (4 samples) and 4 tributaries that were sampled during both field campaigns were characterized by an offset $\Delta D_{2011/2012}$ of 16.6‰ ($\sigma = 1.70$‰) calculated by:

$$\Delta D_{2011/2012} = \sum \left(\frac{\delta D_{sw,2012} + 10^3}{\delta D_{sw,2011} + 10^3} - 1 \right) * \frac{10^3}{n} \tag{2.2}$$

where $\delta D_{sw,2011}$ and $\delta D_{sw,2012}$ are replicate samples from both years and n is the number of replicate samples ($n = 8$) (Table 2.1).

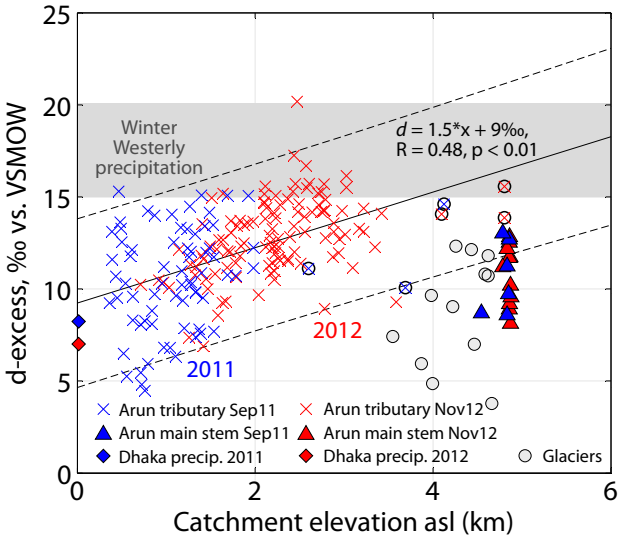

Figure 2.3: *d-excess main stem (triangles) and tributary (crosses) water samples from 2011 and 2012 colour coded in blue and red, respectively (additional black circles indicate glaciated tributaries) (see Table 6.2 for analytical errors). For comparison, Dhaka weighted annual mean precipitation d-excess of 2011 and 2012 (diamonds) is shown together with Winter Westerly precipitation (Karim and Veizer, 2002; Pande et al., 2000) and local glacial melt water d-excess (c.f. Fig. 2.1A and 2.1B) (Racoviteanu et al., 2013).*

2.4.2 Stream water Deuterium excess

Deuterium excess (d) values of September 2011 tributary waters ranged from 4.8 ± 0.8‰ to 15.5 ± 1.6‰ (mean 10.9‰, one standard deviation $\sigma = 2.7$‰) and were lower than November 2012 tributary d (7.2 ± 3.0‰ to 20.3 ± 4.5‰, mean 13.0‰, $\sigma = 2.0$‰) (Fig. 2.3). Average d of replicate tributary samples from November 2012 was 1.8‰ below September 2011 d-excess but statistically insignificant ($n = 4$, $\sigma = 2.1$‰). d was not correlated to catchment elevation in the individual sampling years, but combined d from both years yielded a significant correlation to median catchment elevation ($R = 0.48$, $p < 0.01$) with a d-excess increase (slope) of 1.52‰ km^{-1} and an intercept of 9.49‰ (Fig. 2.3, Table 2.2). However, above 2.5 km catchment elevation deuterium excess did not increase anymore.

Arun main stem water samples covered a comparable d-excess range during both sampling campaigns ranging from 8.8‰ to 13.2‰ ($mean = 11.0$‰, $\sigma = 1.6$‰, $n = 6$) and 8.4‰ to 13.0‰ ($mean = 10.9$‰, $\sigma = 1.9$‰, $n = 11$) in 2011 and 2012, respectively. The d-excess of replicate main stem samples in 2011 was 1.7‰ above 2012 samples ($n = 4$, $\sigma = 1.5$‰). We did not observe a correlation between median catchment elevation and the Arun's main stem d-excess, neither for both years individually, nor for combined data.

2.4.3 Rainfall and snow melt

The temporal analysis of TRMM-recorded rainfall in 2011 and 2012 revealed that 74% and 71% of total annual (January to December) rainfall precipitated during the ISM peak season between June and September, respectively. The catchment-wide mean cumulative annual rainfall (January-December) during the 7 years prior to sampling (2004

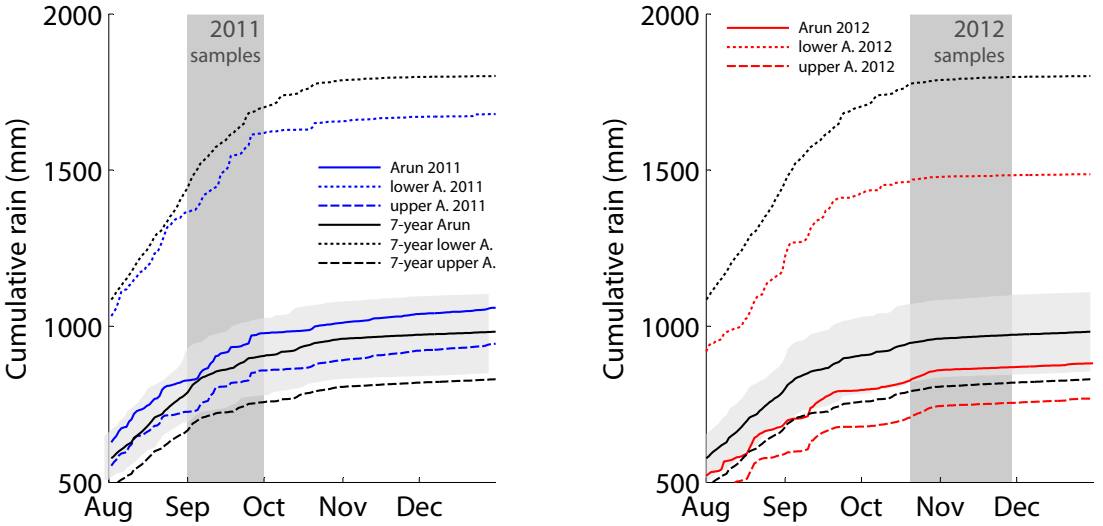

Figure 2.4: *TRMM V3B42 (Bookhagen and Burbank, 2010) derived Jan-Dec cumulative rain during 2011 (left, blue lines) and 2012 (right, red lines) sampling campaigns in comparison with 7-year mean cumulative rainfall (2004-2010). For better visualization of spatial rainfall variability, we show the average cumulative rain of the entire Arun catchment (solid lines), cumulative rain in the lower Arun (dotted lines), and in the upper Arun (dashed lines). Shading denotes sampling periods. X-axis ticks denote the beginning of each month. Note the inter-annual differences between rainfall amounts.*

to 2010) ranged from 838 $mm\ y^{-1}$ (minimum in 2009) to 1128 $mm\ y^{-1}$ (maximum in 2010), with an average of 982 $mm\ y^{-1}$ (1σ standard deviation 127 $mm\ y^{-1}$, 12.9%, Fig. 2.4). In 2011, cumulative annual rain averaged over the entire Arun catchment was 1059 $mm\ y^{-1}$ (35.56 $km^3\ y^{-1}$) and in 2012 it was 881 $mm\ y^{-1}$ (29.58 $km^3\ y^{-1}$), both within one standard deviation of the 7-year mean. Generally, the lower Arun was characterized by higher annual rainfall rates than the much larger upper Arun section (Fig. 2.4). But due to the different areas total rain volumes in the upper Arun were approximately three times larger compared to the lower Arun: The upper Arun 7-year mean of annual cumulative rain was 830 $mm\ y^{-1}$ with a total rain volume of 23.50 $km^3\ y^{-1}$; whereas it was 1808 $mm\ y^{-1}$ for the lower Arun, being equivalent to a rainfall volume of 9.51 $km^3\ y^{-1}$. In 2011, the upper Arun received 944 mm rainfall (26.73 $km^3\ y^{-1}$), whereas the lower part received 1679 mm (8.83 $km^3\ y^{-1}$). In 2012, both parts of the catchment received less rain with 769 $mm\ y^{-1}$ in the upper Arun (21.78 $km^3\ y^{-1}$) and 1487 $mm\ y^{-1}$ in the lower Arun (7.82 $km^3\ y^{-1}$).

MODIS snow cover data revealed that the overall snow cover extent in the Arun Valley prior to and during the two field seasons in September 2011 and November 2012 was more or less stable, with only little snow melt. The minimum snow cover extent in 2011

and 2012 was reached in the middle of July. The Arun catchment average snow cover during the 2011 sampling campaign (2.5%) was on the same order as the 7-year mean (1.9%). The same holds true for the lower Arun (1.8% for both, 2011, and 7-year mean) and the upper part of the catchment (2.6% in 2011, 2.0% 7-year mean). The catchment mean snow cover during the 2012 sampling campaign (3.3%) was 3.4% below the 7-year mean of 6.7%. The lower Arun (3.8% in 2012, 5.0% 7-year mean) and the upper Arun (3.2% in 2012, 7.1% 7-year mean) was characterized by similarly small snow cover. At the beginning of the 2011 sampling campaign, 1.8% of the catchment area was covered with snow (lower Arun: 1.8%, upper Arun: 1.8%). During the first 3 weeks, the total snow cover decreased to 0.5% (lower Arun: 0.4%, upper Arun: 0.6%) and increased during the last six days of sampling to 5.9% (lower Arun: 3.9%, upper Arun: 6.3%). At the beginning of the 2012 field season 4.2% of the Arun catchment was covered with snow (lower Arun: 3.5%, upper Arun: 4.3) and decreased during sampling to 3.1% (upper Arun: 2.9%), although it remained more or less constant in the lower Arun of the catchment.

2.5 Discussion

In order to decipher the effect of ISM intensity on the isotopic composition of surface waters within the Arun Valley, we first consider the effect of Winter Westerly derived moisture and evapotranspiration during both years and discuss how they potentially affect surface water δD values. Subsequently, we evaluate the effect of snow melt contribution on the Arun Valley. Last, we discuss to what extent observed δD_{sw} value pattern in 2011 and 2012 was driven by ISM intensity and assess the consequences for quantitative ISM reconstruction in the central-eastern Himalaya based on stable isotope archives.

2.5.1 Winter Westerlies and evaporative effects

In addition to the ISM, isotopically light Winter Westerly derived precipitation serves as water source for the high altitude part of the Arun catchment, mostly located in the upper Arun section (Hren et al., 2009; Karim and Veizer, 2002; Lang and Barros, 2004). However, most streams sampled in September 2011 that were characterized by comparably D-depleted waters were located at low elevations and hardly receive any snow at all, opposed to the majority of streams sampled in 2012. Hence, stronger D-depletion of surface waters sampled in 2011 was not caused by an enhanced contribution of snow melt in 2011 compared to 2012. This argument is supported by two key observations based on remote sensing snow cover and stream water d-excess: First, MODIS snow cover analysis revealed similar negligible snow cover decline before and during both field seasons, suggesting only minor snow meltwater contributions in September 2011 and November 2012 (Fig. 2.5). Second, Winter Westerly snow contains a large proportion of reworked and evaporative water due to its long transportation path from the Mediterranean, and is therefore characterized by comparably high d-excess of $15 - 20‰$ (Karim and Veizer,

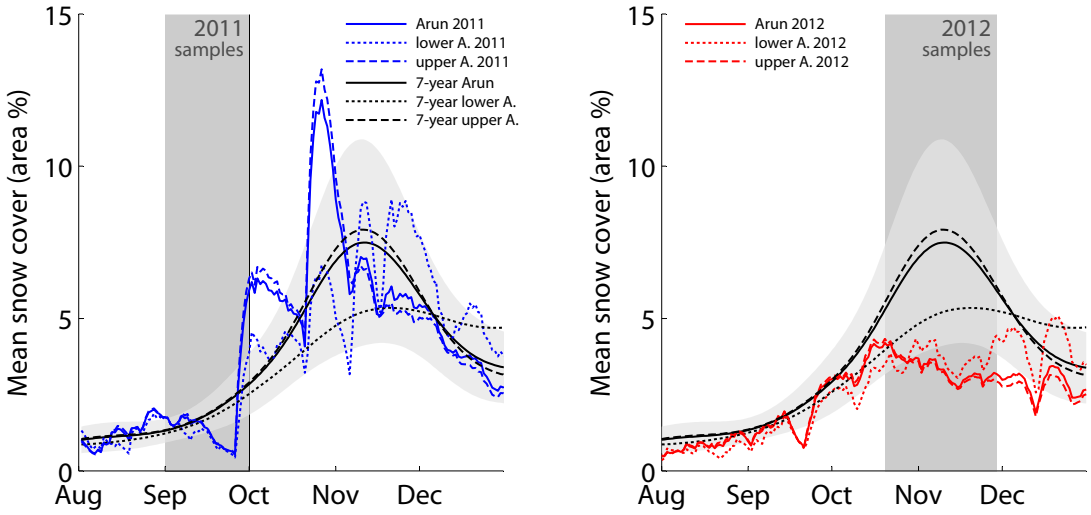

Figure 2.5: *Daily snow-cover extent in 2011 (left, blue lines) and 2012 (right, red lines) in comparison with the 7-year mean (2004 to 2010 mean, black lines). Solid, dashed and dotted lines represent the entire Arun catchment and its upper and lower section, respectively; boxes indicate timing of field seasons. Mean snow cover in 2011 across the entire catchment was within the range of the 7-year mean (2004 to 2010 mean, black lines). In 2012 especially the upper Arun exhibits a lower snow cover compared to the 7-year mean. During both sampling campaigns, overall snow cover reduction was less than 1%, indicating very low melt water release.*

2002; Pande et al., 2000). As Winter Westerly snow would mostly affect the upper Arun, d-excess of snow melt derived water draining the Tibetan Plateau would be higher than that of lower elevated tributaries. In fact, Arun main stem d-excess (11.3‰ in 2011 and 11.0‰ in 2012) was lower than average tributary d-excess and closer to d-excess observed south of the central Himalaya in Dhaka, Bangladesh, (d_{annual} = 8.5‰/7.3‰ in 2011/2012, station of the Global Network of Isotopes in Precipitation, International Atomic Energy Agency, Fig. 2.3), Allahabad, India, (d_{1980} = 7.8‰) and Shillong, India, ($d_{1966-1978}$ = 10.8‰, Araguás Araguás and Froehlich, 1998). Based on snow cover and d-excess observations, we argue that there was no significantly different snow melt in 2011 and 2012. The main melt effect of Winter Westerly derived snow is expected to be expressed through direct surface runoff in spring as well as protracted runoff generated by storm events during the ISM onset in May to June after temporal storage in the vadose zone (Buttle, 1994). Therefore, snowmelt should have no strong impact on water samples taken in September and November.

A possible mechanism affecting δD values leading to the observed $\delta D_{2011/2012}$ is stronger evaporative D-enrichment during 2012. But such enrichment would also lead to significant differences of d-excess values between September 2011 and November 2012 that we did not observe. In addition, remotely sensed evapotranspiration within the Arun catchment during 2011 and 2012 was similar (c.f. appendix 6.2). We thus argue that

stronger evaporative D-enrichment in 2012 can also be neglected as being the cause for the observed inter-annual differences.

Variables	Year	Regression function	R	p
δD vs. elev.	2011	$-9.56x(\pm1.06) - 45.16(\pm1.43)$	-0.73	< 0.01
δD vs. elev.	2012	$-8.23x(\pm0.65) - 33.56(\pm1.54)$	-0.76	< 0.01
δD vs. δ^{18}O	2011	$6.79x(\pm0.23) + 0.72(\pm1.91)$	0.96	< 0.01
δD vs. δ^{18}O	2012	$7.01x(\pm0.16) + 4.99(\pm1.30)$	0.97	< 0.01
d-excess vs elev.	2011&2012	$1.48x(\pm0.19) + 9.49(\pm0.38)$	0.50	< 0.01

Table 2.2: *Results of linear regressions of 2011 and 2012 surface water δD with median catchment elevation (elev.) and $\delta^{18}O$ values. Additionally, the regression of d-excess (both years combined) and median catchment elevation (elev.) is shown. All regressions functions are given with one standard deviation of slope and intercept and with Pearson correlation coefficients R and p-value.*

2.5.2 Glacial melt

As argued above, protracted snow melt of Winter Westerly derived precipitation can be neglected as significant water source in the Arun and its tributaries. In addition, variable glacial melt water contributions during both sampling campaigns cannot explain the offset between 2011 and 2012 δD_{sw} values, as this effect was observed for main stem samples and tributaries with and without glaciated catchments. However, melt water contributions of ablating glaciers along the main Himalayan crest (Bolch et al., 2012; Scherler et al., 2011) might significantly affect the water balance of high altitude catchments, and in particular the Arun main stem. Racoviteanu et al. (2013) presented δD and δ^{18}O values of glaciated streams and glacier mouth water samples from the Dudh Kosi and Trishuli catchments west of the Arun catchment (Fig. 2.1A). Limited to glacier mouth samples only, streams sampled by Racoviteanu et al. (2013) had a mean δD value of -106.3‰ (1σ standard deviation = 11.6‰, n = 12) with a d-excess of 9.0‰ (σ = 2.9‰). The Dasuopu Glacier 125 km west of the Arun was characterized by an average δ^{18}O value of accumulated ice during the past 100 years of -19.88‰ (Yao et al., 2006), equivalent to a δD value of ca. -149.2‰ when converted using the GMWL relationship (Rozanski et al., 1993). Arun main stem δD_{sw} values fall in between isotopically heavy tributary waters dominated by the ISM and glacial melt water (Racoviteanu et al., 2013; Yao et al., 2006). As such, a mixture of both water pools in the Arun main stem waters is conceivable. Observed d-excess of main stem waters also correspond well to glacial melt (Racoviteanu et al., 2013) and reinforces our argument for strong glacial melt mixing as no other water source has the potential to generate observed low main stem d-excess on the southern Tibetan Plateau (Fig. 2.3). The finding of strong glacial melt input mixed with ISM derived rainfall in Arun main stem waters is in agreement with previous findings from the central Himalaya (Racoviteanu et al., 2013). However, Arun main stem δD_{sw} values in September 2011 were lower than in November 2012 (Fig. 2.2A), pointing

towards larger glacial melt fraction in 2011 waters. Contrarily, larger d-excess in 2011 indicates a smaller fraction of glacial melt in 2011 main stem waters, contradicting the statement above. Hence, inter-annual or seasonal variable glacial melt contribution cannot provide a reasonable explanation for the observed isotopic differences in 2011 and 2012 main stem surface waters.

The previous discussion shows that neither snow melt, evaporative effects nor glacial melt provides a reasonable explanation for the difference in δD_{sw} values observed between 2011 and 2012. In the following section, we will discuss the effect of variable ISM strength on surface waters in the Arun Valley.

2.5.3 The effect of ISM intensity on surface water δD values

ISM derived precipitation was the major water source in the eastern Nepalese Himalaya with 71% and 74% of annual (Jan - Dec) precipitation in 2011 and 2012, respectively (Bookhagen and Burbank, 2010). Hence, isotopic lapse rates of $-9.56 \pm 1.08‰\ km^{-1}$ and $-8.24 \pm 0.65‰\ km^{-1}$ in September 2011 and November 2012 likely reflect Rayleigh fractionation effects due to rain out and decreasing temperature (Dansgaard, 1964) along ISM moisture paths across the Himalaya. This effect, sometimes referred to as the altitude effect, is well known and has been observed across major orographic ranges (Rowley, 2007; Rowley and Garzione, 2007). The observed Arun Valley isotope lapse rates are comparable to previous studies from the eastern and central Himalaya (Garzione et al., 2000; Hren et al., 2009), when considering a similar altitudinal range.

Isotope data from the ISM dominated Dhaka GNIP station in Bangladesh, located along the ISM moisture path from the Bay of Bengal to the Himalaya, confirm a strong amount effect on δD_{precip}: whereas 2011 cumulative ISM rainfall (JJAS) at Dhaka was 1241 mm with a weighted mean δD_{precip} value of $-51.0‰$, 2012 JJAS-rainfall was 39% below 2011 ISM rainfall (JJAS, 762 mm) and characterized by a weighted mean δD_{precip} value of -31.8‰, coinciding with a weaker ISM. The Indian Summer Monsoon Index (IMI, Wang and Fan, 1999) showed that 2012 was characterized by an IMI of 1.95 standard deviations below the 1948–2013 average it is normalized to. In fact, only three years between 1948 and 2013 were characterized by a lower IMI: 1972, 1987, and 2009. The 2011 IMI value of -0.56 was close to the 65-year mean. As such, we argue that the enriched δD_{precip} value at Dhaka in 2012 was a consequence of a weaker ISM. It is therefore conceivable that this isotope signature is carried onwards to the Himalayan ranges. Indeed, the $\Delta D_{2011/2012}$ of 20.2‰ at Dhaka is on the order of observed surface water $\Delta D_{2011/2012}$ in the Arun Valley (16.6‰, σ = 1.70‰). In the Arun catchment, the weaker 2012 ISM was also evidenced by TRMM cumulative rainfall rates: 2012 ISM rainfall was 17% lower compared to 2011. Our combined analysis of the Indian Summer Monsoon Index, stationary precipitation amount, stationary δD_{precip} values and remote sensing data strongly suggest that the observed $\Delta D_{2011/2012}$ of tributary and main stem waters in the Arun Valley was a consequence of ISM strength.

2.5.4 Implications for paleo-climate applications

Our analysis suggests that a 17% reduction of cumulative annual rain in the Arun Valley between 2011 and 2012 led to an isotopic enrichment of surface waters of 16.6‰ (σ = 1.7‰) in both, tributary and main stem waters. Although surface waters represent a complex mixture of surface runoff, ground water fed base flow, and other potential water sources, such as glacial melt (Andermann et al., 2012; Oshun et al., 2016), our results imply that the Arun Valley and especially its tributaries located in the lower Arun are very sensitive to ISM intensity, if these other factors did not change significantly. The response of δD_{sw} values to the strength of the previous ISM season indicates that water residence times in the Arun Valley are comparably small, presumably not longer than one year. This observation results in an important implication for the temporal resolution of potential stable isotope records in the Arun Valley that are used for paleo-hydrology: δD_{precip} changes due to ISM strength variability can be theoretically recorded without significant delay or smoothing effects due to hydrologic processes. Therefore, potential δD_{precip} records are rather limited by temporal recording capacities of the proxy.

Our data from the Arun Valley suggest that δD_{sw} values of tributaries, spatially integrating over catchments ranging from $10^{-1} - 10^{2}$ km^2, reflect ISM strength dependent δD_{precip} values. This implies that a continuous time series of surface water δD values and ISM strength allows for a calibration to reconstruct ISM strength based on δD_{sw} values. This is a crucial component for quantitative interpretations of paleo-hydrologic stable isotope proxies in the Arun Valley. But the observed spatial integration capacity of tributaries is also important for stable isotope records concerning a second aspect; e.g. lacustrine biomarker records and speleothems in this region integrate δD_{precip} values on similar or smaller spatial scales as analyzed tributaries. This implies that potential stable isotope archives in the Arun Valley below the snowline record ISM intensity and that they might be used for quantitative paleo-monsoon reconstructions.

For high altitude catchments and the area of the upper Arun, the interpretation of stable hydrogen or oxygen isotope archives is more complex as they yield mixed signals of Winter Westerly precipitation, ISM rainfall and glacial melt. The same applies to the interpretation of fluvial archives along the Arun main stem (Hoffmann et al., 2016): First, in addition to the ISM, they are likely affected by Winter Westerly precipitation in the upper catchment, although it had no effect on sampled main stem waters due to the timing of snow melt several months prior to our sampling campaigns. Second and more importantly, the Arun is affected by glacial melt: its signal is persistent all along the river, even at the southernmost sample site at the Nepalese-Indian border (sample 11104, Koshi Barrage Bridge). But since tributaries south of the Himalayan crest below the snow line predominantly receive ISM derived summer precipitation, we note the high potential of stable isotope archives in that region for qualitative and potentially quantitative paleo-ISM reconstruction.

2.6 Conclusion

In order to evaluate the sensitivity of meteoric water δD and δ^{18}O values in the eastern central-Himalaya to present and potentially past Indian Summer Monsoon (ISM) changes, we followed an approach combining stable isotope measurements and remote sensing data analysis: We first determined δD and δ^{18}O values of the eastern Nepalese Arun River and its tributaries sampled in fall 2011 and 2012. Second, we analysed satellite remote sensing data of rainfall, snow cover, glacial coverage and evapotranspiration related to both sampling campaigns. Our study revealed three key findings: First, we found the 2012 ISM to be significantly weaker than the 2011 ISM with ~20% less June to September rainfall in the Arun Valley. As a consequence, main stem and tributary surface water δD values in 2012 were enriched by ~17‰, emphasizing the sensitivity of the Arun Valley hydrology to ISM intensity and related amount effect (Dansgaard, 1964). Second, δD and d-excess value distributions indicate that high-altitude tributary catchments and the Tibetan Plateau received large volumes of glacial melt in addition to the evident ISM contribution across the entire Arun Valley. Third, remote sensing snow cover data indicated that the Arun receives strong Winter Westerly snowfall, mostly affecting high altitude tributaries and the Tibetan Plateau part north of the Nepalese-Chinese border. But as snow melt takes place during spring and early summer, a respective isotope signature was absent in September 2011 and November 2012 surface waters. Hence, it remains unclear to which extent snow melt affects the Arun Valley hydrology. In order to better determine the effect of variable ISM strength, snow melt, and glacial melt a time series of Arun main stem waters is required. Our data from the Arun Valley indicate that stable isotope proxy records from south of the eastern-central Himalayan crest are suited best to reconstruct past ISM intensity, because tributaries integrate precipitation δD and δ^{18}O values on similar spatial scales as potential stable isotope proxy records and clearly reflect ISM strength as a result of the amount effect.

3 | Climatic and geomorphic drivers of plant organic matter transport in the Arun River, E Nepal

Bernd Hoffmann[1], Sarah J. Feakins[2], Bodo Bookhagen[1], Stephanie M. Olen[1], Danda P. Adhikari[3], Janardan Mainali[4], Dirk Sachse[1,5]

[1] Institute of Earth and Environmental Science, University of Potsdam, Potsdam, Germany
[2] University of Southern California, Department of Earth Sciences, Los Angeles, CA 90089, USA
[3] Tribhuvan University, Department of Geology, Kathmandu, Nepal
[4] University of North Carolina Wilmington, Department of Geography Geology, Wilmington, USA
[5] Helmholtz Centre Potsdam GFZ, German Research Centre for Geosciences, Potsdam, Germany

Earth and Planetary Science Letters, 2016
Revised manuscript EPSL–D–15–01040R1 submitted on February 27^{th}, 2016

Abstract

Fixation of atmospheric CO_2 in terrestrial vegetation, and subsequent export and deposition of terrestrial plant organic matter in marine sediments is an important component of the global carbon cycle, yet it is difficult to quantify. This is partly due to the lack of understanding of relevant processes and mechanisms responsible for organic-matter transport throughout a landscape. Here we present a new approach to identify terrestrial plant organic matter source areas, quantify contributions and ascertain the role of ecologic, climatic, and geomorphic controls on plant wax export in the Arun River catchment spanning the world's largest elevation gradient from 205 to 8848 m asl, in eastern Nepal. Our approach takes advantage of the distinct stable hydrogen isotopic composition (expressed as δD values) of plant wax n-alkanes produced along this gradient, transported in river waters and deposited in flood deposits alongside the Arun River and its tributaries. In mainstem-flood deposits, we found that plant wax n-alkanes were

mostly derived from the lower elevations constituting only a small fraction (15%) of the catchment. Informed by remote sensing data, we tested four differently weighted isotopic mixing models that quantify sourcing of tributary plant-derived organic matter along the Arun and compare it to our field observations. The weighting parameters included catchment area, net primary productivity (NPP) and annual rainfall amount as well as catchment relief as erosion proxy. When weighted by catchment area the isotopic mixing model could not explain field observations on plant wax δD values along the Arun, which is not surprising because the large arid Tibetan Plateau is not expected to be a major source. Weighting areal contributions by annual rainfall and NPP captured field observations within model prediction errors suggesting that plant productivity may influence source strength. However weighting by a combination of rainfall and catchment relief best captured the observed δD value pattern suggesting dominantly erosive control. We conclude that tributaries at the southern Himalayan front with high rainfall, high productivity, high relief and high erosion rates dominate plant wax exports from the catchment.

3.1 Introduction

Fixation of atmospheric carbon in terrestrial plant organic matter and subsequent export into marine basins is one of the key mechanisms responsible for long term carbon burial with a direct impact on global atmospheric CO_2 levels (Berner, 1990; Burdige, 2005). In the Neogene Ganges-Brahmaputra river system, the transfer of organic matter (OM), has been suggested to be more important than the weathering of silicate rocks for atmospheric CO_2 drawdown (France-Lanord and Derry, 1997). Whereas total OM fluxes to marine sinks have previously been estimated using a variety of different methods (France-Lanord and Derry, 1994; Galy et al., 2015, 2011; Goni and Ruttenberg, 1997; Hedges et al., 1994, 1986; Schlünz and Schneider, 2000; Weijers et al., 2009), other studies have sought to understand the sourcing of OM within large river catchments (Bouchez et al., 2014; Galy et al., 2011; Goñi et al., 2014, 2000; Hedges et al., 2000; Kim et al., 2012; Ponton et al., 2014; Tao et al., 2015). Erosion and geomorphic characteristics have been suggested to control catchment scale OM transport (Clark et al., 2013; Galy et al., 2015). But also the significance of runoff for non-petrogenic OM mobilization, in particular triggered by rainstorm events, is increasingly acknowledged (Clark et al., 2013; Hilton et al., 2012; Smith et al., 2013; West et al., 2011). However, climatic and geomorphic drivers are both relevant for organic carbon erosion and mobilization as indicated by several prior studies (Clark et al., 2013; Hilton et al., 2012; Kao and Liu, 1996; Smith et al., 2013; Townsend-Small et al., 2008; Wheatcroft et al., 2010) Specific biomarkers for plants and in particular compound specific isotopic analyses offer promise for tracing plant components of terrestrial organic carbon. The better identification of source regions and climatic and geomorphic controls on transport processes will allow for a better understanding of sourcing of plant waxes for both paleoclimate proxy purposes as well as towards understanding the plant component of the carbon cycle.

Plant-wax lipid biomarkers and their stable isotopic composition (expressed as δD or

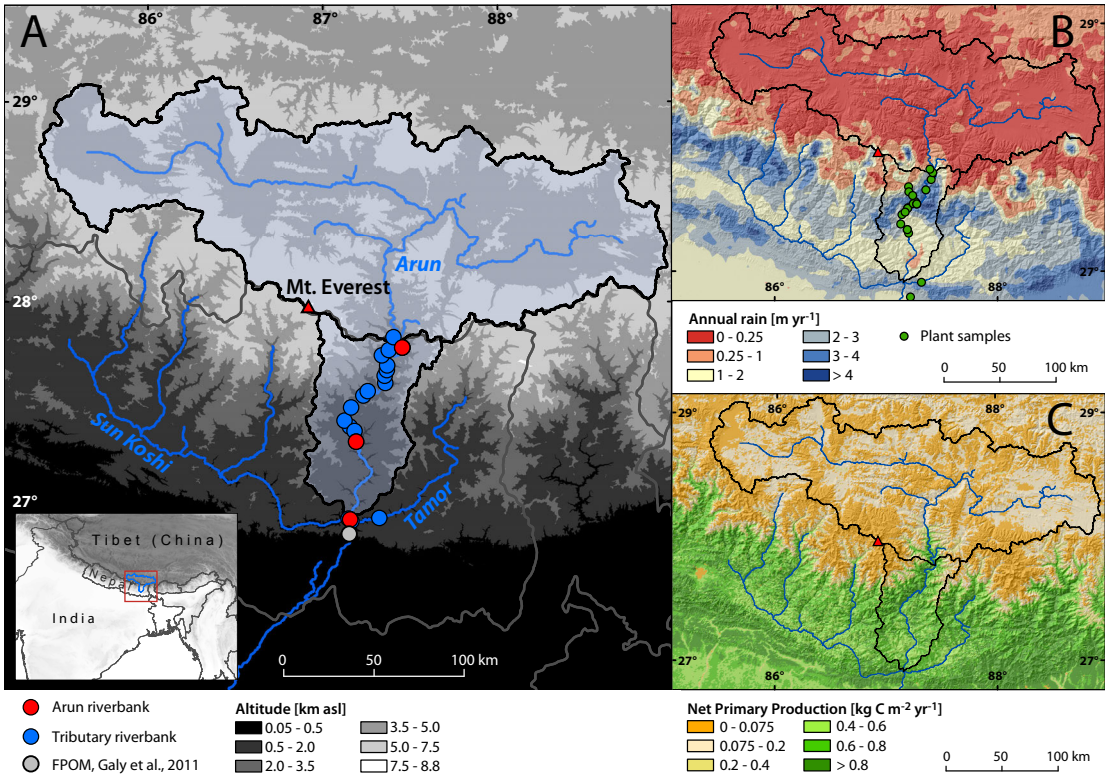

Figure 3.1: *(A) Topographic map delineating two nested Arun catchments (black lines) above the lowermost and the uppermost mainstem flood-deposit samples (red dots). Tributary flood–deposit sample sites are denoted by blue dots, fine particulate organic matter sampling by Galy et al. (2011) is shown as grey dot, coarse particulate organic matter (CPOM) samples are not shown here. Grey lines denote national borders. (B) Mean annual rainfall based on calibrated TRMM 2B31 satellite data (Bookhagen and Burbank, 2010) together with modern vegetation sample sites (green dots). (C) MODIS MOD17A3 net primary productivity (Running et al., 2004) showing bio–productivity across the catchment.*

$\delta^{13}C$ value) are an established tool to reconstruct paleoclimatic changes from sedimentary archives (e.g. Freeman and Colarusso, 2001; Schefuß et al., 2003; Tierney et al., 2008). The well-known altitude effect in precipitation isotopes (Dansgaard, 1964; Gonfiantini et al., 2001) have been shown to be recorded in plant wax δD values of living plants (Bai et al., 2011) and in soils (Ernst et al., 2013; Jia et al., 2008). Hence, plant wax δD values are emerging in applications tracing vascular plant OM within rivers draining catchments with strong topographic gradients (Galy et al., 2011; Ponton et al., 2014). The resilience of plant waxes makes them a persistent tracer for ultimately plant-derived material, whether sourced directly from living plants or after storage in leaf litter and soils. Our approach follows a specific molecule, the C_{29} *n*-alkane, a biomarker for vascular plants. The sources of biochemicals with different rates of degradation and dif-

ferent affinities for attachment and packaging with sediments may of course differ (e.g. Hatten et al., 2012; Hedges et al., 2000, 1994). The compound specific approach carries the power and limitations of this specificity within the heterogeneous OM pool. Depending on lithology, sources of *n*-alkanes can include fossil (petrogenic) organic matter (Tao et al., 2015). Studies employing plant waxes in fluvial catchments have revealed novel insights into transport processes: Galy et al. (2011) for example used δD values of plant wax n-alkanoic acids extracted from riverine fine particulate organic matter within the Ganges-Brahmaputra watershed. At the mouth of the Ganges-Brahmaputra, they found the Indian plains overwhelmed the contributions from the Himalaya. With more detailed progressive downstream sampling within the Madre de Dios River system in the Peruvian Andes, Ponton et al. (2014) similarly reported plant-wax n-alkanoic acid δD values of riverine fine particulate organic matter. While they inferred that this material is representative of its respective catchment, they found a seasonal offset equivalent to ~1km higher sourcing in the wet season, associated with more Andean erosion.

While physical erosion has been suggested to be the main driver of particulate organic carbon transport in large river systems worldwide (Galy et al., 2015), no study has yet attempted to assess the relative importance of biomass, climate, and erosional processes within a heterogeneous catchment. In this study, we quantify catchment-wide plant wax contributions from tributaries to the trans-Himalayan Arun River ($33,508\ km^2$), covering a steep altitudinal (Fig. 3.1A) and climatic (Fig. 3.1B) gradient (c.f. Bookhagen and Burbank, 2006; Olen et al., 2015). Whereas the lower catchment is characterized by tropical to subtropical evergreen forests the higher Himalaya and the Tibetan Plateau are dominated by sparse alpine vegetation consisting of grasses and shrubs (Fig. 3.1C, c.f. appendix 7.1 for more details) (Carpenter and Zomer, 1996; Dobremez and Shakya, 1975). We take advantage of the systematic change of plant wax δD (Ernst et al., 2013; Jia et al., 2008; Kahmen et al., 2013a; Peterse et al., 2009; Sachse et al., 2006; Tipple and Pagani, 2013) along altitudinal and hydrological gradients, and make use of it to characterize plant wax δD values along the Arun valley. Together with these observations we employ remote sensing techniques to estimate sourcing of plant-wax *n*-alkane contributions from across the catchment and identify climatic, ecological, and geomorphic drivers responsible for plant wax export from the tributaries.

3.2 Geographic setting

The Arun River drains the southern Tibetan Plateau (TP) and flows through the eastern Nepalese Himalaya before it confluences with the Tamor and Sun Koshi Rivers in the Siwalik Hills to form the Sapta Kosi (Fig. 3.1A). The altitudinal range of the catchment extends from 8848 *m asl* at the summit of Mount Everest to 203 *m asl* at its outlet into the Sapta Kosi over a horizontal distance of less than 160 *km*. Downstream, the Sapta Kosi continues ultimately into the Bay of Bengal via the Ganges-Brahmatputra River system. All sampled tributaries drain geological units of either the Greater Himalayan Sequence (late Proterozoic to early Paleozoic paragneisses, calc-silicates and schist) or

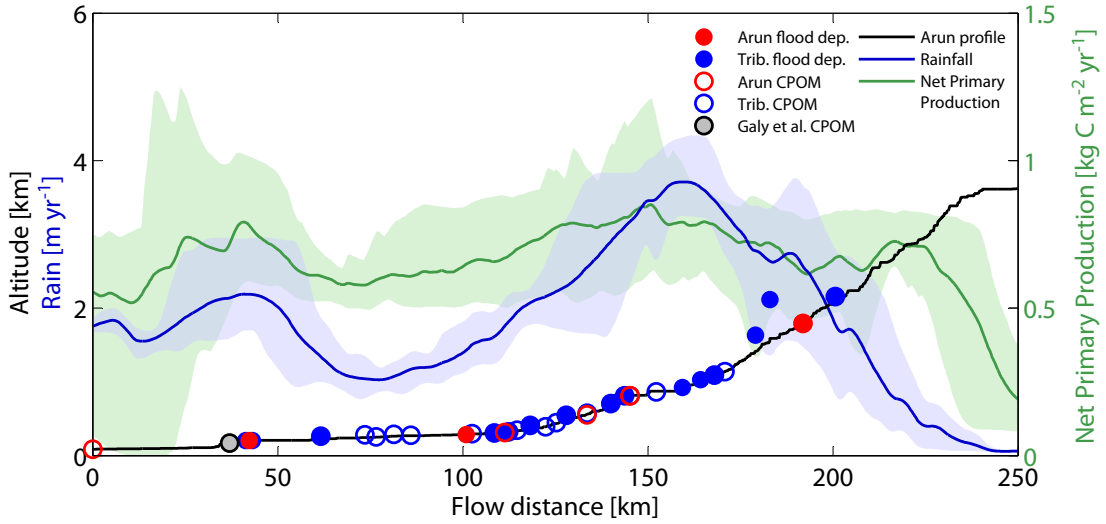

Figure 3.2: *Profile of the Arun River from the lowermost CPOM sample site in the Ganges Plain (not shown in figure 3.1) to the Tibetan Plateau (black) with flood deposit and CPOM sample sites. Additionally, Net primary productivity (green; Running et al., 2004) and mean annual rainfall rates (blue; Bookhagen and Burbank, 2010) are shown with mean (line) and* 5^{th} *to* 95^{th} *percentile (shading) of values from within a* $50 - km$ *wide swath.*

the Lesser Himalayan Sequence (middle Proterozoic orthogneisses, phyllite, augen-gneiss and quartzite) (Bordet, 1961; Jessup et al., 2008; Quade et al., 2003; Stocklin, 1980). Hence, a contribution of petrogenic plant wax *n*-alkanes is not likely. The TP portion of the Arun catchment is dominated by well-preserved Cambrian to Eocene carbonates and siliclastic sedimentary rocks of the Tethyan Tibetan Zone that potentially contribute petrogenic OM to the Arun, including plant wax *n*-alkanes.

The climate of Eastern Nepal is dominated by the Indian Summer Monsoon (ISM) contributing ~70% of the annual rain during its peak season between June and September (Bookhagen and Burbank, 2010). The Siwaliks in the south and the main Himalaya range, including Mount Everest and Makalu, act as orographic barriers to the ISM (Fig. 3.1B, 3.2) (Bookhagen and Burbank, 2006). The Tibetan region of the Arun receives very small amounts of rainfall, but additional snow from winter-westerly disturbances originating from the Caspian, Black and Mediterranean Seas (Bookhagen and Burbank, 2010; Lang and Barros, 2004). As a consequence of the climatic and hydrologic conditions, the vegetation in the Arun valley ranges from near-tropical evergreen forests in the south to sparse alpine vegetation in the high altitude part of the valley (Carpenter and Zomer, 1996; Dobremez and Shakya, 1975).

3.3 Methods

3.3.1 Sampling

Samples were obtained during two sampling campaigns in September 2011 and October/November 2012, indicated by first two digits of sample ID. River water was sampled at 37 locations (8 mainstem and 29 tributaries; see table 3.1). Water samples were taken to accompany each of the flood deposit and CPOM samples (see below). They were stored in gas-tight 2 ml glass vials that were flushed before being filled.

Leaves of modern trees and shrubs were sampled at 17 locations along the Arun Valley, at elevations ranging from 87 to 4070 $m\ asl$. Sampling of the same C3 plant species throughout the catchment was not possible because of ecological turnover of plant communities across the strong climatic gradient. We focus on Shorea robusta, a dry-season deciduous or evergreen tree being dominant below 1500 $m\ asl$, the widespread evergreen tree Schima wallichii and mostly evergreen Rhododendron spp. (c.f. appendix table 7.5), mostly found at the uppermost sites. At each site three individuals from one to three of the dominant tree species have been sampled, in total 113 individual plants. For each tree, 5-20 mature leaves were randomly sampled from approximately 2 m height, then stored and dried in paper bags.

In total 26 samples (20 x tributaries, 6 x Arun) of suspended sediment load ($> 1\ mm$ diameter) were taken. These coarse particulate organic matter (CPOM) samples consist of macroscopic plant debris with varying minor amounts of gravel. In addition we collected 16 tributary and 3 mainstem flood deposit samples in the immediate proximity of streams less than 1 m above the post-monsoon river level and represent seasonal flood deposits of the ISM discharge (for sampling details, see appendix 7.2).

3.3.2 Laboratory Methods

Water-isotope analysis

δ^{18}O and δD values of river water were determined by laser spectroscopy using a Liquid Water Isotope Analyzer (Los Gatos Research, Mountain View, California, USA), at the Institute of Earth and Environmental Sciences, University of Potsdam. Before analysis, samples were filtered through 0.45 μm polyethylene filters. Three standards (-154.3‰, -96.4‰, -9.5‰, Los Gatos Research water isotope standard) were interspersed between every five samples. Out of 6 replicate sample injections, the first three runs were discarded and a mean of the last three measurements was used. To convert sample values to the Vienna Standard Mean Ocean Water (VSMOW)-Standard Light Antarctic Precipitation (SLAP) scale, we used the linear regression function describing the relation between measured and known isotope-standard δ^{18}O and δD values. Precision is reported as one σ of replicate measurements of the standards, and is 0.06‰ and 1‰ for δ^{18}O and δD respectively.

Plant wax extraction and quantification

Flood deposit and CPOM samples were freeze-dried and a total lipid extract (TLE) of the homogenized sample was obtained by extracting the sample on a Dionex ASE 350 accelerated extraction system using 9 : 1 dichloromethane:methanol. Dried leaf samples were ground and a TLE was obtained using ultrasonic extraction with the same solvent mixture. The aliphatic fraction containing plant-wax *n*-alkanes was obtained through solid-phase extraction. For quantitative and qualitative analysis the purified samples were measured using an Agilent GC MSD (Agilent 5975C MSD, Agilent 7890A GC with Agilent J&W HP-5ms column, 30 m x 0.25 m x 0.25 μm film) equipped with an additional FID (for a more detailed description of sample processing see Hoffmann et al., 2013). In order to characterize the samples *n*-alkane distribution, we calculated the average chain length (ACL) using the formula

$$ACL = \frac{\sum C_n * n}{\sum C_n} \tag{3.1}$$

where n is the number of carbon atoms from 25 to 33 and C_n is the relative abundance. The carbon preference index (CPI) was used to quantify odd over even chain length predominance:

$$CPI = 0.5 \frac{\sum_{odd} C_{25-31} + \sum_{odd} C_{27-33}}{\sum_{even} C_{26-32}} \tag{3.2}$$

Plant wax isotope analysis

δD values of flood deposits, CPOM and tree derived *n*-alkanes from the 2012 field campaign were measured at the Institute of Earth and Environmental Sciences at the University of Potsdam. Samples taken in 2011 were measured at the University of Southern California. A Thermo Delta V Plus IRMS coupled to a Thermo Trace 1310 GC (Agilent DB-5 column, 30 m x 0.25 mm x 0.25 μm film) via a Thermo GC Isolink pyrolysis furnace operated at 1420°C was used at Potsdam University. At the Department of Earth Sciences, USC, a Thermo Scientific Trace gas chromatograph equipped with a ZB-5ms column (30 m x 0.25 mm x 1 μm) was coupled to a Thermo Delta V Plus via an Isolink operated at 1420°C. δD values obtained on systems at Potsdam University and the University of Southern California were all normalized to the VSMOW-SLAP scale using the same external standard containing C_{16} to C_{30} *n*-alkanes (A-Mix, A. Schimmelmann, Indiana University, Bloomington), run in triplicates after every 6^{th} sample. The overall analytical accuracy of triplicate A-Mix standard analysis was determined to be 3.2‰ (root mean square 0.9‰, $n = 81$). The H_3+ factor was measured daily and mean values were in the range of 2.99 to 3.37‰ (average = 3.13‰, σ = 0.11‰). δD values are reported as the mean and 1σ of triplicate measurements.

3.3.3 Remote sensing topography and climate analyses

Catchment extent and median elevation were determined using a 90-m ground resolution SRTM digital elevation model (DEM) (USGS, 2006) processed with standard Geographic Information System tools (Schwanghart and Kuhn, 2010). As a first-order approximation for erosion rates within the catchment we calculated topographic relief within a $1.5-km$ radius for each DEM pixel. The distribution of annual rainfall amounts was averaged based on calibrated Tropical Rainfall Measurement Mission (TRMM) satellite data product 3B42 from 1998 to 2010 (Bookhagen and Burbank, 2010); TRMM3B42 data have a $3-hour$ temporal resolution and a 0.25° (~30 km) spatial resolution (Huffman et al., 2007). The Moderate Resolution Imaging Spectroradiometer (MODIS) data product MOD17A3 includes Net Primary Productivity (NPP), a measure for organic matter synthesis reported in $grams$ carbon per m^2 per $year$ and has a spatial resolution of 1 km (~0.01°). The NPP grid used to approximate land-surface biomass is based on the average of cumulated annual carbon-synthesis rates between 2000 and 2011. We also used MODIS annual mean daytime temperature (MOD11C2, Wan and Dozier, 1996) with the same spatial resolution that is based on $8-day$ composites. Presented MODIS annual averages are based on 12 years of data (2001-2012). In order to characterize stream catchments, raster data were resampled using a bilinear algorithm to match the DEM spatial resolution.

3.4 Results

3.4.1 Surface water δD values

Tributaries sampled from 205 to 215 m asl (median catchment elevations 761 to 4124 m asl) had δD_{water} values between −45.9 and −92.5‰ (Fig. 3.3, Table 3.1). The relationship between median catchment elevation and tributary δD_{water} values yielded a slope of -8.3‰ km^{-1} ($R = -0.73$, $p < 0.01$). The mainstem Arun River had decreasing δD_{water} values of -78, -88 and -110‰ from south to north, respectively, as expected due to higher median catchment elevation (4785, 4832 and 4878 m asl, respectively). Mainstem δD_{water} values were not correlated to median catchment elevation.

3.4.2 Plant wax molecular composition

We identified n-alkanes in all plant-leaf samples, ranging from 25 to 33 carbon atoms, i.e. chain length, with nC_{29} and nC_{31} being dominant (appendix table 7.5). The ACL ranged from 26.9 to 31.6 ($mean = 29.1$, $\sigma = 1.0$, $n = 113$). CPI values ranged from 0.9 to 22.7 ($mean = 6.7$, $\sigma = 6$, $n = 113$). Neither plant leaf ACL nor CPI showed a significant relationship with sample site elevation, annual rainfall amount or NPP. Flood deposit and CPOM samples contained plant wax n-alkane distributions that reflect those of plants in the catchment, dominated by nC_{31} and nC_{29} and to a lesser extent nC_{27} (appendix table 7.2). Neither ACL nor CPI of flood deposit and CPOM samples was correlated to

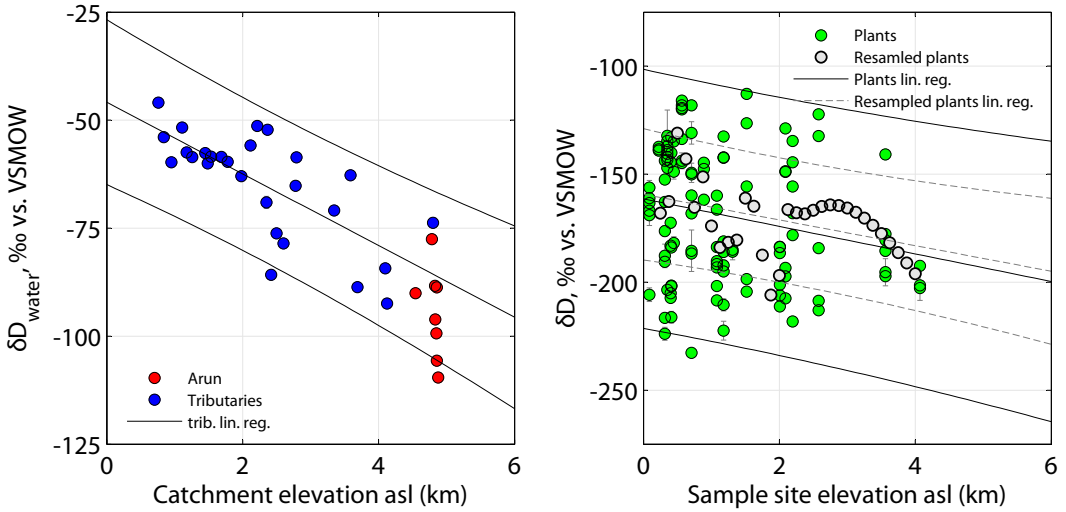

Figure 3.3: *Isotopic gradients with elevation. (A) Surface water δD values vs. median catchment elevation (analytical precision smaller than dots, c.f. Table 3.1). (B) Plant wax nC_{29} δD values of modern tree samples, mixed species (each data point is an individual) along the elevation gradient with standard deviation (green points) and resampled nC_{29} δD values (grey points, 8 samples km^{-1}). Both plots show linear regression and 95% confidence intervals (resampled plant waxes linear regression: $\delta D = -5.9x - 159‰$, $R = -0.44$, $p = 0.01$).*

catchment median elevation, precipitation or temperature. We do not report absolute abundances of plant wax because we selectively sampled apparently carbon-rich deposits in order to obtain sufficient plant wax for hydrogen isotopic determination and thus our sampling scheme was not designed to quantify flux.

3.4.3 Plant-wax *n*-alkane δD values

Plant-wax δD values of living plants (δD_{leaf}) ranged from -78‰ (sample 11004-lc1, nC_{29}, Shorea robusta) to -242‰ (sample 11047-lc3, nC_{31}, Engelhardtia spicata L.). The mean nC_{29} δD_{leaf} value was -168‰ (σ = 30‰, n = 113). Due to strong variability nC_{29} δD_{leaf} values showed only weak correlation with sample site elevation ($R = -0.22$, $p = 0.02$) with a slope of -6.4‰ km^{-1} (Fig. 3.3B). Due to decreasing data density with increasing altitude a spline resampling between 250 and 4000 m *asl* was conducted with a sampling rate of 8 *points* km^{-1}. The respective isotopic lapse rate was -5.9‰ km^{-1} with an intercept of -159‰ ($R = -0.44$, $p = 0.01$, Fig. 3.3B).

Because of low plant wax abundances in flood deposits only nC_{29}-alkane δD values could be obtained in triplicate for all flood deposit (δD_{FD}) and CPOM (δD_{CPOM}) samples. In 42 samples chain length distributions were sufficient to measure additional compounds. We found nC_{29} δD values to be correlated with nC_{27} δD ($R = 0.72$, $p < 0.01$),

nC$_{31}$ δD ($R = 0.69$, $p < 0.01$) and nC$_{33}$ δD values ($R = 0.72$, $p < 0.01$). Hence, we focus on nC$_{29}$ δD values in the subsequent data analysis (see appendix table 7.2 for complete dataset). Regarding tributary flood deposit nC$_{29}$ δD values (δD$_{FD,trib}$) no significant interannual difference was observed between September 2011 ($n = 6$) and November 2012 ($n = 7$) (Wilcoxon-Mann-Whitney-Test rejected, $p = 0.16$). Therefore, we combined the two flood deposit datasets for further analysis. δD$_{FD,trib}$ values ranged from -157‰ to -197‰ ($n = 16$), the linear regression with median catchment elevation yielded a slope of -5.3 ± 2.7‰ km^{-1}, but was not significant within 95% confidence intervals ($R = -0.47$, $p = 0.07$) (Fig. 3.4A). 2011 and 2012 CPOM data was also combined as no significant difference between September 2011 ($n = 16$) and November 2012 ($n = 4$) tributary CPOM nC$_{29}$ δD values (δD$_{CPOM,trib}$) was observed (Wilcoxon-Mann-Whitney-Test rejected, $p = 0.24$). δD$_{CPOM,trib}$ values ranged from -217‰ to -145‰ ($median = -182$‰, $n = 20$), and were not correlated to median catchment elevation. Arun mainstem CPOM δD values were within the same range observed for tributaries and ranged from -210‰ to -175‰ ($n = 6$), but like tributaries showed no trend with elevation. A comparison of tributary δD$_{FD}$ values with the isotopic composition of surface water (Fig. 3.4B) yielded a significant linear relationship, with δD$_{FD,trib} = (0.45 \pm 0.19)\delta$D$_{water} - 147 \pm 13$‰ ($R = 0.54$, $p = 0.03$), but the relationship was not significant for CPOM samples ($R = 0.24$, $p = 0.33$). The three Arun mainstem flood deposits saw a downstream D-enrichment from -206‰ to -184‰. We calculated the isotopic enrichment between mainstem n-alkanes sampled at the highest (Tibetan Plateau, TP) and the lowest (Himalayan Range, HR) location ($\epsilon_{HR/TP}$) to be +27‰ using the equation:

$$\epsilon_{HR/TP} = \left(\frac{\delta \mathrm{D}_{FD,TP} + 10^3}{\delta \mathrm{D}_{FD,HR} + 10^3} - 1 \right) 10^3 \tag{3.3}$$

3.4.4 Remote sensing data

TRMM 3B42 satellite-rainfall data indicate that only 34.7% of the Arun's annual rainfall occurs in the upper 84.8% of the catchment (north of the Nepal-China border) whereas, the majority, 65.3%, is received in the lower 15.2% (between the border and the Arun/Tamor/Sun Koshi confluence). Rainfall peaks at the southern front of the Siwalik Hills (up to 4 $m\ a^{-1}$) and the main Himalayan range (locally $> 5\ m\ a^{-1}$), in between locally dropping to less than 1 $m\ a^{-1}$. MODIS-derived annual mean NPP values follow rainfall distribution: they increase at the southern front of the Siwalik Hills and remain constant until the southern front of the main Himalayan ranges, beyond which NPP drops on the TP as rainfall decreases (Fig. 3.1C, 3.2).

Site		site lon.	site lat.	flow distance	catchm. area [km^2]	site alt. [$m\ asl$]	catchm. alt. [$m\ asl$]	δD_{water} [‰]	δD_{water} stdev. [‰]	FD δD nC_{29} [‰]	FD δD nC_{29} stdev.	CPOM δD nC_{29} [‰]	CPOM δD nC_{29} stdev.
11104	Arun	86.93	26.52	0	57927.00	87	4543	-90.1	0.2			-174.6	0.5
12151	Sun Koshi	87.16	26.91	41	6050.30	205	2351	-69.0	1.4	-187.9	1.3		
12150	Arun	87.15	26.93	42	33508.00	205	4785	-77.5	0.8	-184.3	1.3		
12149	Tamor	87.15	26.93	43	18144.00	205	2497	-76.2	0.5	-190.7	3.4		
11090	Tamor	87.32	26.93	62	5884.70	263	2420	-85.8	0.5	-183.8	1.6	-202.1	1.8
11086	Tributary	87.25	27.12	74	83.94	282	1257	-58.5	0.1			-174.7	3.6
11085	Tributary	87.28	27.15	77	90.57	253	1449	-57.6	0.5			-183.8	0.9
11081	Tributary	87.26	27.18	81	35.09	287	1110	-51.7	0.8			-180.7	0.4
11080	Tributary	87.24	27.22	86	314.11	277	1780	-59.7	0.2			-186.0	0.2
12142	Arun	87.19	27.31	101	31269.00	285	4832	-88.3	0.2	-184.8	3.1		
11075	Tributary	87.18	27.32	103	39.73	298	950	-59.7	0.1			-171.2	1.2
11005	Tributary	87.18	27.37	109	11.35	306	761	-45.9	0.5	-156.6	1.5	-217.2	1.3
11069	Arun	87.16	27.38	111	31189.00	313	4834	-96.1	0.4			-192.3	2.6
11008	Tributary	87.15	27.39	112	12.21	321	840	-53.9	0.3	-174.5	0.6	-177.9	3.8
11010	Tributary	87.13	27.39	115	74.67	344	1536	-58.5	0.7			-143.4	3.8
11013	Tributary	87.12	27.41	118	205.59	409	1981	-63.0	0.1	-161.1	2.6	-178.1	0.6
11018	Tributary	87.14	27.45	122	351.26	392	2601	-78.5	0.1			-193.1	2.0
11020	Tributary	87.15	27.47	125	3.48	448	1175	-57.5	0.2			-182.6	3.0
11023	Tributary	87.16	27.48	128	11.83	546	1486	-60.0	0.3	-173.2	2.6	-192.3	0.6
11029	Arun	87.19	27.51	134	30431.00	553	4850	-99.3	0.4			-209.5	1.5
11028	Tributary	87.19	27.51	134	13.28	573	1689	-58.5	0.5			-159.1	0.5
11037	Tributary	87.23	27.54	140	217.53	704	3688	-88.6	0.9	-174.4	1.6	-186.4	1.0
11043	Tributary	87.25	27.57	144	188.28	812	4124	-92.5	0.5	-180.7	5.0	-187.4	1.7
11049	Arun	87.27	27.56	145	29958.00	812	4858	-105.7	1.1			-183.8	0.3
12009	Arun	87.28	27.57	145	29958.00	812	4858	-88.7	0.3			-184.6	0.5
12005	Tributary	87.31	27.56	152	82.03	865	2368	-52.2	0.6			-162.8	0.5
12026	Tributary	87.35	27.61	159	165.16	922	3347	-70.9	0.6	-197.0	0.8		
12131	Tributary	87.21	27.68	162	0.09	4000	4044	-81.3	0.3	-225.0	1.7		
12032	Tributary	87.35	27.64	164	9.01	1028	2215	-51.3	0.5	-176.3	0.9		
12129	Tributary	87.21	27.69	164	0.96	4070	4203	-78.2	1.8	-221.7	0.8		
12035	Tributary	87.36	27.67	168	80.30	1090	2780	-65.2	0.5	-185.0	0.7	-184.5	0.7
12043	Tributary	87.36	27.69	171	470.80	1138	4802	-73.7	1.1	-159.8	3.3	-180.5	0.6
12054	Tributary	87.33	27.74	179	28.92	1634	2792	-58.6	0.6	-179.6	3.7		
12063	Tributary	87.37	27.77	183	0.01	2115	2115	-55.9	0.3	-161.2	3.5		
12082	Tributary	87.45	27.78	192	95.43	1787	4097	-84.3	0.4	-188.9	0.9		
12083	Arun	87.45	27.78	192	28416.00	1793	4878	-109.6	0.7	-206.3	2.0	-176.1	0.6
12097	Tributary	87.40	27.83	201	8.23	2156	3587	-62.8	0.3	-165.2	2.5	-170.9	0.4

Table 3.1: *Sampling locations with stream water δD values and the hydrogen isotopic composition of nC_{29} plant wax alkanes extracted from flood deposits (FD) and coarse particulate organic matter (CPOM) with triplicate measurement standard deviation (stdev.) (c.f. appendix table 7.2 for further details).*

3.5 Discussion

3.5.1 Elevation gradients in precipitation and stream water isotopic composition

A negative correlation between precipitation isotope ratios and elevation is expected based on the altitude effect (Dansgaard, 1964). For late to post ISM stream waters of the Arun's tributaries, we found a gradient of $-8.3‰\ km^{-1}$ (using catchment median elevation, $\sigma = 1.6‰\ km^{-1}$ and of $-8.8‰\ km^{-1}$ (using mean elevation, $\sigma = 1.5‰\ km^{-1}$), which is within the observed range of gradients of precipitation δD values with elevation in the tropics worldwide (Gonfiantini et al., 2001). It is also comparable to gradients found along other rivers at the southern TP margin after re-evaluating data for comparable elevation ranges, e.g. the Lower Yarlung Tsangpo, Po Tsangpo and Siang Tsangpo Basins in the eastern Himalaya (Hren et al., 2009) and the Kali Gandaki River (Garzione et al., 2000). Even though the stream water isotopic lapse rate might vary throughout the year it represents our best estimate of the D-depletion of precipitation with increasing altitude in the Arun valley, and is consistent with regional observations. The apparent steeper isotopic lapse rate of mainstem waters was expected due to its higher elevation and is related to high altitude fractionation effects (Rowley, 2007) and the complex hydrology of large-scale river systems with significant temporal storage of precipitation (Andermann et al., 2012; Bookhagen and Strecker, 2012).

3.5.2 Plant wax δD values in Arun tributaries

We find the largest variability in modern plants, when comparing the range of isotopic compositions (75^{th} percentile - 25^{th} percentile) in measured samples from living plants (83‰), CPOM (44‰) and flood deposits (35‰) (Fig. 3.5). Similar patterns have been observed when comparing modern catchment vegetation with lake sediments elsewhere (Hou et al., 2007; Sachse et al., 2006). Despite the high variability between plant individuals and species, we find comparable isotopic lapse rates for modern plants ($-6.4‰\ km^{-1}$) and flood deposits in tributaries ($-5.3‰\ km^{-1}$). This suggests that tributary flood deposits represent an integrated sample of plant waxes from their catchments, and is consistent with the findings of Ponton et al. (2014) based on fine particulate OM sampled in the Peruvian Andes.

While deposition of flood deposits occurs primarily during or just past the ISM season, mobilized upstream material likely integrates over years or decades as plant detritus accumulates as leaf litter and in soils. Tributary contribution of petrogenic plant waxes is unlikely for one simple reason: tributaries along the sampling transect drain catchments characterized by high-grade metamorphic rocks lacking organic matter. This argument is supported by three additional observations: first, observed tributary flood deposit CPI values ($mean\ CPI = 8.4$) are much closer to modern angiosperm CPI (~11, Bush and McInerney, 2013) than to petrogenic CPI (typically ~1). Second, mainstem flood

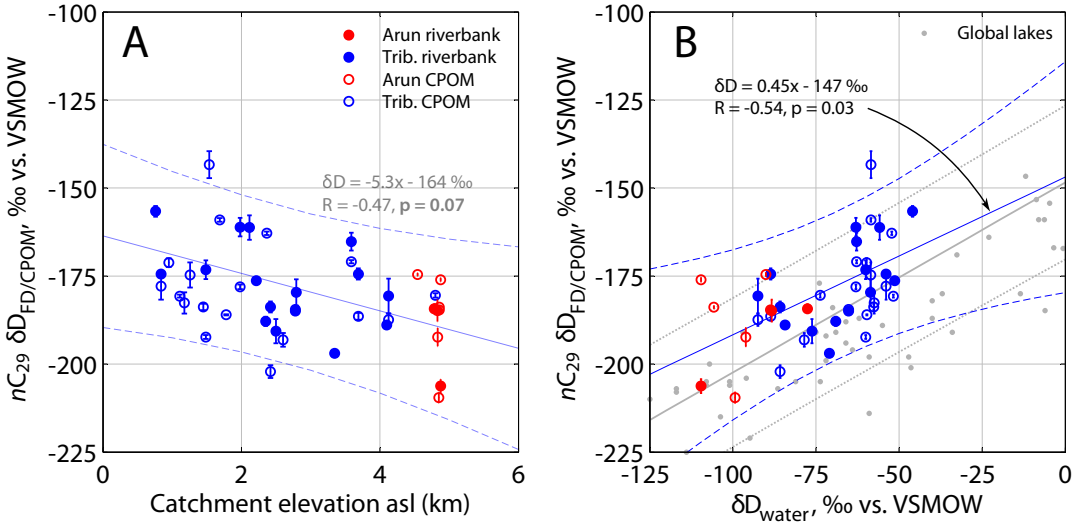

Figure 3.4: *Isotopic composition of plant waxes in sedimentary samples. (A) Shown versus median catchment elevation, including flood deposit and CPOM samples (this study). Note that linear regression based on tributary flood deposits is not statistically significant ($p = 0.07$). (B) As in part (A) but shown versus δD_{water} values. For comparison data of lake sediments versus mean annual precipitation δD values (grey dots) (Garcin et al., 2012; Polissar and Freeman, 2010; Sachse et al., 2004) with regression ($\delta D_{lake} = 0.55\delta D_{rain} + 148‰$, grey line).*

deposit CPI is constant along the sampled transect, indicating no significant input of petrogenic *n*-alkanes with CPI of ~1. Third, Galy et al. (2011) determined the age of nC_{24-32} alkanoic acids extracted from fine particulate organic matter of the Sapta Koshi watershed (Fig. 3.1A) and found it to be 0.05 $10^3 y$ old (*cal.* ^{14}C *age*). As these compounds are exclusive for vascular plant leaf waxes they provide an estimate of the residence time of the vegetation component we sampled using long chain *n*-alkanes. This young age also implies low or negligible petrogenic plant wax input.

CPOM, consisting of macroscopic, undegraded plant debris, showed δD values with reduced variability compared to δD_{leaf} indicating integration across a greater number of individual plants and species across the catchment. However, tributary CPOM δD values ($\delta D_{CPOM,trib}$) showed no significant correlation with δD_{water} values, implying that the catchment area is not evenly represented by CPOM. It is for example conceivable that CPOM was biased towards a few individual plants (e.g., uprooted trees). Hence, we used flood deposit δD values for the evaluation of tributary contributions to the main stem in section 3.5.3.

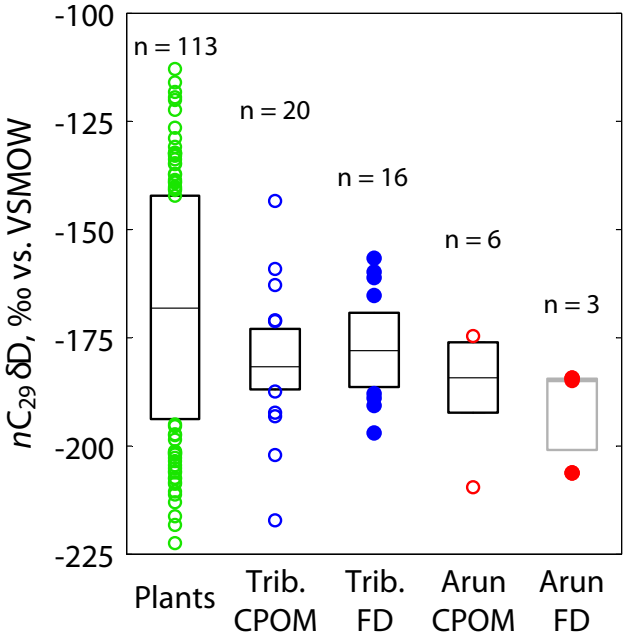

Figure 3.5: *Box plots showing nC_{29} δD values of living plants, mainstem and tributary CPOM and flood deposits across the entire transect. Boxes denote 25^{th} and 75^{th} percentile range, median (line) and outliers (circles).*

3.5.3 Fluvial integration of plant waxes

Mainstem flood deposits were characterized by a downstream increase of δD_{FD} values (Fig. 3.6B) due to inflow from lower elevation tributaries. The effect of tributary plant waxes on the mainstem signal is dominated by two factors: the isotopic composition of tributary plant waxes and its quantities. The latter is expected to be a function of catchment characteristics, including biomass productivity and erosion rates. Since climate, plant cover, and erosion vary along the steep Himalayan passage of the Arun, we do not expect uniform spatial integration across the entire catchment, in contrast to tributaries (this study and Ponton et al., 2014). In order to evaluate plant wax sourcing, we model contributions based on linear weighting of catchment size, biomass productivity, runoff and a proxy for erosion. To test the four weighting approaches we combine them with tributary δD_{wax} value estimates for a mass-weighted isotope mixing of mainstem and tributary plant wax *n*-alkanes and compare predicted vs. measured downstream mainstem δD_{FD} values.

Estimating $\delta D_{FD,trib}$ values for Himalayan tributaries of the Arun River

We sampled 16 accessible tributaries between 205 and 1793 *m* river elevation and report measured $\delta D_{FD,trib}$ values (Table 3.1, Figure 3.6A). Since the elevation to $\delta D_{FD,trib}$ relationship was not significant at the 95% confidence level ($R = -0.47$, $p = 0.07$, $n = 16$, Fig. 3.4A) we aimed for a more precise relation in order to predict $\delta D_{FD,trib}$ values along the sampled transect. Therefore, we tested a multi-parameter approach that indirectly accounts for climatic and plant physiological drivers that affect δD_{leaf} values. We account for plant source water by including mean annual temperature (MAT) and

elevation (Dansgaard, 1964; Garzione et al., 2000; Rowley et al., 2001), and for plant water evapotranspiration by including MAT and annual rainfall rates (MAP) (Feakins and Sessions, 2010; Kahmen et al., 2013b,a). As such, we set up a system of linear equations, where sampled tributary $\delta D_{FD,trib}$ values are described as a function of elevation, MAP and MAT of respective catchments:

$$\begin{cases} \delta D_{FD,trib,1} = x_1 alt_1 + x_2 MAP_1 + x_3 MAT_1 + x_4, \\ \delta D_{FD,trib,2} = x_1 alt_2 + x_2 MAP_2 + x_3 MAT_2 + x_4, \\ \vdots \\ \delta D_{FD,trib,n} = x_1 alt_n + x_2 MAP_n + x_3 MAT_n + x_4 \end{cases} \tag{3.4}$$

where alt_n, MAP_n, and MAT_n represent tributary catchment median estimates of altitude, annual rainfall and mean temperature ($n = 16$). The system of linear equations was numerically solved with $x =$ (-0.0187 -2.4308 -0.0018 -94.06). The multi-parameter model solution yielded a much better correlation with observed $\delta D_{FD,trib}$ values ($R = 0.73$, $p < 0.01$) (c.f. appendix 7.3) and was consequently used to obtain tributary $\delta D_{FD,trib}$ value estimates.

Mixing models for sourcing within the Arun catchment

To constrain and quantify plant wax sourcing contributed to the Arun by its tributaries, we tested four different weighting approaches. In four steps we include ecologic, climatologic, and geomorphic drivers that are expected to influence plant wax productivity and erosive export.

The first approach assumes that plant waxes are homogeneously produced in and exported from the river catchments. Thus, we set up a function where contributions are weighted by catchment areas. We refer to this model as the *catchment-size model*:

$$p_{wax,trib}(i) = \frac{A_{trib}(i)}{A_{trib}(i) + A_{Arun}(i-1)}, \tag{3.5}$$

where $A_{trib}(i)$ is the catchment area of all tributaries between two mainstem sites $i-1$ and i, and $A_{Arun}(i-1)$ the mainstem catchment area above $i-1$.

However, because of the inhomogeneous plant cover distribution throughout individual watersheds (Fig. 3.1C, 3.2), it is likely that regions with more biomass contribute more plant wax than others. Hence, the second approach uses cumulative NPP rates to estimate plant wax derived from catchments between mainstem sites $i-1$ and i. We refer to it as the *biomass model*:

$$p_{wax,trib}(i,j,k) = \frac{\sum NPP_{trib}(i,j)}{\sum NPP_{trib}(i,j) + \sum NPP_{Arun}(i-1,k)}, \tag{3.6}$$

where $\sum NPP_{trib}(i,j)$ is the sum of j NPP rates representing all tributaries between mainstem sites $i-1$ and i and $\sum NPP_{Arun}(i-1,k)$ is the sum of k NPP rates within the Arun catchment above $i-1$.

In our third approach, we evaluate the role of runoff on the mobilization of organic matter. Since runoff and non-petrogenic particulate organic carbon fluxes are linked (Clark et al., 2013; Hilton et al., 2012; Schäfer et al., 2002; Smith et al., 2013; Townsend-Small et al., 2008), we weighted tributary plant wax export by cumulated rainfall. Therefore, we refer to this model as the *runoff model*:

$$p_{wax,trib}(i,j,k) = \frac{\sum TRMM_{trib}(i,j)}{\sum TRMM_{trib}(i,j) + \sum TRMM_{Arun}(i-1,k)}, \tag{3.7}$$

where $p_{wax,trib}(i,j,k)$ is the relative portion of plant wax derived through all tributaries between point $i-1$ and i, and $\sum TRMM_{trib}(i,j)$ and $\sum TRMM_{Arun}(i-1,k)$ represent cumulative rainfall within all tributary pixel j between mainstem sites $i-1$ and i and of all mainstem pixel k upstream site i, respectively.

The last factor known for its effect on organic matter export is erosion (Galy et al., 2015). Erosion rates (Summerfield, 1991) and as well as erosion of organic matter (Hilton et al., 2013, 2012) have been demonstrated to relate to topographic indices, for example local relief and hill slope angle (Olen et al., 2015). Hence, we tested $p_{wax,trib}(i,j,k)$ an additional weighting approach based on the combination of *catchment relief* and the *runoff model*. We refer to it as the *erosion model*:

$$p_{wax,trib}(i,j,k) = \frac{\sum R\ TRMM_{trib}(i,j)}{\sum R\ TRMM_{trib}(i,j) + \sum R\ TRMM_{Arun}(i-1,k)}, \tag{3.8}$$

where factors are similar to the *runoff model* (Eq. 3.7), except that the rainfall grid was pixel-wise multiplied by local relief before weighting.

We combine the four different weighting approaches for tributary plant OM export with respective approximated $\delta D_{FD,trib}$ values (Eq. 3.4) as input parameters for a mixing model predicting $\delta D_{FD,Arun}$ values along the mainstem. The $\delta D_{FD,Arun}$ value at a mainstem site i was calculated by:

$$\delta D_{FD,Arun}(i) = p_{wax,trib}(i)\ \delta D_{FD,trib}(i) + (1 - p_{wax,trib}(i))\ \delta D_{FD,Arun}(i-1), \tag{3.9}$$

where $p_{wax,trib}(i)$ is the relative plant wax contribution of tributaries (fraction between 0 and 1, derived through equations 3.5 to 3.8, respectively) draining the Arun between sites $i-1$ and i. $\delta D_{FD,trib}(i)$ is the estimated tributary plant wax δD value obtained through the multi-parameter model (Eq. 3.4), and $\delta D_{FD,Arun}(i-1)$ is the Arun plant wax δD value at the upstream site $i-1$. The model start value for $\delta D_{FD,Arun}(i-1)$ is the measured δD_{FD} value from the uppermost mainstem flood deposit sample at 1793 *m asl* (-206‰). In order to allow for a potential bias of the $\delta D_{FD,Arun}$ starting value and to evaluate its effect on the model results we additionally ran the model with starting values of -206 ± 20‰. Every simulation step incorporated tributaries draining the mainstem within 25 pixels alongside the DEM derived flow path of the Arun, corresponding to an average flow path length of ~2.6 *km*. A detailed description of error propagation is provided in the appendix 7.4.

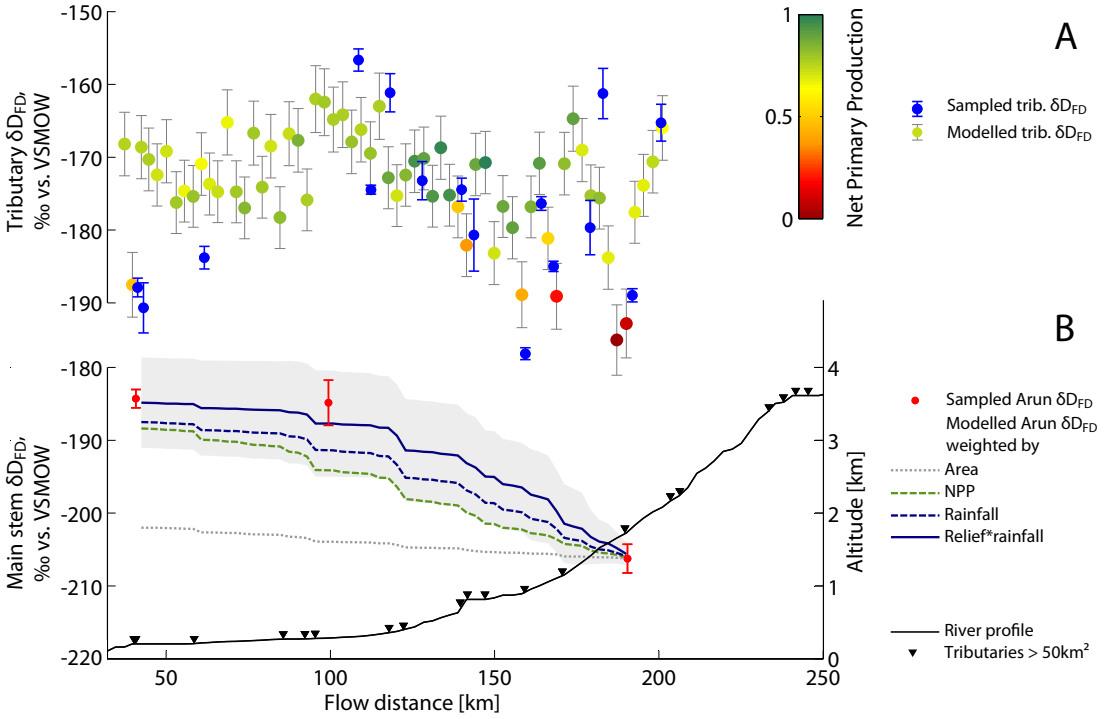

Figure 3.6: *modelling plant wax sources. (A) Tributaries. Modelled flood deposit $\delta D_{FD,trib}$ values with 95% CI (color indicates mean catchment NPP) and measured $\delta D_{FD,trib}$ values (blue circles, error bars, 1σ of triplicate measurements). (B) Arun mainstem. Comparison of model $\delta D_{FD,Arun}$ estimates with mixing proportions of TP and HR sources weighted by catchment size (grey dotted line), NPP (green dashed line), rainfall (blue dashed line) and by rainfall combined with the local relief (blue solid line) with prediction errors for the erosion model (grey shading, see appendix 7.4 for error propagation). Measured $\delta D_{FD,Arun}$ values are denoted as red circles (error bars as in A). Triangles along river profile (black line) indicate confluences with largest tributaries.*

Estimated plant wax contributions

The catchment-size model predicted that Tibetan Plateau sources contribute 85% of plant wax yielding a $\delta D_{FD,Arun}$ value of -202.0 ± 0.3‰ ($\epsilon_{HR/TP} = 5.4 \pm 0.4$‰) at the lowermost Arun mainstem sampling location (observed $\delta D_{FD,Arun} = -184$‰). A much smaller predicted $\epsilon_{HR/TP}$ compared to field observations implied overestimated plant wax export from the TP and confirmed our expectation that fluvial plant wax sourcing in the Arun is not spatially uniform. The biomass model predicted only 41% of plant wax is sourced from the Tibetan Plateau. The predicted $\delta D_{FD,Arun}$ value was -188.4 ± 6.7‰ at the lowest site with an $\epsilon_{HR/TP}$ of $+22.5 \pm 8.4$‰ (Fig 3.6B). Because of the larger uncertainties of NPP including land cover classification (Cracknell et al., 2013), leaf-surface reflectance and climate input (Zhao et al., 2006) resulting $\delta D_{FD,Arun}$

errors were much larger than for the catchment-size model. However, the biomass model captured the downstream $\delta D_{FD,Arun}$ value as well as the intermediate mainstem sample within prediction errors, even though tributary plant wax contributions still appear to be underestimated. But NPP may not be linearly related to the amount of exported plant waxes due to additional physical controls on mobilization and export, including catchment geomorphology and climatic conditions (Clark et al., 2013; Hilton et al., 2012; Smith et al., 2013). In order to account for export capacities, we weighted plant wax contributions by runoff, calculated from remotely-sensed rainfall. The runoff model predicted that 35% of plant wax in the Arun is derived from the Tibetan Plateau, and 65% originates from within the Himalayan Ranges. The modelled isotopic composition at the lowermost sample site was -187.5 ± 6.9‰ with an $\epsilon_{HR/TP}$ of $+23.6 \pm 8.6$‰, also within errors of the lowermost observed $\delta D_{FD,Arun}$ value (-184‰, $\epsilon_{HR/TP} = +27.7 \pm 5$‰). Although $\delta D_{FD,Arun}$ results of the biomass and runoff model were close at the downstream Arun mainstem site, plant wax contributions of the biomass model along the southern half of the transect are higher. Accordingly, runoff-model plant wax contributions were higher for the northern half (Fig. 3.6B), reflecting orographic rainout between 1.5 and 3 *km asl* (Fig. 3.1B and 3.2). However, both models somewhat underestimated tributary plant wax contributions along the Arun indicating an additional parameter that is required in order to obtain the observed $\delta D_{FD,Arun}$ pattern. The erosion model, accounting for runoff and erosive potential (local relief), predicted 27% plant wax from the Tibetan plateau and 73% from the Himalaya with a $\delta D_{FD,Arun}$ value of -184.9 ± 6.2‰ for the lowermost site and $\epsilon_{HR/TP}$ of $+27.0 \pm 7.8$‰, being congruent with observed downstream enrichment. But especially the intermediate sample was predicted best by the erosion model, suggesting that the combination of runoff and a proxy for erosive capacity best describes the export of plant wax in the Arun catchment. This supports recent findings about the role of runoff and erosion on organic matter mobilization in river catchments globally (Clark et al., 2013; Galy et al., 2015; Hilton et al., 2012, 2013; Smith et al., 2013).

Our sensitivity test on potentially inaccurate $\delta D_{FD,Arun}$ starting values by taking the example of the erosion model yielded only small changes for starting values of -206 ± 20‰: the model output for the sensitivity runs was -189.8‰ and -179.4‰, respectively, still matching the observed downstream $\delta D_{FD,Arun}$ value within the models' 95% prediction errors. This implies, that expected natural $\delta D_{FD,Arun}$ value variability of plant waxes representing the TP affects the model to a small extent only.

Implications for the plant-wax paleohydrology proxy

Our spatial sampling along a large trans-Himalayan river showed that δD values of plant waxes extracted from tributary flood deposits are representative for catchment vegetation and δD_{water} values (Fig. 3.4B). We found a relationship of $\delta D_{FD,trib} = 0.45\ \delta D_{water} - 147$‰ ($R = -0.54$, $p = 0.03$) that largely supports earlier studies showing a good correlation in fluvial deposits (Galy et al., 2011; Ponton et al., 2014) and lacustrine archives (Garcin et al., 2012; Huang et al., 2004; Polissar and Freeman, 2010; Sachse et al., 2004). Global data for annual mean precipitation and lacustrine plant

wax n-alkane δD values (Garcin et al., 2012; Polissar and Freeman, 2010; Sachse et al., 2004) are characterized by a slightly steeper slope but comparable regression intercept $\delta D_{wax,lakes} = 0.55\ \delta D_{water} + 148‰$ ($r^2 = 0.8$, $p < 0.01$) (Fig. 3.4B). However, they are the same within the 95% confidence interval (Fig. 3.4B). But most calibration studies in lacustrine environments have compared surface sediment plant wax δD values to annual mean precipitation δD (Garcin et al., 2012; Polissar and Freeman, 2010; Sachse et al., 2004), which is assumed to be the source water in most contexts. We correlate $\delta D_{FD,trib}$ to post ISM surface water instead, being our best estimate of annual mean precipitation δD values. But we have to acknowledge that $\delta D_{water,trib}$ values are unlikely to precisely match plant source water δD as surface waters are affected by additional evaporation and mixing with groundwater and glacier and snow meltwater.

Whereas we confirm the link of $\delta D_{FD,trib}$ values and the isotopic composition of environmental water, our plant wax quantification approach further indicates that plant wax sourcing along the Arun is strongly biased towards tributaries with highest runoff and high erosion capacities. This implies, that tectonic changes on longer geological timescales, e.g., as a consequence of mountain range uplift, would change plant wax source areas of fluvial deposits to the loci of erosion. Hence, the interplay between climatological and geomorphic processes over geologic timescales should to be taken into account when interpreting paleoclimate records from comparable fluvial systems.

3.6 Conclusions

We measured the plant wax hydrogen isotopic composition of plant leaves, river coarse particulate organic matter and flood deposits from the trans-Himalayan Arun River and tributaries in eastern Nepal. We found that plant wax *n*-alkanes in the deposits reflect the isotopic composition of modern plants in their catchments and that those plant waxes carry signatures of the elevation-related gradient in environmental waters. We use these relationships together with remote-sensing data for biomass productivity (NPP), rainfall amount, and relief to understand plant organic matter sources of fluvial deposits. Mixing-models accounting for climatic, biomass, and geomorphic factors suggest that fluvial transport does not uniformly mobilize plant waxes from across the vast catchment area. Instead, sourcing is dominated by tributaries within the lowermost 15% of the catchment, draining the Arun between 205 and 1793 *m* river elevation. Our remote sensing-based modelling approaches demonstrated that the presence of vegetation in the Arun's tributaries is necessary, but not sufficient for high plant organic matter export rates. The best fit to plant wax observational data finds areas with high precipitation (and consequently high NPP) and relief to contribute the largest amount of plant wax, emphasizing the importance of both productivity and erosion processes for plant wax exports. Our novel modelling approach provides quantitative insights into the sourcing of plant-wax biomarkers in this catchment and introduces a new interpretative framework. This framework enables robust interpretations of modern terrestrial plant biomarker sourcing and provides better constraints on the interpretation of plant wax proxy records

in terms of past hydrologic changes in river catchments.

Acknowledgements

BH is grateful to UNVEU 1966, SF was funded through US National Science Foundation (EAR-1227192 and OCE-1401217) and the USC Women in Science and Engineering Program and DS through an Emmy-Noether grant from the German Science Foundation (DFG SA1889/1-1 and 1-2). Thanks to Manoj, Sophia Wagner and Raphael Scheffler for field assistance and Miguel Rincon, Michael Pöhle and Denise Jekel for lab assistance.

4 | Understanding erosion rates in the Himalayan orogen: A case study from the Arun Valley

Stephanie M. Olen[1], Bodo Bookhagen[1], Bernd Hoffmann[1], Dirk Sachse[1,2], Danda P. Adhikari[3], and Manfred R. Strecker[1]

[1] Institute of Earth and Environmental Science, University of Potsdam, Potsdam, Germany
[2] Helmholtz Centre Potsdam GFZ, German Research Centre for Geosciences, Potsdam, Germany
[3] Department of Geology, Tribhuvan University, Kathmandu, Nepal

Published in: Journal of Geophysical Research: Earth Surface, 2015
Issue 120
Pages 2080-2102
doi:10.1002/2014JF003410.

Abstract

Understanding the rates and pattern of erosion is a key aspect of deciphering the impacts of climate and tectonics on landscape evolution. Denudation rates derived from terrestrial cosmogenic nuclides (TCNs) are commonly used to quantify erosion and bridge tectonic (Myr) and climatic (up to several kiloyears) time scales. However, how the processes of erosion in active orogens are ultimately reflected in ^{10}Be TCN samples remains a topic of discussion. We investigate this problem in the Arun Valley of eastern Nepal with 34 new ^{10}Be-derived catchment-mean denudation rates. The Arun Valley is characterized by steep north-south gradients in topography and climate. Locally, denudation rates increase northward, from < 0.2 $mm\ yr^{-1}$ to ~1.5 $mm\ yr^{-1}$ in tributary samples, while main stem samples appear to increase downstream from ~0.2 $mm\ yr^{-1}$ at the border with Tibet to 0.91 $mm\ yr^{-1}$ in the foreland. Denudation rates most strongly correlate with normalized channel steepness ($R^2 = 0.67$), which has been commonly

interpreted to indicate tectonic activity. Significant downstream decrease of ^{10}Be concentration in the main stem Arun suggests that upstream sediment grains are fining to the point that they are operationally excluded from the processed sample. This results in ^{10}Be concentrations and denudation rates that do not uniformly represent the upstream catchment area. We observe strong impacts on ^{10}Be concentrations from local, nonfluvial geomorphic processes, such as glaciation and landsliding coinciding with areas of peak rainfall rates, pointing toward climatic modulation of predominantly tectonically driven denudation rates.

4.1 Introduction

Denudation, the removal of mass from the landscape, is the combined result of tectonic forces that expose rock at the surface and climatic forces that provide the erosive agents to remove it. An effort to understand the relationship between the rates of denudation and the tectonic and/or climatic forces that drive denudation has been a main undertaking in Earth science in recent decades. Many theoretical and field studies have suggested a close link between climate and denudation rates in a variety of geodynamic settings (Reiners et al., 2003; Hales and Roering, 2005; Roe et al., 2008; Moon et al., 2011; Bookhagen and Strecker, 2012; Ferrier et al., 2013a,b; Herman et al., 2013), ultimately resulting in characteristic landscapes in accord with climatic zonation (e.g., Buedel, 1982). In contrast, another group of studies has argued against a strong climatic influence on denudation rates in many orogens and emphasizes a more decisive role of tectonic processes in landscape evolution (e.g., Riebe et al., 2001, 2004; Burbank et al., 2003; Safran et al., 2005; Willenbring and von Blanckenburg, 2010; Godard et al., 2014; Scherler et al., 2014). However, the time scales of these studies differ significantly, from tens (e.g., suspended sediment flux) to millions (e.g., thermochronometry) of years.

Over the last quarter century, the assessment of erosion processes using terrestrial cosmogenic nuclides (TCNs) has been increasingly refined as a widely used method in geomorphology due to its ability to quantify catchment-mean denudation rates on $10^2 - 10^5$ year time scales, thus bridging the gap between instrumentally recorded erosion rates and rates obtained from thermochronology and the stratigraphic records of geologic archives (Bierman and Steig, 1996; Brown et al., 1995; Von Blanckenburg, 2005; Granger et al., 1996, 2013). Several studies have used ^{10}Be concentrations in detrital sand samples to investigate how climate and/or tectonics influence denudation rates in mountain belts around the world (e.g., Safran et al., 2005; Bookhagen and Strecker, 2012; Godard et al., 2014; Scherler et al., 2014). However, the assumptions necessary to calculate catchment-mean denudation rates from a detrital river sand sample are frequently violated in climatically very dynamic, active tectonic environments, and the extent to which ^{10}Be concentrations reflect actual denudation rates is still under debate (e.g., Lupker et al., 2012; McPhillips et al., 2014; Puchol et al., 2014).

Because it has been proposed as a location where tectonic-climate coupling might oc-

cur (e.g., Molnar and England, 1990; Hodges et al., 2004; Thiede et al., 2005; Huntington et al., 2006; Hirschmiller et al., 2014), the Himalaya represents an area where understanding denudation rates is of great scientific importance. The highest mountain range in the world, the Himalaya is rapidly and actively uplifting and eroding (e.g., Molnar and Tapponnier, 1975; Avouac, 2003) and is characterized by an extreme and highly seasonal climate. The Indian summer monsoon (ISM) delivers large amounts of rainfall to the Himalaya, focused along the southern orographic front due to high topographic barriers (Bookhagen and Burbank, 2006, 2010). Monsoonal rainfall drives large discharge events and sediment fluxes toward the Indo–Gangetic foreland (Wulf et al., 2010, 2012) and eventually into submarine fans and beyond (Milliman and Syvitski, 1992; Clift et al., 2001; Curray et al., 2003). Authors of recent studies of ^{10}Be TCN from the Himalaya have argued, however, that climate does not play a decisive role in driving denudation rates, which are instead controlled principally by tectonic deformation and uplift (e.g., Godard et al., 2014; Scherler et al., 2014).

The impact of climate on sediment flux and topography through variability of the ISM may have been stronger in the past (e.g., Goodbred and Kuehl, 2000; Bookhagen et al., 2005a). Evidence exists for a stronger ISM in the early Holocene and a relatively weak ISM during the Last Glacial Maximum and the present day (e.g., Prins and Postma, 2000; Thamban et al., 2002; Fleitmann et al., 2003; Bray and Stokes, 2004; Zhisheng et al., 2011). The early Holocene intensified monsoon was associated with a twofold increase in sediment discharge to the Ganges-Brahmaputra fan (Goodbred and Kuehl, 2000), frequent large landslides in the orogen interior, and overall increased sediment flux in the NW Himalaya (Bookhagen et al., 2005a). Such studies document the sensitivity of the Himalayan system to changes in regional climate and the surface-process regime.

In this study, we present 34 new ^{10}Be TCN catchment-mean denudation rates from the Arun Valley in eastern Nepal to understand how climatic and tectonic processes affect ^{10}Be TCN concentrations and the resulting denudation rate calculations. The north-south flowing Arun is the fourth largest trans-Himalayan river and traverses the orogen through a deeply incised, narrow gorge (Figure 4.1). The Arun Valley is characterized by steep topographic and climatic gradients perpendicular to the strike of the Himalaya. These distinct gradients allow for a robust analysis of different climatic and topographic factors that may influence ^{10}Be concentration in river sand samples and possibly control regional denudation rates.

4.2 Background

4.2.1 Climatic setting

Every year the ISM system delivers heavy, seasonal rainfall to the Himalaya as the Intertropical Convergence Zone migrates northward during the boreal summer (Charney, 1967; Gadgil, 2003). The orographic barrier of the Himalaya focuses monsoonal rainfall

along its southern flank, where mean annual rainfall locally exceeds 5 $m\ yr^{-1}$ (Figure 4.1c) (Bookhagen and Burbank, 2010). The Arun Valley is located relatively close to the Bay of Bengal (Figures 4.1b and 4.1c) and thus the main ISM moisture source. Weather stations maintained by the Nepal Department of Hydrology and Meteorology in the Arun record approximately 60% of annual rainfall during the peak ISM months (June through September); $80-90\%$ of annual rainfall occurs from May to October (c.f. Bookhagen and Burbank, 2010). Because of the deeply incised, N-S oriented gorge, moisture is funneled through the Arun Valley northward into Tibet, resulting in greater rainfall in the upper sectors of the valley than on the surrounding higher-elevation areas (Figure 4.1c).Winter precipitation is primarily focused in the high-altitude regions (Bookhagen and Burbank, 2010; Wulf et al., 2010), and snowfall is common in these areas (Carpenter and Zomer, 1996). Reliable snowfall data from gauging stations, however, are not available in the Arun region as weather stations are principally located at low elevations not affected by snowfall. Bookhagen and Burbank (2010) calculated the snow melt contribution of major Himalayan rivers across the Himalayan orogen and found that approximately 25% of total discharge in the Arun is related to snow melt, as opposed to over 50% in the Western Himalaya.

4.2.2 Geologic and Tectonic Setting

Originating in Tibet, the Arun flows southward through the Himalayan orogen before joining the Sapt Kosi and the Ganges Rivers in the foreland. The course of the river exposes a natural cross section through the mountain belt: from the sedimentary Tethyan series in Tibet, through the Greater or High Himalayan Crystalline (HHC), the Lesser Himalayan Crystalline (LHC), the Siwaliks, and finally to the alluvial plains of the Gangetic foreland (Schelling, 1992; Grujic et al., 2011). An aerially extensive tectonic window, identified by Meier and Hiltner (1993) as the Arun Tectonic Window, exposes LHC rocks below the Main Central Thrust (MCT) along the course of the Arun (Figure 4.1d). The northern extent of this window and the location of the MCT are poorly constrained (e.g., Schelling, 1992). The Arun Tectonic Window corresponds to a large anticline (Wager, 1937), which Montgomery and Stolar (2006) suggested to result from focused bedrock incision of the Arun.

The lithology in the study area is dominated by crystalline metamorphic rocks, principally from the HHC and LHC. The LHC units in the Arun Valley, as mapped by Schelling (1992), are metasediments (e.g., metaquartzite, slate, phyllite, and metagraywacke) and augengneiss. HHC units are comprised of migmatites, paragneiss, and granites. No extensive carbonate or volcanic deposits are exposed, and all mapped lithologic groups are predominantly quartz-bearing. Because the Arun Tectonic Window follows the Arun Valley northward, we do not observe discrete variations in lithology perpendicular to strike within our study area (Figure 4.1d and Figure 4.2).

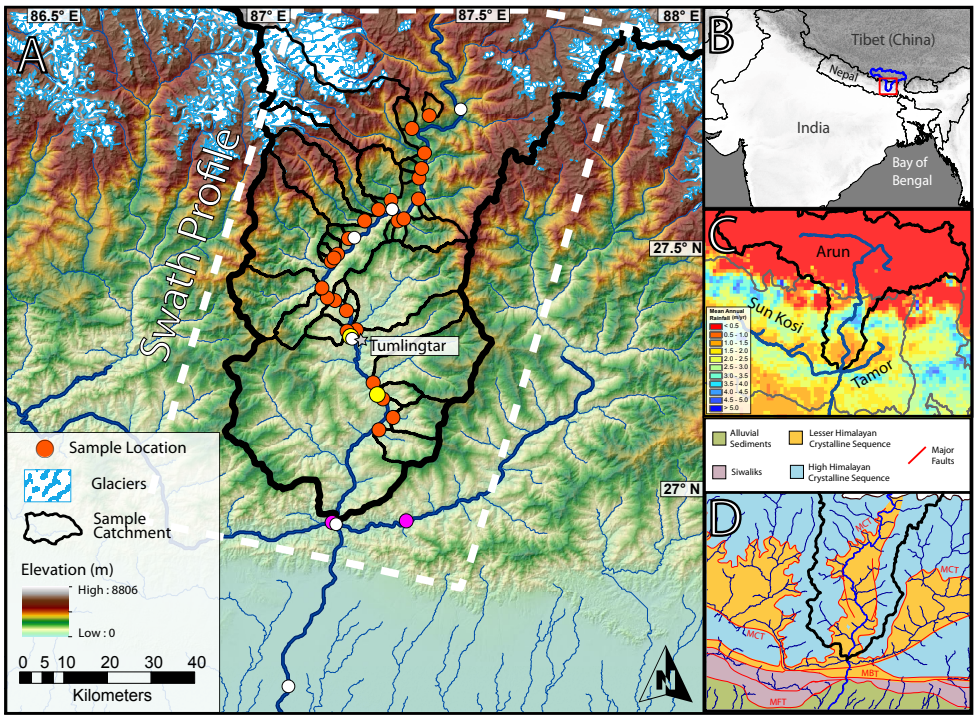

Figure 4.1: *Overview of study area in the Arun Valley, eastern Nepal. (a) Map of study area showing elevation from SRTM 90 − m DEM, river network (dark blue), and glaciers from GLIMS glacier database (light blue/white) (GLIMS and National Snow and Ice Data Center, 2005; http://www.glims.org/). Sample locations of* ^{10}*Be TCN sample sites for tributaries (red) are shown with associated watersheds outlined (black); along with main stem (white), Sun Kosi and Tamor Rivers (pink), and fluvial fill terrace (yellow) sample locations (c.f. Table 4.1). Downstream of the confluence of the Arun, Sun Kosi, and Tamor Rivers, the river is called the Sapt Kosi. The main stem Arun watershed is shown by a thick black outline. The swath area used for Figure 4.3 is shown in dashed white lines. (b) The Arun Valley in the regional context, including area from Figure 4.1a (red), and the entire Arun watershed, including area in Tibet (blue). (c) Mean annual rainfall (mm* yr^{-1}*) from calibrated TRMM 2B31 (Bookhagen and Burbank, 2010) showing double bands of high rainfall at the orographic fronts of the LH and HH and Sapt Kosi River network, including Arun, Sun Kosi, and Tamor (dark blue) and Arun watershed (black). Political boundaries are shown in gray for reference. (d) Geologic map of the study area after Grujic et al. (2011) showing major Himalayan lithologies and faults of eastern Nepal. MFT denotes Main Frontal Thrust, MBT Main Boundary Thrust, and MCT Main Central Thrust. Outline of the Arun watershed is shown in black.*

4.2.3 Geomorphic Setting

As it drains the Himalaya, the Arun displays a steep, graded channel profile in a narrow valley (Figure 4.2). Two large slope-break knickzones north of the Arun gorge, approximately corresponding to the location of the Southern Tibetan Detachment (STD), separate the Himalayan Arun from the Tibetan section of the river, known locally as the Pum Qu. Similar knickzones of tectonic origin are observed in many trans-Himalayan rivers along strike (e.g., Seeber and Gornitz, 1983). Above these knickzones the river has a shallow profile for the remainder of its upstream course and a broad, flat valley. Several fluvial fill terraces in the lower and middle reaches of the Arun have been mapped by Lavé and Avouac (2001), but few are preserved in the upper reaches of the valley. We observed several strath terraces and hanging valleys, particularly in the upper sections of our study area approaching the Tibetan border.

The topography of the Arun Valley is comprised of three principal topographic sectors (Figure 4.3a): the Lesser Himalaya (LH), with an average elevation of ~2 km above sea level (asl) and a mean hillslope angle of ~20°; the Higher Himalaya (HH), where mean elevation rises above 4 km asl and peaks are in excess of 8 km asl, with a mean hillslope angle of ~30° and a topographic transition zone between the Lesser and Higher Himalaya, first identified in other areas along strike of the mountain belt as the Physiographic Transition Zone (PT2) (Hodges et al., 2001), marking a sharp break in topography.

In the Higher Himalaya, the Arun Valley hosts several glaciers (Global Land Ice Measurements from Space (GLIMS) and National Snow and Ice Data Center, 2005; http://www.glims.org/). Larger valley glaciers are predominantly in western tributaries of the Arun. To the east, several small cirque glaciers exist in the Ama Drime and Higher Himalaya, but no large valley glaciers currently occupy these watersheds. In the Nepalese section of the Arun Valley, cirque and valley glaciers exist in the upper reaches of the northernmost tributaries flowing into the Arun, but are less prominent than on the northern flanks of the Higher Himalaya, where extensive glaciation extends down from the northern slopes of the Sagarmatha/Mount Everest and Makalu regions. Valley morphology suggests that past glaciation was more extensive in medium to large high-altitude tributaries, but there is no evidence of glaciers reaching the main stem Arun.

4.3 Methods

4.3.1 Climatic Data and Analysis

Rainfall in the Arun Valley was characterized using remotely sensed data from the Tropical Rainfall Measurement Mission (TRMM). We used the calibrated 12 year average mean annual rainfall product TRMM 2B31 (Bookhagen and Burbank, 2010) with a nominal spatial resolution of 5×5 km. Additionally, we used the National Snow and Ice

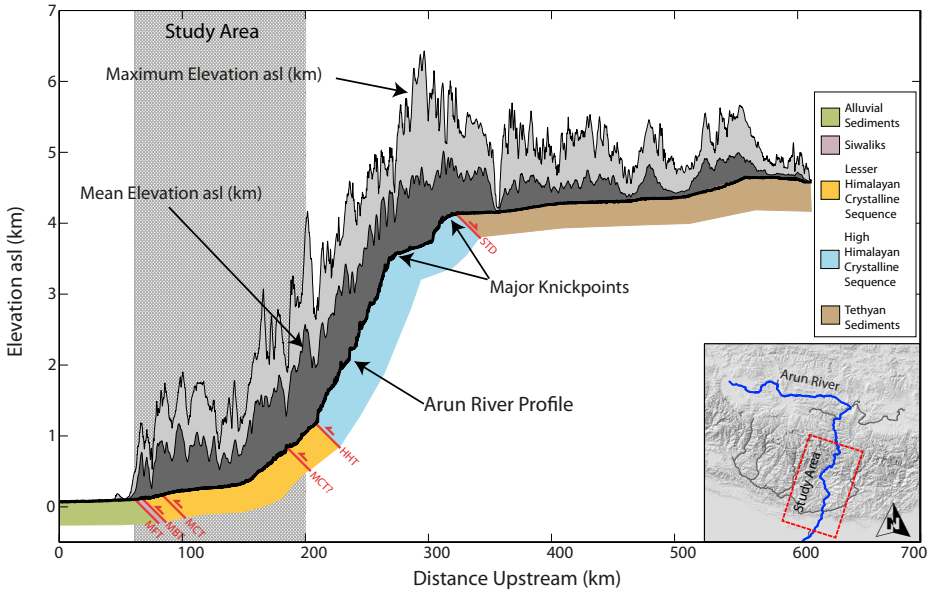

Figure 4.2: *Longitudinal profile of Arun River from the Ganges Plain in the south to its source in southern Tibet. The river profile (black) is shown with mean elevation (dark gray) and maximum elevation (light gray) from a* 1.5 *km swath centered along the course of the river. The two large knickzones are easily visible in the river profile, as well as the transition from a steep graded profile* ($\theta = 0.45$) *to shallow profile* ($\theta = 0.79$) *downstream and upstream of the knickzones, respectively. Surface lithology along the Arun River after Grujic et al. (2011); major fault locations after Schelling (1992) and Grujic et al. (2011). The study area is shown in hatched gray. Inset shows map view of the region, with the Arun trunk stream highlighted in blue.*

Data Center (NSIDC) Global Land Ice Measurements from Space (GLIMS) database to define the location of present-day glaciers within our study area (GLIMS and National Snow and Ice Data Center, 2005; http://www.glims.org/). Due to insufficient data, we do not account for snowfall or glacial melt in any of our climate-based analysis. Because of this, we acknowledge that metrics that depend on stream discharge, such as specific stream power (below), may be underestimated in high-altitude catchments affected by snowfall. We calculated specific stream power (SSP), a measure of potential stream energy per unit area based on the stream power model (e.g., Whipple and Tucker, 1999; Lague, 2014), following Bookhagen and Strecker (2012). SSP (ω, Wm^{-2}) incorporates climatic and topographic factors, such that

$$\omega = \frac{\gamma \times \mathrm{S} \times \mathrm{Q}}{\mathrm{w}}$$

where ω is the specific weight of water (9819 Nm^3), Q is discharge ($m^3 s^{-1}$), S is the

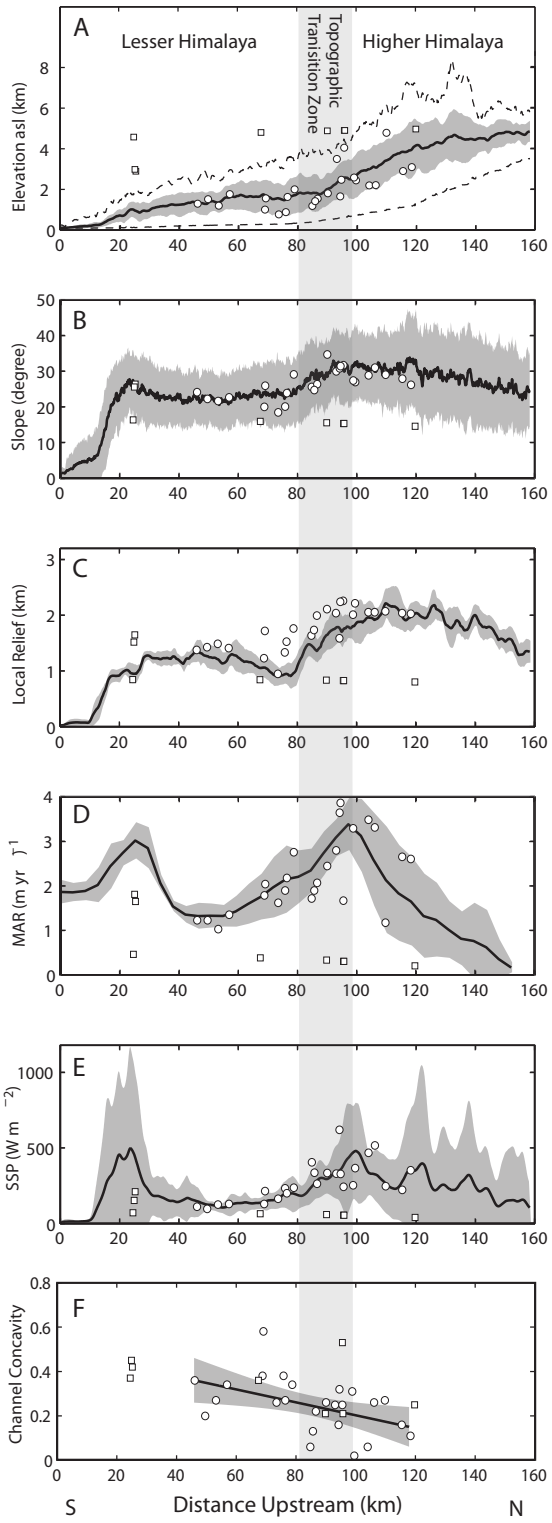

Figure 4.3: *Swath profiles (from swath area in Figure 4.1) of (a) elevation, with Lesser Himalaya, topographic transition zone (shaded gray), and Higher Himalaya denoted; (b) slope; (c) 3km radius relief; (d) mean annual rainfall (Bookhagen and Burbank, 2010); (e) TRMM-weighted specific stream power (SSP); and (f) channel concavity from χ analysis for each sampled tributary and main stem location. Values are averaged across a 75km wide swath area, chosen to include all major tributaries to the Arun River in our study area. Mean swath values are shown in black with $\pm 1\sigma$ in shaded gray. Catchment-mean values from all sampled tributaries (circles) and main stem locations (squares) are shown along swath. Concavity values (F) are shown with linear regression of tributary concavity values and upstream distance; the shaded gray region represents the 95% confidence bounds. The topographic transition zone is shown in all panels by the light gray bar.*

local bed slope (mm^{-1}), and w is the width of the channel (m). To account for the large spatial variations in rainfall in the Arun Valley, and therefore presumably runoff, we determined discharge based on both upstream area and TRMM-derived rainfall. We calculated SSP for every $90 - m$ pixel in the digital elevation model (DEM) and have used an 11-pixel (~1 km) moving average channel-slope filter to remove outliers. SSP values were explicitly calculated from channel slopes. Channel width was defined using a simple scaling model, such that channel width was assumed to increase proportionately to discharge, following a power law relationship with an exponent of 0.4 (Knighton, 1999; Whipple, 2004; Craddock et al., 2007).

4.3.2 Topographic and Geologic Data and Analysis

Topographic analysis was performed on the 90mresolution Shuttle Radar Topography Mission (SRTM) digital elevation model (DEM) v4.1 provided by Consultative Group on International Agricultural Research (CGIAR) Consortium for Spatial Information (http://srtm.csi.cgiar.org/) (Jarvis et al., 2008). The stream network and upstream area was determined after first filling sinks and carving sills in the $90-m$ DEM (Schwanghart and Scherler, 2013). We calculated several metrics to characterize topography in the Arun Valley using a combination of standard geographic information system techniques and TopoToolbox v2 (Schwanghart and Scherler, 2013). Hillslope angle (degrees) and gradient (mm^{-1}) were calculated for each $90 - m$ pixel based on its eight surrounding neighbours. Local relief was calculated for each pixel based on 1 km and 3 km radius averaging windows. Lithology was classified using the map by Schelling (1992). As sampled catchments lie entirely within the LHC and HHC units (ARU-12-11 contains 3% in Tethyan sediments), we quantified catchment lithology by percent area in the High Himalayan Crystalline units (%HHC). We did not perform a more detailed analysis between units within the HHC or LHC.

4.3.3 Channel Concavity and Steepness

Channel concavity is an integral part of the stream power model for bedrock rivers (e.g., Whipple and Tucker, 1999; Whipple, 2004; Wobus et al., 2006) that describes channel evolution through time and varies for different rivers based on a variety of natural conditions (e.g., lithology). We calculated channel concavity for the main stem Arun and each sampled tributary by (1) standard slope-area regression (e.g., Flint, 1974; Wobus et al., 2006) and (2) least squares regression of the χ-transformed stream network (Perron and Royden, 2013; Royden and Taylor Perron, 2013). Because orographic rainfall, as observed in the Arun Valley, has the potential to affect channel concavity in steady state river profiles (e.g., Roe et al., 2002), we additionally performed the slope-area and χ analysis using a TRMM rainfall-weighted flow accumulation grid. The TRMM-weighted flow accumulation grid is calculated using the routines of TopoToolbox v2 (Schwanghart and Scherler, 2013) and results in upstream areas that are weighted to be proportionately "larger" in regions with higher rainfall rates and proportionately "smaller" in regions with lower rainfall rates. In both cases, we separately calculated the channel concavity

for the entire stream network and for the trunk stream in each catchment.

Normalized channel steepness (k_{sn}) (e.g., Wobus et al., 2006) was calculated for the Arun fluvial network in our study area for every 90-m pixel in the channel network. Local channel gradient was calculated for each pixel, then divided by upstream area to calculate channel steepness (k_s); we then normalize channel steepness using (1) the standard reference concavity of $\theta = 0.45$ (e.g., Wobus et al., 2006) and (2) the mean concavity value derived from the χ analysis of all tributaries ($\theta = 0.23 \pm 0.14$). We additionally calculated k_{sn} using a TRMM-weighted flow accumulation grid to account for the potential impact of spatially inhomogeneous rainfall, assuming that regions experiencing higher rainfall may have higher denudation rates within the basin. TRMM-weighted k_{sn} was normalized using (1) $\theta = 0.45$ and (2) $\theta = 0.20 \pm 0.14$, the mean concavity value from the TRMM-weighted χ analysis. For all channel steepness indices, catchment-mean k_{sn} was calculated for the channel network upstream of the sample location.

4.3.4 The ^{10}Be TCN-Derived Denudation Rates

Basin-wide denudation rates were estimated based on in situ ^{10}Be in fluvial river sands (Brown et al., 1995; Bierman and Steig, 1996; Granger et al., 1996). In total, we collected and analysed 34 samples in the Arun Valley, from the border with India in the south to the border with Tibet (China) in the north. Our primary sample targets were (1) the main stem Arun, sampled in intervals along its N-S course; (2) tributaries to the Arun, ranging in size from $< 10\ km^2$ to $> 1000\ km^2$; and (3) the Sun Kosi (ARU-11-27) and Tamor (ARU-11-25) Rivers near their confluence with the Arun. Samples were taken from fresh sand banks on active channels of the main stem Arun and its tributaries. The only exception was ARU-11-12; this sample was taken from a recently abandoned or high water channel as the active channel was not accessible. In total, 7 samples were collected from the main stem Arun, one sample each from the Sun Kosi and Tamor, and 25 samples from tributaries to the Arun. Sample site selection was also dictated by accessibility, limiting our ability to sample some major tributaries. In addition to the 34 samples collected for present-day denudation rates, we sampled paleoriver sands from a large fill terrace at Tumlingtar (ARU-12-21 and ARU-12-22) and from one smaller terrace in the lower reaches of the Arun (ARU-11-21) to quantify ^{10}Be concentrations in transiently stored sediments.

Sample Preparation and Processing

Samples were prepared at the University of Potsdam and the University of California–Santa Barbara following standard procedures (e.g., Bookhagen and Strecker, 2012). A low-ratio ^{9}Be spike (^{10}Be/^{9}Be ratio of $\sim 1 \times 10^{-15}$) was added to the cleaned quartz, and samples were dissolved in hydrofluoric acid. Ion-exchange chromatography was used to extract Beryllium from the dissolved samples (Von Blanckenburg et al., 2004; Bookhagen and Strecker, 2012). Samples were sent to Center for Accelerator Mass Spectrometry, Lawrence Livermore National Laboratory, USA, for accelerator mass spectrometry

measurements. Ratios of $^{10}Be/^{9}Be$ were normalized using the 07KNSTD3110 standard ($^{10}Be/^{9}Be$ ratio of 2.85×10^{-12} (Nishiizumi et al., 2007).

Calculation of Catchment-Mean Denudation Rates

Production rates of cosmogenic ^{10}Be in Arun tributary catchments were calculated for every 90-m pixel of the SRTM DEM, including the effects of altitude, latitude, topography, and glaciation (see below). The same procedure was used for main stem Arun, Sun Kosi, and Tamor samples for every 1 km pixel using the U.S. Geological Survey GTOPO30 global DEM (https://lta.cr.usgs.gov/gtopo30/). Topographic shielding was calculated following Dunne et al. (1999). We used the Lal/Stone scaling procedure (Lal, 1991; Stone, 2000), which takes time dependent muogenic production and nondipole geomagnetic effects into account Balco et al. (2008) and the revised ^{10}Be half-life of 1.387 ± 0.016 Myr (Chmeleff et al., 2010; Korschinek et al., 2010). The $^{10}Be/^{9}Be$ concentrations were corrected using the mean of eight laboratory blanks ($1.43 \times 10^{-14} \pm 1.23 \times 10^{-15}$). The ^{10}Be concentrations were converted to erosion rates using the MATLAB functions of the CRONUS-Earth online calculator version 2.2 (Balco et al., 2008) in an iterative scheme provided by Scherler et al. (2014).

Ice Shielding and Glaciation

Recent studies have shown that present-day and past glaciations reduce ^{10}Be concentrations in detrital quartz and can, when unaccounted for, result in apparent denudation rates that are significantly overestimated (Godard et al., 2012; Glotzbach et al., 2013). To mitigate this effect, we applied an ice-shielding mask to production rate calculations based on present-day glacier cover from the GLIMS glacial database; this assumes that the production rate in ice-covered areas of the catchment is zero and all ^{10}Be in the detrital sample is derived from ice-free surfaces. The ice-shielding mask was applied to three tributary catchments (ARU-11-14, ARU-11-15, and ARU-12-11) where glaciers are currently present, the main stem Arun, the Sun Kosi, and the Tamor. Currently, there is insufficient data about the glacial history of the Arun Valley available to correct for past glacial coverage (e.g., Glotzbach et al., 2013).

4.3.5 Comparison of Topographic and Climatic Metrics and Denudation Rates

To better understand regional influences on denudation rates, we performed a suite of ordinary least squares (OLS) regressions between our TCN denudation rates and catchment-mean topographic and climatic metrics. We excluded outliers (BBRS01, ARU-12-09, and ARU-12-19A), where we observe evidence of recent voluminous landsliding (see section 4.4.3), and presently glaciated tributaries. Glaciated tributaries were excluded from regression analysis because many of the topographic metrics used (e.g., k_{sn} and SSP) assume fluvial processes and are not applicable to glaciated catchments. Due to the high incidence of landsliding (see section 4.4.3) we removed ARU-11-10 and

Table 4.1: *Sample information and basin properties.*
[a] – Coordinates denote location of sample collection. All topographic properties derived from the 90m CGIAR SRTM DEM (Jarvis et al., 2008). Rainfall is based on the 5 km TRMM 2B31 product (Bookhagen and Burbank, 2010), [b] – Channel concavity. Values calculated using least square regression of the χ-transformed stream network (Perron and Royden, 2013; Royden and Taylor Perron, 2013), [c] – Values calculated using standard channel concavity of $\omega = 0.45$, [d] – Values calculated using standard concavity of $\omega = 0.45$ and flow-accumulation grid weighted by mean annual rainfall from TRMM (Tropical Rainfall Measurement Mission) product 2B31, [e] – Values calculated using flow-accumulation grid weighted by mean annual rainfall from TRMM (Tropical Rainfall Measurement Mission) product 2B31.

Sample ID	**Sample Type**	**East.** (m) UTM Z45N	**North.** (m) UTM Z45N	**Mean Basin Elevation** ($m\ asl$)	**Catchment Area** (km^2)	**Total Elevation Range** (m)	**Mean 1-km Relief** (m)	**Mean 3-km Relief** (m)	**Mean Hillslope Angle** ($^\circ$)	**Chan. Conc.**[a]	**Mean k_{sn}** ($m0.9$)[b]	**Mean k_{sn}** Rainfall-w. ($m0.9$)[c]	**Mean SSP** Rainfall-w. (Wm^{-2})[d]	**Mean ann. Rain-fall** ($m\ yr^{-1}$)[e]
ARU-11-01	ARUN	5.19E+05	3.02E+06	4769.00	31260.29	8525.00	416.36	841.30	15.90	0.36	235.40	366.25	63.18	0.38
ARU-11-13	ARUN	5.19E+05	3.04E+06	4848.00	30400.97	8236.00	412.15	832.91	15.50	0.21	411.23	441.69	57.48	0.33
ARU-11-16	ARUN	5.27E+05	3.05E+06	4869.00	29942.76	8046.00	408.62	825.67	15.30	0.53	318.60	512.36	53.46	0.30
ARU-11-26	ARUN	5.15E+05	2.98E+06	4544.00	33500.94	8678.00	416.38	842.12	16.30	0.37	156.02	203.82	69.73	0.46
ARU-11-28	ARUN	4.93E+05	2.93E+06	3849.00	57979.93	8732.00	559.53	1121.50	20.50	0.37	25.86	38.36	124.84	1.03
ARU-12-03	ARUN	5.27E+05	3.05E+06	4869.00	29942.76	8048.00	408.62	825.67	15.30	0.21	318.60	512.36	53.46	0.30
ARU-12-15	ARUN	5.44E+05	3.07E+06	4936.00	28407.20	6888.00	397.33	800.98	14.50	0.25	365.71	162.39	38.36	0.20
ARU-11-25	TAMOR	5.32E+05	2.98E+06	2869.63	5886.36	2468.00	837.73	1648.68	26.38	0.42	283.63	329.67	209.50	1.65
ARU-11-27	S. KOSI	5.15E+05	2.98E+06	2958.08	18100.00	3406.00	767.19	1517.77	25.57	0.45	299.96	341.25	151.62	1.81
ARU-11-03	TRIB.	5.20E+05	3.02E+06	1540.16	387.60	1516.00	819.34	1718.73	25.89	0.58	191.20	300.08	212.45	2.04
ARU-11-04	TRIB.	5.18E+05	3.03E+06	761.96	11.48	378.00	526.26	945.14	18.41	0.26	87.47	109.22	163.36	1.62
ARU-11-05	TRIB.	5.15E+05	3.03E+06	867.32	11.84	631.00	634.38	1330.67	20.06	0.38	127.90	168.70	231.59	1.90
ARU-11-06	TRIB.	5.13E+05	3.03E+06	1606.73	74.19	1023.00	753.74	1527.71	23.90	0.27	212.53	296.88	198.39	2.18
ARU-11-07	TRIB.	5.12E+05	3.03E+06	1979.48	204.45	1130.00	919.51	1761.27	29.17	0.34	236.14	375.32	234.58	2.76
ARU-11-10	TRIB.	5.14E+05	3.04E+06	1173.99	2.67	384.00	858.27	1637.31	25.56	0.06	163.82	211.86	404.50	1.72
ARU-11-11	TRIB.	5.16E+05	3.04E+06	1525.37	10.55	724.00	885.82	1994.85	26.34	0.22	255.86	359.67	263.04	2.07
ARU-11-12	TRIB.	5.19E+05	3.04E+06	1787.03	13.20	699.00	1158.52	2110.22	34.78	0.26	235.87	352.91	333.84	2.45
ARU-11-14	TRIB.	5.23E+05	3.05E+06	3476.99	218.09	1328.00	983.76	2037.86	29.96	0.25	325.63	428.38	329.57	2.80
ARU-11-15	TRIB.	5.25E+05	3.05E+06	4027.25	187.86	1595.00	1109.26	2261.01	31.67	0.25	344.25	382.11	242.46	1.67
ARU-11-18	TRIB.	5.18E+05	3.02E+06	997.13	33.25	742.00	620.36	1228.03	19.96	0.38	140.91	185.96	127.51	1.79
ARU-11-20	TRIB.	5.24E+05	3.01E+06	1744.75	313.97	834.00	720.16	1412.96	22.70	0.34	223.20	275.93	127.60	1.35
ARU-11-22	TRIB.	5.26E+05	3.01E+06	1177.50	35.11	817.00	706.60	1487.80	21.60	0.27	191.39	197.80	123.93	1.03
ARU-11-23	TRIB.	5.27E+05	3.00E+06	1502.34	88.91	887.00	700.26	1424.97	22.17	0.20	219.21	250.31	96.07	1.23
ARU-11-24	TRIB.	5.30E+05	3.00E+06	1280.30	84.19	706.00	694.83	1377.37	24.16	0.36	191.10	215.03	108.75	1.23
ARU-12-01	TRIB.	5.31E+05	3.05E+06	1644.76	8.35	1431.00	691.28	1586.03	30.80	0.16	189.48	332.31	619.50	3.65
ARU-12-02	TRIB.	5.35E+05	3.05E+06	2455.14	81.67	3855.00	1052.03	2241.86	31.46	0.32	293.83	533.85	328.12	3.87
ARU-12-06	TRIB.	5.34E+05	3.05E+06	2420.55	8.53	2128.00	975.46	2214.09	26.96	0.02	285.21	545.28	365.63	4.22
ARU-12-08	TRIB.	5.34E+05	3.06E+06	2170.62	8.87	1938.00	968.00	2057.83	28.84	0.06	342.21	601.97	468.01	3.49
ARU-12-09	TRIB.	5.35E+05	3.06E+06	2193.45	10.29	2248.00	1031.90	2056.13	31.04	0.26	243.63	418.26	516.88	3.32
ARU-12-11	TRIB.	5.36E+05	3.06E+06	4757.83	470.11	7231.00	1010.75	2071.29	29.01	0.27	297.09	314.20	246.15	1.17
ARU-12-12	TRIB.	5.25E+05	3.07E+06	2872.28	27.86	2584.00	962.85	2036.90	27.93	0.16	292.02	433.36	221.28	2.66
ARU-12-13	TRIB.	5.37E+05	3.07E+06	3070.31	16.27	1999.00	887.10	2029.00	26.21	0.11	311.00	475.30	351.75	2.61
ARU-12-19/A	TRIB.	5.28E+05	3.05E+06	2563.93	102.84	3491.00	913.58	2012.41	27.40	0.31	292.67	479.49	252.16	3.30
BBRS01	TRIB.	5.15E+05	3.04E+06	1403.35	9.01	570.00	808.03	1733.43	24.71	0.13	223.87	302.95	335.84	1.90

ARU-11-11 from the regression analysis. ARU-12-06 is a small tributary with a pronounced knickpoint cutting through a perched low-relief topography that may still be subjected to the impact of a previous erosion regime, and we therefore remove ARU-12-06 from the regressions.

Catchment topography has traditionally been characterized by the catchment mean or median value of a chosen metric (e.g., relief and k_{sn}). Despite this common assumption, catchment topography is often not normally distributed, especially in transient landscapes. In order to perform a more robust comparison between denudation rates and catchment climate and topography, we extend our regression analysis beyond the catchment mean or median metric value. To do this, we calculate every 5^{th} percentile from the 10^{th} to 90^{th} percentile of the data and use percentile values to perform multiple OLS regressions of our catchment-mean denudation rates against catchment topographic and climatic metrics. Additionally, we performed Lilliefors (Louter and Koerts, 1970; Lilliefors, 1969) and skewness tests to decide if catchment metrics are normally or non-normally distributed at the 95% confidence level.

4.3.6 The ^{10}Be Mass Balance Calculations

Standard TCN denudation rate calculation assumes that a fluvial sand sample is a uniform representative sample of the entire upstream area. Models of downstream sediment transport typically assume that particles $< 2\ mm$ diameter are kept in suspension in high-energy mountain rivers (e.g., Sklar et al., 2006; Chatanantavet et al., 2010), further suggesting that a detrital sand sample would be uniformly sourced from the upstream area. We test this assumption by comparing ^{10}Be concentrations from main stem Arun samples from upstream regions on the border with Tibet to ^{10}Be concentrations from the confluence of the Arun, Sun Kosi, and Tamor. We performed a simple mass balance calculation to determine if the changes in ^{10}Be concentration can be achieved under the assumption of uniform upstream sediment sourcing by solving for (1) variable mass flux from the southern flanks of the Himalaya and (2) variable ^{10}Be concentration in the southern flanks of the Himalaya:

$$\mathrm{Con.}_{Confluence} = \frac{\mathrm{Area}_{Tibet}\mathrm{MF}_{Tibet}\mathrm{Con.}_{Tibet} + \mathrm{Area}_{H}\mathrm{MF}_{H}\mathrm{Con.}_{H}}{\mathrm{Area}_{Confluence}\mathrm{MF}_{Confluence}}$$

where *Tibet* represents the area upstream of northernmost sample, *Confluence* represents the area upstream of the southernmost sample before the Sapt Kosi confluence, H denotes the Himalaya between the border with Tibet and the Sapt Kosi confluence, *Con.* is measured ^{10}Be concentration in the detrital sample, and *MF* represents the mass flux ($g\ cm^{-2}\ yr^{-1}$). To solve for mass flux, we assume that the mean ^{10}Be concentration from Arun tributaries is representative of the ^{10}Be concentration of the Himalaya in the region. To solve for variable ^{10}Be concentration, we assume that $MF_H = MF_{Confluence} - MF_{Tibet}$.

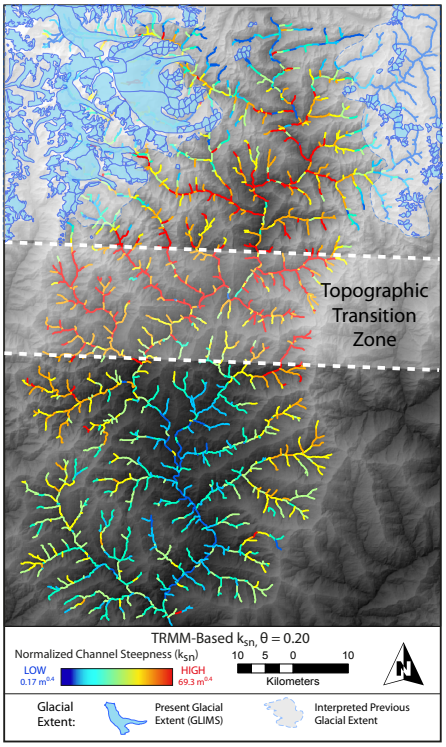

Figure 4.4: *TRMM-weighted k_{sn} (θ = 0.20). Theta values are derived from the mean tributary channel concavity values from χ analysis. Values of k_{sn} were calculated using the 90-m SRTM DEM for every pixel in the stream network, then averaged over 1 km long stream segments. All k_{sn} calculations follow a similar pattern as shown, with relatively low k_{sn} values in the LH, a steep increase in the topographic transition zone, and a continuation of high k_{sn} values in the HH. Present-day glacial extent based on the GLIMS Glacier Database and the authors' interpretation of previous glacial extent is shown in blue. Normalized channel steepness values are low in these regions corresponding to glacial valley morphology.*

4.4 Results

4.4.1 Topography and Climate

In general, elevation and topographic steepness metrics (e.g., hillslope angle, local relief, and channel steepness) increase from south to north across the Arun Valley (Figure 4.3 and Table 4.1). Mean hillslope angle across the study area ranges from $< 5°$ in the alluvial plain to $> 30°$ in the Higher Himalaya (Figure 4.3b); 3 *km* radius relief similarly increases from < 100 *m* in the alluvial plain to ~1 *km* in the LH, then sharply increases at the topographic transition zone into the HH, where it exceeds 2 *km* (Figure 4.3c). Discrete increases in hillslope angle and local relief are observed at both the LH and HH orographic barriers. Sampled catchments are located in the Lesser and Higher Himalaya where hillslope angle and relief are moderate to high. In sampled fluvial tributaries, mean hillslope angles range from 18° to 35°; 3 *km* relief ranges from 876 *m* to 2261 *m* (Figure 4.3 and Table 4.1).

Channel concavity derived from χ analysis of the main stem Arun in our study area indicates a generally graded river profile with a concavity of 0.451 until the first large knickpoint in southern Tibet (Figure 4.2). The channel concavity of tributary streams decreases steadily from 0.57 in the south to 0.02 in the north (Table 4.1 and Figure 4.3f),

indicating more uniformly steep channels approaching Tibet; tributary channel concavity calculated from TRMM-weighted flow accumulation does not significantly differ from the nonweighted concavity values at the 95% confidence level. Unlike hillslope angle and relief, no discrete break in concavity values is observed at the topographic transition zone.

Normalized channel steepness is low throughout the Lesser Himalaya in the main stem Arun and tributary channels but increases rapidly at the topographic transition zone (Figure 4.4). Throughout the Higher Himalaya, k_{sn} remains high; low values in the upper reaches of some tributaries correspond to glacial valley morphology. Catchment-mean values of k_{sn} for fully fluvial sample tributaries range from 87 $m^{0.9}$ to 342 $m^{0.9}$, normalized by $\theta = 0.45$; for $\theta = 0.23$ catchment mean k_{sn} values range from 2.78 $m^{0.46}$ to 11.34 $m^{0.46}$ (Table 4.1). Minimum and maximum k_{sn} values correspond to small tributaries ($< 20\ km^2$) that lie entirely in the LHC and HHC units, respectively. TRMM weighted flow accumulation results in higher k_{sn} values throughout the HH and LH, ranging from 109 $m^{0.9}$ to 602 $m^{0.9}$ normalized by $\theta = 0.45$ and 1.92 $m^{0.4}$ to 9.17 $m^{0.4}$ normalized by $\theta = 0.20$ (see Table 8.1 in appendix chapter 8). TRMM-weighted k_{sn} has a strong, positive linear correlation with unweighted k_{sn} ($R^2 = 0.88, 0.97$ for standard reference concavity ($\theta = 0.45$) and χ-determined channel concavity, respectively).

Mean annual rainfall follows a steep, two-tiered gradient (c.f. section 4.2.1), increasing from ~2 $m\ yr^{-1}$ in the alluvial plain to $> 3\ m\ yr^{-1}$ at the front of the LH/Siwaliks, then decreases rapidly to $< 2\ m\ yr^{-1}$ in the rain shadow of the LH orographic barrier; rainfall steadily increases over the next 40 km approaching the HH orographic barrier to a peak of ~4 $m\ yr^{-1}$, then decreases into Tibet (Figure 4.3d). Within our sampled catchments, catchment-mean annual rainfall ranges from 1.03 $m\ yr^{-1}$ (ARU-11-22) directly north of the LH orographic barrier to 4.22 $m\ yr^{-1}$ in the Higher Himalaya (ARU-12-06).

TRMM-weighted SSP follows a similar pattern to mean annual precipitation (Figure 4.3e), with peaks of ~500 Wm^{-2} at the LH and HH orographic barriers and variably high values ($200 - 500\ Wm^{-2}$) throughout the HH. A sixfold range of catchment-mean SSP values is observed in sampled tributaries,with catchment-mean SSP ranging from 104 Wm^{-2} in the Lesser Himalaya to 620 Wm^{-2} (Table 4.1) at the topographic transition zone, where rainfall and channel slopes are high.

4.4.2 The ^{10}Be Concentration in River-Sediment Samples

Sample ^{10}Be concentrations are recorded in Table 4.2 and Figure 4.5. We observe two main signals in main stem Arun ^{10}Be concentration: (1) a high ^{10}Be concentration in the north of the study area and (2) a low ^{10}Be concentration in the lower reaches of the Arun and Sapt Kosi. Downstream ^{10}Be concentrations in the main stem Arun are similar to ^{10}Be concentrations from tributaries in the Higher and Lesser Himalaya, as well as low ^{10}Be concentrations observed from the Sun Kosi and Tamor Rivers. Tributary ^{10}Be concentrations are an order of magnitude lower than the northern, high ^{10}Be main stem

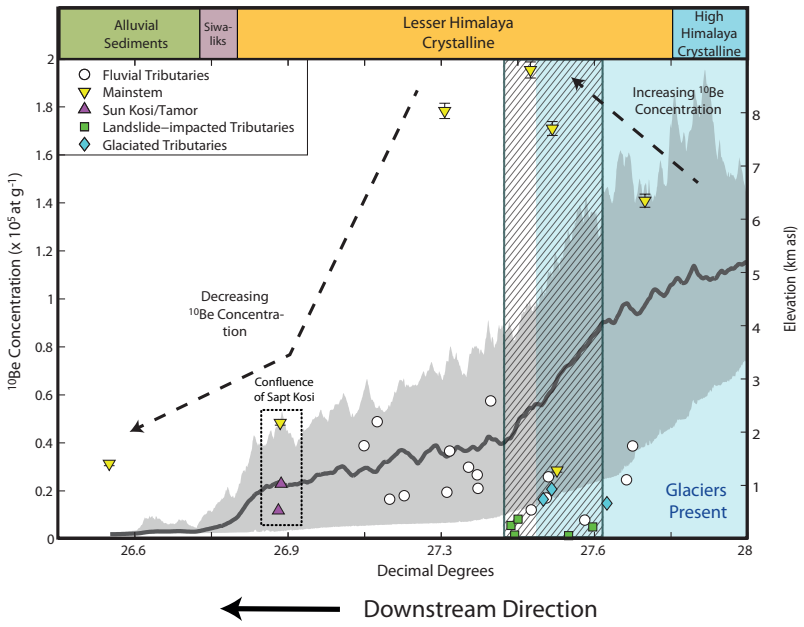

Figure 4.5: *The ^{10}Be concentration from main stem Arun (yellow triangle), Sun Kosi and Tamor Rivers (purple triangle), fluvial tributaries (white circle), glaciated tributaries (blue diamond), and landslide-impacted tributaries (green square). Lithology along the Arun River from Grujic et al. (2011). Mean elevation is shown in black with minimum/maximum elevation in shaded gray, taken from a 75 km swath along the Arun Valley. Glaciated regions of the Higher Himalaya are shaded blue. A region of marked landsliding is shown as gray hatch. Note the increasing ^{10}Be concentration south of the Tibetan Plateau through the HHC and the decreasing ^{10}Be concentration in the LH, which we associated with downstream fining of material derived from the Tibetan Plateau.*

Arun samples and show a northward decrease from the LH to HH. Within the tributaries, the lowest ^{10}Be concentrations are observed within the transition to the Higher Himalaya and in presently glaciated catchments.

4.4.3 The ^{10}Be Catchment-Mean Denudation Rates

Main Stem Arun, Sun Kosi, Tamor, and Sapt Kosi

Catchment-mean denudation rates in the main stem Arun decrease from the confluence of the Arun, Tamor, and Sun Kosi Rivers (0.75 ± 0.06 $mm\ yr^{-1}$ at ARU-11-26) northward to the border with Tibet (0.24 ± 0.02 $mm\ yr^{-1}; n = 4$) (Figure 4.6a and Table 4.2). Near their confluence with the Arun, the Sun Kosi and Tamor have denudation rates of 0.82 ± 0.06 $mm\ yr^{-1}$ and 1.39 ± 0.11 $mm\ yr^{-1}$, respectively. The Sapt Kosi, measured

Table 4.2: *^{10}Be TCN concentrations and denudation rates.*

	Sample	Quartz Mass $(g)^a$	Muonic Production Rate $(atoms\ g^{-1}yr^{-1})^b$	Mean Spalliogenic Pr. Rate $(atoms\ g^{-1}yr^{-1})^b$	Topographic Shielding^c	Ice Shielding^d	^{10}Be conc. $(atoms\ g^{-1})^e$	$\pm^{10}$Be $(atoms\ g^{-1})$	Basin-Average Denudation $(mm\ yr^{-1})^f$	Apparent Age $(yr)^g$	Used in Regression Analysis?
Arun, Sun Kosi, Tamor	ARU-11-01	149.37	0.74	65.16	0.999	0.943	1.78 10^5	3.18 10^3	0.22 ± 0.02	2.74 10^3	NO^h
	ARU-11-13	72.41	0.75	67.12	0.999	0.941	1.95 10^5	3.34 10^3	0.21 ± 0.02	2.92 10^3	NO^h
	ARU-11-16	69.87	0.76	67.89	0.999	0.940	1.71 10^5	2.88 10^3	0.24 ± 0.02	2.53 10^3	NO^h
	ARU-11-25	124.71	0.48	26.39	0.997	0.849	1.18 10^4	4.44 10^2	1.39 ± 0.11	445.4164	NO^h
	ARU-11-26	125.70	0.71	62.83	0.999	0.946	4.84 10^4	9.88 10^2	0.75 ± 0.06	7.79 10^2	NO^h
	ARU-11-27	88.55	0.50	30.34	0.997	0.930	2.29 10^4	5.17 10^2	0.82 ± 0.06	745.5625	NO^h
	ARU-11-28	153.06	0.62	48.59	0.998	0.938	3.13 10^4	8.22 10^2	0.91 ± 0.07	6.48 10^2	NO^h
	ARU-12-03	102.78	0.76	67.65	0.999	0.940	2.85 10^4	6.97 10^2	1..35 ± 0.11	4.22 10^2	NO^h
	ARU-12-15	152.31	0.77	69.32	0.999	0.943	1.41 10^5	2.73 10^3	0.29 ± 0.02	2.04 10^3	NO^h
Lesser Himalaya	ARU-11-03	170.66	0.31	12.55	0.964	1.000	1.94 10^4	2.60 10^2	0.47 ± 0.03	1.50 10^3	YES
	ARU-11-04	108.20	0.24	6.46	0.993	1.000	2.99 10^4	7.18 10^2	0.19 ± 0.01	4.48 10^3	YES
	ARU-11-05	173.45	0.24	6.97	0.987	1.000	2.67 10^4	4.17 10^2	0.22 ± 0.01	3.72 10^3	YES
	ARU-11-06	216.55	0.31	12.44	0.983	1.000	2.10 10^4	6.16 10^2	0.43 ± 0.03	1.66 10^3	YES
	ARU-11-07	99.87	0.35	15.77	0.970	1.000	5.75 10^4	1.03 10^3	0.19 ± 0.01	3.60 10^3	YES
	ARU-11-18	96.92	0.26	7.76	0.984	1.000	3.66 10^4	5.08 10^2	0.18 ± 0.01	4.59 10^3	YES
	ARU-11-20	46.62	0.33	13.54	0.985	1.000	1.80 10^4	1.49 10^2	0.54 ± 0.04	1.31 10^3	YES
	ARU-11-22	85.74	0.27	8.89	0.981	1.000	1.66 10^4	1.56 10^2	0.42 ± 0.03	1.82 10^3	YES
	ARU-11-23	138.93	0.30	11.56	0.935	1.000	4.88 10^4	8.43 10^2	0.18 ± 0.01	4.15 10^3	YES
	ARU-11-24	226.03	0.28	9.60	0.982	1.000	3.88 10^4	7.64 10^2	0.19 ± 0.01	3.95 10^3	YES
Transition Zone	ARU-11-10	122.01	0.27	8.67	0.938	1.000	5.61 10^3	7.27 10^1	1.21 ± 0.08	6.32 10^2	NO^i
	ARU-11-11	110.40	0.30	11.17	0.971	1.000	8.24 10^3	5.67 10^1	1.00 ± 0.06	7.24 10^2	NO^i
	ARU-11-12	103.54	0.33	13.13	0.835	1.000	1.21 10^4	3.58 10^2	0.78 ± 0.06	9.05 10^2	YES
	ARU-12-01	202.79	0.31	11.99	0.981	1.000	1.71 10^4	5.74 10^2	0.51 ± 0.04	1.40 10^3	YES
	ARU-12-02	200.02	0.40	20.79	0.958	1.000	2.59 10^4	3.81 10^2	0.53 ± 0.04	1.24 10^3	YES
	ARU-12-06	206.34	0.39	19.68	0.974	1.000	9.12 10^4	1.59 10^3	0.15 ± 0.01	4.59 10^3	NO^k
	BBRS01	104.18	0.29	9.94	0.980	1.000	1.61 10^3	2.50 10^1	4.58 ± 0.30	1.58 10^2	NO^i
Higher Himalaya	ARU-11-14 l	107.16	0.55	37.45	0.921	0.944	1.65 10^4	2.09 10^2	1.36 ± 0.10	4.39 10^2	NO^j
	ARU-11-15 l	163.54	0.64	31.30	0.925	0.710	2.07 10^4	2.83 10^2	0.94 ± 0.07	6.57 10^2	NO^j
	ARU-12-08	166.05	0.37	16.83	0.960	1.000	7.85 10^3	2.99 10^1	1.44 ± 0.10	4.61 10^2	YES
	ARU-12-09	149.74	0.37	17.19	0.955	1.000	4.97 10^3	2.95 10^2	2.30 ± 0.21	2.86 10^2	NO^i
	ARU-12-11	142.05	0.75	36.29	0.951	0.688	1.48 10^4	2.92 10^2	1.48 ± 0.11	4.05 10^2	NO^j
	ARU-12-12	215.14	0.45	27.26	0.865	1.000	2.47 10^4	1.30 10^3	0.68 ± 0.06	9.32 10^2	YES
	ARU-12-13	190.31	0.47	28.99	0.725	1.000	3.87 10^4	1.18 10^3	0.47 ± 0.04	1.33 10^3	YES
	ARU-12-19A l	138.89	0.42	22.43	0.971	1.000	1.36 10^3	2.72 10^1	10.36 ± 0.76	6.01 10^1	NO^i

[a] – Mass of quartz dissolved for ^{10}Be extraction, [b] – Production rate calculations were performed for every grid point of the $90-m$ DEM using the Lal/Stone scaling scheme (Lal, 1991; Stone, 2000). Production rate depends on altitude, latitude, and topographic and ice shielding, [c] – Topographic shielding based on 90-m SRTM DEM following Dunne et al. (1999), [d] – Ice shielding is based on present ice coverage from the National Snow & Ice Data Center (NSIDC) Global Land Ice Measurements from Space (GLIMS) database, [e] – Derived from blank-corrected AMS measurements undertaken at Lawrence Livermore National Laboratory and normalized to ICN standard (Nishiizumi et al., 2007), [f] – Denudation rates are calculated with a bedrock density of 2.6 $g\ cm^{-3}$ and an attenuation length for spallation of $\lambda = 160\ g\ cm^2$, [g] – Time over which denudation rates are averaged (yr), [h] – Mainstem sample, or other tributary that integrates entire topographic and climatic gradient, [i] – Landslide-impacted tributary with apparent denudation rate that likely does not represent temporal average, [j] – Glaciated tributary, [k] – Small tributary ($< 10\ km^2$) with pronounced transient profile.

in the alluvial plain, records a denudation rate of $0.91 \pm 0.07\ mm\ yr^{-1}$. This marks a fivefold decrease in main stem denudation rates across the Arun/Sapt Kosi River from the alluvial plain to Tibet. Similarly, the relatively high denudation rates in the Sun Kosi and Tamor Rivers that drain the southern flanks of the Himalaya are 5 to 7 times greater than in the upper reaches of the Arun.

Tributary Catchments

The highly dynamic orogenic environment of the Himalaya includes several nonfluvial processes (e.g., landsliding and glaciation) that complicate the interpretation of TCN-derived denudation rates (e.g., Brown et al., 1995; Niemi et al., 2005; Yanites et al., 2009; Godard et al., 2012). To avoid these complications, we first present denudation rates from fluvial tributaries that do not show evidence of recent landsliding or glaciation, then describe results from glacial and landslide-impacted catchments. Fluvial tributaries show an order-of-magnitude northward increase in catchment-mean denudation rates from the Lesser to Higher Himalaya (Figure 4.6b and Table 4.2). Denudation rates in the LH are low to moderate ($< 0.5\ mm\ yr^{-1}$) and vary over a relatively narrow range (~$0.2 - 0.5\ mm\ yr^{-1}$) ($n = 10$). Denudation rates increase in the topographic transition zone (~$0.5 - 0.8\ mm\ yr^{-1}$) ($n = 3$) and are highest in the Higher Himalaya ($1.44\ mm\ yr^{-1}$ in ARU-12-08), then appear to decrease further into the orogen (e.g., $0.47\ mm\ yr^{-1}$ in ARU-12-13) ($n = 3$). Higher denudation rates in the topographic transition zone and the Higher Himalaya, however, may be mainly driven by glacial and hillslope processes.

Glaciers occupy some tributary valleys in the Higher Himalaya (Figure 4.6) and have the potential to alter TCN denudation rates. We observe high denudation rates in the heavily glaciated Barun Valley (ARU-12-11, $1.48 \pm 0.11\ mm\ yr^{-1}$), as well as in two less glaciated valleys directly south of the Barun (ARU-11-14, $1.36 \pm 0.10\ mm\ yr^{-1}$; ARU-11-15, $0.94 \pm 0.07\ mm\ yr^{-1}$). However, there are fundamental problems interpreting denudation rates from these valleys: (1) shielding of bedrock from cosmogenic rays by glacial ice, (2) the assumption of steady state erosion through time (Bierman and Steig, 1996), and (3) the assumption that each area in the basin contributes sediment

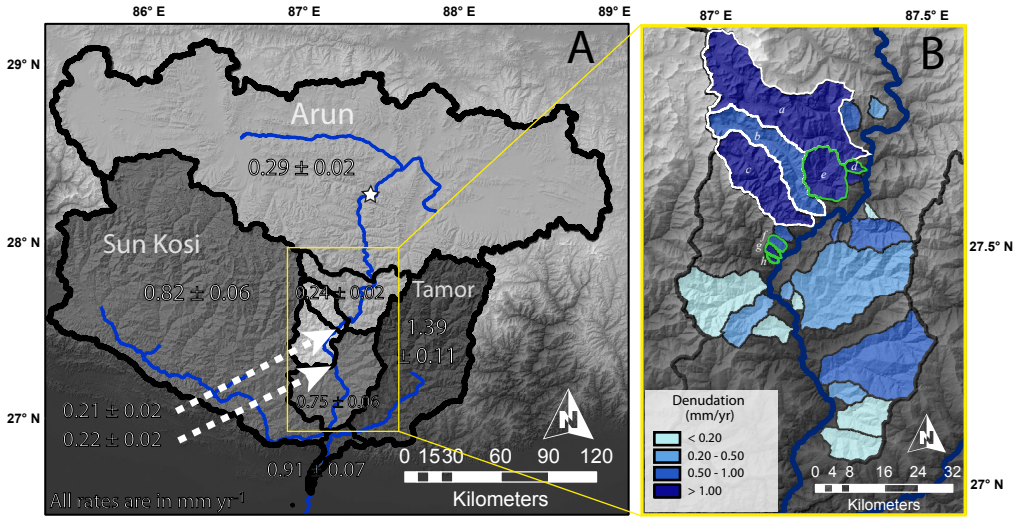

Figure 4.6: *TCN catchment-mean denudation rates for (a) the main stem Arun, Sun Kosi, Tamor, and Sapt Kosi, showing northward decrease in apparent denudation rate, and (b) sampled tributaries to the Arun, showing northward increase in the Himalaya. Denudation rates are shown alongside the river network (blue), elevation (hillshade), and the major knickzones in the main stem Arun (star). All denudation rates are shown in mm yr^{-1}. Glaciated tributaries are outlined in white ((a) ARU-12-11, (b) ARU-11-15, and (c) ARU-11-14). Landslide-impacted tributaries outlined in green ((d) ARU-12-09, (e) ARU-12-19A, (f) ARU-11-11, (g) BBRS01, and (h) ARU-11-10).*

in proportion to long-term erosion rates. The dynamics of glacial erosion and sediment delivery are complicated and poorly understood and are likely not steady through time. All of these processes may result in an overestimation of true denudation rates (Godard et al., 2012; Glotzbach et al., 2013) The application of an ice-shielding grid to the denudation rate calculation accounts for glacial shielding of sediment in the detrital sample, thus producing more reliable denudation rate estimates. However, we note that we cannot account for possible nonsteady state or proportionate denudation through time and therefore consider denudation rates from glacial catchments as apparent denudation rates that may differ from temporal averages.

Landsliding is common throughout the steep-slope terrain of the Himalaya (e.g., Bookhagen et al., 2005b; Dahal and Hasegawa, 2008). Because landslides frequently erode material from below the absorption depth of cosmogenic nuclides, they have the potential to dilute the ^{10}Be signal within a detrital sample. If the catchment is sufficiently large and well-mixed, TCN concentrations from landslide-dominated catchments can still provide reliable denudation rates (Niemi et al., 2005; Yanites et al., 2009). How-

ever, small, poorly mixed catchments or samples collected shortly after recent landslide events may result in calculated denudation rates that do not reflect the time-averaged denudation rate (Yanites et al., 2009). To quantify the potential impact of landsliding on our samples, we mapped visible landslide scars in all sampled tributary catchments using high-resolution imagery from Google Earth (see figure 8.1 in the appendix (chapter 8) for further information) (Fisher et al., 2012). While small landslides are ubiquitous in the study area, we observed five catchments with a pronounced amount of landsliding as a percentage of total catchment area: three small catchments ($< 10\ km^2$) in the topographic transition zone (ARU-11-10, ARU-11-11, and BBRS01) and one small catchment ($\sim 10\ km^2$) and one medium-sized catchment ($\sim 100\ km^2$) in the Higher Himalaya (ARU-12-09 and ARU-12-19A, respectively). In each catchment, the landslide area is markedly higher than the 0.001% of total catchment area proposed by Yanites et al. (2009) that will still produce a reliable denudation rate. BBRS01, ARU-12-09, and ARU-12-19A have anomalously high apparent denudation rates ($4 - 10\ mm\ yr^{-1}$), and the five landslide-affected tributaries represent the lowest observed ^{10}Be concentrations in our study area. Due to the likely recent delivery of material from below the ^{10}Be absorption depth from landslides in these samples, measured ^{10}Be concentrations may not be representative of the temporal average. We therefore consider the calculated denudation rates as maximum apparent denudation rates.

A more complex picture of denudation across the Arun Valley emerges when we consider the entire set of denudation rates, incorporating glacial and landslide-impacted apparent denudation rates. We observe largely fluvial denudation through the Lesser Himalaya, with low to moderate rates that do not vary considerably ($0.2-0.5\ mm\ yr^{-1}$). In the topographic transition zone, fluvial denudation rates increase ($0.5-0.8\ mm\ yr^{-1}$) concurrent with an increase in landsliding, with apparent denudation rates of $\sim 5\ mm\ yr^{-1}$. This marks the changeover to an erosion regime that is more variable in both rates and processes. Significant landsliding continues at the front of the Higher Himalaya (ARU-12-09 and ARU-12-19A) with maximum denudation rates in excess of $10\ mm\ yr^{-1}$. Glaciation additionally begins to play a role in the Higher Himalaya, maintaining denudation rates similar to the highest fluvial denudation rates ($\sim 0.9 - 1.5\ mm\ yr^{-1}$). Fluvial denudation rates, meanwhile, appear to decrease into the Higher Himalaya away from the high-relief, high-rainfall frontal zone (e.g., ARU-12-13).

4.5 Discussion

The ^{10}Be TCN samples from the Arun Valley record a pronounced northward increase in denudation rates across the Himalaya in tributary catchments and a fourfold decrease in main stem denudation rates from the lower reaches of the Arun to the upper reaches bordering Tibet. In a dynamic environment such as the Himalaya, several factors can influence ^{10}Be concentrations (e.g., nonuniform sediment sourcing and transient sediment storage) (Bierman and Steig, 1996; Granger et al., 1996; Von Blanckenburg, 2005). However, we did not find evidence of major impacts from potentially variable sediment

sourcing or transiently stored sediments on our measured ^{10}Be concentrations and calculated denudation rates (see appendix chapter 8 for details of the analyses performed). Below, we further discuss the interpretation of ^{10}Be concentrations and denudation rate calculation.

4.5.1 Downstream Evolution of Main Stem ^{10}Be Concentration

In order to better understand the impact of regional factors on denudation rates, we first consider measured ^{10}Be concentrations directly (Table 4.2 and Figure 4.5). For the following discussion, we interpret the two distinct groupings of ^{10}Be concentrations discussed in section 4.4.2 as (1) the Tibetan signal, comprising high ^{10}Be concentrations measured in the upper reaches of the main stem Arun, and (2) the Himalayan signal, comprising low ^{10}Be concentrations measured in tributaries to the Arun, the Sun Kosi, and Tamor and from the downstream sections of the main stem Arun.

Downstream Fining

One of the most prominent features of the ^{10}Be concentrations is the pronounced downstream reduction of ^{10}Be in the main stem Arun (Figure 4.5). This order-of-magnitude difference must be the result of either (1) a large sediment flux from the Himalaya able to sufficiently dilute the ^{10}Be signal from Tibet to the levels recorded at the Sapt Kosi confluence or (2) significant sediment storage within the Himalayan section of the valley. Comparing the ^{10}Be concentration in ARU-11-13 (high ^{10}Be) and ARU-11-26 (low ^{10}Be), we solve the mass balance problem presented in equation 4.3.6 as

$$Con._{\mathrm{ARU-11-26}} = \frac{Area_{\mathrm{ARU-11-13}} MF_{\mathrm{ARU-11-13}} Con._{\mathrm{ARU-11-13}} + Area_{\mathrm{H}} MF_{\mathrm{H}} Con._{\mathrm{H}}}{Area_{\mathrm{ARU-11-26}} MF_{\mathrm{ARU-11-26}}}$$

where H denotes the Himalaya between Tibet and the Sapt Kosi confluence and MF represents the mass flux ($g\ cm^{-2}\ yr^{-1}$) (Tables 4.1 and 4.2 and Figure 4.7). To solve for mass flux, we assume that the mean ^{10}Be concentration from Arun tributaries ($2.56 \times 10^4 \pm 4.6 \times 10^2$ at g^{-1}; $n = 20$) is representative of the ^{10}Be concentration of the entire Himalayan section of the valley. However, using this ^{10}Be concentration, the resulting mass flux for the southern flanks of the Himalaya is negative ($-0.12\ g\ cm^{-2}\ yr^{-1}$), indicating sediment storage in a region where no significant modern sediment storage is observed (see appendix chapter 8). As such, it is impossible to reconcile the ^{10}Be concentration measured at ARU-11-26 with a positive mass flux from the Himalaya under these assumptions. Similarly, if we define the Himalayan mass flux as $MF_H = MF_{26} - MF_{13}$ ($0.15\ g\ cm^{-2}\ yr^{-1}$), the calculated ^{10}Be concentration is likewise negative, a physical impossibility unless the system is undergoing either sedimentation or sediment loss through grain fining. We therefore assume that the collected sample cannot be a uniform representation of the upstream area. Instead, we suggest that downstream sediment fining continues for particles $< 2\ mm$, resulting in the Tibetan sediment passing through our

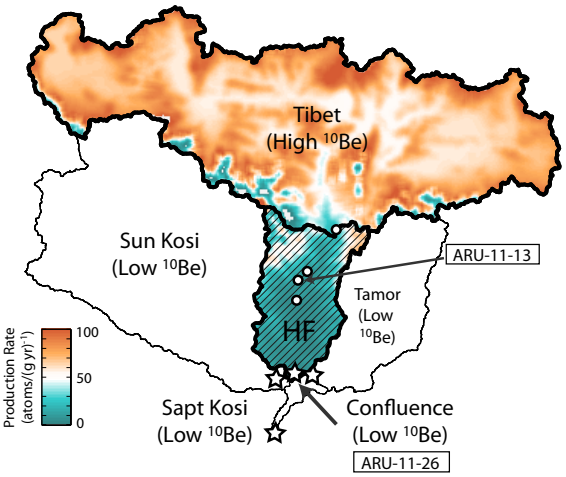

Figure 4.7: *Schematic of main stem ^{10}Be concentration mass balance calculations on map showing ^{10}Be production rates. Observed ^{10}Be concentrations at main stem Arun and other major river sand sample locations are shown as circles (high observed ^{10}Be, ~10^5 atoms g^{-1}) or stars (low observed ^{10}Be, ~10^4 atoms g^{-1}). The Tibet, Himalaya (HF), and confluence locations used in the mass balance calculation are highlighted; Himalayan section of the catchment shown in hatch. Higher ^{10}Be production rates (atoms g^{-1} yr^{-1}) in Tibet compared to the Himalaya results in a distinct signal that allows for the detection of downstream fining from Tibet to the confluence of the Sapt Kosi.*

$250 - 750$ μm sample sieve. This effect is identifiable in the Arun due to the large difference in ^{10}Be production rate between the high-altitude, low-relief Tibetan region (high ^{10}Be production) and the relatively low-altitude, high-relief Himalaya (low ^{10}Be production; Figure 4.7). However, similar problems could remain undetected in sufficiently large watersheds with uniform or near-uniform ^{10}Be production rates, such as the Sun Kosi or Tamor or large watersheds in other orogens.

The exclusion of upstream sediment grains from the analysed samples results in estimated denudation rates that do not reflect the entire upstream area. We therefore interpret the calculated "high" denudation rates from the main stem Arun (e.g., ARU-11-26, 0.75 $mm\ yr^{-1}$) as primarily reflecting the denudation rate of the southern flanks of the Himalaya and not the Tibetan section of the watershed, resulting in an overestimation of the true denudation rate for the watershed. This finding calls into question the use of large watersheds or distal sampling sites to characterize regional denudation rates, particularly in the Himalaya and in trans-Himalayan rivers. Recent studies have highlighted differences in ^{10}Be concentrations in different grain size fractions from detrital sand samples (McPhillips et al., 2014; Puchol et al., 2014). While the motivation for these analyses has been primarily to quantify the impact of landslide processes and focus on larger grain and cobble sizes, measuring ^{10}Be concentration from various grain size fractions, including those < 200 μm, may also mitigate the problems downstream fining poses for denudation rate estimation.

Climate-Driven Dilution of ^{10}Be Concentration

The northernmost main stem sample, ARU-12-15, has a noticeably lower ^{10}Be concentration than nearby samples from the northern main stem Arun, resulting in a local southward increase in ^{10}Be concentration before the more drastic decrease near the topographic transition zone. This southward increase of ^{10}Be is restricted to the glaciated portion of the Higher Himalaya (Figure 4.5). Glaciated catchments measure among the lowest ^{10}Be concentrations in the Arun Valley. North of our study area, extensive glaciation exists on the northern flank of the HH. Specifically, a large and heavily glaciated tributary that drains the northern slopes of the Sagarmatha/Everest massif joins the Arun approximately 10 km north of the sampling point of ARU-12-15. This nearby influx of highly shielded sediment may locally dilute the ^{10}Be concentration measured at ARU-12-15 before it is measured again over 40 km downstream. A modelled ^{10}Be concentration for ARU-12-15 assuming an erosion rate of 0.2 $mm\ yr^{-1}$ (approximate denudation rate from nearby main stem samples ARU-11-01, ARU-11-13, and ARU-11-16; Figure 4.6 and Table 4.2) and the mean upstream production rate is nearly 1.5 times the measured value (2.09×10^5 at g^{-1} modelled as opposed to 1.41×10^5 at g^{-1} measured in ARU-12-15), suggesting that a large, local influx of low ^{10}Be sediment is responsible for the ^{10}Be concentration measured at ARU-12-15. We also observe a relatively low ^{10}Be concentration (and therefore higher apparent denudation rate) in the Tamor compared to the main stem Arun or the Sun Kosi. Glaciers occupy a larger area of the Tamor Basin (~15%) compared to these other large rivers (~5.7%), and the higher degree of glaciation in the Tamor may be the cause of lower ^{10}Be concentrations and higher apparent denudation rates.

In addition to local dilution from glacial input, we observe one main stem sample in the northern section of the study area (ARU-12-03) with a low ^{10}Be ratio where we would expect to measure a high ^{10}Be signal from Tibet. This sample was taken less than 2 km downstream of a medium-sized tributary with large, recent landslides (ARU-12-19A) that are likely to have diluted the ^{10}Be concentration of the main stem sample (ARU-12-19A has the lowest measured ^{10}Be concentration in our data set). Landsliding predates the 2012 field season when samples ARU-12-03 and ARU-12-19A were collected. The timing of the large landslides in ARU-12-19A is not easily constrained with high-resolution imagery due to high cloud cover and poor image resolution, but some landslide scars are visible as early as 2009. A nearby sample collected in 2011 (ARU-11-16) does not show the low ^{10}Be concentration derived from the landslide. This may be due to the timing of the landslides or to different sediment sourcing in the river system during and after the monsoon season (e.g., Lupker et al., 2012).

It is notable that landslide-impacted tributaries are focused at the front of the Higher Himalaya where elevation, rainfall, and relief rapidly increase from the Lesser Himalaya. While relief and elevation remain high throughout the Higher Himalaya, rainfall decreases northward toward the high topography. Landslide-impacted tributaries are focused in a zone where both relief and rainfall peak, showing the importance of focused

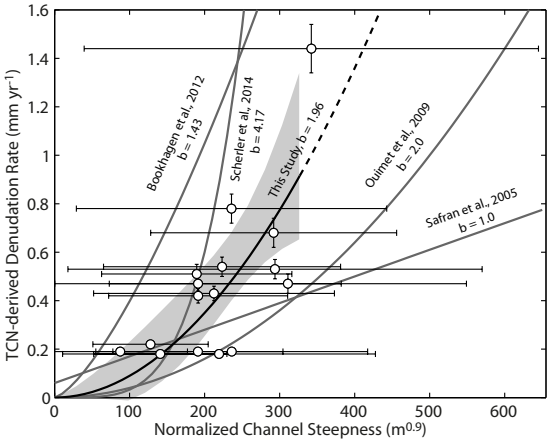

Figure 4.8: *Power law relationship of the standard area-weighted k_{sn} ($\theta = 0.45, R^2 = 0.54$) and denudation rates, shown with 95% confidence interval in shaded gray compared to published relationships from Bookhagen and Strecker (2012); Ouimet et al. (2009); Safran et al. (2005) and Scherler et al. (2014). The observed power law exponent b (from the relationship $y = ax^b$) for the Arun is $b = 1.96$ (95% confidence interval; upper and lower bounds $b = 0.33, 1.19$).*

rainfall in triggering mass movements (Figure 4.5).

4.5.2 Denudation Gradient Across the Arun Valley

In general, denudation rates in tributaries to the Arun increase from south to north coincident with the increase of topographic metrics such as hillslope angle, k_{sn}, and local relief (Figure 4.3 and Table 4.3). Due to the tectonic window, nearly all sampled basins are composed of both LHC and HHC units and no major lithologic boundaries are crossed by the main stem Arun in our study area (Figure 4.1d). Although the percentage of HHC rocks increases northward as the Arun Tectonic Window narrows and denudation rates increase, no relationship is observed between catchment-mean denudation rates and lithology (see Figure 8.2).

The across-strike pattern of northward increasing denudation rates we observe is similar to those reported by Godard et al. (2014) and Scherler et al. (2014). In both studies, denudation rates in the Lesser Himalaya are reported between ~0.1 and 0.5 $mm\ yr^{-1}$ and increase rapidly at the transition to the Higher Himalaya, where denudation rates exceed 1 $mm\ yr^{-1}$. The similar pattern between the Arun Valley and the results of studies where denudation rates are fit to tectonic drivers suggests that, at first order, a similar process drives the rates and pattern of denudation in the Arun Valley. We note, however, that the highest rates of denudation ($> 2\ mm\ yr^{-1}$) reported by Godard et al. (2014) and Scherler et al. (2014) are derived from regions with high rainfall rates and high local relief, similar to where we found the highest incidence of landslide-impacted catchments in the Arun, and may be overestimations of true denudation rate.

Previous studies have suggested a nonlinear relationship between topographic metrics (e.g., slope and k_{sn}) and denudation rates, such that for a given topographic metric, $(topographic\ metric)^b \sim denudation\ rate$, with power law values ranging from $b = 1$ to $b = 4$ (Safran et al., 2005; Ouimet et al., 2009; DiBiase et al., 2010; DiBiase and Whipple, 2011; Bookhagen and Strecker, 2012; Fisher et al., 2013; Scherler et al., 2014). We ob-

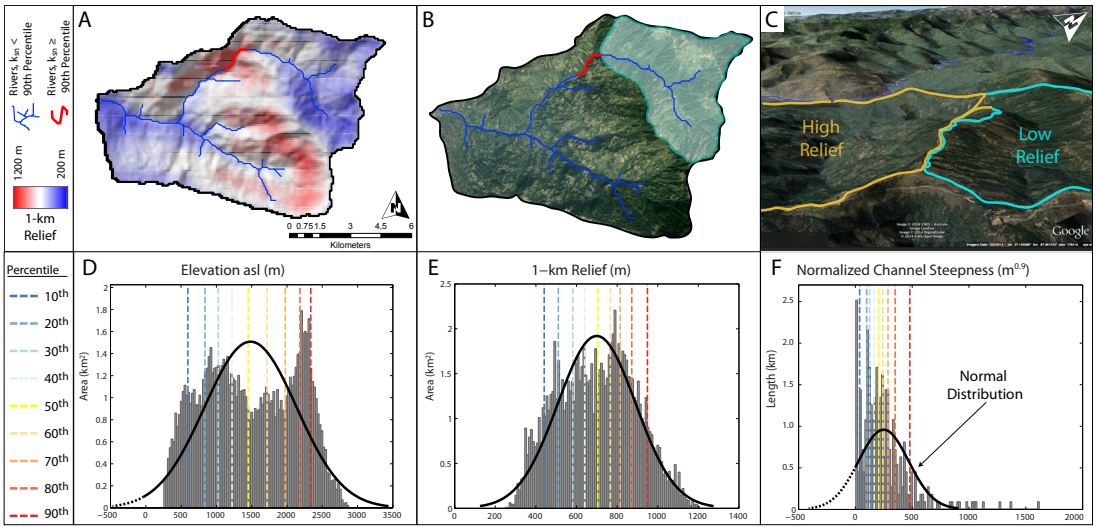

Figure 4.9: *Example catchment demonstrating non-normal topographic distribution (ARU-11-23). (a) The 1 km relief map of the catchment, paired with 90^{th} percentile of k_{sn} located at the foot of the transient surface. (b) Our interpretation of the relief map, with perched, low-relief surface shown in blue. (c) Google Earth view of low-relief topography. Histograms of topographic metrics: (d) elevation (m asl), (e) 1 km relief (m), and (f) k_{sn} ($m^{0.46}$), shown with approximate normal distribution (black line) and percentile values (dashed lines).*

serve the highest correlation between denudation rate and χ determined k_{sn} ($R^2 = 0.66$ for area-weighted k_{sn}, $R^2 = 0.67$ for TRMM-weighted k_{sn}, compared to $R^2 = 0.54$, 0.57 for area- and TRMM-weighted for the standard k_{sn} normalized by $\theta = 0.45$). The power law relationship between k_{sn} and denudation rate in our data set ranges from $b = 1.33 - 1.96$, similar to studies in other active tectonic environments (Figure 4.8, and references therein). Fluvial incision models (e.g., Whipple and Tucker, 1999; Snyder et al., 2003; Sklar and Dietrich, 2004; Lague et al., 2005) predict a monotonic relationship between channel slope and rock uplift at steady state, and numerous studies have shown positive correlations between k_{sn} and rock uplift (e.g., Snyder et al., 2000; Kirby and Whipple, 2001; DiBiase et al., 2010). The large knickpoints in the main stem Arun upstream of our study area (Figure 4.2) and several perched low-relief surfaces (see section 4.5.3 below), however, cast doubt on the assumption that the Arun is in landscape equilibrium. Localized high k_{sn} values have also been shown to correlate with areas where the river is adjusting to a transient perturbation. When this is the case, high k_{sn} values will follow knickzones as they propagate through the channel network as it adjusts to the perturbation (e.g., base-level drop and change in uplift rates) (e.g., Wobus et al., 2006). Such a perturbation can be climatic or tectonic; however, several studies along strike have found evidence for relatively high uplift rates in the Higher Himalaya with respect to the Lesser Himalaya (e.g., Lavé and Avouac, 2001; Godard

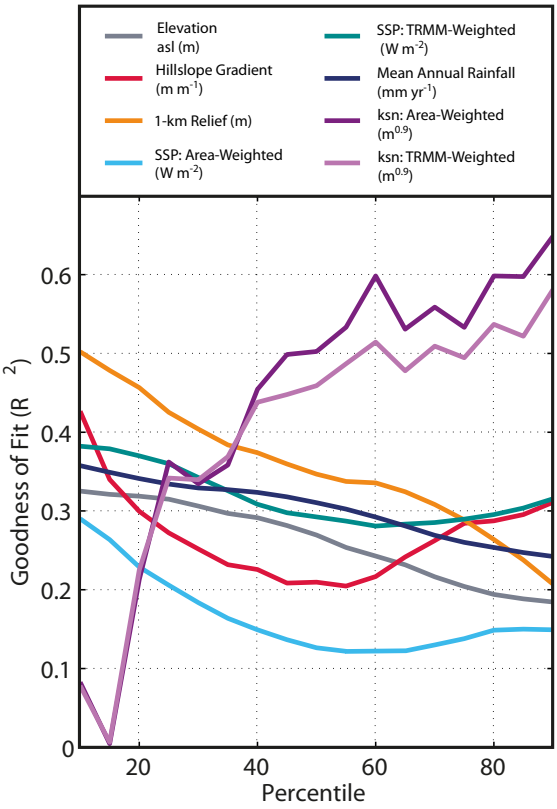

Figure 4.10: *Regression results between various catchment-mean topographic and climatic metrics and denudation rates based on percentiles of catchment metrics and denudation rates, showing the variable goodness of fit depending on which catchment value is used. Normalized channel steepness values calculated using channel concavity from χ analysis, showing the moderately strong correlation between k_{sn} and denudation rates.*

et al., 2004; Herman et al., 2010; Coutand et al., 2014). We therefore associate high k_{sn} and corresponding high denudation rates with locally high uplift rates.

Although we observe a moderately strong correlation between denudation rates and k_{sn}, our denudation rates correlate poorly with many other standard topographic and climatic metrics (Table 4.3). We were not able to constrain several factors of the fluvial network, such as channel width, depth, and geometry. Recent studies have highlighted the importance of channel width and geometry in the streampower model and in erosional proxies, such as specific stream power (Fisher et al., 2013). In our SSP calculations, we scaled channel width to discharge following a power law relationship (Knighton, 1999; Whipple, 2004; Craddock et al., 2007). This approach results in channel width increasing nonlinearly as upstream area increases. However, the low concavity values we derived from χ analysis of the fluvial network indicate that many channels in the Arun continue to have steep channels gradients in their lower reaches and thus narrow channel widths (Yanites et al., 2010; Fisher et al., 2012). Discharge scaling is therefore likely an inaccurate estimate of channel width in this environment and may explain why SSP poorly describes denudation rates in the Arun compared to other orogens (e.g., Bookhagen and Strecker, 2012. Similar scaling issues may exist in other regions with steep channels and low concavity.

Table 4.3: *Results of the regression analysis between ^{10}Be TCN-derived denudation rates and catchment climate and topographic metrics[a].*
[a] – all regression coefficients were calculated using an ordinary least squares (OLS) power law regression model.

Metric	All fluvial tributaries					Landslide-affected tributaries				
	R^2	F-value	p	a	b	R^2	F-value	p	a	b
				$y = ax^b$					$y = ax^b$	
Topographic Metrics										
Hillslope Gradient	0.19	5.80	0.028	1.32	1.35	0.35	13.01	0.003	1.49	1.67
1-km Relief	0.23	6.48	0.021	$1.47\ 10^{-5}$	1.57	0.37	11.81	0.004	$2.35\ 10^{-6}$	1.84
Area-SSP	0.26	2.81	0.112	$3.56\ 10^{-2}$	0.51	0.26	2.98	0.106	$3.56\ 10^{-2}$	0.51
Area-k_{sn} ($\theta = 0.45$)	0.18	3.79	0.068	$1.26\ 10^{-3}$	1.11	0.54	11.33	0.005	$1.08\ 10^{-5}$	1.96
Area-k_{sn} ($\theta = 0.23$)	0.26	5.47	0.032	$5.72\ 10^{-2}$	1.14	0.66	16.59	0.001	$1.14\ 10^{-2}$	1.90
Climatic Metrics										
TRMM	0.04	1.19	0.291	$3.73\ 10^{-1}$	0.34	0.23	6.40	0.024	$1.90\ 10^{-1}$	0.92
TRMM-SSP	0.35	4.99	0.039	$1.06\ 10^{-2}$	0.69	0.35	7.10	0.019	$1.06\ 10^{-2}$	0.69
TRMM-k_{sn} ($\theta = 0.45$)	0.15	3.30	0.087	$1.26\ 10^{-2}$	0.64	0.57	14.83	0.002	$2.04\ 10^{-4}$	1.33
TRMM-k_{sn} ($\theta = 0.20$)	0.23	5.04	0.038	$1.30\ 10^{-1}$	0.85	0.67	19.14	0.001	$3.44\ 10^{-2}$	1.59

4.5.3 Percentile Regression of Catchment Characteristics and Denudation Rates

In dynamic landscapes, topography and topographic metrics within a catchment may not always follow a normal or Gaussian distribution. Such skewed or multi-modal catchment distributions can result in mean or median values that are not the best representatives of the data population. Lilliefors tests suggested a non-normal distribution of elevation, hillslope gradient, 1 *km* local relief, and mean annual rainfall in all sampled catchments at a 95% confidence level. On the other hand, k_{sn} values do not show evidence of non-normal distributions in some basins; however, this result may be an artefact of sample size, as a smaller sample is less likely to reject the null hypothesis of normal distribution. Similarly, we found a systematic positive skew (right-tail) in the distribution of hillslope gradient and k_{sn} (see Table 8.2).

Figure 4.9 shows an example of how such non-normal distributions may arise within a catchment as the result of transient topography. Relatively small areas of perched, low-relief topography were observed throughout the study area. Here a low-relief area in the upper reaches of the catchment (Figure 4.9c) results in a bimodal distribution of elevation and quasi-bimodal distribution of 1 *km* local relief (Figures 4.9d and 4.9e). High k_{sn} is focused at the foot of the perched low-relief area where knickpoints propagate into relict topographies and the catchment moves toward equilibrium. As shown in the histograms of elevation, local relief, and k_{sn}, the normal distribution and associated statistics (mean and standard deviation) assumed by averaging do not fit the data population. While catchments with transient features are likely to be the most problematic in this regard, evidence for skewed and non-normal distributions were found in all catchments for nearly all metrics. Figure 4.10 shows the goodness of fit (R^2) of the regression analysis using the catchment-mean value and the catchment percentile values of various topographic and climatic metrics. The strength of the correlation between denudation

rate and catchment topography and climate varies by as much as a factor of 6 (e.g., k_{sn}) depending on the metric and the percentile used. In the case of k_{sn}, the correlation increases positively with the percentile used. However, the systematic positive skew in the distribution of k_{sn} values in sampled catchments suggests that channel segments where $k_{sn} > 90^{th}$ percentile comprise relatively small portion of the channel network. Thus, the rate of denudation may be most sensitive to, and focused at, locations in the catchment that do not correspond with standard averaging techniques (e.g., mean, median, or mode). The disconnect between catchment average statistics, the catchment distribution of topographic metrics, and the areas (sometimes small) that correlate best with denudation rates highlights the problem of uniformly characterizing catchments in a highly dynamic landscape. While such topographic metrics are useful first-order approximations, they are far from exact proxies for the processes that drive erosion.

4.6 Conclusions

Based on our 34 new ^{10}Be TCN measurements in eastern Nepal combined with field observations and topographic and climatic analyses, we reach the following conclusions:

- Catchment-mean denudation rates show an order-of-magnitude northward increase from the Lesser Himalaya to the Higher Himalaya, as elevation, hillslope, and channel steepness increase. The spatial pattern of denudation rates is most strongly correlated with normalized channel steepness, following a nonlinear power law relationship $[k_{sn}]^b$~*denudation rate* with best fit parameter for $b = 1.89$ ($\theta = 0.23$, $R^2 = 0.66$, 95% confidence interval $b_{lower} = 1.01$, $b_{upper} = 2.27$). The strong relationship between denudation rates and k_{sn}, as well as a similar observed pattern of denudation rates derived from studies arguing for tectonic drivers (Godard et al., 2014; Scherler et al., 2014), suggests a prominent role of rock uplift in forcing denudation rates in the Himalaya (c.f. Godard et al., 2014; Scherler et al., 2014). However, we observe multiple climatic influences on the processes of erosion in the Arun Valley, such as the extent of glaciation and localized landsliding in the area of peak rainfall and relief.

- Nonfluvial processes such as extensive glaciation and landsliding upstream of sample sites can cause local dilution of ^{10}Be concentrations in detrital samples. Local dilution of detrital sand from the main stem Arun demonstrates that such processes can even impact very large watersheds that are typically assumed to integrate upstream perturbations (e.g., landslides). When left unaccounted for, dilution of ^{10}Be concentration caused by local geomorphic processes could result in overestimation of catchment-mean denudation rates.

- Downstream fining of fluvial sand continues past $< 2\ mm$ diameter grains, resulting in sand grains sourced from upstream (Tibetan) sections of the watershed passing through the 250 μm sieve in samples collected downstream. Therefore, downstream main stem Arun samples are likely representative of the Himalayan section of the

catchment, rather than the entire watershed. Although the Arun provides a well-suited setting to record this effect, the exclusion of fined upstream sediment may also occur undetected in large watersheds in other mountain belts. We therefore call into question the use of distal detrital samples to characterize denudation rates in extensive mountainous catchments. Consequently, sampling multiple grain sizes in high-mountain environments may yield a more robust characterization of denudation rates, including potentially fined upstream sediments.

- Non-normal distribution of catchment topographic and climatic parameters in many sampled basins in our study highlights the importance of using caution when choosing how to characterize catchments with regard to erosion processes. Skewed and multimodal distributions of catchment topography and variations in sensitivity to denudation rates suggest that while such topographic metrics may be a useful first-order approximation of the processes that drive erosion at the regional scale, they are far from ideal proxies at the catchment scale.

4.7 Acknowledgments

This project was funded by the graduate school GRK1364 “Shaping Earth’s Surface in a Variable Environment: Interactions between tectonics, climate, and biosphere in the African-Asian monsoonal region“ of the German Science Foundation (Deutsche Forschungsgemeinschaft (DFG) project GRK 1364/2). In addition, funding for one field season and all analytical work was provided by the HIMPAC research project (Himalayas: Modern and Past Climates), funded by DFG (STR 373/27-1 nd 28-1) We thank Dirk Scherler and Taylor Schildgen for their valuable discussions; Ed Sobel, Burch Fisher, and Jessica Thompson for their help with laboratory work; and Bhim Chand of Earth’s Paradise GeoTrekking for logistical support in the field. Finally, we thank Nicole Gasparini, Elizabeth Safran, and Ken Ferrier for their constructive input into greatly improving this manuscript.

5 | Discussion & Conclusion

In order to answer the research questions listed in chapter 1, I identified sources of plant OM exported by the Arun River and the controlling factors behind plant OM mobilization. In this context, I investigated the Arun's hydrology, plant OM sourcing and cosmogenic nuclide derived denudation rates along the Arun Valley, as described in chapters 2, 3, and 4, respectively. In the following sections the key results of each chapter are briefly summarized with regard to the research questions of chapter 1 before I link and summarize respective findings in a wider context in the last two sections.

5.1 Arun Valley Hydrology

The major goal of the hydrological analysis of the present dissertation (chapter 2) was to decipher how strongly the isotopic composition of environmental waters in eastern Nepal is affected by inter-annual Indian Summer Monsoon intensity variability and its associated amount effect in precipitation δD values (Dansgaard, 1964). I analysed surface water δD values along the Arun River and its tributaries at the end and after the ISM season, together with satellite remote sensing data of rainfall, snow cover, glacial coverage, and evapotranspiration. As a reference for ISM intensity, I used precipitation stationary data and its isotopic composition from Bangladesh, as well as an ISM intensity index. Because the meteorological station in Dhaka, Bangladesh is located on the ISM pathway, where moist air masses move inland from the Bay of Bengal towards the Nepalese Himalaya, it is well-suited for a direct comparison with Arun Valley surface waters. Our data analysis revealed a very strong ISM amount effect on non-glaciated tributaries located south of the main Himalayan crest. Despite seasonal sampling in the late Monsoon/early post-Monsoon phase, spatiotemporal analysis of remotely sensed snow cover revealed that the higher elevated portion of these tributaries receive snow during the winter season, potentially through Winter Westerlies. Based on δD and d-excess values, I could also show, that the Arun mainstem and its glaciated high altitude tributaries receive significant amounts of glacial melt, primarily during the late to post monsoon phases.

Regarding mechanisms facilitating plant OM export, ISM derived surface runoff is certainly a considerable factor. But it is known that OM mobilization and export on larger scales is primarily controlled by erosion (Galy et al., 2015). By the example of the Arun Valley I showed that a combination of both is required for plant OM mobi-

lization in regional-scale catchments. Apart from the erosional capacity of runoff, water availability is one of the key factors controlling net primary productivity, meaning the photosynthetically driven biosynthesis of plant tissue. Additionally, I showed that tributary derived plant OM along the sampled transect is dominated by recent vegetation, and that the input of petrogenic or fossil plant OM can be neglected (chapter 3, appendix chapter 7). Hence, the availability of water confines modern net primary productivity and therefore plant OM stored along the sampled transect being potentially mobilized and exported.

5.2 Plant Organic Matter Sources

The first and second research questions formulated in the introduction (chapter 1) aimed to identify plant organic matter sources in the Arun Valley and to determine drivers of plant OM mobilization and export. As plant wax *n*-alkanes are resilient molecules produced by all higher land plants, they were taken as a representative fraction for plant OM in the Arun Valley. Since it is hard to to quantify plant waxes draining a catchment, I studied the spatial distribution of plant wax *n*-alkane δD values in flood deposits and mixing processes with the Arun mainstem. In order to identify plant organic matter sources I made use of the gradual change of plant wax *n*-alkane δD values I found in tributary flood deposit samples with increasing elevation (c.f. sections 1.3.2 and 3.4.3): by following the mainstem of the Arun downstream its tributaries contribute increasingly D–enriched plant–wax *n*-alkanes. Hence, the isotopic composition of mainstem flood deposit plant waxes gradually changes from very low δD values at the uppermost sample site to D-enriched plant waxes at the lowermost site. I set up a multi-proxy model to estimate the isotopic composition of tributary derived plant wax *n*-alkanes and fitted it to known δD values of sampled tributaries. Accordingly, the observed D-enrichment in plant waxes along the mainstem, together with the modelled isotopic composition of tributary plant wax δD values, can then be used to compute the relative contributions of tributary plant waxes required in order to obtain the observed mainstem D-enrichment.

The basic assumption behind the following approach is that parameters controlling plant OM export are proportional to the relative amount exported. In order to account for driving parameters controlling tributary plant OM export along the Arun, I weighted relative tributary plant wax contributions by natural characteristics of the tributaries. To test different parameters, I wrote a mass weighted isotopic mixing model of plant waxes along the Arun mainstem and compared the results to the observed downstream pattern. Four different runs of mass weighted isotope mixing were tested based on *catchment size*, catchment wide cumulative *net primary productivity*, *runoff*, and a combination of *runoff* * *local relief*.

First of all, I found more than 70% of plant waxes extracted from flood deposits directly north of the confluence with the Tamor and Sun Koshi Rivers (c.f. 1.2) originate from the lowermost 15% of the Arun catchment. Hence, the upper 85% of the catchment are inadequately represented in the Arun deposits. This implies that plant wax export of the Arun tributaries cannot be a function of *catchment size*. Instead, the weighted iso-

tope mixing based on *net primary productivity*, *runoff*, and *runoff∗local relief* resulted in a downstream D-enrichment of plant waxes at the lowermost sample site matching my actual observations. But only *runoff∗local relief* weighting also captured the intermediate mainstem sample δD value and the associated strong enrichment of mainstem flood deposit plant waxes in the upper half of the sampled transect. From that observation, I inferred two key conclusions: first, that more plant waxes are sourced from the upper half of the sampled transect compared to the lower half. Second, it implied that both runoff and erosion (approximated by local relief) are proportional to plant OM export in the Arun Valley, suggesting that they are important drivers of plant OM export in fluvial systems.

5.3 Arun Valley Denudation

Available data about erosion and denudation in the eastern Nepalese Himalaya are sparse and difficult to infer from previous studies from central Nepal or Bhutan, since the respective regions are characterized by either distinct climatic and ecological conditions or different topography, relief, and or geology. Hence, we present a new dataset of ^{10}Be terrestrial cosmogenic nuclide concentrations in river sands sampled along the Arun mainstem and from its tributaries in order to investigate the spatial variability of catchment mean denudation rates across strike the eastern Nepalese Himalaya. Respective ^{10}Be concentrations in river sands allow for a comparison between the Tibetan Plateau and the Arun's Himalayan tributaries.

^{10}Be TCN derived denudation rates in the Arun Valley increased by an order of magnitude ($< 0.2\ mm\ yr^{-1}$ to ~1.5 $mm\ yr^{-1}$) from the Lesser to the Higher Himalaya, following increasing hillslope angle and channel steepness. Denudation rates correlated best by a power law relationship with normalized channel steepness, k_{sn}. In other regions of the Himalaya, such relationships were interpreted as evidence that tectonic uplift is a major control of denudation and erosion (Godard et al., 2014; Scherler et al., 2014). Additionally, we note a strong effect of enhanced landsliding (where monsoonal rainfall and relief peaks) and the extent of glaciation on measured ^{10}Be concentrations: landsliding and extensive glaciation caused local dilution of ^{10}Be concentrations in detrital sands. Despite the fact that it is typically assumed that large catchments, such as the Arun, integrate upstream pertubations (e.g., through landsliding), we note that they have the potential to locally dilute detrital sand ^{10}Be TCNs.

Along the Arun, we observed a downstream fining of fluvial sand. In a large watershed, such as the Arun, continued downstream fining had the effect that material from its upper reaches were operationally excluded from the final sample during the sieving process. Hence, Arun mean catchment denudation rates are likely over-predicted due to lack of high ^{10}Be concentration Tibetan Plateau sands. Therefore, we argue that mean catchment denudation rates derived from detrital sand ^{10}Be TCNs might be biased towards lower tributaries in large river catchments.

In the context of plant OM sourcing in the Arun Valley, one would expect highest plant OM contributions where denudation rates and erosion are highest. However, this notion

is based on two assumptions: first, that there is plant OM available in respective regions for potential mobilization. Second, it is assumed that mean catchment denudation is spatially uniform within respective catchments or, in other words, that erosion is not only occurring in stream channels but also on hillslopes. I showed in chapter 3 that plant waxes, and likely also plant OM in general, are predominantly sourced from the same region that is characterized by highest denudation rates.

5.4 Recent plant OM erosion and past Denudation

When comparing the results of chapters 3 and 4, I find highest plant OM export and highest denudation rates being congruent in the upper section of the sampled transect along the Arun. The same holds true for monsoonal derived rainfall, apparent from figure 3.1C and 3.2, even though not discussed in chapter 2. However, from this conformity one could not infer a causal relationship as denudation rates are averaged over the last $10^2 - 10^3 yrs$, whereas plant OM export in sampled tributaries represent processes that work on the order of $10^0 - 10^2$ y.

Conceivably, all three chapters' observations (chapters 2 to 4) are direct or indirect consequences of increased uplift of the upper sampled part of the Arun Valley due to tectonic processes related to the collision of the Indian and Eurasian continental plates. Increased uplift caused higher incision and denudation since the early stages of the building of the Nepalese Himalaya (Lavé and Avouac, 2001) and also generated steep topography. The latter causes present day orographic rainfall on one hand and also facilitates high net primary productivity and plant OM export on the other. Hence, the coinciding observations of chapters 2, 3, and 4 are autocorrelated and refer to the same cause. Still, a comparison of past denudation rates and more or less recent plant OM export can be instructive.

On continental scales it has been previously shown that erosion and runoff are key drivers of terrestrial organic matter export, including plant waxes, towards sedimentary sinks (Galy et al., 2015; Hilton et al., 2013). Since the quantitative plant wax contribution model worked best when weighting by the erosion proxy *runoff*local relief* (Summerfield, 1991), these findings are confirmed now on a regional scale by the present thesis. Considering the locus of erosion derived through ^{10}Be TCN concentrations, I infer that highest erosion rates have been consistent in the Arnu Valley for the past $10^2 - 10^3$ y. Therefore, highest plant OM export is most likely linked to the same section of the Arun for several 10^3 y and therefore much longer than recent residence times of plant OM. This implication is highly relevant in the context of plant wax biomakers as stable isotope paleo-climate proxies in the eastern Nepalese Himalaya: if the plant wax sourcing in the Arun Valley was consistent throughout the last $10^2 - 10^3$ y, plant wax isotope proxies can even be interpreted as quantitative proxies, which is a big advantage compared to other geographic settings or other paleo-climate proxies such as pollen records or authigenic trace elements recorded in sediments.

5.5 Conclusion & Outlook

The key finding of the present thesis is that erosion and runoff are major controls for plant wax *n*-alkane mobilization and export in the eastern Nepalese Arun Valley. The investigation of denudation rates (chapter 4) and hydrology (chapter 2) in the Arun Valley revealed that maximum denudation and runoff coincide as they are both direct or indirect consequences of tectonic uplift. Tectonic uplift causes increased denudation and the formation of the Himalayan mountian ranges forces orographic rain out at the southern Himalayan front of northward moving Indian Summer Monsoon moisture. In turn, orographic rain out facilitates high primary net productivity as well as increased landsliding.

Beyond these findings, I developed a quantitative model to predict plant wax *n*-alkane sourcing in a climatic and ecological heterogeneous setting based on remote sensing data. First, the sourcing of plant waxes is strongly relevant for the paleo-climate community as plant waxes extracted from sediments are increasingly exploited as paleo-hydrological proxy. Therefore, actual plant wax sources need to be taken into account for a meaningful interpretation of the proxy. Second, these achievements are important as they allow for a detailed insight into plant wax sourcing in medium scale river catchments which is highly relevant in the context of the global carbon cycle, regarding plant OM transport to long term sedimentary carbon sinks. However, my findings about plant wax sourcing need to be confirmed for bulk plant OM, as other plant tissue than plant waxes is potentially affected differently by erosion, runoff, and degradation. Besides that, one future task is the enhancement of the modelling approach for plant wax sourcing in two different ways: first, more precise and more accurate remote sensing data will reduce model prediction uncertainties for different weighting factors such as runoff and net primary productivity. Second, the reliability of differently weighted plant wax contributions was tested using flood deposit plant wax δD values of the Arun and its tributaries. The significance of the test could be enhanced with a larger dataset on tributary, and especially mainstem flood deposit plant wax δD values. However, the plant organic matter sourcing model I presented in chapter 3 offers manifold opportunities for future investigations of plant OM sourcing in river catchments.

6 | Appendix to Chapter 2

6.1 Snow cover and snow water equivalent

AMSR-E/Aqua Daily L3 Global Snow Water Equivalent (SWE) EASE-Grids, Version 2 (Tedesco et al., 2004)is a measure for water bound in the snow column if melted (unit mm). Since SWE is only available until October 2011, snow melt prior to and during our second field campaign could not be determined. In order to assess whether snow melt or snow accumulation prevailed in the Arun Valley before and during both field campaigns, we used the MODIS MOD10C1 snow cover data product from January 2004 until the end of 2012 as a qualitative measure for snow melt/accumulation instead (Hall

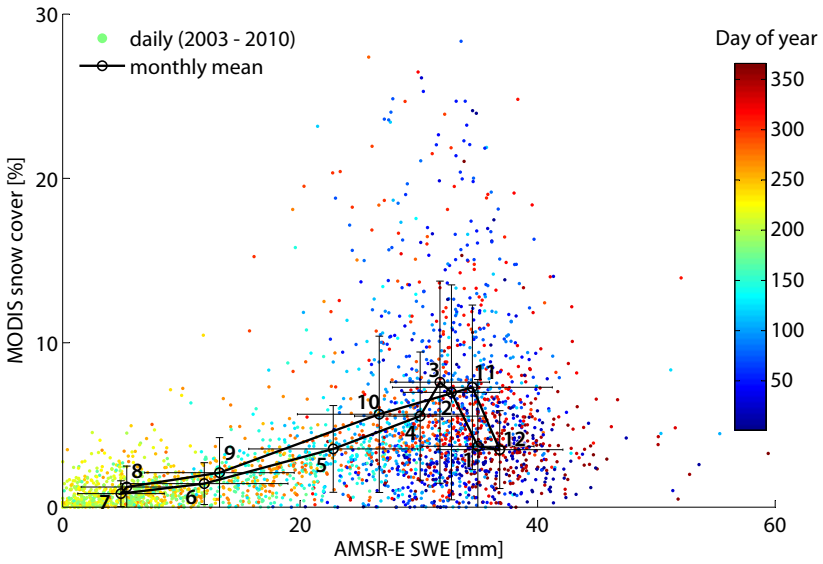

Figure 6.1: *Seasonal variability of AMSR-E derived snow water equivalent (Tedesco et al., 2004) and MODIS derived snow cover data product MOD10C1 (Hall et al., 2002). Black circles denote monthly means with error bars showing one standard deviation, colors indicate day of year of daily measurements. Prior to and throughout both sampling campaigns (August to November) SWE and snow cover are linearly correlated ($R = 0.59$, $p < 0.01$, $n = 918$), even though the seasonal relation of SWE and snow cover is described by a hysteresis.*

et al., 2002). Because SWE and snow cover extend are not necessarily linearly correlated throughout the year, we compared daily SWE and snow cover data of 2709 days (9 yrs) within the time frame of June 21^{st}, 2002 (start of MOD10C1 time series) to October 10^{th}, 2011 (end of AMSR-E time series). For both data sets we calculated daily averages of the Arun catchment above its confluence with the Tamor and Sun Koshi Rivers.

The relationship between SWE and snow cover varies throughout the year, describing the hysteresis shown in 6.1. But for the time frame one month prior to and during both field campaigns (August to November), we found SWE to be linearly correlated with snow cover. The regression describing Aug-Nov snow cover as a function of SWE was $y = 0.20 + 0.21$ ($R = 0.59$, $p < 0.01$, $n = 918$). Since SWE and snow cover are linearly correlated between August and November, we suggest that snow cover can be used for a qualitative analysis and to determine whether snow has been accumulated or if snow melt generated additional runoff.

6.2 MODIS evapotranspiration

Monthly MODIS MOD16A2 evapotranspiration data (Mu et al., 2011) of years 2011 and 2012 have been analyzed in order to evaluate the potential effect of evapotranspiration on the isotopic composition of environmental waters. The data had a spatial resolution of 5 km and was averaged for the Arun catchment upstream of its confluence with the Tamor and Sun Koshi Rivers. As shown in Figure 6.2 evapotranspiration was similar in

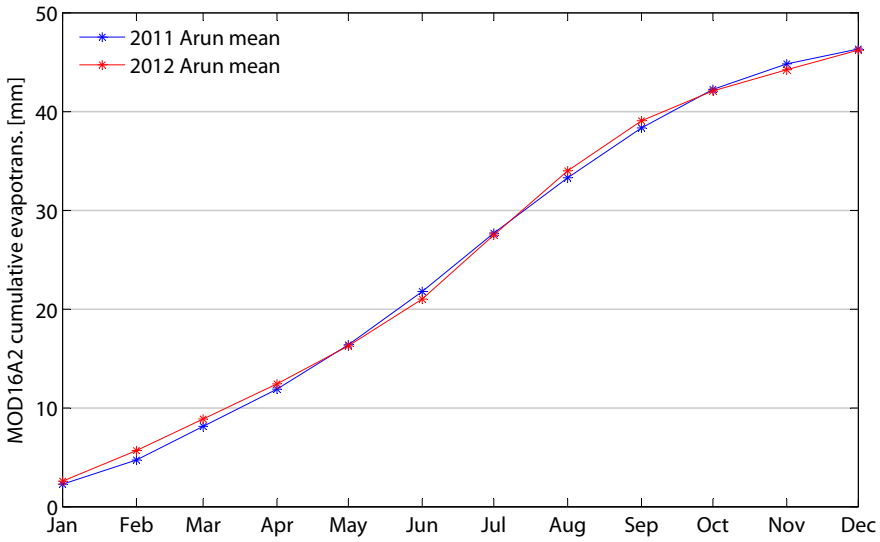

Figure 6.2: *Plot of MODIS MOD16A2 cumulative monthly evapotranspiration within the Arun catchment (Mu et al., 2011) between 2011 and 2012. The data show low inter-annual variability and imply that evapotranspiration is not a cause of the observed D-enrichment in surface waters 2012 compared to 2011 waters.*

both years. Hence, we infer that evapotranspirational D-enrichment of environmental water cannot have caused the observed isotopic difference of 16.6‰ between 2011 and 2012 surface water δD values.

7 | Appendix to Chapter 3

7.1 Vegetation distribution

The vegetation in the lower Arun Valley is characterized by near-tropical dipterocarp monsoon forest ($< 1000m$) with large stands of Shorea robusta in its upper part. Subtropical forests ($1000-2000m$) are dominated by Schima Wallichii and Castanopsis spp. Temperate forests in higher elevation parts of the valley ($2000-3000m$) are characterized by a mix of evergreen (Quercus, Persea, Rhododendron) and deciduous (Acer, Prunus) taxa. Fir, birch and Rhododendron stands dominate mountainous alpine forests until the treeline at ~$4000m$ (Carpenter and Zomer, 1996; Dobremez and Shakya, 1975). The area up to $500m$ above the tree line is characterized by alpine woody shrubs dominated by Rhododendron spp. followed by alpine meadow and subnival plant communities in even higher elevations (Carpenter and Zomer, 1996).

7.2 CPOM and flood deposit samples

Suspended organic matter floating in the river was sampled with a net (20x30cm, mesh-size $1mm$). The net was held in the stream for 10 to 30 minutes, depending on the concentration of coarse suspended organic matter in the stream. At some streams 30 min were not enough to catch enough organic matter for later GC/GC-IRMS analysis. They are referred to as coarse particular organic matter (CPOM) and were collected at 6 mainstem locations and from 20 tributaries (Fig. 3.1A, 3.2). However, samples were mostly composed of macroscopic plant debris with additional weights of coarse sand.

19 flood deposits have been sampled, three from the Arun and 16 from its tributaries. Out of these 16 two were taken from the Sun Koshi River and one from the Tamor, both covering almost the same climatic and ecologic gradient as the Arun itself. Wherever tributaries of more than ~$10m$ width or the Arun were accessible samples were taken in the immediate vicinity of respective streams up to $1m$ off the river level. We selected OM rich flood deposits that consisted of fine to coarse sands (c.f. Table 7.1 and Fig. 7.1 for grainsize distributions). It turned out that about 10 samples had too low n-alkane abundances for stable isotope analysis, justifying our sampling strategy. Most flood deposits were found between large boulders, 1-5 m below the apparent river channel maximum height reached during the ISM peak season. Hence, we are confident that

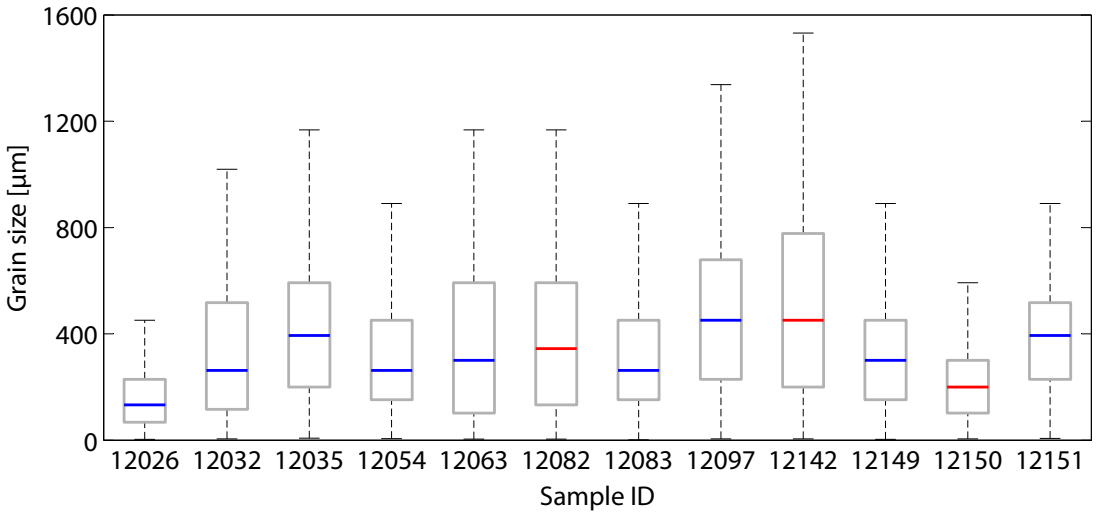

Figure 7.1: *Grain size distribution of flood deposits sampled in 2012. Tributary samples are indicated by a blue medians, mainstem sample medians are denoted red.*

sampled flood deposits were deposited during the aftermath of the most recent ISM season.

In order to rule out potential OM and therefore plant wax fractionation processes due to sampling of different sediment load fractions we analyzed grain size distributions of flood deposits sampled in 2012. After homogenized samples were split $5ml$ of H_2O_2 (10%) were added in order to remove OM. After 10 days samples were centrifuged 5 times to remove H_2O_2 and a dispersing agent (Na_3PO_4, $35.68g\ l^{-1}$) was added. After stirring for one day each sample's grain size distribution was determined 10 times on a Laser Scattering Particle Size Distribution Analyzer LA-950V2, Retsch Technology, at the GFZ German Research Centre for Geosciences, Section 5.1, Geomorphology, Potsdam, Germany.

Mean and median grain sizes were on the same order of magnitude for all samples (Table 7.1, Fig 7.1). No correlation of grain size distribution and plant wax properties such as δD_{FD}, average chain length (ACL) and carbon preference index (CPI) was observed (Table 7.1), in either the tributary or mainstem samples. Therefore, we find that any sorting of grain size does not appear to result in isotopic effects in the associated plant wax component.

7.3 Comparison of δD_{FD} estimation approaches

Since altitude and tributary δD_{FD} values were not correlated on a 95% significance level, we used an alternative multiproxy approach in order to estimate tributary δD_{FD} values. Figure 7.2 visualizes the improvement of tributary δD_{FD} predictions based on the multi-proxy model. Predictions based on the multiproxy approach have much smaller

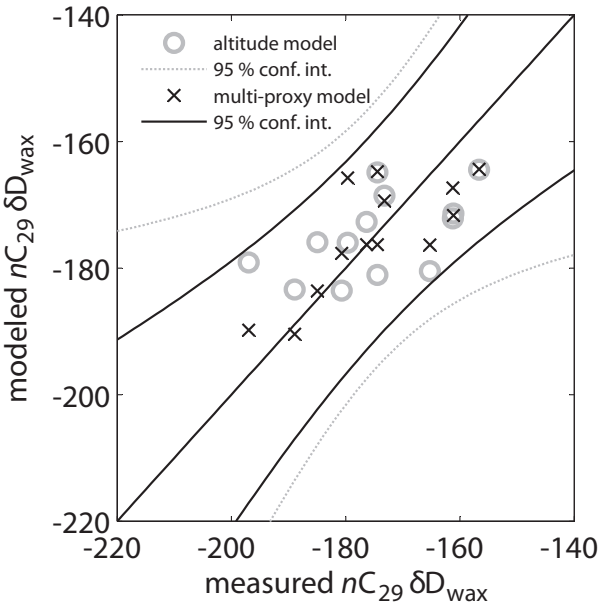

Figure 7.2: *Measured versus modelled tributary δD_{FD} values based on altitude dependent δD_{FD} predictions (grey circles) and our multiproxy prediction approach (black crosses) based on altitude, annual mean temperature and annual rainfall. For both approaches 95% confidence intervals are given as grey dotted line and black solid line, respectively.*

95%-prediction uncertainty than predictions based on the insignificant altitude to δD$_{FD}$ value relationship.

7.4 Errors of plant wax contribution

Prediction errors of plant wax contribution $p_{wax,trib}(i)$ depend on the uncertainty of the grids being used for contribution weighting. In this section we describe plant wax contribution errors for all four weighting approaches presented in the main manuscript. Please note that the main stem property above site i is given as the sum of all tributary catchment pixel between sites $i-1$ and i and the mainstem catchment pixel above $i-1$ (e.g. denominators of equations 3.5 to 3.8) to keep equations as simple and short as possible.

The *catchment-size model* uncertainties are based on DEM errors and resulting catchment extent. Based on equation 3.5 the weighting error for the area of tributaries between Arun sites $i-1$ and i is defined as

$$\sigma^2_{p_{wax,trib}}(i) = \left(\frac{\partial p_{wax,trib}}{\partial A_{trib}(i)}\right)^2 \sigma^2_{A_{trib}}(i) + \left(\frac{\partial p_{wax,trib}}{\partial A_{Arun}(i)}\right)^2 \sigma^2_{A_{Arun}}(i), \tag{7.1}$$

with $\sigma^2_{A,trib}(i)$ and $\sigma^2_{A,Arun}(i)$ being uncertainties for tributary and Arun catchment size, respectively. We define the catchment size error as one additional pixel layer surrounding the entire watershed. For simplicity we assume, that catchments are squares. Hence

$$\sigma^2_{p_{wax,trib}}(i) = \left(\frac{1}{A_{Arun}(i)}\right)^2 \left(4\sqrt{A_{trib}(i)}\right)^2 + \left(\frac{A_{trib}(i)}{A^2_{Arun}(i)}\right)^2 \left(4\sqrt{A_{Arun}(i)}\right)^2, \tag{7.2}$$

where $4\sqrt{A_{trib}(i)}$ and $4\sqrt{A_{Arun}(i)}$ are areas equivalent to one additional pixel layer surrounding simplified square catchments.

The error of *biomass model* predictions based on net primary productivity (NPP) are difficult to quantify, as Modis NPP comes along without any estimates for data product errors. It has been shown that MODIS MOD17A3 NPP estimates strongly vary with underlying, potentially mistaken climate data, maximum light use efficiency (LUE) (Zhao et al., 2006) and land cover classification (Cracknell et al., 2013). Cleveland et al. (2015) compared three different approaches to quantify NPP in a tropical forest and found an average NPP rate of $1108g\ C\ m^{-2}\ yr^{-1}$ with one σ being 10.83%. Considering that there is no better error estimate we used the observed standard deviation of 10.83% from Cleveland et al. (2015) in order to obtain a meaningful error for NPP weighted tributary plant wax contributions. Based on equation 7 errors of relative tributary plant wax contributions are:

$$\sigma^2_{p_{wax,trib}}(i) = \left(\frac{\partial p_{wax,trib}}{\partial NPP_{trib}(i)}\right)^2 \sigma^2_{NPP_{trib}}(i) + \left(\frac{\partial p_{wax,trib}}{\partial NPP_{Arun}(i)}\right)^2 \sigma^2_{NPP_{Arun}}(i), \tag{7.3}$$

where $\sigma_{NPP_{trib}}(i)$ and $\sigma_{NPP_{Arun}}(i)$ are errors for cumulative tributary and Arun mainstem NPP, respectively. Hence, $\sigma^2_{p_{wax,trib}}(i)$ is defined as follows:

$$\begin{aligned}\sigma^2_{p_{wax,trib}}(i) = &\left(\frac{1}{\sum NPP_{Arun}(i)}\right)^2 \left(0.1083 \sum NPP_{trib}(i)\right)^2 \\ &+ \left(\frac{-\sum NPP_{trib}(i)}{\sum NPP^2_{Arun}(i)}\right)^2 \left(0.1083 \sum NPP_{Arun}(i)\right)^2,\end{aligned} \tag{7.4}$$

where $\sigma^2_{p_{wax,trib}}(i)$ is the error of predicted plant wax tributary contributions between Arun sites $i-1$ and i, and $0.1083 \sum NPP_{trib}(i)$ and $0.1083 \sum NPP_{Arun}(i)$ are cumulated errors of tributary and Arun mainstem catchment NPP, respectively.

The precision of the TRMM 3B42 rainfall product in the Himalayas varies strongly with the frequency of extreme rainfall events and elevation (Bharti and Singh, 2015). Therefore, the equation for the applied runoff model uncertainty is a little more complex as it depends on tributary and mainstem median elevation (e) and TRMM rainfall:

$$\begin{aligned}\sigma^2_{p_{wax,trib}}(i,e) &= \left(\frac{\partial p_{wax,trib}}{\partial TRMM_{trib}(i)}\right)^2 \sigma^2_{TRMM_{trib}}(i,e) \\ &\quad + \left(\frac{\partial p_{wax,trib}}{\partial TRMM_{Arun}(i)}\right)^2 \sigma^2_{TRMM_{Arun}}(i,e), \\ &= \left(\frac{1}{\sum TRMM_{trib}(i)}\right)^2 \sigma^2_{TRMM_{trib}}(i,e) \\ &\quad + \left(\frac{-\sum TRMM_{trib}(i)}{\sum TRMM^2_{Arun}(i)}\right)^2 \sigma^2_{TRMM_{Arun}}(i,e),\end{aligned} \tag{7.5}$$

where $\sigma^2_{p_{wax,trib}}(i)$ is the uncertainty of predicted relative plant wax contributions of all tributaries between Arun sites $i-1$ and i based on the uncertainty of TRMM derived tributary catchment rainfall $\sigma_{TRMM_{trib}}(i,e)$ and Arun mainstem catchment rainfall $\sigma_{TRMM_{Arun}}(i,e)$ uncertainty above i. $\sigma_{TRMM_{trib}}(i,e)$ and $\sigma_{TRMM_{Arun}}(i,e)$ are products of tributary and Arun cumulative annual rainfall with an elevation dependent error between 0.048% for altitudes between 1000 and 2000m *asl* and 0.4333% for altitudes above 5000m *asl* (Bharti and Singh, 2015).

The *erosion model* error includes net primary productivity (TRMM) and local relief (R) errors for tributaries and the Arun catchment. Based on the function for $p_{wax,trib}(i)$ (Equation 3.8) for relative tributary plant wax contributions the propagated error $\sigma_{p_{wax,trib}}(i,e)$ is defined as:

$$\begin{aligned}\sigma^2_{p_{wax,trib}}(i,e) &= \left(\frac{\partial p_{wax,trib}}{\partial R \cdot TRMM_{trib}(i)}\right)^2 \sigma^2_{R\cdot TRMM_{trib}}(i,e) \\ &\quad + \left(\frac{\partial p_{wax,trib}}{\partial R \cdot TRMM_{Arun}(i)}\right)^2 \sigma^2_{R\cdot TRMM_{Arun}}(i,e), \\ &= \left(\frac{1}{\sum R \cdot TRMM_{trib}(i)}\right)^2 \sigma^2_{R\cdot TRMM_{trib}}(i,e) \\ &\quad + \left(\frac{-\sum R \cdot TRMM_{trib}(i)}{\sum R \cdot TRMM^2_{Arun}(i)}\right)^2 \sigma^2_{R\cdot TRMM_{Arun}}(i,e),\end{aligned} \tag{7.6}$$

with the error term $\sigma^2_{R\cdot TRMM_{trib}}(i,e)$ being the product of errors calculated in equations 7.5 and the DEM uncertainty: since local relief is the difference between the lowermost and the highest point within a 1.5-km radius of a pixel, the local relief error is the sum of the uncertainty for the maximum and minimum points within the radius. That sum equals twice the DEM uncertainty, being $2 \cdot 5m$ (Jarvis et al., 2008).

In order to obtain errors for the isotope mixing model (Equation 3.9) the uncertainty of $p_{wax,trib}(i)$ calculated with equations 7.2 – 7.6 were propagated together with the uncertainty of tributary $\delta\mathrm{D}_{FD}$ value estimates. Based on the derivation of Equation 3.9

the error $\sigma_{\delta D_{FD,Arun}}(i)$ was calculated as follows:

$$\begin{aligned}\sigma^2_{\delta D_{FD,Arun}}(i) = &\left(\frac{\partial \delta D_{FD,Arun}(i)}{\partial p_{wax,trib}(i)}\right)^2 \\ &+ \left(\frac{\partial \delta D_{FD,Arun}(i)}{\partial \delta D_{FD,trib}(i)}\right)^2 \\ &+ \left(\frac{\partial \delta D_{FD,Arun}(i)}{\partial \delta D_{FD,Arun}(i-1)}\right)^2 \qquad (7.7)\end{aligned}$$

$$\begin{aligned}= &\left(\delta D_{FD,trib}(i) - \delta D_{FD,Arun}(i-1)\right)^2 \sigma^2_{p_{wax,trib}}(i) \\ &+ p^2_{wax,trib}(i)\sigma^2_{\delta D_{FD,trib}}(i) \\ &+ \left(1 - p_{wax,trib}(i)\right)^2 \sigma^2_{\delta D_{FD,Arun}}(i-1),\end{aligned}$$

where $p_{wax,trib}(i)$ is the relative plant wax contribution of tributaries between Arun sites $i-1$ and i (Equations 3.5 – 3.8) with the respective model uncertainty $\sigma_{p_{wax,trib}}(i)$ (Equations 7.2 – 7.6), $\delta D_{FD,trib}(i)$ the modelled tributary plant wax δD value with its error $\sigma_{\delta D_{FD,trib}}(i)$ and $\delta D_{FD,Arun}(i-1)$ the Arun mainstem plant wax δD value at site $i-1$ with its respective uncertainty $\sigma_{\delta D_{FD,Arun}}(i-1)$. Model uncertainties are given in Table **??**, the uncertainty for the erosion model is shown in figure 3.6B.

7.5 Tables

Site	**mean**	**1σ**	**med.**	**10^{th} prct**	**25^{th} prct**	**75^{th} prct**	**90^{th} prct**	**δD_{FD}**	**ACL wax**	**CPI wax**
12142	539	440	452	45	200	777	1168	-185	30.1	8.5
12097	498	380	452	77	229	679	1020	-165	29.5	6.6
12151	397	238	394	101	229	517	679	-188	29.2	6.8
12063	383	356	301	34	101	592	890	-161	29.5	9.1
12082	415	357	344	51	133	592	890	-189	28.5	14.1
12083	345	279	262	68	152	452	679	-206	29.2	7.7
12035	459	341	394	89	200	592	890	-185	30.0	10.0
12054	342	278	262	68	152	452	679	-180	28.2	12.3
12032	382	370	262	51	116	517	890	-176	29.0	9.1
12149	348	265	301	51	152	452	679	-191	28.4	10.4
12026	178	157	133	39	68	229	394	-197	29.8	6.8
12150	227	164	200	59	101	301	452	-184	29.4	7.9
								δD_{FD}	**ACL wax**	**CPI wax**
						mean grain size	R	0.38	0.19	0.14
							P	0.22	0.55	0.67
						median grain size	R	0.34	0.23	0.02
							P	0.27	0.48	0.95

Table 7.1: *Grain size distribution of flood deposits sampled in 2012 including mean values of 10 replicate measurements of respective samples, standard deviation (1σ), median, and 10^{th} to 90^{th} percentiles (all given in μm). Additionally, correlation coefficients of mean and median grain sizes with δD_{FD}, ACL and CPI are shown with respective p-values.*

Table 7.2: *Details of sampled streams with surface water δD and $\delta^{18}O$ values.*
site number, location (easting & northing in dec. degree), flow distance from lowermost main stem sample, sample site elevation, median catchm. elevation, mean catchm. elevation, catchm. elevation standard deviation, catchm. mean annual day temperature (MODIS), annual cumulative rain (TRMM), surface water δD, surface water δD st.dev., surface water $\delta^{18}O$, surface water $\delta^{18}O$ st.dev., d-excess.

sample		lon.	lat.	flow dist.	area	site alt.	med alt.	mean alt.	alt. stdev	mean MAT	rain	δD water	δD water stdev	δ^{18}O water	δ^{18}O water stdev	d-excess
11104	Arun	86.93	26.52	0	57927.00	87	4543	3848	1655	17.9	272	-90.1	0.2	-12.38	0.20	8.9
12151	trib.	87.16	26.91	41	6050.30	205	2351	2815	1665	15.2	1677	-69.0	1.4	-10.06	0.14	11.4
12150	Arun	87.15	26.93	42	33508.00	205	4785	4553	1194	18.5	153	-77.5	0.8	-11.12	0.08	11.4
12149	trib.	87.15	26.93	43	18144.00	205	2497	2957	1725	16.9	1920	-76.2	0.5	-10.93	0.04	11.2
11090	trib.	87.32	26.93	62	5884.70	263	2420	2871	1653	14.8	1650	-85.8	0.5	-12.31	0.10	12.7
11086	trib.	87.25	27.12	74	83.94	282	1257	1288	494	22.9	1088	-58.5	0.1	-8.81	0.04	11.9
11085	trib.	87.28	27.15	77	90.57	253	1449	1489	649	22.5	1119	-57.6	0.5	-8.73	0.06	12.2
11081	trib.	87.26	27.18	81	35.09	287	1110	1169	449	24.3	1025	-51.7	0.8	-7.70	0.04	9.9
11080	trib.	87.24	27.22	86	314.11	277	1780	1741	670	20.4	1358	-59.7	0.2	-8.83	0.03	10.9
12142	Arun	87.19	27.31	101	31269.00	285	4832	4779	858	18.1	146	-88.3	0.2	-12.59	0.05	12.4
11075	trib.	87.18	27.32	103	39.73	298	950	993	373	20.5	2126	-59.7	0.1	-8.78	0.12	10.5
11005	trib.	87.18	27.37	109	11.35	306	761	763	197	23.5	1892	-45.9	0.5	-6.34	0.03	4.8
11069	Arun	87.16	27.38	111	31189.00	313	4834	4789	835	18.0	145	-96.1	0.4	-13.44	0.15	11.4
11008	trib.	87.15	27.39	112	12.21	321	840	874	277	23.0	1897	-53.9	0.3	-7.79	0.02	8.4
11010	trib.	87.13	27.39	115	74.67	344	1536	1616	683	16.2	2281	-58.5	0.7	-8.80	0.03	11.9
11013	trib.	87.12	27.41	118	205.59	409	1981	1983	726	14.3	3038	-63.0	0.1	-9.29	0.03	11.4
11018	trib.	87.14	27.45	122	351.26	392	2601	2666	1046	11.3	2834	-78.5	0.1	-11.23	0.01	11.3
11020	trib.	87.15	27.47	125	3.48	448	1175	1189	345	20.8	1982	-57.5	0.2	-8.59	0.03	11.2
11023	trib.	87.16	27.48	128	11.83	546	1486	1490	472	19.0	2300	-60.0	0.3	-9.29	0.04	14.3
11029	Arun	87.19	27.51	134	30431.00	553	4850	4855	711	18.2	143	-99.3	0.4	-13.66	0.05	10.0
11028	trib.	87.19	27.51	134	13.28	573	1689	1728	562	17.6	2628	-58.5	0.5	-8.68	0.04	11.0
11037	trib.	87.23	27.54	140	217.53	704	3688	3472	1032	4.4	1859	-88.6	0.9	-12.37	0.12	10.3
11043	trib.	87.25	27.57	144	188.28	812	4124	4028	1272	2.9	1124	-92.5	0.5	-13.40	0.04	14.8
11049	Arun	87.27	27.56	145	29958.00	812	4858	4878	672	18.3	142	-105.7	1.1	-14.82	0.08	12.9
12009	Arun	87.28	27.57	145	29958.00	812	4858	4878	672	18.3	142	-88.7	0.3	-12.23	0.02	9.2
12005	trib.	87.31	27.56	152	82.03	865	2368	2449	732	15.7	4209	-52.2	0.6	-8.41	0.06	15.0
12026	trib.	87.35	27.61	159	165.16	922	3347	3294	877	11.3	3491	-70.9	0.6	-10.42	0.05	12.5
12131	trib.	87.21	27.68	162	0.09	4000	4044	4049	32	4.1	1497	-81.3	0.3	-11.67	0.01	12.1
12032	trib.	87.35	27.64	164	9.01	1028	2215	2184	415	14.1	3342	-51.3	0.5	-7.82	0.01	11.2
12129	trib.	87.21	27.69	164	0.96	4070	4203	4208	99	4.0	1289	-78.2	1.8	-11.68	0.05	15.2
12035	trib.	87.36	27.67	168	80.30	1090	2780	2841	808	13.3	3292	-65.2	0.5	-9.30	0.14	9.2
12043	trib.	87.36	27.69	171	470.80	1138	4802	4762	1187	1.3	1042	-73.7	1.1	-10.97	0.15	14.1
12054	trib.	87.33	27.74	179	28.92	1634	2792	2869	591	6.3	1948	-58.6	0.6	-8.94	0.10	13.0
12063	trib.	87.37	27.77	183	0.01	2115	2115	2115	0	11.5	2677	-55.9	0.3	-8.73	0.07	14.0
12082	trib.	87.45	27.78	192	95.43	1787	4097	4029	723	9.3	1495	-84.3	0.4	-12.32	0.01	14.2
12083	Arun	87.45	27.78	192	28416.00	1793	4878	4945	531	18.7	138	-109.6	0.7	-14.92	0.08	9.8
12097	trib.	87.40	27.83	201	8.23	2156	3587	3511	522	5.8	1641	-62.8	0.3	-9.04	0.02	9.5

Table 7.3: Flood Deposits – *Details of flood deposit plant wax* n*-alkane samples: site number, flood deposit plant wax* n*-alkane average chain length (ACL, 3.1) and carbon preference index (CPI, 3.2), relative abundances of long chain plant wax* n*-alkanes from 25 to 33 carbon atoms (conC_i) and δD_{FD} values (in ‰, vs. VSMOW-SLAP) for odd chain lengths with triplicate measurement standard deviation (stdev, also in ‰).*

site	ACL	CPI	con nC$_{25}$	con nC$_{26}$	con nC$_{27}$	con nC$_{28}$	con nC$_{29}$	con nC$_{30}$	con nC$_{31}$	con nC$_{32}$	con nC$_{33}$	δD nC$_{25}$	δD nC$_{25}$ std	δD nC$_{27}$	δD nC$_{27}$ std	δD nC$_{29}$	δD nC$_{29}$ std	δD nC$_{31}$	δD nC$_{31}$ std	δD nC$_{33}$	δD nC$_{33}$ std
11104																					
12151	29.2	6.8	0.08	0.02	0.17	0.04	0.28	0.03	0.25	0.02	0.10	-165.7	1.4	-181.7	0.6	-187.9	1.3	-199.5	0.4	-156.0	2.7
12150	29.4	7.9	0.07	0.02	0.16	0.03	0.29	0.03	0.27	0.02	0.11	-195.1	2.1	-186.0	0.6	-184.3	1.3	-183.4	0.0	-170.2	0.3
12149	28.4	10.4	0.04	0.01	0.47	0.03	0.19	0.02	0.15	0.02	0.06	-187.2	2.8			-190.7	3.4	-183.0	1.9	-173.1	2.3
11090	30.3	5.8	0.04	0.02	0.10	0.03	0.22	0.03	0.27	0.05	0.24			-198.0	6.2	-183.8	1.6	-180.5	1.5	-179.1	0.9
11086																					
11085																					
11081																					
11080																					
12142	30.1	8.5	0.03	0.01	0.11	0.02	0.22	0.03	0.39	0.03	0.15			-181.7	8.9	-184.8	3.1	-178.5	4.1	-160.9	1.6
11075																					
11005	29.7	5.8	0.01	0.00	0.05	0.04	0.47	0.07	0.28	0.03	0.05					-156.6	1.5	-149.1	1.5		
11069																					
11008	29.2	8.6	0.07	0.00	0.14	0.04	0.41	0.04	0.24	0.02	0.05			-167.5	3.6	-174.5	0.6	-170.5	1.7		
11010																					
11013	29.3	9.3	0.05	0.01	0.18	0.03	0.34	0.03	0.27	0.02	0.08			-161.0	16.1	-161.1	2.6	-153.0	3.2		
11018																					
11020																					
11023	28.8	8.7	0.07	0.02	0.26	0.03	0.33	0.03	0.17	0.02	0.07			-172.5	10.8	-173.2	2.6	-172.8	10.2		
11029																					
11028																					
11037	29.6	7.1	0.06	0.03	0.16	0.03	0.26	0.03	0.28	0.02	0.14			-172.6	5.3	-174.4	1.6	-173.5	2.0	-165.0	5.6
11043	29.6	7.8	0.06	0.01	0.16	0.03	0.28	0.03	0.26	0.02	0.14			-195.2	3.5	-180.7	5.0	-181.2	5.2	-176.1	5.4
11049																					
12009																					
12005																					
12026	29.8	6.8	0.05	0.02	0.13	0.04	0.28	0.03	0.28	0.03	0.15			-193.2	0.8	-197.0	0.8	-187.3	0.5	-188.2	1.7
12131	29.1	5.3	0.11	0.05	0.16	0.04	0.26	0.03	0.23	0.02	0.09	-231.2	1.7	-229.9	2.7	-225.0	1.7	-225.7	1.2	-216.4	1.3
12032	29.0	9.1	0.09	0.02	0.19	0.03	0.32	0.03	0.24	0.02	0.06	-178.6	3.5	-182.7	0.9	-176.3	0.9	-167.9	0.8	-153.9	2.4
12129	28.6	5.8	0.14	0.05	0.22	0.04	0.25	0.02	0.18	0.02	0.08	-227.1	0.8	-227.8	0.3	-221.7	0.8	-220.0	0.3	-208.9	1.5
12035	30.0	10.0	0.03	0.01	0.09	0.03	0.28	0.03	0.45	0.02	0.07			-157.4	0.5	-185.0	0.7	-183.0	2.5		
12043	29.4	4.1	0.07	0.00	0.16	0.04	0.24	0.04	0.26	0.10	0.10			-150.8	2.7	-159.8	3.3	-157.8	2.8		
12054	28.2	12.3	0.07	0.02	0.42	0.03	0.27	0.01	0.13	0.01	0.03	-183.3	1.6	-189.1	1.4	-179.6	3.7	-176.5	4.4		
12063	29.5	9.1	0.04	0.01	0.16	0.03	0.30	0.03	0.34	0.02	0.07			-146.8	3.9	-161.2	3.5	-167.8	1.7	-153.1	1.1
12082	28.5	14.1	0.04	0.02	0.38	0.03	0.29	0.01	0.19	0.01	0.03			-175.6	2.0	-188.9	0.9	-175.3	1.3		
12083	29.2	7.7	0.08	0.02	0.14	0.03	0.27	0.05	0.40	0.00	0.00	-186.6	3.8	-179.3	1.2	-206.3	2.0	-210.4	0.7		
12097	29.5	6.6	0.08	0.02	0.15	0.04	0.26	0.04	0.27	0.02	0.13					-165.2	2.5	-168.2	1.3	-156.5	1.2

Table 7.4: CPOM *– Details of coarse particulate organic matter (CPOM) plant wax* n*-alkane samples: site number, CPOM plant wax* n*-alkane average chain length (ACL, 3.1) and carbon preference index (CPI, 3.2), relative abundances of long chain plant wax* n*-alkanes from 25 to 33 carbon atoms (connC_i), and δD_{CPOM} values (in ‰, vs. VSMOW-SLAP) for odd chain lengths with triplicate measurement standard deviation (stdev, also in ‰).*

site	ACL	CPI	con nC_{25}	con nC_{26}	con nC_{27}	con nC_{28}	con nC_{29}	con nC_{30}	con nC_{31}	con nC_{32}	con nC_{33}	δD nC_{25}	δD nC_{25} std	δD nC_{27}	δD nC_{27} std	δD nC_{29}	δD nC_{29} std	δD nC_{31}	δD nC_{31} std	δD nC_{33}	δD nC_{33} std
11104	29.3	7.1	0.11	0.03	0.19	0.03	0.23	0.02	0.21	0.02	0.16			-171.1	3.8	-174.6	0.5	-165.5	3.2		
12151																					
12150																					
12149																					
11090	29.2	9.4	0.07	0.02	0.19	0.03	0.34	0.02	0.20	0.02	0.12			-185.7	0.8	-202.1	1.8	-187.4	2.5		
11086	31.3	7.2	0.02	0.01	0.06	0.02	0.10	0.02	0.30	0.05	0.42			-187.0	11.0	-174.7	3.6	-181.8	0.8	-181.0	1.1
11085	29.2	8.3	0.08	0.02	0.19	0.03	0.30	0.03	0.24	0.02	0.09			-182.4	4.2	-183.8	0.9	-169.5	0.3		
11081	29.3	8.2	0.08	0.02	0.16	0.03	0.31	0.03	0.25	0.03	0.10			-176.9	0.7	-180.7	0.4	-172.4	1.9		
11080	28.6	8.1	0.07	0.03	0.27	0.05	0.36	0.02	0.14	0.01	0.05			-185.3	2.9	-186.0	0.2				
12142	28.8	6.9	0.14	0.03	0.18	0.03	0.25	0.02	0.26	0.03	0.05										
11075	30.3	7.9	0.05	0.01	0.07	0.02	0.24	0.03	0.33	0.04	0.22			-178.5	2.2	-171.2	1.2	-180.3	0.8	-186.4	2.4
11005	29.4	11.0	0.00	0.01	0.07	0.03	0.63	0.03	0.18	0.01	0.03					-217.2	1.3				
11069	28.4	6.0	0.23	0.05	0.15	0.02	0.24	0.03	0.17	0.02	0.09					-192.3	2.6				
11008	30.3	5.5	0.01	0.03	0.05	0.03	0.29	0.05	0.38	0.04	0.13					-177.9	3.8	-179.0	1.7		
11010	29.4	2.0	0.05	0.07	0.15	0.09	0.20	0.08	0.19	0.07	0.11			-151.1	0.6	-143.4	3.8	-141.4	4.2		
11013	29.4	12.4	0.06	0.01	0.19	0.02	0.24	0.03	0.30	0.03	0.11			-185.0	2.4	-178.1	0.6	-163.3	5.8		
11018	29.7	11.3	0.03	0.01	0.12	0.02	0.41	0.02	0.22	0.02	0.15					-193.1	2.0	-165.2	3.7		
11020	30.6	6.9		0.03	0.05	0.01	0.20	0.04	0.49	0.04	0.14					-182.6	3.0	-194.7	6.0		
11023	30.5	5.7		0.04	0.08	0.02	0.22	0.04	0.38	0.04	0.18					-192.3	0.6	-218.1	0.5		
11029	29.5	13.2	0.09	0.01	0.13	0.02	0.25	0.02	0.39	0.02	0.08			-215.1	3.9	-209.5	1.5	-170.9	0.4		
11028	30.8	6.3	0.00	0.00	0.02	0.01	0.21	0.05	0.46	0.06	0.18					-159.1	0.5	-149.1	0.3	-118.5	1.5
11037	29.6	8.8	0.05	0.02	0.17	0.03	0.31	0.02	0.21	0.02	0.16			-190.6	0.8	-186.4	1.0	-166.9	2.4		
11043	29.0	7.0	0.08	0.02	0.37	0.05	0.00	0.03	0.31	0.02	0.11			-196.5	6.6	-187.4	1.7	-183.0	0.8		
11049	29.0	14.7	0.06	0.01	0.29	0.02	0.23	0.01	0.29	0.01	0.06			-183.5	2.9	-183.8	0.3	-182.7	0.1		
12009	28.8	12.6	0.07	0.01	0.31	0.03	0.24	0.02	0.24	0.02	0.06	-209.7	0.611	-189.1	0.6	-184.6	0.5	-173.7	0.8	-152.1	1.1
12005	30.4	8.3	0.04	0.01	0.07	0.02	0.17	0.03	0.45	0.04	0.17			-159.2	0.8	-162.8	0.5	-168.7	0.7	-162.7	0.7
12026																					
12131																					
12032																					
12129																					
12035	28.4	11.3	0.09	0.02	0.32	0.03	0.31	0.02	0.17	0.01	0.03	-184.5	1.5	-189.1	1.0	-184.5	0.7	-169.1	0.5		
12043	29.5	10.3	0.05	0.01	0.19	0.02	0.24	0.03	0.37	0.02	0.07			-181.7	1.7	-180.5	0.6	-153.3	0.7	-140.9	3.2
12054																					
12063																					
12082																					
12083	28.5	10.3	0.11	0.03	0.31	0.03	0.27	0.01	0.19	0.01	0.05	-180.2	2.3	-180.5	0.5	-176.1	0.6	-171.1	0.5	-164.2	1.0
12097	30.5	9.0	0.01	0.01	0.07	0.01	0.16	0.04	0.53	0.04	0.13			-190.1	1.5	-170.9	0.4	-159.6	0.5	-147.7	0.5

Table 7.5: Plant Samples *– details of plant samples with sample number, site longitude (lon), site latitude (lat), site elevation (alt), sampled species, n-alkane δD values (in ‰, vs. VSMOW-SLAP) for odd chain lengths from 25 to 33 carbon atoms with triplicate measurement standard deviation (stdev, also in ‰), and plant wax n-alkane average chain length (ACL, 3.1) and carbon preference index (CPI, 3.2).*

sample	lon	lat	alt	species	δD nC_{25}	δD nC_{25} stdev	δD nC_{27}	δD nC_{27} stdev	δD nC_{29}	δD nC_{29} stdev	δD nC_{31}	δD nC_{31} stdev	δD nC_{33}	δD nC_{33} stdev	ACL	CPI
11004a1	87.19	27.35	315	*Terminalia arjuna*							-144	7			30.1	2.8
11004a2	87.19	27.35	315								-150	2			30.5	3.0
11004a3	87.19	27.35	315						-188	5	-224	1			30.9	3.6
11004b1	87.19	27.35	315	*Lagerstromia indica*					-176	2	-180	2			29.7	5.4
11004b2	87.19	27.35	315						-216	0	-216	3			30.2	5.6
11004b3	87.19	27.35	315						-224	3	-225	0			30.2	8.2
11004c1	87.19	27.35	315	*Shorea robusta*							-91	3			30.5	3.4
11004c2	87.19	27.35	315								-218	1	-197	1	31.6	22.5
11004c3	87.19	27.35	315						-191	1	-195	2	-172	1	31.1	12.8
11011a1	87.13	27.39	412	*Schima wallichii*					-216	3					28.9	5.3
11011a2	87.13	27.39	412						-202	3	-190	3			29.1	5.1
11011a3	87.13	27.39	412						-202	1	-182	3			29.4	7.6
11011c1	87.13	27.39	412	*Shorea robusta*			-151	1	-140	3	-133	6			29.0	2.0
11011c2	87.13	27.39	412				-179	2	-184	1	-186	0	-175	3	30.1	1.4
11011c3	87.13	27.39	412				-143	2	-133	3	-123	2			29.5	2.3
11020a1	87.15	27.47	448	*Shorea robusta*			-138	2	-135	2	-132	3	-112	4	29.4	1.7
11020a2	87.15	27.47	448				-180	2	-182	3	-189	3	-178	8	29.5	1.5
11020a3	87.15	27.47	448				-153	4	-149	3	-162	1	-157	11	29.4	1.8
11033a1	87.20	27.52	708	*Ficus semicordata*			-165	9	-149	4	-169	2	-135	4	29.4	1.9
11033a2	87.20	27.52	708				-176	2	-160	1	-174	3	-158	9	29.9	1.2
11033a3	87.20	27.52	708				-174	5	-168	1	-175	4	-134	8	29.7	1.8
11033b1	87.20	27.52	708	*Schima wallichii*			-143	4	-150	1	-145	4			29.8	3.8
11033b2	87.20	27.52	708				-237	19	-233	1	-214	5			29.1	2.9
11033b3	87.20	27.52	708						-185	10	-148	12			29.0	3.2
11033c1	87.20	27.52	708	*Shorea robusta*			-127	4	-118	2	-120	4	-97	5	28.8	2.8
11033c2	87.20	27.52	708				-183	2	-187	0	-193	1	-183	1	29.4	6.4
11033c3	87.20	27.52	708				-141	6	-131	5	-135	7	-122	12	29.2	5.4
11047a1	87.27	27.57	1180	*Schima wallichii*			-115	16	-142	1	-106	5			28.9	2.4
11047a2	87.27	27.57	1180				-123	13	-133	1	-112	5			30.0	0.9
11047a3	87.27	27.57	1180				-120	15	-142	1	-106	4			29.7	0.9
11047b1	87.27	27.57	1180	*Rhus wallichii*			-238	7	-210	3	-197	6	-146	28	28.7	4.0
11047b2	87.27	27.57	1180				-206	6	-192	3	-188	1	-183	2	29.0	2.7
11047b3	87.27	27.57	1180				-183	8	-195	1	-190	1	-188	2	28.7	2.6
11047c1	87.27	27.57	1180	*Engelhardtia spicata L.*			-196	1	-186	2					28.6	4.4
11047c2	87.27	27.57	1180				-182	1	-181	0					29.0	2.0
11047c3	87.27	27.57	1180				-241	1	-222	4	-242	4			29.4	9.4
11052a1	87.25	27.56	888	*Schima wallichii*			-135	11	-145	2	-125	2			29.0	5.6
11052a2	87.25	27.56	888						-162	2	-141	1			29.4	8.6
11052a3	87.25	27.56	888				-159	4	-148	1	-136	3			28.9	3.6
11060a1	87.17	27.49	566	*Shorea robusta*			-120	1	-116	2	-107	2	-102	3	29.9	1.5
11060a2	87.17	27.49	566				-130	2	-120	2	-115	1	-130	7	29.7	1.3
11060a3	87.17	27.49	566				-125	3	-118	1	-117	1	-103	5	29.4	1.4
11060a4	87.17	27.49	566				-129	1	-119	0	-118	1	-111	0	29.6	1.5
11060b1	87.17	27.49	566	*Schima wallichii*			-181	23	-145	0	-124	3			29.0	2.6
11060b2	87.17	27.49	566				-164	18	-134	1	-125	2			29.1	4.0
11060b3	87.17	27.49	566				-177	4	-144	4	-127	3			28.8	3.4

sample	lon	lat	alt	species	δD nC$_{25}$	δD nC$_{25}$ stdev	δD nC$_{27}$	δD nC$_{27}$ stdev	δD nC$_{29}$	δD nC$_{29}$ stdev	δD nC$_{31}$	δD nC$_{31}$ stdev	δD nC$_{33}$	δD nC$_{33}$ stdev	ACL	CPI
11072a1	87.19	27.35	315	*Schima wallichii*			-195	29	-144	1	-133	7			28.8	2.9
11072a2	87.19	27.35	315				-230	20	-163	2	-150	3			29.4	5.5
11072a3	87.19	27.35	315				-196	33	-152	0	-134	9			28.9	3.3
11091b1	87.32	26.92	350	*Mimosa lucida or*			-173	7	-132	2	-140	0	-138	1	29.9	2.2
11091b2	87.32	26.92	350				-140	18	-142	3	-143	3	-122	9	29.7	3.0
11091b3	87.32	26.92	350				-138	3	-139	2	-142	2	-139	1	29.7	2.1
11091c1	87.32	26.92	350	*Shorea robusta*			-208	1	-203	1	-199	4	-180	1	29.4	1.4
11091c2	87.32	26.92	350				-155	1	-147	1	-144	1	-128	3	29.3	2.1
11091c3	87.32	26.92	350				-180	15	-137	17	-146	1	-109	9	30.0	1.3
11091c4	87.32	26.92	350				-148	2	-141	1	-124	3	-112	8	29.3	1.9
11091c5	87.32	26.92	350				-142	1	-135	1	-127	3	-115	1	29.4	1.5
11091c6	87.32	26.92	350				-149	2	-143	2	-130	1	-106	8	28.8	1.9
11104a1	86.93	26.52	87	*Magnifera indica*			-234	74	-167	2	-159	2	-152	4	29.9	1.4
11104a2	86.93	26.52	87				-334	117	-161	5	-162	1	-151	2	30.1	1.4
11104a3	86.93	26.52	87				-187	12	-156	2	-145	2	-141	1	30.2	2.0
11104b1	86.93	26.52	87	*Delonix r.*			-171	18	-206	3	-190	0	-170	4	29.2	14.7
11104b2	86.93	26.52	87	*Albizia*			-182	17	-169	2	-160	2	-139	4	29.4	2.9
11104b3	86.93	26.52	87	*julibrissin D.*			-186	12	-163	10	-154	12	-128	27	29.2	4.8
11106a1	87.22	26.81	225	*Shorea robusta*			-154	2	-138	0	-141	1	-135	4	29.6	1.7
11106a2	87.22	26.81	225				-148	1	-139	0	-136	3	-133	3	29.4	1.8
11106a3	87.22	26.81	225				-147	1	-137	0	-134	3	-121	5	28.8	1.6
12013a1	87.28	27.55	1519	*Schima wallichii*	-125	2	-128	1			-121	0			28.7	4.6
12013a2	87.28	27.55	1519		-120	4	-119	2	-113	0	-109	0			28.9	6.4
12013a3	87.28	27.55	1519				-130	0	-126	0	-120	0			29.0	4.9
12037a1	87.36	27.67	1080	*Zizyphus recurva*					-166	2	-185	1	-200	1		
12037a2	87.36	27.67	1080				-125	11	-160	2	-171	0	-168	1		
12037a3	87.36	27.67	1080		-99	2	-162	3	-184	1	-188	0	-194	0		
12037b2	87.36	27.67	1080	*Engelhartia*	-168	7	-194	0	-193	1	-167	3				
12037b3	87.36	27.67	1080	*spicata*	-158	1	-193	0	-190	0	-156	2	-120	5		
12037c1	87.36	27.67	1080	*Alnus nepalensis*	-173	3	-204	0	-202	1	-182	3				
12037c2	87.36	27.67	1080		-182	3	-203	0	-208	1	-198	7				
12037c3	87.36	27.67	1080		-171	3	-190	0	-192	1	-171	3				
12068a1	87.41	27.75	2091	*Alnus nepalensis*	-176	1	-193	1	-197	1	-198	1			27.0	
12068a2	87.41	27.75	2091		-189	1	-193	0	-193	1					26.9	14.1
12068a3	87.41	27.75	2091		-196	0	-205	1	-208	0					27.3	14.2
12068b1	87.41	27.75	2091	*Rhododendron arboreum*	-130	1	-136	1	-149	1	-135	0			28.3	6.4
12068b2	87.41	27.75	2091		-112	1	-120	1	-129	0	-127	1			28.2	5.5
12068b3	87.41	27.75	2091				-147	1	-149	0	-148	2			28.7	12.6
12090a1	87.42	27.81	2578	*Rhododendron arboreum*	-120	4	-136	3	-132	2					28.5	4.7
12090a2	87.42	27.81	2578		-122	3	-135	4	-132	1	-134	0			28.7	5.9
12090a3	87.42	27.81	2578		-103	0	-120	1	-122	1	-118	1			27.9	3.1
12090b1	87.42	27.81	2578	*Alnus nepalensis*	-201	2	-209	1	-213	1	-132	1			27.0	19.5
12090b2	87.42	27.81	2578		-175	1	-196	0	-209	1	-138	1			27.0	16.9
12090b3	87.42	27.81	2578		-178	2	-184	1	-184	1	-125	2			27.1	16.4
12099a1	87.40	27.84	2196	*Rhododendron arboreum*	-136	1	-141	1	-135	0					28.6	14.3
12099a2	87.40	27.84	2196		-146	3	-155	1	-156	0	-145	2			28.4	11.1
12099a3	87.40	27.84	2196		-129	1	-136	2	-145	0	-145	1			28.8	20.3
12099b1	87.40	27.84	2196	*Alnus nepalensis*	-186	3	-180	1	-178	1					27.2	8.6
12099b2	87.40	27.84	2196		-175	1	-171	1	-168	1					27.3	22.7
12099b3	87.40	27.84	2196		-194	2	-213	0	-218	2					27.2	14.2
12112a1	87.28	27.56	1519	*Alnus nepalensis*	-170	2	-195	1	-204	1					27.3	11.8
12112a2	87.28	27.56	1519				-151	1	-156	1					27.7	18.8
12112a3	87.28	27.56	1519		-161	3	-188	1	-199	2					27.1	17.2

sample	lon	lat	alt	species	δD nC$_{25}$	δD nC$_{25}$ stdev	δD nC$_{27}$	δD nC$_{27}$ stdev	δD nC$_{29}$	δD nC$_{29}$ stdev	δD nC$_{31}$	δD nC$_{31}$ stdev	δD nC$_{33}$	δD nC$_{33}$ stdev	**ACL**	**CPI**
12129a1	87.21	27.69	4070	*Rh.*					-203	0	-207	0	-200	1	30.8	10.4
12129a2	87.21	27.69	4070	*campanulata*					-201	7	-210	0	-204	4	31.0	10.6
12129a3	87.21	27.69	4070	*aeruginos.*					-192	0	-193	1	-188	1	30.8	12.3
12133a1	87.21	27.65	3562	*Rh.*	-205	1	-200	12	-178	0					30.1	8.6
12133a2	87.21	27.65	3562	*campanulata*	-218	3	-201	18	-180	1	-170	0	-165	0	30.5	9.9
12133a3	87.21	27.65	3562	*aeruginos.*					-141	2	-147	1	-147	0	29.7	0.4
12133b1	87.21	27.65	3562						-197	2	-201	1	-193	7	27.8	7.7
12133b2	87.21	27.65	3562	*Rhododendron*	-230	0	-226	2	-195	6	-202	1	-191	1	27.8	4.9
12133b3	87.21	27.65	3562		-219	1	-218	3	-186	3	-191	0	-190	2	31.1	9.0
12136a1	87.24	27.62	2006		-175	0	-177	0	-184	1					27.5	22.1
12136a2	87.24	27.62	2006	*Alnus*	-179	0	-183	1	-184	0	-191	3			27.4	15.7
12136a3	87.24	27.62	2006	*nepalensis*	-180	1	-183	0	-186	1					27.2	12.1
12136b1	87.24	27.62	2006						-206	0					29.0	19.4
12136b2	87.24	27.62	2006	*Rhododendron*					-211	1					29.0	22.5
12136b3	87.24	27.62	2006						-201	0					29.0	18.3
12144a1	87.20	27.32	400	*Shorea robusta*			-171	2	-183	2	-183	2	-175	2	29.7	1.6
12144a2	87.20	27.32	400				-137	2	-144	0	-143	0	-130	0	29.8	1.9
12144c1	87.20	27.32	400						-172	2	-161	4				
12144c2	87.20	27.32	400	*Schima*					-207	0	-195	1				
12144c3	87.20	27.32	400	*wallichii*					-205	0	-197	2				

8 | Appendix to Chapter 4

8.1 Introduction

The supporting material here gives additional information on catchment topography and characteristics and further explanations of methods used in the manuscripts. Table 8.1 contains catchment characteristics calculated as described in section 4.3.1 of the manuscript. Table 8.2 contains the results of tests for normal distribution, skewness, and transience in each catchment as described in section 4.3.5. Table 8.3 contains the regression results, calculated as described in manuscript section 4.5.2, used in Figure 4.9. Supporting information Text 8.2 describes analyses used to explore the robustness of our ^{10}Be data. Figures 8.1-8.4 expound upon important aspects of the manuscript that did not directly contribute to our major conclusions.

8.2 Potential impact of transiently stored sediment on ^{10}Be denudation rate calculation

Fluvial fill terraces are found along the lower and middle reaches of the Arun (e.g., Lavé and Avouac, 2001). Stored sediment can impact ^{10}Be TCN-derived denudation rates by accumulation of secondary ^{10}Be after material is eroded from bedrock, resulting in anomalously high ^{10}Be concentrations and apparently lower denudation rates (Granger et al., 1996). In the Arun Valley, measured ^{10}Be concentrations from terraces are significantly lower by a factor of 20 than in modern fluvial sands, 3.33 x $104 atoms\ g^{-1}$ in Tumlingtar terrace (the average of ARU-12-21 and ARU-12-22) compared to 1.78 Ã $105 atoms\ g^{-1}$ in adjacent mainstem sample (ARU-11-01), and would therefore cause a dilution rather than a concentration of ^{10}Be atoms. When the residence time of transiently stored sediment (e.g., fluvial terraces) is longer than the erosional timescale of TCN denudation, transiently stored sediments may impact ^{10}Be TCN denudation rates (Granger et al., 1996). The erosional timescale of mainstem catchments from the Arun ($1 - 4 kyr$) is shorter than estimated ages of fill terraces mapped in the valley (Table 4.2) (Lavé and Avouac, 2001). Thus, stored sediments could potentially impact ^{10}Be concentrations in the present-day Arun fluvial sands. Assuming an average 10% error on denudation rates, we estimate that 5-10% or more of a detrital sand sample must be derived from fill terraces to impact the denudation rates and to exceed the standard

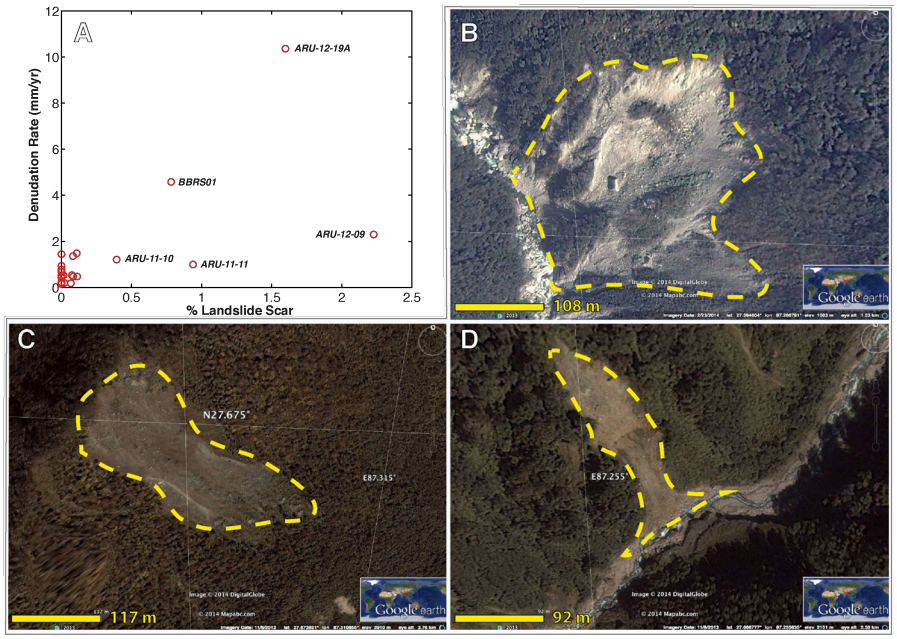

Figure 8.1: *(A) Determination of landslide-impacted catchments by percent-area covered by landslide scars, showing outlying sample catchments. (B-D) Example landslides from Google Earth for catchments ARU-12-19A (B,D) and ARU-12-09 (C). Landslide scar area was determined using Google Earth^{TM} high resolution imagery.*

error. Making the simplifying assumption that we have spatially-uniform denudation, this would be equivalent to a fill-terrace area of $1600 - 1900 km^2$ in the mainstem Arun watershed. The estimated area of fluvial fill terraces in the Arun Valley is ~$200 km^2$, and we therefore assume that stored sediment does not have a measurable impact on our catchment-mean denudation rates. However, we acknowledge that we are not able to constrain the area of stored sediment in the Tibetan section of the watershed and that erosion may be focused along the fill terraces.

8.3 Tables

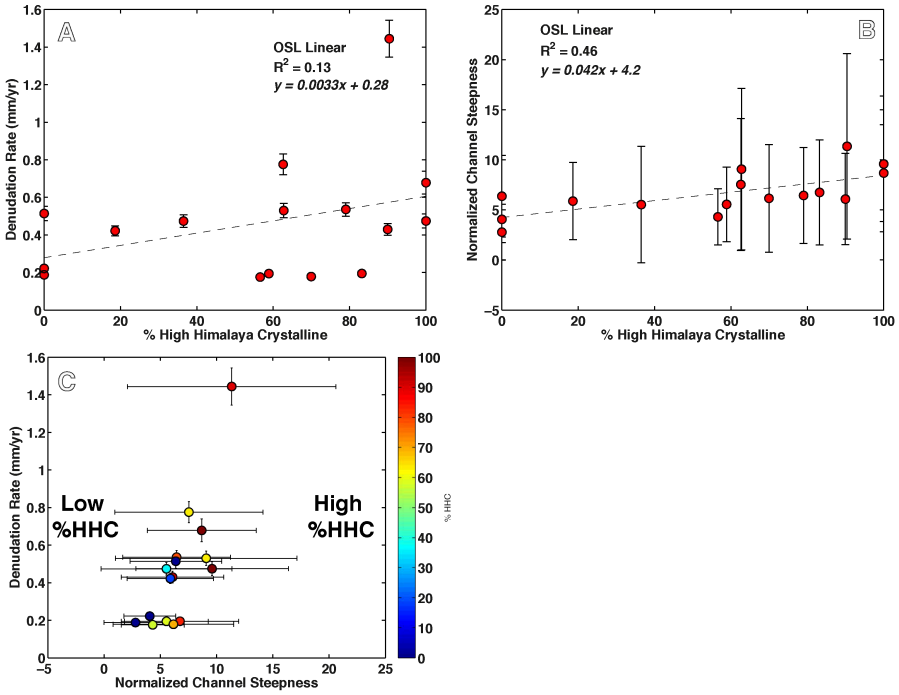

Figure 8.2: *Relationship between lithology (% High Himalayan Crystalline), denudation, and k_{sn}. (A) OLS linear regression of %HHC and denudation. (B) OLS linear regression of %HHC and ksn. (C) k_{sn} versus denudation, showing possible modulation of k_{sn}-denudation relationship by lithology. Lithologic units are based on Schelling (1992), as described in section 4.3.2.*

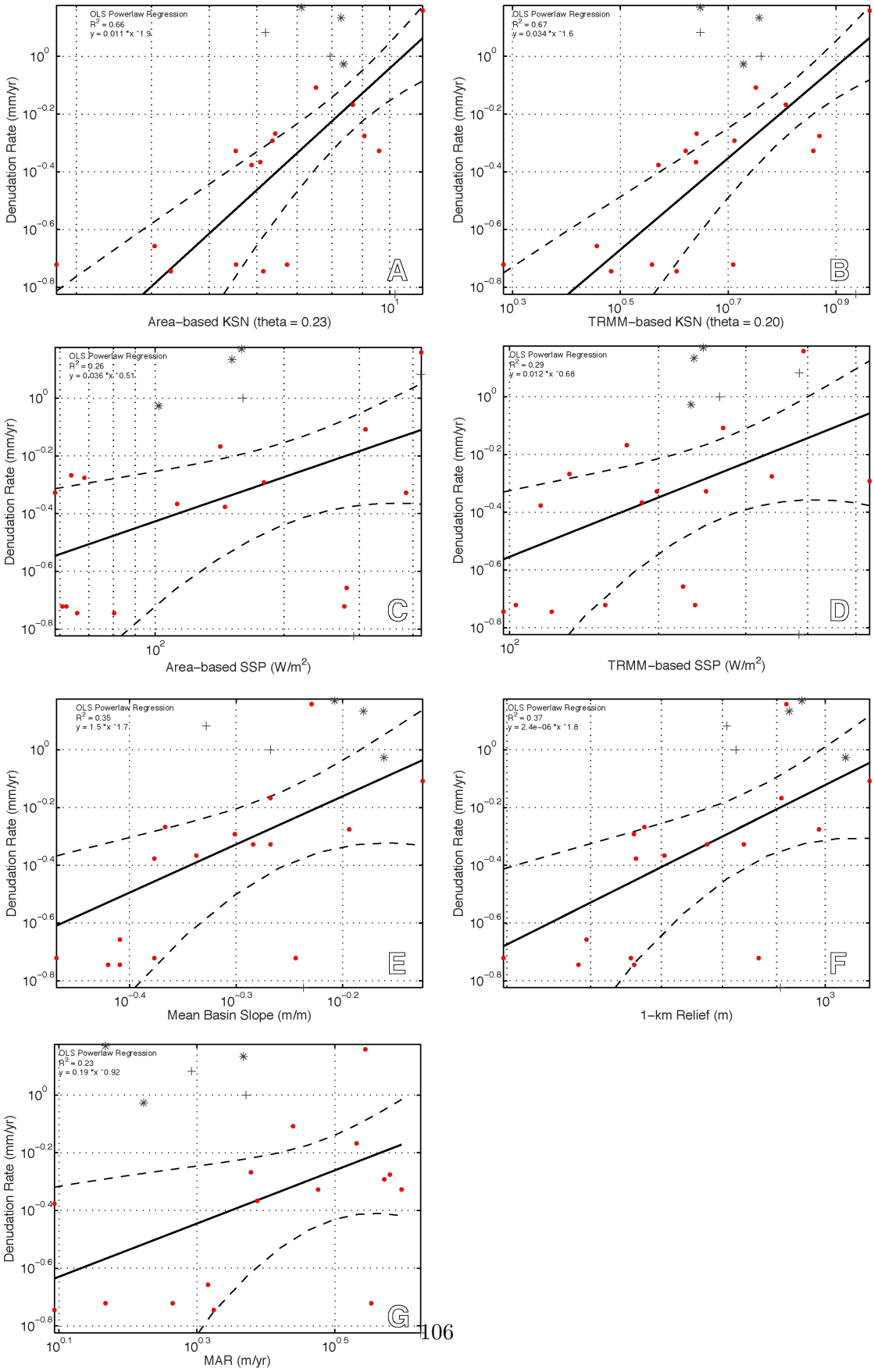

Figure 8.3: *OLS power-law regressions of (A) area-weighted k_{sn}; (B) TRMM-weighted k_{sn}; (C) area-weighted SSP; (D) TRMM-weighted SSP; (E) slope; (F) local relief; (G) TRMM mean annual rainfall. Red circles are data included in regression analysis. Grey stars represent glaciated tributaries; grey crosses represent landslide-impacted and non-equilibrium tributaries. All glaciated and landslide-impacted catchments have been excluded from the power-law regression analysis.*

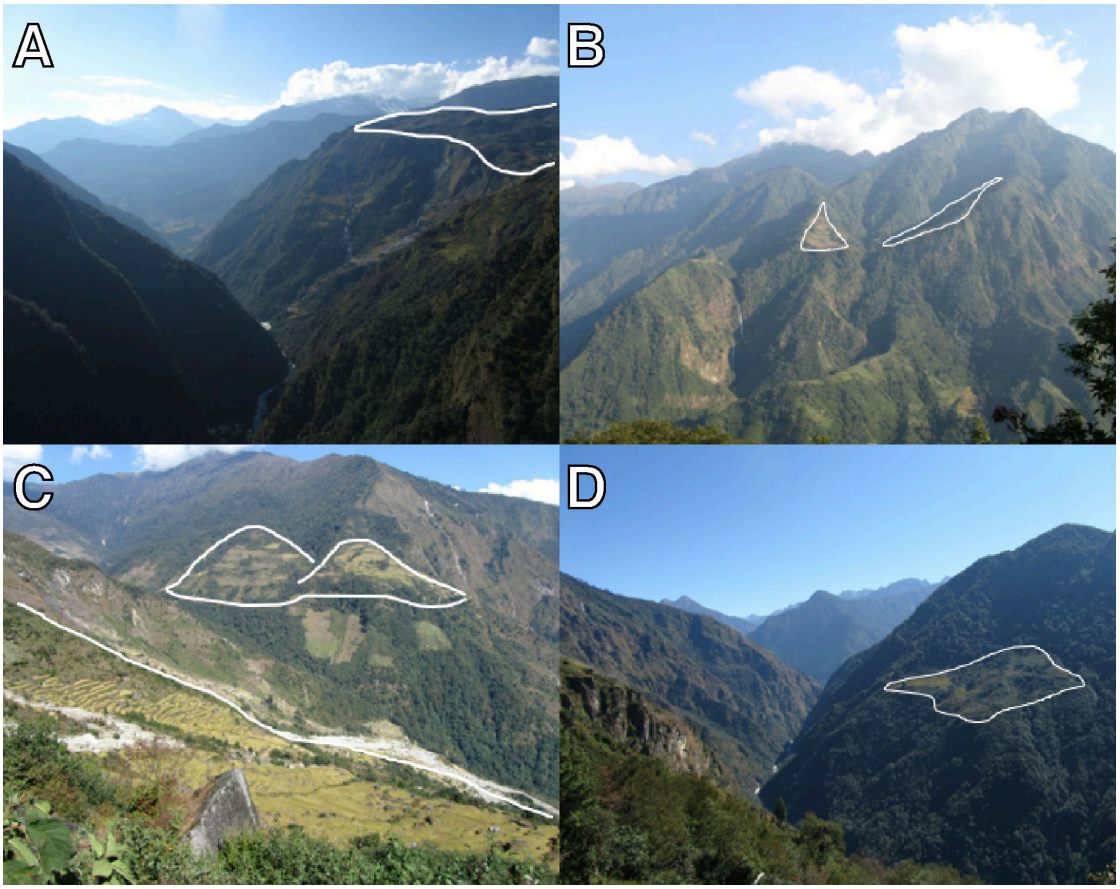

Figure 8.4: *Photographs of perched low-relief surfaces (outlined in white) along the mainstem Arun river in the Higher Himalaya. Photo (B) shows perched low-relief surfaces in sample basin ARU-12-06.*

Table 8.1: *Extended basin statistics. Lithology is taken from Schelling (1992). Simplified lithologic units are grouped by Lesser Himalaya Crystalline (LHC), High Himalayan Crystalline (HHC), and Tethyan Sediments and we do not make further differentiation between lithologies. All stream network statistics were calculated with area-weighted flow accumulation and TRMM mean annual rainfall weighted flow accumulation using the Topotoolbox v.2 functions for MATLAB (Schwanghart and Scherler, 2013).*

[a] – calculated for every pixel of the 90-m SRTM DEM based on its 8 neighbours, [b] – calculated for every pixel in the stream network based on upstream and downstream pixels, then averaged over stream network in each basin, [c] – calculated from slope-area regression of the entire stream network upstream of each sample location, [d] – calculated from χ-transformed channel profile for the entire stream network upstream of each sample location, [e] – calculated from χ-transformed channel profile for the trunk stream upstream of each sample location, [f] – calculated using the standard channel concavity of 0.45 and area based on unweighted upstream area from each sample location, [g] – calculated using the channel concavity of 0.23 from the χ-transformed stream network and area based on unweighted upstream area from each sample location, [h] – each metric here is calculated the same as c-g; however, the flow accumulation grid (and therefore upstream area) has been weighted by TRMM-derived rainfall.

	Lithology			Topography	Metrics calculated by upstream area			
Sample	% TS	%HHC	%LHC	Mean Hillslope Grd. $(m/m)^a$	Mean Stream Grd. $(m/m)^b$	Theta (Slope-Area Regression) [c]	Stream Channel Concavity [d]	Trunk Channel Concavity [e]
ARU-11-01	-	-	-	0.56	0.06	-0.60	0.36	0.35
ARU-11-13	-	-	-	0.65	0.09	0.11	0.21	0.27
ARU-11-16	-	-	-	0.62	0.08	-0.60	0.21	0.25
ARU-11-26	-	-	-	0.44	0.02	-0.59	0.53	0.50
ARU-11-28	-	-	-	0.24	0.01	-0.99	0.37	0.43
ARU-12-03	-	-	-	0.62	0.08	-0.60	0.21	0.25
ARU-12-15	-	-	-	0.29	0.01	-0.38	0.25	0.08
ARU-11-25	-	-	-	0.54	0.03	-0.31	0.42	0.39
ARU-11-27	-	-	-	0.52	0.01	-0.31	0.45	0.44
ARU-11-03	0	37	63	0.54	0.09	-0.59	0.58	0.46
ARU-11-04	0	0	100	0.34	0.08	-0.76	0.26	0.26
ARU-11-05	0	0	100	0.39	0.11	-0.44	0.38	0.39
ARU-11-06	0	90	10	0.46	0.11	-0.31	0.27	0.29
ARU-11-07	0	83	17	0.57	0.08	-0.39	0.34	0.31
ARU-11-10	0	48	52	0.47	0.20	0.84	0.06	0.07
ARU-11-11	0	63	37	0.54	0.21	-0.15	0.22	0.28
ARU-11-12	0	92	8	0.75	0.21	-0.50	0.26	0.29
ARU-11-14	0	95	5	0.66	0.13	-0.31	0.25	0.22
ARU-11-15	0	57	43	0.69	0.11	-0.32	0.25	0.25
ARU-11-18	0	79	21	0.38	0.10	-0.51	0.38	0.36
ARU-11-20	0	19	81	0.43	0.07	-0.43	0.34	0.41
ARU-11-22	0	59	41	0.42	0.13	-0.62	0.27	0.33
ARU-11-23	0	70	30	0.39	0.11	-0.33	0.20	0.09
ARU-11-24	0	0	100	0.42	0.09	-0.50	0.36	0.39
ARU-12-01	0	63	37	0.50	0.18	0.20	0.16	0.17
ARU-12-02	0	87	13	0.64	0.18	-0.36	0.32	0.31
ARU-12-06	0	23	77	0.58	0.30	0.23	0.02	-0.02
ARU-12-08	0	90	10	0.59	0.30	-0.36	0.06	0.09
ARU-12-09	0	88	12	0.67	0.21	-0.09	0.26	0.24
ARU-12-10	0	44	56	0.85	0.13	-0.62	0.33	0.36
ARU-12-11	1	98	1	0.62	0.08	-0.26	0.27	0.08
ARU-12-12	0	100	0	0.54	0.22	-0.40	0.16	0.17
ARU-12-13	0	100	0	0.52	0.27	-0.53	0.11	0.10
ARU-12-19A	0	79	21	0.57	0.14	-0.35	0.31	0.31
BBRS01	0	24	76	0.47	0.22	-0.39	0.13	0.21

Sample	Metrics calculated by upstream area				Metrics calculated by TRMM-weighted flow accumulation[h]						
	Mean k_{sn} ($\theta = 0.45$) [f]	stdev. k_{sn} ($\theta = 0.45$)	Mean k_{sn} ($\theta = 0.23$) [g]	stdev. k_{sn} ($\theta = 0.23$)	θ (Sope-Area Regression)	Stream Channel Concavity	Trunk Channel Concavity	Mean k_{sn} ($\theta = 0.45$)	stdev. k_{sn} ($\theta = 0.45$)	Mean k_{sn} ($\theta = 0.23$)	stdev. k_{sn} ($\theta = 0.23$)
ARU-11-01	235.40	295.14	4.42	5.57	-0.49	0.34	0.33	366.25	456.07	3.13	3.93
ARU-11-13	411.23	531.47	6.81	8.32	0.21	0.11	0.22	441.69	653.42	3.97	5.10
ARU-11-16	318.60	351.35	6.12	6.73	-0.56	0.18	0.01	512.36	572.30	4.41	4.85
ARU-11-26	156.02	187.63	3.00	3.80	-0.38	0.53	0.52	203.82	253.22	1.97	2.54
ARU-11-28	25.86	67.85	0.55	1.50	-0.86	0.20	0.25	38.36	102.36	0.39	1.07
ARU-12-03	318.60	351.35	6.12	6.73	-0.56	0.18	0.01	512.36	572.30	4.41	4.85
ARU-12-15	365.71	12280.90	4.91	97.12	-0.34	0.21	0.06	162.39	5334.42	1.90	35.08
ARU-11-25	283.63	407.22	4.72	6.00	-0.11	0.28	0.37	329.67	470.54	2.89	3.72
ARU-11-27	299.96	1244.26	4.92	16.21	-0.15	0.44	0.50	341.25	1632.60	2.97	10.61
ARU-11-03	191.20	190.85	5.53	5.82	-0.27	0.49	0.45	300.08	329.33	4.18	4.65
ARU-11-04	87.47	89.68	2.78	2.79	-0.77	0.26	0.25	109.22	111.84	1.92	1.92
ARU-11-05	127.90	76.83	4.05	2.31	-0.43	0.39	0.35	168.70	101.80	2.86	1.63
ARU-11-06	212.53	160.49	6.08	4.55	-0.32	0.26	0.28	296.88	223.21	4.37	3.32
ARU-11-07	236.14	181.14	6.74	5.23	-0.34	0.35	0.31	375.32	289.23	5.12	4.04
ARU-11-10	163.82	133.40	6.20	5.04	0.87	0.05	0.06	211.86	172.49	4.45	3.62
ARU-11-11	255.86	117.82	7.95	3.62	-0.21	0.21	0.25	359.67	165.44	5.77	2.63
ARU-11-12	235.87	206.82	7.53	6.59	-0.56	0.25	0.27	352.91	308.91	5.64	4.95
ARU-11-14	325.63	386.96	8.29	7.77	-0.12	0.14	0.16	428.38	527.60	5.72	5.44
ARU-11-15	344.25	392.66	8.37	8.26	-0.11	0.13	0.21	382.11	471.03	5.35	5.53
ARU-11-18	140.91	88.79	4.31	2.80	-0.49	0.35	0.34	185.96	119.19	3.04	2.02
ARU-11-20	223.20	157.97	6.44	4.78	-0.31	0.34	0.41	275.93	199.44	4.38	3.31
ARU-11-22	191.39	119.27	5.88	3.85	-0.69	0.25	0.32	197.80	123.65	3.72	2.48
ARU-11-23	219.21	208.51	6.15	5.37	-0.27	0.18	0.09	250.31	240.00	4.02	3.51
ARU-11-24	191.10	113.34	5.54	3.72	-0.44	0.34	0.37	215.03	128.65	3.62	2.51
ARU-12-01	189.48	126.78	6.37	4.08	0.12	0.14	0.16	332.31	223.88	5.15	3.28
ARU-12-02	293.83	276.03	9.07	8.06	-0.33	0.31	0.30	533.85	507.81	7.40	6.67
ARU-12-06	285.21	248.82	10.20	8.57	0.09	0.01	-0.01	545.28	475.51	8.64	7.23
ARU-12-08	342.21	302.75	11.34	9.27	-0.37	0.05	0.09	601.97	532.94	9.17	7.43
ARU-12-09	243.63	274.92	7.94	8.14	0.00	0.24	0.22	418.26	471.88	6.33	6.41
ARU-12-10	296.50	231.21	8.54	7.10	-0.49	0.26	0.31	456.94	365.36	6.40	5.45
ARU-12-11	297.09	429.66	7.12	7.85	-0.16	0.24	0.07	314.20	463.30	4.45	4.91
ARU-12-12	292.02	163.88	8.67	4.84	-0.49	0.14	0.16	433.36	242.47	6.41	3.57
ARU-12-13	311.00	238.02	9.59	6.78	-0.48	0.10	0.10	475.30	366.47	7.21	5.09
ARU-12-19A	292.67	244.65	8.54	6.62	-0.40	0.30	0.28	479.49	401.04	6.59	5.09
BBRS01	223.87	132.69	7.55	4.60	-0.37	0.13	0.19	302.95	180.61	5.44	3.34

Table 8.2: *Results of tests for distribution shape and transient topography in sampled catchments.*

	Results of Lilliefors test for normal sample dist. a					Results of skewness test b				
Sample	alt	MAR	h.g. (m/m)	$1-km$ Relief	k_{sn} $(m0.46)$	alt	MAR	h.g. (m/m)	$1-km$ Relief	k_{sn} $(m0.46)$
ARU-11-03	1	1	1	1	1	1.12	0.68	1.17	0.31	2.35
ARU-11-04	1	1	1	1	0	0.05	-2.74	0.93	0.91	0.58
ARU-11-05	1	1	1	1	0	0.49	3.21	1.77	-0.66	0.64
ARU-11-06	1	1	1	1	1	0.24	-1.01	0.59	0.19	1.07
ARU-11-07	1	1	1	1	1	0.03	0.37	0.68	-0.53	1.12
ARU-11-10	0	1	1	1	0	0.17	3.97	0.55	-0.74	0.2
ARU-11-11	1	1	1	1	0	0.07	7.85	1.76	-0.74	-0.89
ARU-11-12	1	1	1	1	0	0.22	-0.07	0.77	-1.16	1.08
ARU-11-14	1	1	1	1	1	-0.43	-0.56	1.01	-0.2	3.09
ARU-11-15	1	1	1	1	1	-0.11	0.45	0.98	0.36	1.68
ARU-11-18	1	1	1	1	0	0.47	0.27	0.38	-0.12	0.32
ARU-11-20	1	1	1	1	1	-0.06	0.73	0.85	-0.36	0.77
ARU-11-22	1	1	1	1	0	0.41	1.97	0.75	-0.74	0.48
ARU-11-23	1	1	1	1	1	0.01	-0.59	1.34	-0.08	1.93
ARU-11-24	1	1	1	1	1	0.15	0.48	0.53	-0.35	0.79
ARU-12-01	1	1	1	1	0	-0.3	-0.69	0.84	-0.13	1.09
ARU-12-02	1	1	1	1	1	0.54	-0.66	0.95	-0.16	3.33
ARU-12-06	1	1	1	1	1	-0.44	-10.68	1	-0.63	1.9
ARU-12-08	1	1	1	1	0	-0.22	-0.89	2.07	-0.09	1.79
ARU-12-11	1	1	1	1	1	-0.27	0.76	0.97	0.79	2.61
ARU-12-12	1	1	1	1	0	0.22	-1.93	1.37	-0.54	0.3
ARU-12-13	1	1	1	1	0	0.02	1.03	1.61	0.33	0.83
BBRS01	1	1	1	1	0	-0.12	-1.47	1.31	-0.16	0.27

Table 8.3: *OLS goodness-of-fit results of percentile regression. Power-law exponent p assumes metric ~ denudation^p and describes the relationship between denudation and topography, where $p = 1/b$.*

	Elevation		Slope		Relief		SSP area		SSP rain		TRMM		k_{sn} area		k_{sn} rain	
Perc.	R^2	p	R^2	p	R^2	p	R^2	p	R^2	p	R^2	p	R^2	p	R^2	p
10	0.33	1.47	0.43	0.58	0.5	0.58	0.29	1	0.38	1	0.36	1.01	0.08	-12.54	0.08	-12.77
15	0.32	1.39	0.34	0.63	0.48	0.58	0.26	1.09	0.38	1	0.35	1.02	0	44.24	0.01	37.23
20	0.32	1.32	0.3	0.66	0.46	0.57	0.23	1.26	0.37	1.01	0.34	1.02	0.21	1.01	0.23	1.13
25	0.32	1.27	0.27	0.69	0.43	0.59	0.21	1.41	0.36	1.03	0.33	1.02	0.36	0.8	0.34	0.9
30	0.31	1.24	0.25	0.71	0.4	0.59	0.18	1.59	0.34	1.07	0.33	1.02	0.33	0.8	0.34	0.93
35	0.3	1.21	0.23	0.72	0.38	0.59	0.16	1.8	0.33	1.12	0.33	1.01	0.36	0.81	0.37	0.93
40	0.29	1.18	0.23	0.74	0.37	0.58	0.15	2.04	0.31	1.18	0.32	1	0.45	0.7	0.44	0.81
45	0.28	1.17	0.21	0.76	0.36	0.58	0.14	2.31	0.3	1.24	0.32	1	0.5	0.59	0.45	0.76
50	0.27	1.16	0.21	0.76	0.35	0.58	0.13	2.6	0.29	1.29	0.31	1	0.5	0.6	0.46	0.75
55	0.25	1.16	0.2	0.77	0.34	0.58	0.12	2.85	0.29	1.35	0.3	1	0.53	0.55	0.49	0.69
60	0.24	1.16	0.22	0.75	0.34	0.57	-0.84	0.03	0.28	1.42	0.29	1	0.6	0.51	0.51	0.65
65	0.23	1.16	0.24	0.71	0.32	0.57	0.12	3.28	0.28	1.46	0.28	1.02	0.53	0.57	0.48	0.72
70	0.22	1.17	0.26	0.69	0.31	0.57	0.13	3.38	0.29	1.53	0.27	1.05	0.56	0.56	0.51	0.69
75	0.2	1.18	0.28	0.65	0.29	0.59	0.14	3.46	0.29	1.58	0.26	1.07	0.53	0.57	0.49	0.71
80	0.19	1.19	0.29	0.65	0.26	0.62	0.15	3.45	0.3	1.63	0.25	1.09	0.6	0.51	0.54	0.65
85	0.19	1.2	0.3	0.64	0.24	0.65	0.15	3.62	0.3	1.66	0.25	1.12	0.6	0.49	0.52	0.64
90	0.18	1.19	0.31	0.65	0.21	0.71	0.15	3.73	0.32	1.67	0.24	1.14	0.65	0.43	0.58	0.56

Bibliography

Ambach, W., Dansgaard, W., Eisner, H., MØller, J., 1968. The altitude effect on the isotopic composition of precipitation and glacier ice in the Alps. Tellus 20 (4), 595–600.

Andermann, C., Longuevergne, L., Bonnet, S., Crave, A., Davy, P., Gloaguen, R., 2012. Impact of transient groundwater storage on the discharge of Himalayan rivers. Nature Geoscience 5 (2), 127–132.
URL http://www.nature.com/doifinder/10.1038/ngeo1356

Araguás Araguás, L., Froehlich, K., 1998. Stable isotope composition of precipitation over southeast Asia. Journal of Geophysical Research 103 (D22), 28721 – 28742.
URL http://onlinelibrary.wiley.com/doi/10.1029/98JD02582/full

Avouac, J.-P., 2003. Mountain Building, Erosion, and the Seismic Cycle in the Nepal Himalaya. Advances in Geophysics 46, 1–80.
URL http://linkinghub.elsevier.com/retrieve/pii/S0065268703460019

Bai, Y., Fang, X., Gleixner, G., Mügler, I., 2011. Effect of precipitation regime on dD values of soil n-alkanes from elevation gradients - Implications for the study of paleo-elevation. Organic Geochemistry 42 (7), 838–845.
URL http://dx.doi.org/10.1016/j.orggeochem.2011.03.019

Balco, G., Stone, J. O., Lifton, N. a., Dunai, T. J., 2008. A complete and easily accessible means of calculating surface exposure ages or erosion rates from 10Be and 26Al measurements. Quaternary Geochronology 3 (3), 174–195.
URL http://www.sciencedirect.com/science/article/pii/S1871101407000647

Berkelhammer, M., Sinha, A., Mudelsee, M., Cheng, H., Edwards, R. L., Cannariato, K., 2010. Persistent multidecadal power of the Indian Summer Monsoon. Earth and Planetary Science Letters 290 (1-2), 166–172.
URL http://dx.doi.org/10.1016/j.epsl.2009.12.017

Berner, R. A., 1990. Atmospheric Carbon Dioxide Levels Over Phanerozoic Time. Science 249 (4975), 1382–1386.

Bharti, V., Singh, C., 2015. Evaluation of error in TRMM 3B42V7 precipitation estimates over the Himalayan region. Journal of Geophysical Research: Atmospheres 120, 1 – 16.

Bierman, P., Steig, E. J., 1996. Estimating rates of denudation using cosmogenic isotope abundances in sediment. Earth Surface Processes and Landforms 21 (2), 125–139.
URL http://doi.wiley.com/10.1002/(SICI)1096-9837(199602)21:2<125::AID-ESP511>3.0.CO;2-8

Blisniuk, P. M., Stern, L. a., 2005. Stable isotope paleoaltimetry: A critical review. American Journal of Science 305 (10), 1033–1074.

Bolch, T., Kulkarni, a., Kaab, a., Huggel, C., Paul, F., Cogley, J. G., Frey, H., Kargel, J. S., Fujita, K., Scheel, M., Bajracharya, S., Stoffel, M., 2012. The State and Fate of Himalayan Glaciers. Science 336 (6079), 310–314.
URL http://www.sciencemag.org/content/336/6079/310.short

Bookhagen, B., Burbank, D. W., 2006. Topography, relief, and TRMM-derived rainfall variations along the Himalaya. Geophysical Research Letters 33 (8), L08405.
URL http://doi.wiley.com/10.1029/2006GL026037

Bookhagen, B., Burbank, D. W., 2010. Toward a complete Himalayan hydrological budget: Spatiotemporal distribution of snowmelt and rainfall and their impact on river discharge. Journal of Geophysical Research 115 (F03019).
URL http://doi.wiley.com/10.1029/2009JF001426

Bookhagen, B., Strecker, M. R., 2012. Spatiotemporal trends in erosion rates across a pronounced rainfall gradient: Examples from the southern Central Andes. Earth and Planetary Science Letters 327-328, 97–110.
URL http://dx.doi.org/10.1016/j.epsl.2012.02.005

Bookhagen, B., Thiede, R. C., Strecker, M. R., feb 2005a. Abnormal monsoon years and their control on erosion and sediment flux in the high, arid northwest Himalaya. Earth and Planetary Science Letters 231 (1-2), 131–146.
URL http://linkinghub.elsevier.com/retrieve/pii/S0012821X0400696X

Bookhagen, B., Thiede, R. C., Strecker, M. R., 2005b. Late Quaternary intensified monsoon phases control landscape evolution in the northwest Himalaya. Geology 33 (2), 149.
URL http://geology.gsapubs.org/cgi/doi/10.1130/G20982.1

Bordet, P., 1961. Recheres géologiques dans l'Himalaya du Nepal, Région du Makalu. C.N.R.S., Paris.

Bouchez, J., Galy, V., Hilton, R. G., Gaillardet, J., Moreira-Turcq, P., Pérez, M. A., France-Lanord, C., Maurice, L., 2014. Source, transport and fluxes of Amazon River particulate organic carbon: Insights from river sediment depth-profiles. Geochimica et Cosmochimica Acta 133, 280–298.
URL http://linkinghub.elsevier.com/retrieve/pii/S0016703714001410

Bray, H. E., Stokes, S., 2004. Temporal patterns of arid-humid transitions in the south-eastern Arabian Peninsula based on optical dating. Geomorphology 59 (1-4), 271–280.
URL http://www.sciencedirect.com/science/article/pii/S0169555X03003283

Breitenbach, S. F. M., Adkins, J. F., Meyer, H., Marwan, N., Kumar, K. K., Haug, G. H., 2010. Strong influence of water vapor source dynamics on stable isotopes in precipitation observed in Southern Meghalaya, NE India. Earth and Planetary Science Letters 292 (1-2), 212–220.
URL http://dx.doi.org/10.1016/j.epsl.2010.01.038

Brown, E. T., Stallard, R. F., Larsen, M. C., Raisbeck, G. M., Yiou, F., 1995. Denudation rates determined from the accumulation of in situ-produced 10Be in the luquillo experimental forest, Puerto Rico. Earth and Planetary Science Letters 129 (1-4), 193–202.
URL http://www.sciencedirect.com/science/article/pii/0012821X9400249X

Buedel, J., 1982. Climatic Geomorphology. Princeton University Press, Princeton, NJ.

Burbank, D. W., Blythe, a. E., Putkonen, J., Pratt-Sitaula, B., Gabet, E., Oskin, M., Barros, a., Ojha, T. P., 2003. Decoupling of erosion and precipitation in the Himalayas. Nature 426 (6967), 652–655.
URL http://dx.doi.org/10.1038/nature02187

Burdige, D. J., 2005. Burial of terrestrial organic matter in marine sediments: A re-assessment. Global Biogeochemical Cycles 19 (4), 1–7.
URL http://doi.wiley.com/10.1029/2004GB002368

Bush, R. T., McInerney, F. A., sep 2013. Leaf wax n-alkane distributions in and across modern plants: Implications for paleoecology and chemotaxonomy. Geochimica et Cosmochimica Acta 117, 161–179.
URL http://dx.doi.org/10.1016/j.gca.2013.04.016http://linkinghub.elsevier.com/retrieve/pii/S0016703713002317

Buttle, J., 1994. Isotope hydrograph separations and rapid delivery of pre-event water from drainage basins. Progress in Physical Geography 18 (1), 16–41.

Carpenter, C., Zomer, R., 1996. Forest ecology of the Makalu-Barun National Park and Conservation Area, Nepal. Mountain Research and Development 16 (2), 135–148.
URL <GotoISI>://A1996UR67200004

Charney, J. G., 1967. The intertropical convergence zone and the Hadley circulation of the atmosphere. Proc. WMO/IUCG Symp. Nu- mer. Weather Predict. Jpn. Meteorol. Agency III, 73–79.

Chatanantavet, P., Lajeunesse, E., Parker, G., luce Malverti, Meunier, P., 2010. Physically based model of downstream fining in bedrock streams with lateral input. Water Resour. Res. 46 (2), W02518.
URL http://dx.doi.org/10.1029/2008WR007208

Chmeleff, J., von Blanckenburg, F., Kossert, K., Jakob, D., 2010. Determination of the 10Be half-life by multicollector ICP-MS and liquid scintillation counting. Nuclear Instruments and Methods in Physics Research, Section B: Beam Interactions with Materials and Atoms 268 (2), 192–199.
URL http://dx.doi.org/10.1016/j.nimb.2009.09.012

Clark, K. E., Hilton, R. G., West, A. J., Malhi, Y., Gröcke, D. R., Bryant, C. L., Ascough, P. L., Robles Caceres, A., New, M., 2013. New views on âoldâ carbon in the Amazon River: Insight from the source of organic carbon eroded from the Peruvian Andes. Geochemistry, Geophysics, Geosystems 14 (5), 1644–1659.
URL http://doi.wiley.com/10.1002/ggge.20122

Clift, P. D., Shimizu, N., Layne, G. D., Blusztajn, J. S., Gaedicke, C., Schluter, H. U., Clark, M. K., Amjad, S., 2001. Development of the Indus Fan and its significance for the erosional history of the Western Himalaya and Karakoram. Geological Society of America Bulletin 113 (8), 1039–1051.
URL http://gsabulletin.gsapubs.org/cgi/content/abstract/113/8/1039

Coutand, I., Whipp, D. M., Grujic, D., Bernet, M., Fellin, M. G., Bookhagen, B., Landry, K. R., Ghalley, S. K., Duncan, C., 2014. Geometry and kinematics of the Main Himalayan Thrust and Neogene crustal exhumation in the Bhutanese Himalaya derived from inversion of multithermochronologic data. Journal of Geophysical Research: Solid Earth 119 (2), 1446–1481.
URL http://dx.doi.org/10.1002/2013JB010891

Cracknell, A. P., Kanniah, K. D., Tan, K. P., Wang, L., 2013. Evaluation of MODIS gross primary productivity and land cover products for the humid tropics using oil palm trees in Peninsular Malaysia and Google Earth imagery. International Journal of Remote Sensing 34 (20), 7400–7423.
URL <GotoISI>://WOS:000322767600027

Craddock, W. H., Burbank, D. W., Bookhagen, B., Gabet, E. J., 2007. Bedrock channel geometry along an orographic rainfall gradient in the upper Marsyandi River valley in central Nepal. J. Geophys. Res. 112 (F3), F03007.
URL http://dx.doi.org/10.1029/2006JF000589

Craig, H., 1961. Isotopic Variations in Meteoric Waters. Science (New York, N.Y.) 133 (3465), 1702–1703.

Curray, J. R., Emmel, F. J., Moore, D. G., 2003. The Bengal Fan: Morphology, geometry, stratigraphy, history and processes. Marine and Petroleum Geology 19 (10), 1191–1223.
URL http://www.sciencedirect.com/science/article/pii/S0264817203000357

Dahal, R. K., Hasegawa, S., 2008. Representative rainfall thresholds for landslides in the Nepal Himalaya. Geomorphology 100 (3-4), 429–443.
URL http://www.sciencedirect.com/science/article/pii/S0169555X08000172

Dansgaard, W., 1964. Stable isotopes in precipitation. Tellus 16 (4), 436–468.

Dansgaard, W., Clausen, H. B., Gundestrup, N., Hammer, C. U., Johnsen, S. F., Kristinsdottir, P. M., Reeh, N., 1982. A new Greenland deep ice core. Science 218 (4579), 1273–1277.

DeCelles, P. G., Gehrels, G., Quade, J., LeReau, B., Spurlin, M., 2000. Tectonic Implications of U-Pb Zircon Ages of the Himalayan Orogenic Belt in Nepal. Science 288 (5465), 497–499.

DeWalle, D., Edwards, P., Swistock, B., Aravena, R., Drimmie, R., 1997. Seasonal Isotope Hydrology of three Appalachian Forest Catchments. Hydrological Processes 11, 1895–1906.

DiBiase, R. A., Whipple, K. X., 2011. The influence of erosion thresholds and runoff variability on the relationships among topography, climate, and erosion rate. Journal of Geophysical Research 116 (F4), F04036.
URL http://doi.wiley.com/10.1029/2011JF002095

DiBiase, R. a., Whipple, K. X., Heimsath, A. M., Ouimet, W. B., 2010. Landscape form and millennial erosion rates in the San Gabriel Mountains, CA. Earth and Planetary Science Letters 289 (1-2), 134–144.
URL http://dx.doi.org/10.1016/j.epsl.2009.10.036

Dobremez, J., Shakya, P., 1975. Carte Ecologique du Népal. VI. Region BiratnagarâKanchenjunga 1: 250, 000. Documents De Cartographie Ecologique XVI (1), 33–46.
URL http://ecologie-alpine.ujf-grenoble.fr/articles/DCE_1975__16__33_0.pdf

Dunne, J., Elmore, D., Muzikar, P., 1999. Scaling factors for the rates of production of cosmogenic nuclides for geometric shielding and attenuation at depth on sloped surfaces. Geomorphology 27 (1-2), 3–11.
URL http://www.sciencedirect.com/science/article/pii/S0169555X98000865

Eglinton, T. I., Eglinton, G., 2008. Molecular proxies for paleoclimatology. Earth and Planetary Science Letters 275 (1-2), 1–16.
URL http://linkinghub.elsevier.com/retrieve/pii/S0012821X08004391

Ellehoj, M. D., Steen-Larsen, H. C., Johnsen, S. J., Madsen, M. B., 2013. Ice-vapor equilibrium fractionation factor of hydrogen and oxygen isotopes: Experimental investigations and implications for stable water isotope studies. Rapid Communications in Mass Spectrometry 27 (19), 2149–2158.
URL http://www.ncbi.nlm.nih.gov/pubmed/23996388

Ernst, N., Peterse, F., Breitenbach, S. F. M., Syiemlieh, H. J., Eglinton, T. I., 2013. Biomarkers record environmental changes along an altitudinal transect in the wettest place on Earth. Organic Geochemistry 60, 93–99.

Feakins, S. J., Sessions, A. L., 2010. Controls on the D/H ratios of plant leaf waxes in an arid ecosystem. Geochimica et Cosmochimica Acta 74 (7), 2128–2141.
URL http://dx.doi.org/10.1016/j.gca.2010.01.016

Ferrier, K. L., Huppert, K. L., Perron, J. T., 2013a. Climatic control of bedrock river incision. Nature 496 (7444), 206–209.
URL http://dx.doi.org/10.1038/nature11982

Ferrier, K. L., Taylor Perron, J., Mukhopadhyay, S., Rosener, M., Stock, J. D., Huppert, K. L., Slosberg, M., 2013b. Covariation of climate and long-term erosion rates across a steep rainfall gradient on the Hawaiian island of Kaua'i. Bulletin of the Geological Society of America 125 (7), 1146–1163.
URL http://gsabulletin.gsapubs.org/content/early/2013/02/21/B30726.1.abstract

Fisher, G. B., Amos, C. B., Bookhagen, B., Burbank, D. W., Godard, V., 2012. Channel widths, landslides, faults, and beyond: The new world order of high-spatial resolution Google Earth imagery in the study of earth surface processes. Geological Society of America Special Papers 492, 1–22.
URL http://specialpapers.gsapubs.org/content/492/1.abstract

Fisher, G. B., Bookhagen, B., Amos, C. B., 2013. Channel planform geometry and slopes from freely available high-spatial resolution imagery and DEM fusion: Implications for channel width scalings, erosion proxies, and fluvial signatures in tectonically active landscapes. Geomorphology 194 (0), 46–56.
URL http://dx.doi.org/10.1016/j.geomorph.2013.04.011

Fleitmann, D., Burns, S. J., Mudelsee, M., Neff, U., Kramers, J., Mangini, A., Matter, A., 2003. Holocene Forcing of the Indian Monsoon Recorded in a Stalagmite from Southern Oman. Science 300 (5626), 1737–1739.
URL http://www.sciencemag.org/cgi/doi/10.1126/science.1083130

Flint, J. J., 1974. Stream gradient as a function of order, magnitude, and discharge. Water Resources Research 10 (5), 969.

France-Lanord, C., Derry, L., 1997. Organic carbon burial forcing of the carbon cycle from Himalayan erosion. Nature 390 (6655), 65–67.

France-Lanord, C., Derry, L. A., 1994. d13C of organic carbon in the Bengal Fan: Source evolution and transport of C3 and C4 plant carbon to marine sediments. Geochimica et Cosmochimica Acta 58 (21), 4809–4814.
URL http://linkinghub.elsevier.com/retrieve/pii/0016703794902100

Freeman, K., Colarusso, L., 2001. Molecular and isotopic records of C4 grassland expansion in the late miocene. Geochimica et Cosmochimica Acta 65 (9), 1439–1454.
URL http://linkinghub.elsevier.com/retrieve/pii/S0016703700005731

Friedman, I., Machta, L., Soller, R., 1962. Water-vapor exchange between a water droplet and its environment. Journal of Geophysical Research 67 (7), 2761–2766.
URL http://dx.doi.org/10.1029/JZ067i007p02761

Gadgil, S., 2003. The Indian Monsoon and its Variability. Annual Review of Earth and Planetary Sciences 31 (1), 429–467.
URL http://www.annualreviews.org/doi/abs/10.1146/annurev.earth.31.100901.141251

Galy, V., Eglinton, T., France-Lanord, C., Sylva, S., 2011. The provenance of vegetation and environmental signatures encoded in vascular plant biomarkers carried by the Ganges-Brahmaputra rivers. Earth and Planetary Science Letters 304 (1-2), 1–12.
URL http://dx.doi.org/10.1016/j.epsl.2011.02.003

Galy, V., France-Lanord, C., Beyssac, O., Faure, P., Kudrass, H., Palhol, F., nov 2007. Efficient organic carbon burial in the Bengal fan sustained by the Himalayan erosional system. Nature 450 (November), 407–410.
URL http://www.ncbi.nlm.nih.gov/pubmed/18004382

Galy, V., Peucker-Ehrenbrink, B., Eglinton, T., 2015. Global carbon export from the terrestrial biosphere controlled by erosion. Nature 521 (7551), 204–207.
URL http://www.ncbi.nlm.nih.gov/pubmed/25971513

Garcin, Y., Schwab, V. F., Gleixner, G., Kahmen, A., Todou, G., Séné, O., Onana, J.-M., Achoundong, G., Sachse, D., 2012. Hydrogen isotope ratios of lacustrine sedimentary n-alkanes as proxies of tropical African hydrology: Insights from a calibration transect across Cameroon. Geochimica et Cosmochimica Acta 79, 106–126.
URL http://linkinghub.elsevier.com/retrieve/pii/S0016703711007149

Garzione, C. N., Quade, J., DeCelles, P. G., English, N. B., nov 2000. Predicting paleoelevation of Tibet and the Himalaya from ??18O vs. altitude gradients in meteoric water across the Nepal Himalaya. Earth and Planetary Science Letters 183 (1-2), 215–229.
URL http://linkinghub.elsevier.com/retrieve/pii/S0012821X00002521http://www.sciencedirect.com/science/article/pii/S0012821X00002521

Glotzbach, C., R??ttjer, M., Hampel, A., Hetzel, R., Kubik, P. W., 2013. Quantifying the impact of former glaciation on catchment-wide denudation rates derived from cosmogenic 10Be. Terra Nova.
URL http://dx.doi.org/10.1111/ter.12085

Godard, V., Bourles, D. L., Spinabella, F., Burbank, D. W., Bookhagen, B., Fisher, G. B., Moulin, A., Leanni, L., 2014. Dominance of tectonics over climate in Himalayan denudation. Geology 42 (3), 243–246.
URL http://geology.gsapubs.org/cgi/doi/10.1130/G35342.1

Godard, V., Burbank, D. W., Bourlès, D. L., Bookhagen, B., Braucher, R., Fisher, G. B., 2012. Impact of glacial erosion on ¹⁰ Be concentrations in fluvial sediments of the Marsyandi catchment, central Nepal. Journal of Geophysical Research 117 (F3), F03013.
URL http://doi.wiley.com/10.1029/2011JF002230

Godard, V., Cattin, R., Lavé, J., 2004. Numerical modeling of mountain building: Interplay between erosion law and crustal rheology. Geophysical Research Letters 31 (23), n/a–n/a.
URL http://doi.wiley.com/10.1029/2004GL021006

Gonfiantini, R., Roche, M. A., Olivry, J. C., Fontes, J. C., Zuppi, G. M., 2001. The altitude effect on the isotopic composition of tropical rains. Chemical Geology 181 (1-4), 147–167.

Goñi, M. a., Moore, E., Kurtz, A., Portier, E., Alleau, Y., Merrell, D., 2014. Organic matter compositions and loadings in soils and sediments along the Fly River, Papua New Guinea. Geochimica et Cosmochimica Acta 140, 275–296.

Goni, M. a., Ruttenberg, K. C., 1997. Sources and contribution of terrigenous organic carbon to surface sediments in the Gulf of Mexico. Nature 389 (SEPTEMBER), 275–278.
URL http://search.ebscohost.com/login.aspx?direct=true&db=a9h&AN=9709281168&site=ehost-live

Goñi, M. A., Yunker, M. B., MacDonald, R. W., Eglinton, T. I., 2000. Distribution and sources of organic biomarkers in arctic sediments from the Mackenzie River and Beaufort Shelf. Marine Chemistry 71 (1-2), 23–51.
URL http://www.sciencedirect.com/science/article/pii/S0304420300000372

Goodbred, S. L., Kuehl, S. A., 2000. Enormous Ganges-Brahmaputra sediment discharge during strengthened early Holocene monsoon. Geology 28 (12), 1083–1086.
URL http://journals.allenpress.com/jrnlserv/?request=get-abstract&issn=0091-7613&volume=28&page=1083

Granger, D. E., Kirchner, J. W., Finkel, R., 1996. Spatially Averaged Long-Term Erosion Rates Measured from in Situ-Produced Cosmogenic Nuclides in Alluvial Sediment. The Journal of Geology 104 (3), 249–257.
URL http://www.jstor.org/stable/30068190

Granger, D. E., Lifton, N. A., Willenbring, J. K., 2013. A cosmic trip: 25 years of cosmogenic nuclides in geology. Geological Society of America Bulletin 125 (9-10), 1379–1402.
URL http://gsabulletin.gsapubs.org/cgi/doi/10.1130/B30774.1

Grujic, D., Warren, C. J., Wooden, J. L., 2011. Rapid synconvergent exhumation of Miocene-aged lower orogenic crust in the eastern Himalaya. Lithosphere 3 (5), 346–366.
URL http://lithosphere.gsapubs.org/lookup/doi/10.1130/L154.1

Hales, T. C., Roering, J. J., 2005. Climate-controlled variations in scree production, Southern Alps, New Zealand. Geology 33 (9), 701–704.

Hall, D. K., Riggs, G. A., Salomonson, V. V., DiGirolamo, N. E., Bayr, K. J., 2002. MODIS snow-cover products. Remote Sensing of Environment 83 (1-2), 181–194.

Hatten, J. A., Goñi, M. A., Wheatcroft, R. A., 2012. Chemical characteristics of particulate organic matter from a small, mountainous river system in the Oregon Coast Range, USA. Biogeochemistry 107 (1-3), 43–66.

Hayes, J. M., 2001. Fractionation of Carbon and Hydrogen Isotopes in Biosynthetic Processes. Reviews in Mineralogy and Geochemistry 43 (1), 225–277.
URL http://rimg.geoscienceworld.org/cgi/doi/10.2138/gsrmg.43.1.225

Hedges, J. I., Clark, W. A., Quay, P. D., Richey, J. E., Devol, A. H., Santos, U. d. M., 1986. Compositions and fluxes of particlate organic material in the Amazon River.

Hedges, J. I., Cowie, G. L., Richey, J. E., Quay, P. D., Benner, R., Strom, M., Forsberg, B. R., 1994. Origins and processing of organic matter in the Amazon River as indicated by carbohydrates and amino acids. Limnology and Oceanography 39 (4), 743–761.

Hedges, J. I., Mayorga, E., Tsamakis, E., McClain, M. E., Aufdenkampe, A., Quay, P., Richey, J. E., Benner, R., Opsahl, S., Black, B., 2000. Organic matter in Bolivian tributaries of the Amazon River: A comparison to the lower mainstream. Limnology and Oceanography 45 (7), 1449–1466.

Hendy, C. H., 1971. The isotopic geochemistry of speleothems-I. The calculation of the effects of different modes of formation on the isotopic composition of speleothems and their applicability as palaeoclimatic indicators. Geochimica et Cosmochimica Acta 35 (8), 801–824.

Hendy, C. H., Wilson, a. T., 1968. Palaeoclimatic Data from Speleothems. Nature 219 (5149), 48–51.

Herman, F., Copeland, P., Avouac, J.-P., Bollinger, L., Mahéo, G., Le Fort, P., Rai, S., Foster, D., Pêcher, A., Stüwe, K., Henry, P., 2010. Exhumation, crustal deformation, and thermal structure of the Nepal Himalaya derived from the inversion of thermochronological and thermobarometric data and modeling of the topography. Journal of Geophysical Research 115 (B6), B06407.
URL http://doi.wiley.com/10.1029/2008JB006126

Herman, F., Seward, D., Valla, P. G., Carter, A., Kohn, B., Willett, S. D., Ehlers, T. A., 2013. Worldwide acceleration of mountain erosion under a cooling climate. Nature 504 (7480), 423–426.
URL http://dx.doi.org/10.1038/nature12877

Hilton, R. G., Galy, A., Hovius, N., Kao, S.-J., Horng, M.-J., Chen, H., 2012. Climatic and geomorphic controls on the erosion of terrestrial biomass from subtropical mountain forest. Global Biogeochemical Cycles 26 (3), n/a–n/a.
URL http://doi.wiley.com/10.1029/2012GB004314

Hilton, R. G., Galy, A., West, a. J., Hovius, N., Roberts, G. G., 2013. Geomorphic control on the d15N of mountain forests. Biogeosciences 10 (3), 1693–1705.
URL http://www.biogeosciences.net/10/1693/2013/

Hirschmiller, J., Grujic, D., Bookhagen, B., Coutand, I., Huyghe, P., Mugnier, J.-L., Ojha, T., 2014. What controls the growth of the Himalayan foreland fold-and-thrust belt? Geology 42 (3), 247–250.
URL http://geology.gsapubs.org/cgi/doi/10.1130/G35057.1

Hodges, K. V., Hurtado, J. M., Whipple, K. X., 2001. Southward extrusion of Tibetan crust and its effect on Himalayan tectonics. Tectonics 20 (6), 799–809.
URL http://dx.doi.org/10.1029/2001TC001281

Hodges, K. V., Wobus, C., Ruhl, K., Schildgen, T., Whipple, K., 2004. Quaternary deformation, river steepening, and heavy precipitation at the front of the Higher Himalayan ranges. Earth and Planetary Science Letters 220 (3-4), 379–389.
URL http://www.sciencedirect.com/science/article/pii/S0012821X04000639

Hoffman, P. F., Kaufman, A. J., Halverson, G. P., Schrag, D. P., 1998. A Neoproterozoic snowball earth. Science 281 (5381), 1342–1346.

Hoffmann, B., Kahmen, A., Cernusak, L. a., Arndt, S. K., Sachse, D., 2013. Abundance and distribution of leaf wax n-alkanes in leaves of acacia and eucalyptus trees along a strong humidity gradient in Northern Australia. Organic Geochemistry 62, 62–67.

Hoffmann, B., Olen, S. M., Bookhagen, B., Feakins, S. J., Adhikari, D. P., Sachse, D., 2016. Ecologic, climatic and geomorphic drivers of plant organic matter transport in the trans-Himalayan Arun River catchment, E Nepal. Earth and Planetary Science Letters.

Hou, J., D'Andrea, W. J., MacDonald, D., Huang, Y., 2007. Hydrogen isotopic variability in leaf waxes among terrestrial and aquatic plants around Blood Pond, Massachusetts (USA). Organic Geochemistry 38 (6), 977–984.

Houghton, J. T., Jenkins, G. J., Ephraums, J. J., 1990. Climate Change: The IPCC Scientific Assessment, Report prepared for Intergovernmental Panel on Climate Change by Working Group I.

Hren, M. T., Bookhagen, B., Blisniuk, P. M., Booth, A. L., Chamberlain, C. P., 2009. delta O-18 and delta D of streamwaters across the Himalaya and Tibetan Plateau: Implications for moisture sources and paleoelevation reconstructions. Earth And Planetary Science Letters 288 (1-2), 20–32.

Huang, Y., Shuman, B., Wang, Y., Webb, T., 2004. Hydrogen isotope ratios of individual lipids in lake sediments as novel tracers of climatic and environmental change: A surface sediment test. Journal of Paleolimnology 31 (3), 363–375.

Huffman, G. J., Bolvin, D. T., Nelkin, E. J., Wolff, D. B., Adler, R. F., Gu, G., Hong, Y., Bowman, K. P., Stocker, E. F., feb 2007. The TRMM Multisatellite Precipitation Analysis (TMPA): Quasi-Global, Multiyear, Combined-Sensor Precipitation Estimates at Fine Scales. Journal of Hydrometeorology 8 (1), 38–55.
URL http://journals.ametsoc.org/doi/abs/10.1175/JHM560.1

Huntington, K. W., Blythe, A. E., Hodges, K. V., 2006. Climate change and Late Pliocene acceleration of erosion in the Himalaya. Earth and Planetary Science Letters 252 (1-2), 107–118.
URL http://www.sciencedirect.com/science/article/pii/S0012821X06006856

Jarvis, A., Reuter, H. I., Nelson, A., 2008. Hole-filled SRTM for the globe Version 4, available from the CGIAR-CSI SRTM 90m Database (http://srtm.csi.cgiar.org).

Jessup, M. J., Newell, D. L., Cottle, J. M., Berger, A. L., Spotila, J. A., 2008. Orogen-parallel extension and exhumation enhanced by denudation in the trans-Himalayan Arun River gorge, Ama Drime Massif, Tibet-Nepal. Geology 36 (7), 587.
URL http://geology.gsapubs.org/cgi/doi/10.1130/G24722A.1

Jia, G., Wei, K., Chen, F., Peng, P., 2008. Soil n-alkane δD vs. altitude gradients along Mount Gongga, China. Geochimica et Cosmochimica Acta 72 (21), 5165–5174.
URL http://linkinghub.elsevier.com/retrieve/pii/S0016703708004912

Johansson, M., Holmberg., K. E., 1969. Separation of heavy water in phase equilibria involving pure water or salt-water systems. Acta Chemica Scandinavica 23 (3), 765–781.

Johnsen, S., Dahl-jensen, D., Dansgaard, W., Gundestrup, N. S., 1995. Greenland palaeotemperatures derived from GRIP bore hole temperature and ice core isotope profiles.

Kahmen, A., Hoffmann, B., Schefuß, E., Arndt, S. K., Cernusak, L. A., West, J. B., Sachse, D., 2013a. Leaf water deuterium enrichment shapes leaf wax n-alkane δD values of angiosperm plants II: Observational evidence and global implications. Geochimica et Cosmochimica Acta 111, 50–63.
URL http://linkinghub.elsevier.com/retrieve/pii/S0016703712005017

Kahmen, A., Schefuß, E., Sachse, D., 2013b. Leaf water deuterium enrichment shapes leaf wax n-alkane δD values of angiosperm plants I: Experimental evidence and mechanistic insights. Geochimica et Cosmochimica Acta 111, 39–49.
URL http://linkinghub.elsevier.com/retrieve/pii/S0016703712005005

Kao, S.-J., Liu, K.-K., 1996. Particulate organic carbon export from a subtropical mountainous river (Lanyang Hsi) in Taiwan. Limnology and Oceanography 41, 1749–1757.

Karim, A., Veizer, J., 2002. Water balance of the Indus River Basin and moisture source in the Karakoram and western Himalayas: Implications from hydrogen and oxygen isotopes in river water. Journal of Geophysical Research: Atmospheres 107, 1–12.

Kasting, J. F., Ackerman, T. P., 1986. Climatic Consequences of Very High Carbon Dioxide Levels in the Earth's Early Atmosphere. Science (New York, N.Y.) 234 (4782), 1383–1385.

Kim, J. H., Zell, C., Moreira-Turcq, P., Pérez, M. a. P., Abril, G., Mortillaro, J. M., Weijers, J. W. H., Meziane, T., Sinninghe Damsté, J. S., 2012. Tracing soil organic carbon in the lower Amazon River and its tributaries using GDGT distributions and bulk organic matter properties. Geochimica et Cosmochimica Acta 90, 163–180.

Kirby, E., Whipple, K., 2001. Quantifying differential rock-uplift rates via stream profile analysis. Geology 29 (5), 415.
URL http://geology.gsapubs.org/cgi/doi/10.1130/0091-7613(2001)029<0415:QDRURV>2.0.CO;2

Knighton, a. D., 1999. Downstream variation in stream power. Geomorphology 29 (3-4), 293–306.
URL http://www.sciencedirect.com/science/article/pii/S0169555X9900015X

Korschinek, G., Bergmaier, A., Faestermann, T., Gerstmann, U. C., Knie, K., Rugel, G., Wallner, A., Dillmann, I., Dollinger, G., von Gostomski, C. L., Kossert, K., Maiti, M., Poutivtsev, M., Remmert, A., 2010. A new value for the half-life of 10Be by Heavy-Ion Elastic Recoil Detection and liquid scintillation counting. Nuclear Instruments and Methods in Physics Research, Section B: Beam Interactions with Materials and Atoms 268 (2), 187–191.
URL http://dx.doi.org/10.1016/j.nimb.2009.09.020

Kotlia, B. S., Ahmad, S. M., Zhao, J. X., Raza, W., Collerson, K. D., Joshi, L. M., Sanwal, J., 2012. Climatic fluctuations during the LIA and post-LIA in the Kumaun Lesser Himalaya, India: Evidence from a 400 y old stalagmite record. Quaternary International 263, 129–138.
URL http://dx.doi.org/10.1016/j.quaint.2012.01.025

Kotlia, B. S., Singh, A. K., Joshi, L. M., Dhaila, B. S., 2015. Precipitation variability in the Indian Central Himalaya during last ca. 4,000 years inferred from a speleothem record: Impact of Indian Summer Monsoon (ISM) and Westerlies. Quaternary International 371, 244–253.
URL http://www.sciencedirect.com/science/article/pii/S1040618214008313

Lague, D., 2014. The stream power river incision model: evidence, theory and beyond. Earth Surface Processes and Landforms 39 (1), 38–61.
URL http://doi.wiley.com/10.1002/esp.3462

Lague, D., Hovius, N., Davy, P., 2005. Discharge, discharge variability, and the bedrock channel profile. Journal of Geophysical Research: Earth Surface 110 (4), 1–17.
URL http://dx.doi.org/10.1029/2004JF000259

Lal, D., 1991. Cosmic ray labeling of erosion surfaces: in situ nuclide production rates and erosion models. Earth and Planetary Science Letters 104 (2-4), 424–439.
URL http://www.sciencedirect.com/science/article/pii/0012821X9190220C

Lang, T. J., Barros, A. P., 2004. Winter Storms in the Central Himalayas. Journal of the Meteorological Society of Japan 82 (3), 829–844.

Lavé, J., Avouac, J. P., 2001. Fluvial incision and tectonic uplift across the Himalayas of central Nepal. Journal of Geophysical Research 106 (B11), 26561.
URL http://dx.doi.org/10.1029/2001JB000359

Lechler, A. R., Niemi, N. a., jan 2011. Controls on the spatial variability of modern meteoric δ 18O: Empirical constraints from the western U.S. and east Asia and implications for stable isotope studies. American Journal of Science 311 (8), 664–700.
URL http://www.ajsonline.org/cgi/doi/10.2475/08.2011.02

Li, Y., Wang, N., Zhou, X., Zhang, C., Wang, Y., 2014. Synchronous or asynchronous Holocene Indian and East Asian summer monsoon evolution: A synthesis on Holocene Asian summer monsoon simulations, records and modern monsoon indices. Global and Planetary Change 116, 30–40.

Liang, F., Brook, G. A., Kotlia, B. S., Railsback, L. B., Hardt, B., Cheng, H., Edwards, R. L., Kandasamy, S., 2015. Panigarh cave stalagmite evidence of climate change in the Indian Central Himalaya since AD 1256: Monsoon breaks and winter southern jet depressions. Quaternary Science Reviews 124 (SEPTEMBER), 145–161.
URL http://linkinghub.elsevier.com/retrieve/pii/S0277379115300561

Lilliefors, H. W., 1969. On the Kolmogorov-Smirnov Test for the Exponential Distribution with Mean Unknown. Journal of the American Statistical Association 64 (325), 387–389.

Lister, G. S., Kelts, K., Zao, C. K., Yu, J.-Q., Niessen, F., 1991. Lake Qinghai, China: closed-basin like levels and the oxygen isotope record for ostracoda since the latest Pleistocene. Palaeogeography, Palaeoclimatology, Palaeoecology 84 (1-4), 141–162.

Liu, W., Yang, H., 2008. Multiple controls for the variability of hydrogen isotopic compositions in higher plant n-alkanes from modern ecosystems. Global Change Biology 14 (9), 2166–2177.

Louter, A. S., Koerts, J., 1970. On the Kuiper test for normality with mean and variance unknown. Statistica Neerlandica 24 (2), 83–87.
URL http://doi.wiley.com/10.1111/j.1467-9574.1970.tb00110.x

Lupker, M., Blard, P. H., Lavé, J., France-Lanord, C., Leanni, L., Puchol, N., Charreau, J., Bourlès, D., 2012. 10Be-derived Himalayan denudation rates and sediment budgets in the Ganga basin. Earth and Planetary Science Letters 333-334 (0), 146–156.
URL http://www.sciencedirect.com/science/article/pii/S0012821X12001872

Malik, N., Bookhagen, B., Mucha, P. J., 2016. Spatiotemporal patterns and trends of Indian monsoonal rainfall extremes. Geophysical Research Letters, 1–22.

McPhillips, D., Bierman, P. R., Rood, D. H., 2014. Millennial-scale record of landslides in the Andes consistent with earthquake trigger. Nature Geosci 7 (12), 925–930.
URL http://dx.doi.org/10.1038/ngeo2278

Meier, K., Hiltner, E., 1993. Deformation and metamorphism within the Main Central Thrust zone, Arun Tectonic Window, eastern Nepal. Geological Society, London, Special Publications 74 (1), 511–523.
URL http://sp.lyellcollection.org/cgi/doi/10.1144/GSL.SP.1993.074.01.34

Merlivat, L., Nief, G., 1967. Fractionnement isotopique lors des changements dâétat solide-vapeur et liquide-vapeur de l'eau à des températures inférieures à 0Â°C. Tellus 19 (1), 122–127.
URL http://tellusa.net/index.php/tellusa/article/view/97562://publication/doi/10.1111/j.2153-3490.1967.tb01465.x

Milliman, J. D., Syvitski, J. P. M., 1992. Geomorphic/Tectonic Control of Sediment Discharge to the Ocean: The Importance of Small Mountainous Rivers. The Journal of Geology 100 (5), 525–544.

Molnar, P., England, P., 1990. Late Cenozoic uplift of mountain ranges and global climate change: chicken or egg? , Published online: 05 July 1990; | doi:10.1038/346029a0 346 (6279), 29–34.
URL http://www.nature.com/nature/journal/v346/n6279/abs/346029a0.html

Molnar, P., England, P., Martinod, J., 1993. Mantle dynamics, uplift of the Tibetan Plateau, and the Indian monsoon. Reviews of Geophysics 31 (4), 357–396.

Molnar, P., Tapponnier, P., 1975. Cenozoic Tectonics of Asia : Effects of a Continental Collision. Science 189 (4201), 419–426.
URL http://www.sciencemag.org/content/189/4201/419.short

Montgomery, D. R., Stolar, D. B., 2006. Reconsidering Himalayan river anticlines. Geomorphology 82 (1-2), 4–15.

Mooley, D. a., Parthasarathy, B., 1984. Fluctuations in All-India summer monsoon rainfall during 1871-1978. Climatic Change 6 (3), 287–301.

Moon, S., Page Chamberlain, C., Blisniuk, K., Levine, N., Rood, D. H., Hilley, G. E., 2011. Climatic control of denudation in the deglaciated landscape of the Washington Cascades. Nature Geoscience 4 (7), 469–473.
URL http://www.nature.com/doifinder/10.1038/ngeo1159

Mu, Q., Zhao, M., Running, S. W., 2011. Improvements to a MODIS global terrestrial evapotranspiration algorithm. Remote Sensing of Environment 115 (8), 1781–1800.
URL http://dx.doi.org/10.1016/j.rse.2011.02.019

Niemi, N. a., Oskin, M., Burbank, D. W., Heimsath, A. M., Gabet, E. J., 2005. Effects of bedrock landslides on cosmogenically determined erosion rates. Earth and Planetary Science Letters 237 (3-4), 480–498.
URL http://www.sciencedirect.com/science/article/pii/S0012821X0500467X

Nishiizumi, K., Imamura, M., Caffee, M. W., Southon, J. R., Finkel, R. C., McAninch, J., 2007. Absolute calibration of 10Be AMS standards. Nuclear Instruments and Methods in Physics Research, Section B: Beam Interactions with Materials and Atoms 258 (2), 403–413.
URL http://www.sciencedirect.com/science/article/pii/S0168583X07003850

Ohsawa, M., Shakya, P. R., Numata, M., May, N., 1986. Distribution and Succession of West Himalayan Forest Types in the Eastern Part of the Nepal Himalaya. Mountain Research and Development 6 (2), 143–157.

Olen, S. M., Bookhagen, B., Hoffmann, B., Sachse, D., Adhikari, D. P., Strecker, M. R., 2015. Understanding erosion rates in the Himalayan orogen: A case study from the Arun Valley. Journal of Geophysical Research: Earth Surface 120, 2080–2102.
URL http://doi.wiley.com/10.1002/2014JF003410

Oshun, J., Dietrich, W. E., Dawson, T. E., Fung, I., 2016. Water resources research. Water Resources Research 52.

Ouimet, W. B., Whipple, K. X., Granger, D. E., 2009. Beyond threshold hillslopes: Channel adjustment to base-level fall in tectonically active mountain ranges. Geology 37 (7), 579–582.
URL http://geology.gsapubs.org/cgi/doi/10.1130/G30013A.1

Pagani, M., Pedentchouk, N., Huber, M., Sluijs, A., Schouten, S., Brinkhuis, H., Sinninghe Damsté, J. S., Dickens, G. R., Expedition 302 Scientists, Backman, J., Clemens, S., Cronin, T., Eynaud, F., Gattacceca, J., Jakobsson, M., Jordan, R., Kaminski, M., King, J., Koc, N., Martinez, N. C., McInroy, D., Moore Jr, T. C., O'Regan, M., Onodera, J., Pälike, H., Rea, B., Rio, D., Sakamoto, T., Smith, D. C., St John, K. E. K., Suto, I., Suzuki, N., Takahashi, K., Watanabe, M., Yamamoto, M., 2006. Arctic hydrology during global warming at the Palaeocene/Eocene thermal maximum. Nature 442 (7103), 671–675.
URL http://www.nature.com/doifinder/10.1038/nature05043

Pande, K., Padia, J. T., Ramesh, R., Sharma, K., 2000. Stable isotope systematics of surface water bodies in the Himalayan and Trans-Himalayan (Kashmir) region. Proc. Indian Acad. Sci. (Earth Planet. Sci.) 109 (1), 109–115.

Parthasarathy, B., Rupa Kumar, K., Kothawale, D. R., 1992. Indian summer monsoon rainfall indices: 1871-1990. Meteorological Magazine 121 (1441), 174–186.

Perron, J. T., Royden, L., 2013. An integral approach to bedrock river profile analysis. Earth Surface Processes and Landforms 38 (6), 570–576.
URL http://www.scopus.com/inward/record.url?eid=2-s2.0-84876481926&partnerID=tZOtx3y1

Peterse, F., van der Meer, M. T. J., Schouten, S., Jia, G., Ossebaar, J., Blokker, J., Sinninghe Damsté, J. S., 2009. Assessment of soil n-alkane δD and branched tetraether membrane lipid distributions as tools for paleoelevation reconstruction. Biogeosciences Discussions 6 (5), 2799–2807.

Petit, R. J., Raynaud, D., Basile, I., Chappellaz, J., Ritz, C., Delmotte, M., Legrand, M., Lorius, C., Pe, L., 1999. Climate and atmospheric history of the past 420,000 years from the Vostok ice core, Antarctica. Nature 399, 429–413.

Poage, M. A., Chamberlain, C. P., 2001. EMPIRICAL RELATIONSHIPS BETWEEN ELEVATION AND THE STABLE ISOTOPE COMPOSITION OF PRECIPITATION AND SURFACE WATERS: CONSIDERATIONS FOR STUDIES OF PALEOELEVATION CHANGE. American Journal of Science JANUARY 301 (January), 1–15.

Polissar, P. J., Freeman, K. H., 2010. Effects of aridity and vegetation on plant-wax δD in modern lake sediments. Geochimica et Cosmochimica Acta 74 (20), 5785–5797.
URL http://linkinghub.elsevier.com/retrieve/pii/S0016703710003583

Ponton, C., Giosan, L., Eglinton, T. I., Fuller, D. Q., Johnson, J. E., Kumar, P., Collett, T. S., 2012. Holocene aridification of India. Geophysical Research Letters 39 (3), 1–6.

Ponton, C., West, A. J., Feakins, S. J., Galy, V., aug 2014. Leaf wax biomarkers in transit record river catchment composition. Geophysical Research Letters 41 (18), 6420–6427.
URL http://doi.wiley.com/10.1002/2014GL061328

Prins, M. A., Postma, G., 2000. Effects of climate , sea level , and tectonics unraveled for last deglaciation turbidite records of the Arabian Sea. Geology 28 (4), 375–378.
URL http://geology.gsapubs.org/content/28/4/375.abstract

Puchol, N., Lavé, J., Lupker, M., Blard, P.-H., Gallo, F., France-Lanord, C., 2014. Grain-size dependent concentration of cosmogenic 10Be and erosion dynamics in a landslide-dominated Himalayan watershed. Geomorphology 224 (0), 55–68.
URL http://www.sciencedirect.com/science/article/pii/S0169555X14003201

Quade, J., English, N., DeCelles, P. G., 2003. Silicate versus carbonate weathering in the Himalaya: A comparison of the Arun and Seti River watersheds. Chemical Geology 202 (3-4), 275–296.

Rach, O., Brauer, A., Wilkes, H., Sachse, D., jan 2014. Delayed hydrological response to Greenland cooling at the onset of the Younger Dryas in western Europe. Nature Geoscience 7 (2), 109–112.
URL http://www.nature.com/doifinder/10.1038/ngeo2053

Racoviteanu, A. E., Armstrong, R., Williams, M. W., 2013. Evaluation of an ice ablation model to estimate the contribution of melting glacier ice to annual discharge in the Nepal Himalaya. Water Resources Research 49 (January), 5117–5133.

Ramesh, R., Sarin, M., 1992. Stable isotope study of the Ganga (Ganges) river system. Journal of Hydrology 139 (December 1982), 49–62.

Raymo, M. E., Ruddiman, W. F., 1992. Tectonic forcing of late Cenozoic climate. Nature 359 (6391), 117–122.

Reiners, P. W., Ehlers, T. A., Mitchell, S. G., Montgomery, D. R., 2003. Coupled spatial variations in precipitation and long-term erosion rates across the Washington Cascades. Nature 426 (6967), 645–647.
URL http://dx.doi.org/10.1038/nature02111

Riebe, C. S., Kirchner, J. W., Finkel, R. C., 2004. Erosional and climatic effects on long-term chemical weathering rates in granitic landscapes spanning diverse climate regimes. Earth and Planetary Science Letters 224 (3-4), 547–562.
URL http://www.sciencedirect.com/science/article/pii/S0012821X04003401

Riebe, C. S., Kirchner, J. W., Granger, D. E., Finkel, R. C., 2001. Strong tectonic and weak climatic control of long-term chemical weathering rates. Geology 29 (6), 511–514.
URL http://geology.gsapubs.org/content/29/6/511.abstract

Roe, G. H., Montgomery, D. R., Hallet, B., 2002. Effects of orographic precipitation variations on the concavity of steady-state river profiles. Geology 30 (2), 143–146.
URL http://geology.gsapubs.org/content/30/2/143.abstract

Roe, G. H., Whipple, K. X., Fletcher, J. K., 2008. Feedbacks among climate, erosion, and tectonics in a critical wedge orogen. American Journal of Science 308 (7), 815–842.
URL http://www.ajsonline.org/cgi/doi/10.2475/07.2008.01

Rohrmann, A., Strecker, M. R., Bookhagen, B., Mulch, A., Sachse, D., Pingel, H., Alonso, R. N., Schildgen, T. F., Montero, C., 2014. Can stable isotopes ride out the storms? The role of convection for water isotopes in models, records, and paleoaltimetry studies in the central Andes. Earth and Planetary Science Letters 407, 187–195.
URL http://linkinghub.elsevier.com/retrieve/pii/S0012821X14005767

Rowley, D. B., 2007. Stable Isotope-Based Paleoaltimetry: Theory and Validation. Reviews in Mineralogy and Geochemistry 66 (1), 23–52.
URL http://rimg.geoscienceworld.org/cgi/doi/10.2138/rmg.2007.66.2

Rowley, D. B., Garzione, C. N., 2007. Stable Isotope-Based Paleoaltimetry. Annual Review of Earth and Planetary Sciences 35 (1), 463–508.
URL http://www.annualreviews.org/doi/abs/10.1146/annurev.earth.35.031306.140155

Rowley, D. B., Pierrehumbert, R. T., Currie, B. S., 2001. A new approach to stable isotope-based paleoaltimetry: implications for paleoaltimetra and paleohypsometry of the High Himalaya since the Late Miocene. Earth and Planetary Science Letters 5836 (2001), 1–17.

Royden, L., Taylor Perron, J., 2013. Solutions of the stream power equation and application to the evolution of river longitudinal profiles. Journal of Geophysical Research: Earth Surface 118 (2), 497–518.
URL http://doi.wiley.com/10.1002/jgrf.20031

Rozanski, K., Araguás-Araguás, L., Gonfiantini, R., 1993. Isotopic patterns in modern global precipitation. Climate change in continental isotopic records (JANUARY), 1–36.
URL http://www.agu.org/books/gm/v078/GM078p0001/GM078p0001.shtml

Running, S. W., Nemani, R. R., Heinsch, F. A., Zhao, M., Reeves, M., Hashimoto, H., 2004. A Continuous Satellite-Derived Measure of Global Terrestrial Primary Production. BioScience 54 (6), 547.

Sachse, D., Radke, J., Gleixner, G., 2004. Hydrogen isotope ratios of recent lacustrine sedimentary n-alkanes record modern climate variability. Geochimica et Cosmochimica Acta 68 (23), 4877–4889.
URL http://linkinghub.elsevier.com/retrieve/pii/S0016703704004417

Sachse, D., Radke, J., Gleixner, G., 2006. dD values of individual n-alkanes from terrestrial plants along a climatic gradient - Implications for the sedimentary biomarker record. Organic Geochemistry 37 (4), 469–483.

Safran, E. B., Bierman, P. R., Aalto, R., Dunne, T., Whipple, K. X., Caffee, M., 2005. Erosion rates driven by channel network incision in the Bolivian Andes. Earth Surface Processes and Landforms 30 (8), 1007–1024.
URL http://doi.wiley.com/10.1002/esp.1259

Sanwal, J., Kotlia, B. S., Rajendran, C., Ahmad, S. M., Rajendran, K., Sandiford, M., 2013. Climatic variability in Central Indian Himalaya during the last ∼1800 years: Evidence from a high resolution speleothem record. Quaternary International 304, 183–192.
URL http://dx.doi.org/10.1016/j.quaint.2013.03.029

Sarkar, S., Prasad, S., Wilkes, H., Riedel, N., Stebich, M., Basavaiah, N., Sachse, D., 2015. Monsoon source shifts during the drying mid-Holocene: Biomarker isotope based evidence from the core âmonsoon zoneâ (CMZ) of India. Quaternary Science Reviews 123 (December), 144–157.
URL http://www.sciencedirect.com/science/article/pii/S0277379115300299

Schäfer, J., Blanc, G., Lapaquellerie, Y., Maillet, N., Maneux, E., Etcheber, H., 2002. Ten-year observation of the Gironde tributary fluvial system: fluxes of suspended matter, particulate organic carbon and cadmium. Marine Chemistry 79 (3-4), 229–242.

Schefuß, E., Kuhlmann, H., Mollenhauer, G., Prange, M., Pätzold, J., 2011. Forcing of wet phases in southeast Africa over the past 17,000 years. Nature 480 (7378), 509–512.
URL http://www.nature.com/doifinder/10.1038/nature10685

Schefuß, E., Ratmeyer, V., Stuut, J.-B. W., Jansen, J., Sinninghe Damsté, J. S., 2003. Carbon isotope analyses of n-alkanes in dust from the lower atmosphere over the central eastern Atlantic. Geochimica et Cosmochimica Acta 67 (10), 1757–1767.
URL http://linkinghub.elsevier.com/retrieve/pii/S001670370201414X

Schelling, D., 1992. The tectonostratigraphy and structure of the eastern Nepal Himalaya. Tectonics 11 (5), 925–943.
URL http://onlinelibrary.wiley.com/doi/10.1029/92TC00213/abstract

Scherler, D., Bookhagen, B., Strecker, M. R., 2011. Spatially variable response of Himalayan glaciers to climate change affected by debris cover. Nature Geoscience 4 (3), 156–159.
URL http://dx.doi.org/10.1038/ngeo1068

Scherler, D., Bookhagen, B., Strecker, M. R., 2014. Tectonic control on 10Be-derived erosion rates in the Garhwal Himalaya, India. Journal of Geophysical Research: Earth Surface 119 (2), 83–105.
URL http://doi.wiley.com/10.1002/2013JF002955

Schlünz, B., Schneider, R. R., 2000. Transport of terrestrial organic carbon to the oceans by rivers: re-estimating flux and burial rates. International Journal of Earth Sciences 88 (4), 599–606.

Schwanghart, W., Kuhn, N. J., 2010. TopoToolbox: A set of Matlab functions for topographic analysis. Environmental Modelling and Software 25 (6), 770–781.
URL http://dx.doi.org/10.1016/j.envsoft.2009.12.002

Schwanghart, W., Scherler, D., 2013. Short Communication: TopoToolbox 2 â an efficient and user-friendly tool for Earth surface sciences. Earth Surface Dynamics Discussions 1 (1), 261–275.
URL http://www.earth-surf-dynam-discuss.net/1/261/2013/

Schwark, L., Zink, K., Lechterbeck, J., 2002. Reconstruction of postglacial to early Holocene vegetation history in terrestrial Central Europe via cuticular lipid biomarkers and pollen records from lake sediments. Geology 30 (5), 463–466.

Seeber, L., Gornitz, V., 1983. River profiles along the Himalayan arc as indicators of active tectonics. Tectonophysics 92 (4), 335–367.
URL http://www.sciencedirect.com/science/article/pii/0040195183902019

Sessions, A. L., Burgoyne, T. W., Schimmelmann, A., Hayes, J. M., sep 1999. Fractionation of hydrogen isotopes in lipid biosynthesis. Organic Geochemistry 30 (9), 1193–1200.
URL http://linkinghub.elsevier.com/retrieve/pii/S0146638099000947

Singh, J. S., Singh, S. P., 1987. Forest Vegetation of the Himalaya. The Botanical Review 53 (1), 80–192.

Sinha, A., Berkelhammer, M., Stott, L., Mudelsee, M., Cheng, H., Biswas, J., 2011. The leading mode of Indian Summer Monsoon precipitation variability during the last millennium. Geophysical Research Letters 38 (15), 2–6.

Sinha, A., Cannariato, K. G., Stott, L. D., Cheng, H., Edwards, R. L., Yadava, M. G., Ramesh, R., Singh, I. B., 2007. A 900-year (600 to 1500 A.D.) record of the Indian summer monsoon precipitation from the core monsoon zone of India. Geophysical Research Letters 34 (16), 1–5.

Sinha, A., Cannariato, K. G., Stott, L. D., Li, H.-C., You, C.-F., Cheng, H., Edwards, R. L., Singh, I. B., 2005. Variability of Southwest Indian summer monsoon precipitation during the Bølling-llerød. Geology 33 (10), 813.
URL http://geology.gsapubs.org/cgi/doi/10.1130/G21498.1

Sklar, L. S., Dietrich, W. E., 2004. A mechanistic model for river incision into bedrock by saltating bed load. Water Resources Research 40 (6), n/a–n/a.
URL http://doi.wiley.com/10.1029/2003WR002496

Sklar, L. S., Dietrich, W. E., Foufoula-Georgiou, E., Lashermes, B., Bellugi, D., 2006. Do gravel bed river size distributions record channel network structure? Water Resources Research 42 (6), n/a–n/a.
URL http://doi.wiley.com/10.1029/2006WR005035

Smith, F. a., Freeman, K. H., 2006. Influence of physiology and climate on dD of leaf wax n-alkanes from C3 and C4 grasses. Geochimica et Cosmochimica Acta 70 (5), 1172–1187.

Smith, J. C., Galy, A., Hovius, N., Tye, A. M., Turowski, J. M., Schleppi, P., 2013. Runoff-driven export of particulate organic carbon from soil in temperate forested uplands. Earth and Planetary Science Letters 365, 198–208.
URL http://dx.doi.org/10.1016/j.epsl.2013.01.027

Snyder, N. P., Whipple, K. X., Tucker, G. E., Merritts, D. J., 2000. Landscape response to tectonic forcing: Digital elevation model analysis of stream profiles in the Mendocino triple junction region, northern California. Geological Society of America Bulletin 112 (8), 1250–1263.
URL http://gsabulletin.gsapubs.org/cgi/doi/10.1130/0016-7606(2000)112<1250:LRTTFD>2.0.CO;2

Snyder, N. P., Whipple, K. X., Tucker, G. E., Merritts, D. J., 2003. Channel response to tectonic forcing: Field analysis of stream morphology and hydrology in the Mendocino triple junction region, northern California. Geomorphology 53 (1-2), 97–127.
URL http://www.sciencedirect.com/science/article/pii/S0169555X02003495

Soulsby, C., Malcolm, R., Helliwell, R., Ferrier, R. C., Jenkins, A., 2000. Isotope hydrology of the Allt a' Mharcaidh catchment, Cairngorms, Scotland: Implications for hydrological pathways and residence times. Hydrological Processes 14 (4), 747–762.

Stocker, T. F., Qin, D., Plattner, G. K., Tignor, M., Allen, S. K., Boschung, J., Nauels, A., Xia, Y., Bex, B., Midgley, B. M., 2013. IPCC, 2013: climate change 2013: the physical science basis. Contribution of working group I to the fifth assessment report of the intergovernmental panel on climate change.

Stocklin, J., feb 1980. Geology of Nepal and its regional frame: Thirty-third William Smith Lecture. Journal of the Geological Society 137 (1), 1–34.
URL http://jgs.lyellcollection.org/cgi/doi/10.1144/gsjgs.137.1.0001

Stone, J. O., 2000. Air pressure and cosmogenic isotope production. Journal of Geophysical Research 105 (1), 23753.

Summerfield, M. A., 1991. Global geomorphology: an introduction to the study of landforms. Longman Scientific Technical, Harlow, Essex, England.

Tao, S., Eglinton, T. I., Montluçon, D. B., McIntyre, C., Zhao, M., 2015. Pre-aged soil organic carbon as a major component of the Yellow River suspended load: Regional significance and global relevance. Earth and Planetary Science Letters 414, 77–86.
URL http://linkinghub.elsevier.com/retrieve/pii/S0012821X15000175

Tedesco, M., Kelly, R., Foster, J. L. L., Chang, A. T. C. T. C., 2004. AMSR-E/Aqua Daily L3 Global Snow Water Equivalent EASE-Grids, Version 2.

Thamban, M., Purnachandra Rao, V., Schneider, R. R., 2002. Reconstruction of late Quaternary monsoon oscillations based on clay mineral proxies using sediment cores from the western margin of India. Marine Geology 186 (3-4), 527–539.
URL http://www.sciencedirect.com/science/article/pii/S0025322702002682

Thiede, R. C., Arrowsmith, J. R., Bookhagen, B., McWilliams, M. O., Sobel, E. R., Strecker, M. R., 2005. From tectonically to erosionally controlled development of the Himalayan orogen. Geology 33 (8), 689–692.
URL http://geology.gsapubs.org/content/33/8/689.abstract

Thompson, L. G., Yao, T., Mosley-Thompson, E., Davis, M. E., Henderson, K. A., Lin, P. N., 2000. A high-resolution millennial record of the South Asian Monsoon from Himalayan ice cores. Science 289 (5486), 1916–1919.
URL <GotoISI>://WOS:000089355800040://www.sciencemag.org/content/289/5486/1916.full.pdf

Tierney, J. E., Russell, J. M., Huang, Y., Damste, J. S. S., Hopmans, E. C., Cohen, A. S., 2008. Northern Hemisphere Controls on Tropical Southeast African Climate During the Past 60,000 Years. Science 322 (5899), 252–255.
URL http://www.sciencemag.org/cgi/doi/10.1126/science.1160485

Tipple, B. J., Pagani, M., nov 2013. Environmental control on eastern broadleaf forest speciesâ leaf wax distributions and D/H ratios. Geochimica et Cosmochimica Acta 111, 64–77.
URL http://linkinghub.elsevier.com/retrieve/pii/S0016703712006242

Townsend-Small, A., McClain, M. E., Hall, B., Noguera, J. L., Llerena, C. A., Brandes, J. A., 2008. Suspended sediments and organic matter in mountain headwaters of the Amazon River: Results from a 1-year time series study in the central Peruvian Andes. Geochimica et Cosmochimica Acta 72 (3), 732–740.

USGS, 2006. Shuttle Radar Topography Mission. Global Land Cover Facility, University of Maryland, College Park.

Von Blanckenburg, F., 2005. The control mechanisms of erosion and weathering at basin scale from cosmogenic nuclides in river sediment. Earth and Planetary Science Letters 237 (3), 462–479.

Von Blanckenburg, F., Hewawasam, T., Kubik, P. W., 2004. Cosmogenic nuclide evidence for low weathering and denudation in the wet, tropical highlands of Sri Lanka. Journal of Geophysical Research: Earth Surface 109 (F3).

Wager, L. R., 1937. The Arun River Drainage Pattern and the Rise of the Himalaya. The Geographical Journal 89 (3), 239–250.

Wan, Z., Dozier, J., 1996. A generalized split-window algorithm for retrieving land-surface temperature from space. IEEE Transactions on Geoscience and Remote Sensing 34 (4), 892–905.

Wang, B., Fan, Z., 1999. Choice of South Asian Summer Monsoon Indices. Bulletin of the American Meteorological Society 80 (4), 629–638.

Weijers, J. W., Schouten, S., Schefuß, E., Schneider, R. R., Sinninghe Damsté, J. S., jan 2009. Disentangling marine, soil and plant organic carbon contributions to continental margin sediments: A multi-proxy approach in a 20,000 year sediment record from the Congo deep-sea fan. Geochimica et Cosmochimica Acta 73 (1), 119–132.
URL http://linkinghub.elsevier.com/retrieve/pii/S0016703708006145

Wen, R., Tian, L., Weng, Y., Liu, Z., Zhao, Z., 2012. The altitude effect of δ 18O in precipitation and river water in the Southern Himalayas. Chinese Science Bulletin 57 (14), 1693–1698.
URL http://link.springer.com/10.1007/s11434-012-4992-7

West, A. J., Lin, C.-W., Lin, T.-C., Hilton, R. G., Liu, S.-H., Chang, C.-T., Lin, K.-C., Galy, A., Sparkes, R. B., Hovius, N., 2011. Mobilization and transport of coarse woody debris to the oceans triggered by an extreme tropical storm. Limnol. Oceanogr. 56 (1), 77–85.

Wheatcroft, R. A., Goñi, M. A., Hatten, J. A., Pasternack, G. B., Warrick, J. A., 2010. The role of effective discharge in the ocean delivery of particulate organic carbon by small, mountainous river systems. Limnology and Oceanography 55 (1), 161–171.

Whipple, K., Tucker, G., 1999. Dynamics of the stream-power river incision model: Implications for height limits of mountain ranges, landscape response timescales, and research needs. Journal of Geophysical Research 104 (B8), 17661–17674.

Whipple, K. X., 2004. Bedrock Rivers and the Geomorphology of Active Orogens. Annual Review of Earth and Planetary Sciences 32 (1), 151–185.
URL http://www.annualreviews.org/doi/abs/10.1146/annurev.earth.32.101802.120356

Willenbring, J. K., von Blanckenburg, F., 2010. Long-term stability of global erosion rates and weathering during late-Cenozoic cooling. Nature 465 (7295), 211–214.
URL http://dx.doi.org/10.1038/nature09044

Wobus, C., Whipple, K. X., Kirby, E., Snyder, N., Johnson, J., Spyropolou, K., Crosby, B., Sheehan, D., 2006. Tectonics from topography: procedurses, promise, and pitfalls. Geological Society of America Special Paper 398 (04), 55–74.

Wulf, H., Bookhagen, B., Scherler, D., 2010. Seasonal precipitation gradients and their impact on fluvial sediment flux in the Northwest Himalaya. Geomorphology 118 (1-2), 13–21.

Wulf, H., Bookhagen, B., Scherler, D., 2012. Climatic and geologic controls on suspended sediment flux in the Sutlej River Valley, western Himalaya. Hydrology and Earth System Sciences 16 (7), 2193–2217.
URL http://www.hydrol-earth-syst-sci.net/16/2193/2012/http://www.hydrol-earth-syst-sci.net/16/2193/2012/hess-16-2193-2012.pdf

Wulf, H., Bookhagen, B., Scherler, D., 2016. Differentiating between rain, snow, and glacier contributions to river discharge in the western Himalaya using remote-sensing data and distributed hydrological modeling. Advances in Water Resources 88, 152–169.
URL http://www.sciencedirect.com/science/article/pii/S0309170815003000

Yanites, B. J., Tucker, G. E., Anderson, R. S., 2009. Numerical and analytical models of cosmogenic radionuclide dynamics in landslide-dominated drainage basins. Journal of Geophysical Research 114 (F1), F01007.
URL http://www.agu.org/pubs/crossref/2009/2008JF001088.shtml

Yanites, B. J., Tucker, G. E., Mueller, K. J., Chen, Y. G., Wilcox, T., Huang, S. Y., Shi, K. W., 2010. Incision and channel morphology across active structures along the Peikang River, central Taiwan: Implications for the importance of channel width. Geological Society of America Bulletin 122 (7-8), 1192–1208.
URL <GotoISI>://WOS:000278351300016://gsabulletin.gsapubs.org/content/122/7-8/1192.full.pdf

Yao, T., Guo, X., Thompson, L., Duan, K., Wang, N., Pu, J., Xu, B., Yang, X., Sun, W., jan 2006. δ 18O record and temperature change over the past 100 years in ice cores on the Tibetan Plateau. Science in China Series D 49 (1), 1–9.
URL http://link.springer.com/10.1007/s11430-004-5096-2

Zhao, M., Running, S. W., Nemani, R. R., 2006. Sensitivity of Moderate Resolution Imaging Spectroradiometer (MODIS) terrestrial primary production to the accuracy of meteorological reanalyses. Journal of Geophysical Research: Biogeosciences 111 (1), 1–13.

Zhisheng, A., Clemens, S. C., Shen, J., Qiang, X., Jin, Z., Sun, Y., Prell, W. L., Luo, J., Wang, S., Xu, H., Cai, Y., Zhou, W., Liu, X., Liu, W., Shi, Z., Yan, L., Xiao, X., Chang, H., Wu, F., Ai, L., Lu, F., 2011. Glacial-Interglacial Indian Summer Monsoon Dynamics. Science 333 (6043), 719–723.
URL http://www.sciencemag.org/cgi/doi/10.1126/science.1203752

Zhou, Y., Grice, K., Stuart-Williams, H., Farquhar, G. D., Hocart, C. H., Lu, H., Liu, W., 2010. Biosynthetic origin of the saw-toothed profile in δ13C and δ2Î of n-alkanes and systematic isotopic differences between n-, iso- and anteiso-alkanes in leaf waxes of land plants. Phytochemistry 71 (4), 388–403.
URL http://linkinghub.elsevier.com/retrieve/pii/S0031942209005299

List of Figures

List of Tables

Selbständigkeitserklärung

Ich erkläre, dass ich die vorliegende Arbeit selbständig und nur unter Verwendung der angegebenen Literatur und Hilfsmittel angefertigt habe.

Potsdam, den 12.04.2016 Bernd Hoffmann